HAL open science

Luminescent nanomaterials for diagnostic applications

Chien-Wei Hsu

To cite this version:

Chien-Wei Hsu. Luminescent nanomaterials for diagnostic applications. Other. Université de Strasbourg, 2015. English. NNT : 2015STRAF022 . tel-01270177v1

HAL Id: tel-01270177

https://theses.hal.science/tel-01270177v1

Submitted on 5 Feb 2016 (v1), last revised 9 Feb 2016 (v2)

HAL is a multi-disciplinary open access archive for the deposit and dissemination of scientific research documents, whether they are published or not. The documents may come from teaching and research institutions in France or abroad, or from public or private research centers.

L'archive ouverte pluridisciplinaire **HAL**, est destinée au dépôt et à la diffusion de documents scientifiques de niveau recherche, publiés ou non, émanant des établissements d'enseignement et de recherche français ou étrangers, des laboratoires publics ou privés.

UNIVERSITÉ DE STRASBOURG

ÉCOLE DOCTORALE DES SCIENCES CHIMIQUES

Institut de Science et d'Ingénierie Supramoléculaires

THÈSE

présentée par :

Chien-Wei HSU

soutenue le : **01 Septembre 2015**

pour obtenir le grade de : **Docteur de l'université de Strasbourg**

Discipline/ Spécialité : Sciences Chimiques / Chimie

Luminescent Nanomaterials for diagnostic applications

THÈSE dirigée par :

Mme DE COLA Luisa	Professeur, Université de Strasbourg

RAPPORTEURS :

M. THOMPSON Mark	Professeur, University of Southern California
M. BONIFAZI Davide	Professeur, University of Namur

AUTRES MEMBRES DU JURY :

M. DOUDIN Bernard	Professeur, Université de Strasbourg

故天將降大任於斯人也，

必先苦其心志，勞其筋骨，餓其體膚，

空乏其身，行拂亂其所為，

所以動心忍性，增益其所不能。

–孟子 «孟子•告子下»

"**Thus, when Heaven is about to confer a great office on any man,**

it first exercises his mind with suffering, and his sinews and bones with toil.

It exposes his body to hunger, and subjects him to extreme poverty.

It confounds his undertakings.

By all these methods it stimulates his minds,

hardens his nature, and supplies his incompentencies."

--Mencius (Mengzi, Gaozi, Part II)

Table of Contents

Résume……..……..1

Chapter 1 General Introduction……19

1.1 Introduction of diagnostic methods…….20

1.2 Introduction of luminescent labels……..22

1.2.1 Organic fluorophores……...…..……....23

1.2.2 Metal complexes.....……...23

1.2.3 Quantum dots…….27

1.3 Silicon nanoparticles (Si NPs)……...……28

1.3.1 Si NPs Synthetic methods….……29

1.3.2 Surface chemistry of Si NPs……...32

1.3.3 Luminescent properties of Si NPs……..33

1.4 Electrochemiluminescence……...……34

1.3.1 ECL in Ir(III) complexes……....35

1.3.2 ECL in nanomaterials……..……...36

1.5 Scope the thesis……...38

Chapter 2 Novel Ir(III) Complexes for ECL Applications……..….45

2.1 Introduction……46

2.2 Synthesis of complexes……...……...48

2.3 Crystal structure……48

2.4 Absorption and emission spectroscopy…….……50

2.5 Computational calculation……..……53

2.6 Electrochemistry…….……58

2.7 Electrochemiluminescence……59

2.8 Cell imaging of Ir(III) complex 2……...64

2.9 Conclusion……..65

2.10 Experimental section……66

Chapter 3 Synthesis and Characterization of Silicon Nanoparticles..75

3.1 Introduction……...76

3.2 Synthesis and characterization of Si NPs……...…77

3.3 Photophysical properties……....85

3.4 Conclusion……..88

3.5 Experimental section……..89

Chapter 4 Silicon Nanoparticles for Bioimaging……..95

4.1 Introduction……..……..96

4.2 Synthesis and characterization……...…98

4.3 Photophysical properties……...…104

4.4 In vitro imaging……..……107

4.5 Conclusion……..……113

4.6 Experimental section……..114

Chapter 5 Nano-system of Si NPs and Pt(II) Complexes.……121

5.1 Introduction……..…122

5.2 Synthesis and characterization……..……124

5.3 Photophysical properties……..131

5.4 In vitro study……136

5.5 Conclusion……....140

5.6 Experimental section……141

Chapter 6 Nanoparticles-Metal Complex Hybrid Nanosystems for ECL Applications……...……..149

6.1 Introduction……..……150

6.2 Ruthenium complexes–carbon dots nanosystems……152

6.2.1 Synthesis……..152

6.2.2 Characterization……...……152

6.2.3 Photophysical properties……155

6.2.4 Electroluminescence (ECL)……...…158

6.3 Iridium complexes–silicon nanoparticles nanosystems……162

6.3.1 Synthesis……..162

6.3.2 Characterization……...162
6.3.3 Photophysical properties…….165
6.3.4 Electroluminescence (ECL)……....168
6.4 Conclusion……...…….172
6.5 Experimental section……...….173

Chapter 7 Instrumental Methods……179
7.1 UV-Vis absorption measurement…….180
7.2 Emission measurement…….180
7.3 Time resolved Spectroscopy measurement…….…..182
7.4 Transmission Electron Microscopy (TEM)…….….183
7.5 Scanning Transmission Electron Microscopy (STEM)…….……...184
7.6 Confocal Microscopy……...…185
7.7 X-ray photoelectron spectroscopy (XPS)…….186
7.8 Electrochemistry……...187

Summary…….……..191

Acknowledgements……...……197

Curriculum Vitae……..199

Résume

Les matériaux luminescents basés sur des fluorophores organiques sont très utilisés dans les systèmes opto-électroniques, les détecteurs de gaz et de substances chimiques ainsi que dans la bio-imagerie. Cependant, les petits déplacements de Stokes, les courtes durées de vie à l'état excités ainsi que le photoblanchiement sont des inconvénients majeurs, notamment dans la bio-imagerie.[1] A l'opposé, les complexes organo-métalliques et les «points quantiques» («quantum dots» en anglais) sont considérés comme outils potentiels pour leurs rendements quantiques de photoluminescence élevés, leurs longues durées de vie à l'état excités ainsi que leur résistance au photoblanchiement. Les applications de complexes organométalliques et de « quantum dots » dans la bio-détection, la bio-imagerie et le domaine dit de «drug delivery» sont de nos jours de plus en plus étudiées.[2-4]

L'objectif de ma thèse intitulée "Nanomatériaux luminescents pour applications en diagnostic" porte sur la synthèse, la caractérisation et les applications en bio-imagerie de nanomatériaux de très petite taille (< 5 nm). Comme le montre la figure S1, ces travaux portent sur la modification sur la surface de nanoparticules de silicium par des sucres et des molécules jouant le rôle d'« étiquettes luminescentes » appliqués à l'imagerie cellulaire. De plus, une série de complexes d'Iridium(III) a été synthétisée et utilisée pour des applications en électrochemiluniescence (ECL). L'ECL est un outil d'imagerie qui génère, dans les molécules luminescentes, un état excité sans excitation par la lumière et qui attire de plus en plus l'attention dans les analyses biologiques en raison de sa sensitivité. Les Si NPs ont été également fonctionnalisées avec des complexes métalliques pour améliorer les propriétés à l'état excité, en particulier les durées de vie. Une comparaison avec des « carbon dots » et l'étude des ces deux types

de nanoparticules (carbone et silicium) en ECL a été réalisée.

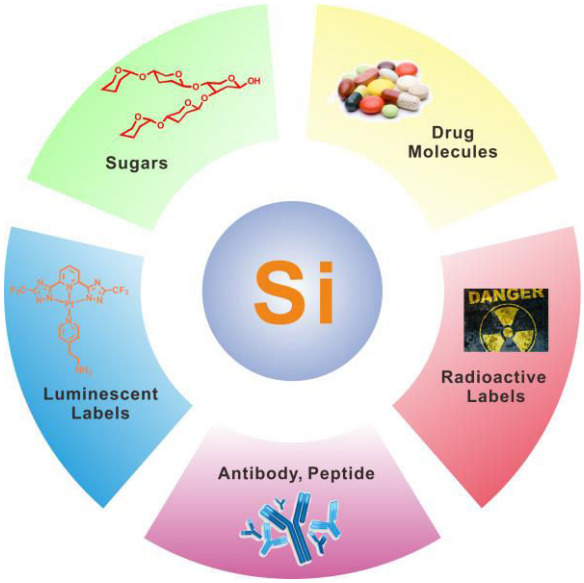

Figure S1. Nanoparticules de silicium et leurs modifications à la surface

Ma thèse est divisée en 7 chapitres. Le chapitre 1 traite d'une brève introduction sur les matériaux, ainsi que sur les « étiquettes luminescentes » (luminescent labels), tels que des fluorophores organiques, des complexes métalliques et des « quantum dots » ; pour l'imagerie optique. Les méthodes de diagnostic utilisées de nos y jours y sont également mentionnées. En plus de cela, une introduction sur les nanoparticules de silicium (Si NPs) et leurs méthodes de préparation reportées dans la littérature sont mises en avant. Finalement, pour aider le lecteur à se familiariser avec cette technique plutôt rare, le principe de l'électrochemiluminescence (ECL) est présenté.

Le chapitre 2 présente de nouveaux complexes d'iridium(III) pour des applications en ECL. L'électrochemiluminescence est le procédé dans lequel les espèces sont générées à certaines électrodes et les espèces présentes en solution subissent des réactions de transfert d'électron à haute énergie pour former des états excités émissifs. En tant qu'outil de détection, cela apporte à la fois une technique de luminescence et

une haute sensitivité, également due à l'absence de source de lumière excitante.[5] Parmi toutes les variétés de procédure d'ECL reportées jusqu'à présent,[6] la plus étudiée et utilisée est basée sur le complexe ruthénium trisbipyridine $[Ru(bpy)_3]^{2+}$,[7] en tant qu'émetteur et la tri-n-propylamine(TPA) en tant que co-réactant. Ce système fourni une haute efficacité en milieu aqueux. Il s'agit de la base même de plusieurs bio et immuno-essais, tests sur la nourriture et sur l'eau, ou de la détection de séquence d'ADN présents sur le marché.[5] Cependant, Une plus haute sensitivité d'ECL ainsi que différentes couleurs d'émission sont désirées en raison de l'augmentation de la demande pour la précision ou le multiplexage de dignostics. Une approche prometteuse est donc de remplacer $[Ru(bpy)_3]^{2+}$ par des complexes d'iridium cyclométallés.

Les complexes phosphorescents d'iridium(III) jouent un rôle important dans les OLEDs ainsi que dans la bio-imagerie en raison de leurs rendements quantiques de photoluminescence élevés, leurs longues durées de vie à l'état excités, leur grands déplacements de Stokes. Leur modifiable émission du bleu au rouge obtenue par modification des ligands, est sûrement une intéressante stratégie.[8-11] Cependant, la haute efficacité d'ECL dans les régions du bleu et du vert et toujours rare.[12] Dans le but d'augmenter l'efficacité et de modifier la couleur d'ECL, nous avons développé une série de nouveaux complexes d'iridium avec des ligands ayant une longue π-conjugaison et des ligands auxiliaires chélatants. Les complexes obtenus ont été caractérisés et utilisés pour des mesures d'ECL. En effet, un ligand N^N (1H-pyrazole[5,4-h]quinoline) à longue π conjugaison et deux ligands C^N ancillaires de type dfppy, ppy, pq ou piq, coordinés à un ion d'Iridium(III) ont mené à la formation de quatres complexes **1** à **4** (Figure S2), avec de bons rendements et des propriétés photophysiques et électrochimiques pleinement étudiées. La structure crystalline de **3** a été obtenue et montre une géométrie octahédrale avec deux phénylisoquinolines en

position trans, et un ligand N^N coordiné è l'ion métallique. Des mesures d'ECL ont été réalisées selon trois méthodes : annihilation, co-réactif TPA et co-réactif BPO. Les complexes **1** à **3** montrent une faible efficacité ECL avec les méthodes d'annihilation et co-réactif TPA, en raison de l'instabilité de l'espèce redox et un niveau d'énergie non compatible avec celui de TPA. Cependant, avec la méthode dite co-réactif BPO, tous les complexes montrent une moyenne à forte efficacité ECL comparée à celle du standard $[Ru(bpy)_3]^{2+}$, particulièrement le complexe **4** qui affiche une efficacité 2,18 fois supérieure à $[Ru(bpy)_3]^{2+}$.

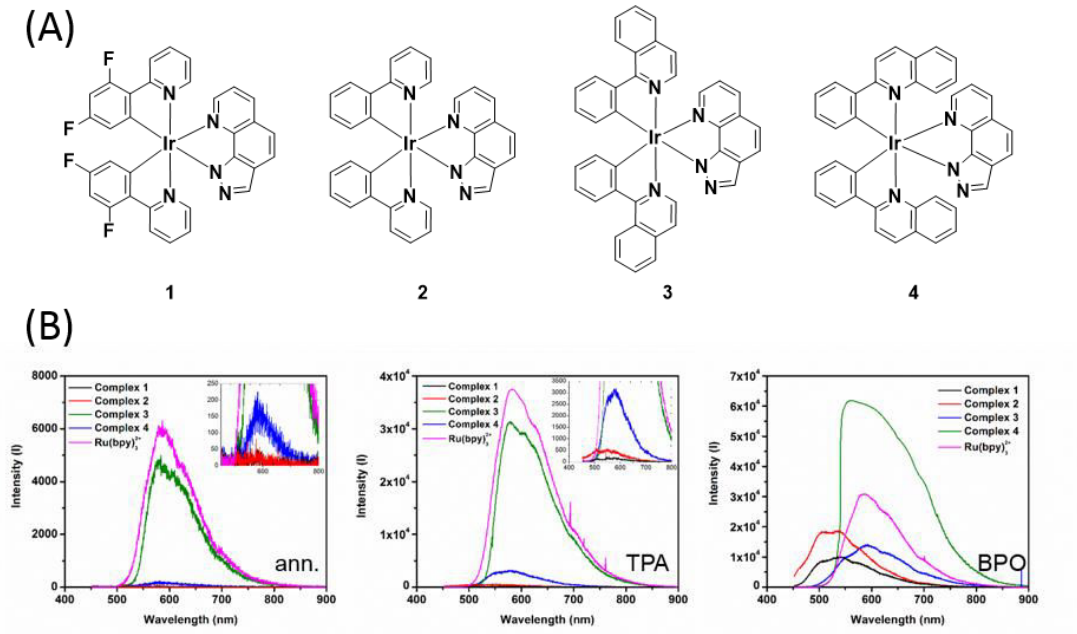

Figure S2. (A) Stucture des complexes d'Iridium. (B) Spectres ECL des complexes d'Iridium 1 à obtenus par différentes méthodes. (Gauche) méthode d'annihilation (milieu) méthode co-réctif TPA (droite) co-réactif BPO.

Les nanoparticules de silicium (Si-NPs), en tant que «quantum dots», sont étudiées depuis plus de vingt ans pour leurs propriétés photoluminescentes, leur stabilité optique et électronique, leur biocompatibilité et leur possibilité de modification à la surface.[13,

[14] En comparaison avec d'autres «quantum dots», elles sont moins toxiques et présentent une grande biocompatibilité.[15] Dans la littérature, il existe plusieurs méthodes de synthèse de Si NPs telles que l'ablation par laser, la gravure électrochimique, les procédés mécaniques, la décomposition en phase gaseuse et les procédés en solution.[16] Les procédés en solution permettent un contrôle de la taille ainsi que de la fonctionnalisation. Tilley et al. ont reporté une méthode par réduction dans des micelles.[14] D'autre part, les méthodes utilisant l'oxydation sont reportées par Kauzlarich et utilisant Mg_2Si et Br_2 en tant qu'agent oxydant.[17] Dans notre groupe, une méthode de réduction pour obtenir des Si NPs avec des terminaisons de type amine a été reportée. Dans ce cas, les Si NPs ont montré une biocompatibilité concluante et leur utilisation en tant que marqueurs dans la bio-imagerie a été étudiée dans les cellules BV2.[18]

Le chapitre 3 montre la fonctionnalisation des Si NPs avec deux différents groupements fonctionnels à la surface, à savoir amino et carboxylate. Des images au microscope électronique à transmission (TEM) et au microscope électronique à balayage par transmission (STEM) montrent des particules de 3,1 nm pour les Si-NH_2 NPs et 3,9 nm pour les Si-COOH NPs. Dans le cas de Si-COOH NPs, le groupement fonctionnel à la surface est identifié par spectroscopie infrarouge à transformée de Fourier (FTIR). En effet, la bande large à 2500 ~ 3600 cm^{-1} et la bande à 1730 cm-1 correspondent à la vibration de la liaison C=O de l'acide carboxylique. Les bandes à 2789, 1570, et 1375 cm^{-1} correspondent à la vibration des chaînes alkyles. La bande à 1260 cm^{-1} est typique de la liaison Si-C.[19] Enfin, Nous pouvons voir une bande de faible intensité à 1000 ~ 1100 cm^{-1} correspondant aux vibrations des liaisons- Si-O, montre la formation, bien que faible, de silice.

Dans le chapitre 4, les Si-COOH NPs ont ensuite été couplées avec des molécules de glucose (Si-Glc NPs) et utilisées en bio-imagerie. Les images STEM de Si-Glc NPs montrent l'agrégation des particules pour former des particules de plus grande taille (20 nm) ce qui a déjà été montré dans la littérature par des interactions sucre-sucre.[20] Les spectres FTIR montrent la formation de la liaison amide (1648 cm^{-1}, élongation de C=O) et 1565 cm^{-1} (N-H). Le potential zeta change de -37.60 ± 1.9 mV (Si-COOH NPs) à -15.38 ± 2.8 mV (Si-Glc NPs). L'aperçu général par spectroscopie photoélectronique aux rayons-X (XPS) montre que les Si-Glc NPs contiennent les élements Si, C, O et N. L'énergie de liaison 2p du silicium a été détectée à 101.68 eV (signal pour Si-C). En revanche, aucun signal indiquant la formation de Si-O (104 eV) n'a été observé. Les measures photophysiques ont été réalisées dans l'éthanol (Figure S3). Les particules exhibent une absorption continue sans bande signifiante dans le spectre de l'UV-Visible due à la bande interdite indirecte du silicium. L'émission de ces deux particules (Si-COOH et Si-Glc NPs) sont à respectivement à 474 et 465 nm. La durée de vie à l'état excité présente des déclins multi-exponentiels. En effet, pour Si-COOH-NPs les valeurs sont de 1.4 ns (50.9%), 3.67 ns (42.7%), 10.88 ns (6.4%). Concernant Si-Glc NPs, les valeurs sont de 0.26 ns (67.5%), 3.03 ns (26.9%), 8.95 ns (5.6%). En analysant la corrélation rotationnelle de la durée de vie par des mesures de déclin d'anisotropie, de fortes interactions entre Si-Glc NPs et l'éthylène glycol utilisé en tant que solvant ont été observées, ayant pour conséquence un plus long déclin d'anisotropie. Ceci est bien la preuve que les molécules de glucose sont liées aux Si NPs.

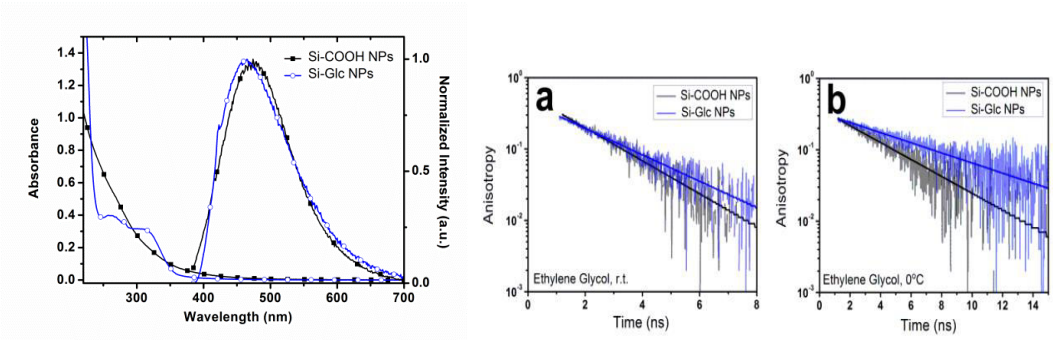

Figure S3. (gauche) Propriétés photophysiques de Si-COOH et Si-Glc NPs. Tous les échantillons on été mesurées dans de l'éthanol en présence d'oxygène, et les spectres d'émission ont été obtenu à λex = 375 nm. (droite) spectres de déclin d'anisotropie de Si-COOH et Si-Glc NPs. (a) éthylène glycol, température ambiante. (b) éthylène glycol, 0°C.

Les études *in vitro* (Figure S4) montrent que les Si-Glc NPs sont internalisées rapidement par les cellules HeLa, et les particules sont principalement localisées dans le lysosome (coefficient de chevauchement= 0.84) avec toutefois une plus petite portion dans le réticulum endoplasmique (coefficient de chevauchement= 0.62). Cette internalisation rapide est très probablement due à la présence de transporteur de glucose (GLUT) qui existe dans plusieurs cellules cancéreuses.[21, 22] Concernant les Si-COOH NPs, elles ont également été internalisées par les cellules HeLa et localisées dans le lysososme (coefficient de chevauchement= 0.87) ainsi dans le réticulum endoplasmique (coefficient de chevauchement= 0.86). Des tests de viabilité des cellules révèlent que les deux Si NPs sont biocompatibles et non toxiques envers les cellules HeLa. En effet, même à forte concentration, (100 µg/mL), la viabilité des cellules demeure assez élevée, 80.7% pour Si-COOH NPs et 84.5% pour Si-Glc NPs.

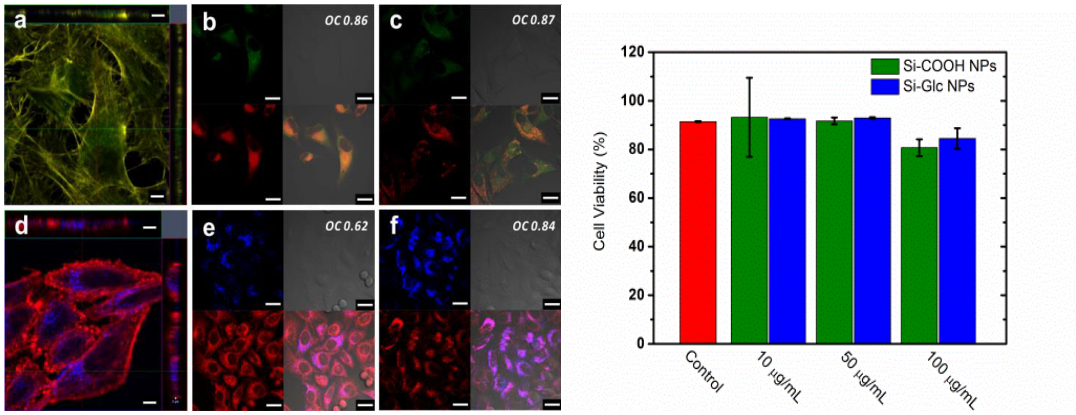

Figure S4. (gauche) imagerie au microscope confocal de Si-COOH NPs à 100 µg/mL (a)-(c) et Si Glc NPs à 100 µg/mL (d)-(f) dans ses cellules HeLa. (a) «Z stack» de Si-COOH NPs après 24h de temps d'incubation (b) Localisation cellulaire de Si-COOH NPs dans le réticulum endoplasmique (c) localisation cellulaire de Si-COOH NPs dans le lysosome. (d) «Z stack» de Si-Gln NPs après 24h (e) localisation cellulaire de Si-Gln NPs dans le réticulum endoplasmique (f) localisation cellulaire de Si-Gln dans le lysosome. Echelle : 5 µm pour (a) et (d); 20 µm pour (b), (c), (e) et (f) (droite) Test de viabilité des cellules de Si-COOH NPs et de Si-Glc NPs à différentes concentrations (10, 50 et 100 µg/mL) dans des cellules HeLa après 24 heures de temps d'incubation.

Le chapitre 5 décrit le couplage des Si NPs avec des complexes de Platine(II). Les complexes de platine, avec des ligands appropriés, ont d'intéressantes proprieties de luminescence qui, dans certains cas, peut-être modulé par leur tendance à former des agrégats. EN effet, l'agrégation peut causer une intéraction entre les orbitales dz2, ce qui a pour conséquence un nouvel état excité appelé transfert de charge de métal-métal-à-ligand (MMLCT). Cette découverte a été exploitée pour des OLEDs blanches en controllant le ratio entre le monomère et l'excimère, la lumière blanche étant formée en utilisant une seule molécule. [23] De plus, les complexes de Pt(II) forment des fibres et exhibent une émission anisotropique sous excitation avec la lumière polarisée.[24, 25] Récemment, des emissions induites par aggregation (en anglais «aggregation-induced

emission» AIE) ont été obserés dans des complexes de Pt(II).[26, 27] En ajoutant un mauvais solvant, les complexes de Pt(II) ont une tendance à s'agréger et à améliorer l'emission par formation de l'état ^{3}MMLCT. De tels changements ont été récemment explorées pour la bio-imagerie car la luminescence peut-être très intense et la durée de vie à l'état excité de l'ordre de la centaine de nanosecondes. Durant ces travaux, l'étude du comportement de complexes de Pt(II) conjugués à des Si NPs modifiés par des groupements acide carboxylique ainsi que leurs propriétés luminescentes.

Deux complexes de Pt(II) Pt-CF3 et Pt-tmp (formules: Figure S5) ont été synthétisés en mélangeant $Pt(DMSO)_2Cl_2$, les ligands 2,6-bis(triazolyl)pyridine et 4-[2-(N-tBoc)aminoethyl]pyridine dans l'acétonitrile à reflux pendant 15 heures. Le groupement t-Boc a été deprotégé dans une solution de 15% d'acide trifluoroacétique (TFA) dans le dichlorométhane. Le groupement amine a été protégé pour éviter la chélation au platine lors de la première étape La Figure S6 montre les spectres d'absorption UV-Visible, mesurés dans le méthanol à 10^{-5} M. Le complexe Pt-CF3 exhibe deux bandes à 252 et 298nm (transition $\pi\pi^*$, $\varepsilon = 1.6 \times 10^4$ and 1.1×10^4 $cm^{-1}M^{-1}$) ainsi que des bandes dans la région 350-450 nm (transition MLCT, $\varepsilon = 0.6 \times 103$ $cm^{-1}M^{-1}$). Le complexe Pt-tmp exibe une bande intense à 282 nm (transition LC du ligand tridentate $\varepsilon = 2.0 \times 10^4$ $cm^{-1}M^{-1}$) ainsi que des bandes larges dans la région 385-500nm (MLCT, $\varepsilon = 1.2 \times 10^3$ $cm^{-1}M^{-1}$) L'émission à l'état solide de ces complexes est centrée à 570nm pour Pt-CF3 et 592 nm pour Pt-tmp. L'émission est attribuée à la formation d'agrégats. La durée de vie de l'état excité à l'état solide de Pt-CF3 montre un déclin multi-exponentiel avec des valeurs de 0.40 (47.3%), 0.86 (26.8%), 0.1 (25.9%) µs, alors que pour Pt-tmp elles sont de 0.83 (44.6%), 0.18 (35.7%), 2.37 (19.7%) µs. Les rendements quantiques d'émission à l'état solide ont été mesurés à l'aide d'une sphère intégrante. Les valeurs sont 30% pour Pt-CF3 et 6% pour Pt-tmp.

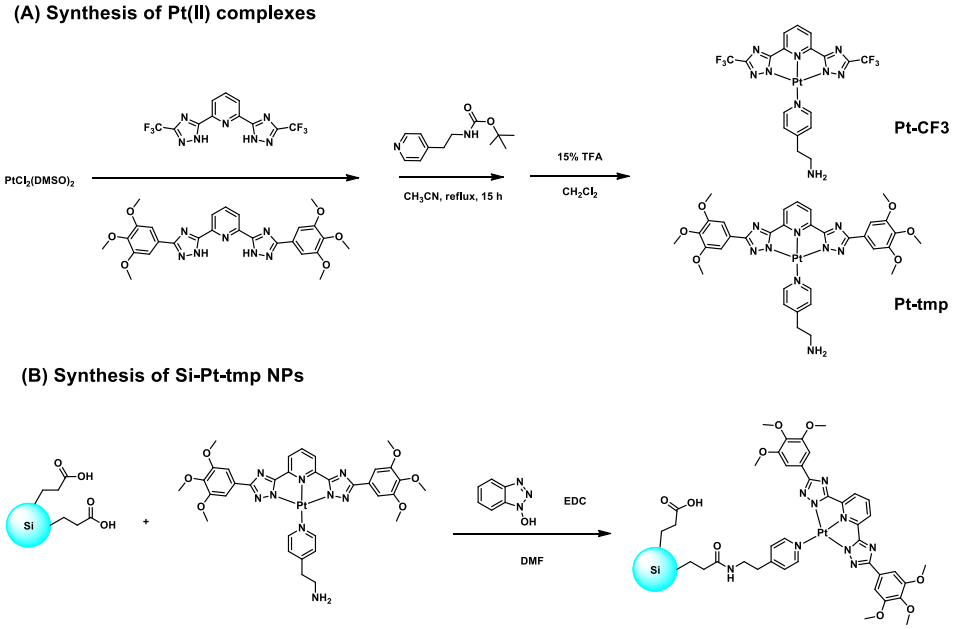

Figure S5. (A) Voie de synthèse schématique des complexes de Pt(II) étudiés et (B) couplage aux Si-NPs: Si-Pt-tmp-NPs.

Le complexe amino Pt-tmp a ensuite été couplé à Si-COOH NPs avec l'agent de couplage EDC pour former Si-[Pt] NPs et a été purifié par chromatographie par exclusion stérique (LH-20). Les spectres FTIR montrent la présence du groupement carbonyle de l'acide carboxylique à 1714cm^{-1} (élongation) et du groupement amide à 1635 cm^{-1} (élongation). Nous pouvons en déduire que le couplage n'est pas total, car des groupements acide sont toujours à la surface de la nanoparticule. L'aperçu général de l'analyse XPS a révélé les éléments Si, Pt, C, O et N. L'énergie de liaison des électrons Si 2p est de 101.9 eV, ce qui est attribué à la liaison Si-C. Les propriétés photophysiques ont été mesurées dans le méthanol et à l'état solide en présence d'oxygène (Figure S6) Après modification avec les complexes de Pt(II), les Si-[Pt] NPs montrent un spectre d'absorpion similaire aux Si NPs, avec un épaulement supplémentaire à 275 nm attribué à l'absorption du complexe de platine. L'émission de Si-[Pt] NPs dans le méthanol comporte deux bandes d'émission sous une excitation à 325 nm. L'émission à 460 nm est attribuée à Si NPs et celle à 525 nm au complexe de

platine. A l'état solide, Si-tmp NPs montre une émission très intense à 550 nm.

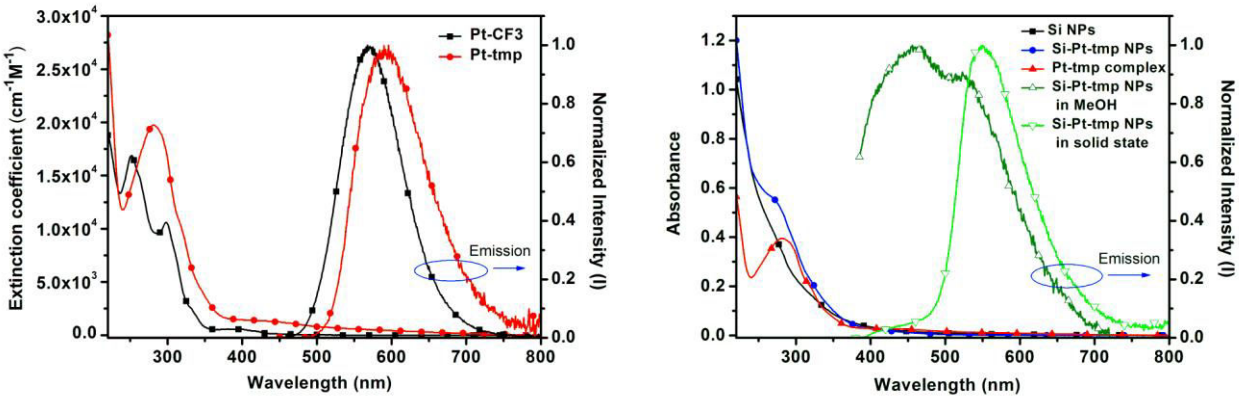

Figure S6. (gauche) spectres d'absorption UV-Visible (méthanol, 10^{-5}M) et émission à l'état solide de Pt-CF_3 et Pt-tmp (λex 400 nm) (droite) Spectres d'absorption de Si NPs , Si-Pt-tmp NPs et Pt-tmp dans le méthanol et spectre d'émission de Si-Pt-tmp NPs dans le méthanol (λex 325 nm) et à l'état solide (λex 325 nm).

Deux complexes de Platine (II) Pt-CF_3 et Pt-tmp, ont été synthétisées et conjuguées aux Si-COOH NPs. Les deux types de nanoparticules ont été caractérisées par spectroscopie infrarouge à transformée de Fourier (FT-IR) et spectroscopie à photoélectrons induite aux rayons X (XPS). Si-[PtCF3] NPs montre une intéressante émission induite par agrégation (AIE). Les nanoparticules on été dispersées dans du méthanol et de l'eau, en tant que « non-solvant », a été ajouté. En ajoutant de l'eau, l'intensité d'émission augmente et un effet batochrome et observé. (Figure S7) L'augmentation de l'émission est due à l'empilement du complexe de Platine(II), (voir chapitre 5 pour plus de détails), l'agrégation protégeant le système de l'oxygène, évitant donc l'extinction de luminescence. L'effet bathochrome est quant à lui dû aux interactions Pt-Pt, se traduisant par une nouvelle transition, dite transfert de charge métal-métal- à ligand (MMLCT). Cependant, le système Si-[Pttmp] NPs ne présente

pas d'effet AIE aussi marquant que le précédant système. De plus, Ces deux nanoparticules couplées on été assimilés par des cellules HeLa, indiquant que ces particules sont de bonnes « étiquettes luminescentes » pour la bio-imagerie.

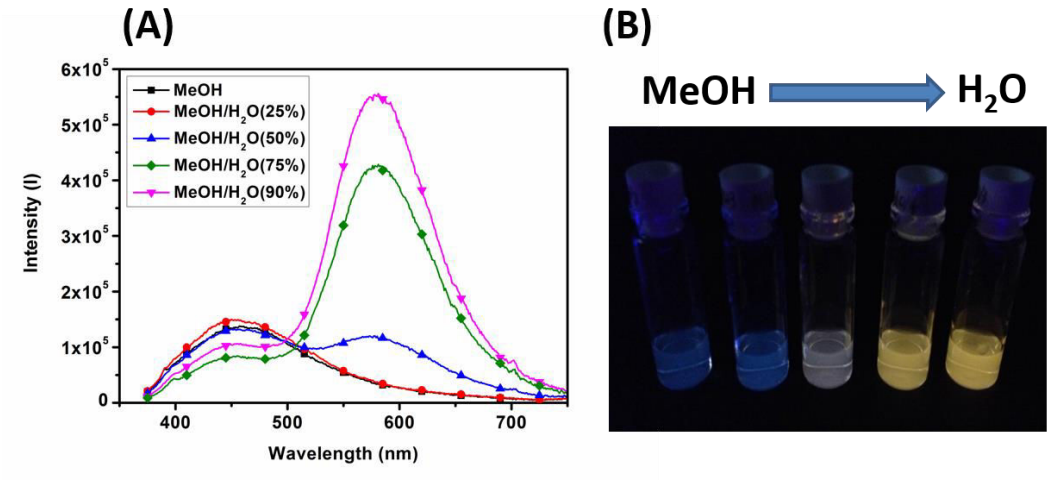

Figure S7. (A) Spectres d'émission de Si-[PtCF3]-2 NPs dans un mélange méthanol/eau, à différentes proportions ; avec une excitation à 340nm. (B) Echantillons sous irradiation UV, avec différentes proportions méthanol/eau.

Le chapitre 6 reporte deux nano-systèmes: un complexe de Ruthénium conjugué à des « carbons dots » (C-[Ru] NPs) et un complexe d'Iridium conjugué à des nanoparticules de silicium (C-[Ir] NPs). L'électrochemiluminescence (ECL) et la méthode la plus sensible utilisée pour la détection de biomolécules à concentration subpicolmolaire. La sensitivité est principalement due au manque de photo-excitation pour générer l'état excité de l'analyte marqué et au bas bruit de fond, lui-même dû à l'excitation sélective des marqueurs.[28] L'ECL demande l'utilisation d'un luminophore et bien que la référence utilisée jusqu'à présent est un dérivé de $[Ru(bpy)_3]^{2+}$, la recherche basée sur des complexes métalliques tels que le ruthénium et l'iridium ont montré une efficacité plus élevée en ECL que la référence.[29, 30] Récemment, les

nanoparticules de silice encapsulant des complexes métalliques ont montré de l'ECL et il est intéressant de noter que la coquille de silice protège le complexe métallique, qui est hydrophobique, de la solution aqueuse.[31, 32] Cependant, l'émission plus faible que celle des échantillons marqueurs ainsi que la grande taille des particules sont des inconvénients qui n'ont, jusqu'à présent toujours pas été surmontés. Nous avons donc decidé de developper des «carbon dots» couvert par $[Ru(bpy)_3]^{2+}$ pour des applications en ECL, profitant de la petite taille et de l'utilisation des nanoparticules uniquement en tant que plateforme multi-marqueurs. Egalement en raison de la présence de plusieurs fonctionnalités sur les particules, le système reste soluble dans l'eau et l'efficacité ECL se révèle être plus efficace que $[Ru(bpy)_3]^{2+}$. Les « carbon dots »sont de petits et plats systèmes et sont disponibles dans nos laboratoires, synthétisés par le groupe du Pr. Michele Maggini. La présence de groupements amines et carboxylates les rend hydorphyliques et facilite leur fonctionalisation. Ces groupements se révèlent être également responsables de l'émission, cette dernière dépendant beaucoup de la longueur d'onde d'excitation.[33]

Afin de comparer l'efficacité ECL avec le standard $[Ru(bpy)_3]^{2+}$, la concentration des complexes métalliques dans les nano-systèmes est suivie par mesures d'absorption UV-Visible et contrôlée à 10^{-5} M. Les expériences ECL ont été réalisées dans une solution de ProCell utilisant du TPA comme co-réactant et appliquant une tension de 1,4 V sur une électrode en carbone vitreux. Il est intéressant de ne constater aucune extinction de luminescence des complexes métalliques, ces derniers conservant la même performance lorsqu'ils sont lies aux « carbon dots ». (Figure S8) Le spectre ECL montre que C-[Ru] NPs possède une efficacité ECL légèrement supérieure (107%) que $[Ru(bpy)_3]^{2+}$ seul (100%). L'autre nano-système, Si-[Ir] NPs, montre une efficacité ECL inférieure (75%), probablement due à la lente diffusion de masse de Si NPs.

Actuellement, des travaux sont en progrès pour optimiser le système et pour évaluer le nombre de complexes par particules.

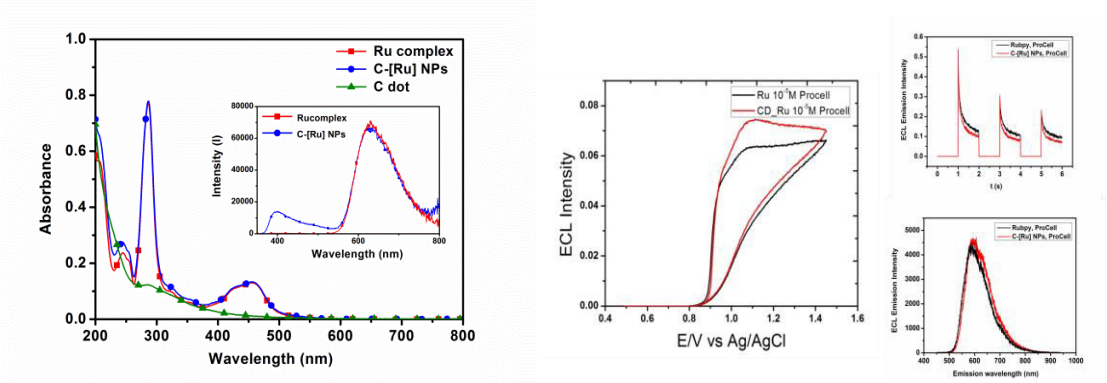

Figure S8. (gauche) Spectres UV-Visible de “carbon dots” C-[Ru] NPs and $[Ru(bpy)_3]^{2+}$, utilisé comme standard, dans l’eau. A l’interieur : spectre d’émission de C-[Ru] NPs et du standard dans l’eau. (droite)Spectres de voltammétrie cyclique et d’ECL du système étudié.

Dans le chapitre 7, les instruments et techniques utilisées dans cette thèse, ainsi que les détails expérimentaux sont résumés.

En conclusion, cette thèse montre que des nanoparticules de très petite taille peuvent être un outil intéressant dans le diagnostic et l’imagerie *in vitro* et éventuellement *in vivo*. Nous avons démontré la synthèse et la modification à la surface de Si NPs. Si-Glc NPs montrent une haute assimilation cellulaire et biocompatibilité, il s’agit donc de matériaux très prometteurs pour des applications supplémentaires, en particulier des travaux sont en cours pour observer la traversée de la barrière hémato-encéphalique pour l’imagerie du cerveau. Si-Pt NPs montrent, quant à eux, un intéressant effet AIE et permettant des applications bio-imagerie. De nouvelles “étiquettes ECL” basées sur des complexes d’Iridium(III) et des nanoparticules avec des modifications à la surface,

utilisant des complexes métalliques. Ces deux systèmes, présentant de hautes efficacités ECL, nous donnent la direction pour la conception de nouvelles sondes ECL. De plus, nous avons démontré la synthèse et la modification à la surface des Si NPs.

Ce travail a été supporté financièrement par Helmhotz Virtual Institute “Functional nanomaterials for multimodality cancer imaging” (Nano-Tracking, Agreement Number VH-VI-421 ; réalisé avec des collaborations avec d’autres unités. Helmholtz-Zentrum Dresden-Rossendorf (Allemagne), University of Heidelberg (Allemagne), University College Dublin (Irlande) et Monash University (Australie). (Allemagne), University College Dublin (Irlande) et Monash University (Australie)

http://www.hzdr.de/db/Cms?pNid=2452

Reference

1. V. Fernandez-Moreira, F. L. Thorp-Greenwood and M. P. Coogan, *Chem. Commun.*, 2010, **46**, 186-202.
2. Q. Zhao, C. Huang and F. Li, *Chem. Soc. Rev.*, 2011, **40**, 2508-2524.
3. M. Mauro, A. Aliprandi, D. Septiadi, N. S. Kehr and L. De Cola, *Chem. Soc. Rev.*, 2014, **43**, 4144-4166.
4. M. V. Kovalenko, L. Manna, A. Cabot, Z. Hens, D. V. Talapin, C. R. Kagan, V. I. Klimov, A. L. Rogach, P. Reiss, D. J. Milliron, P. Guyot-Sionnnest, G. Konstantatos, W. J. Parak, T. Hyeon, B. A. Korgel, C. B. Murray and W. Heiss, *ACS Nano*, 2015.
5. A. J. Bard, *Electrogenerated Chemiluminescence*, Marcel Dekker, New York, 2004.
6. W. Miao, *Chem. Rev.*, 2008, **108**, 2506-2553.
7. M. M. Richter, *Chem. Rev.*, 2004, **104**, 3003-3036.
8. S. Lamansky, P. Djurovich, D. Murphy, F. Abdel-Razzaq, H.-E. Lee, C. Adachi, P. E. Burrows, S. R. Forrest and M. E. Thompson, *J. Am. Chem. Soc.*, 2001, **123**, 4304-4312.
9. C.-H. Yang, M. Mauro, F. Polo, S. Watanabe, I. Muenster, R. Fröhlich and L. De Cola, *Chem. Mater.*, 2012, **24**, 3684-3695.
10. S. Zanarini, M. Felici, G. Valenti, M. Marcaccio, L. Prodi, S. Bonacchi, P. Contreras-Carballada, R. M. Williams, M. C. Feiters, R. J. M. Nolte, L. De Cola and F. Paolucci, *Chem. Eur. J.*, 2011, **17**, 4640-4647.
11. J. I. Kim, I.-S. Shin, H. Kim and J.-K. Lee, *J. Am. Chem. Soc.*, 2005, **127**, 1614-1615.
12. S. Zanarini, M. Felici, G. Valenti, M. Marcaccio, L. Prodi, S. Bonacchi, P. Contreras-Carballada, R. M. Williams, M. C. Feiters, R. J. M. Nolte, L. De Cola and F. Paolucci, *Chem. Eur. J.*, 2011, **17**, 4640-4647.
13. J. R. Heath, *Science*, 1992, **258**, 1131-1133.
14. J. H. Warner, A. Hoshino, K. Yamamoto and R. D. Tilley, *Angew. Chem. Int. Ed.*, 2005, **117**, 4626-4630.
15. C. Kirchner, T. Liedl, S. Kudera, T. Pellegrino, A. Muñoz Javier, H. E. Gaub, S. Stölzle, N. Fertig and W. J. Parak, *Nano Lett.*, 2005, **5**, 331-338.
16. S. Chinnathambi, S. Chen, S. Ganesan and N. Hanagata, *Adv. Healthcare Mater.*, 2014, **3**, 10-29.
17. Q. Liu and S. M. Kauzlarich, *Mater. Sci. Eng. B*, 2002, **B96**, 72.
18. M. Rosso-Vasic, E. Spruijt, Z. Popovic, K. Overgaag, B. van Lagen, B. Grandidier, D. Vanmaekelbergh, D. Dominguez-Gutierrez, L. De Cola and H. Zuilhof, *J. Mater. Chem.*, 2009, **19**, 5926-5933.

19. L. Ruizendaal, S. P. Pujari, V. Gevaerts, J. M. Paulusse and H. Zuilhof, *Chem Asian J*, 2011, **6**, 2776-2786.
20. C. Tu, X. Ma, P. Pantazis, S. M. Kauzlarich and A. Y. Louie, *J. Am. Chem. Soc.*, 2010, **132**, 2016-2023.
21. P. M. A. de Farias, B. S. Santos, F. D. Menezes, A. G. Brasil Jr, R. Ferreira, M. A. Motta, A. G. Castro-Neto, A. A. S. Vieira, D. C. N. Silva, A. Fontes and C. L. Cesar, *Appl. Phys. A*, 2007, **89**, 957-961.
22. T. Suzuki, A. Iwazaki, H. Katagiri, Y. Oka, J. L. Redpath, E. J. Stanbridge and T. Kitagawa, *Eur. J. Biochem.*, 1999, **262**, 534-540.
23. L. Murphy, P. Brulatti, V. Fattori, M. Cocchi and J. A. G. Williams, *Chem. Commun.*, 2012, **48**, 5817-5819.
24. C. A. Strassert, C.-H. Chien, M. D. Galvez Lopez, D. Kourkoulos, D. Hertel, K. Meerholz and L. De Cola, *Angew. Chem. Int. Ed.*, 2011, **50**, 946-950.
25. M. Mauro, A. Aliprandi, C. Cebrian, D. Wang, C. Kubel and L. De Cola, *Chem. Commun.*, 2014, **50**, 7269-7272.
26. K. M.-C. Wong and V. W.-W. Yam, *Acc. Chem. Res.*, 2011, **44**, 424-434.
27. H. Honda, Y. Ogawa, J. Kuwabara and T. Kanbara, *Eur. J. Inorg. Chem.*, 2014, **2014**, 1865-1869.
28. L. Hu and G. Xu, *Chem. Soc. Rev.*, 2010, **39**, 3275-3304.
29. M.-J. Li, P. Jiao, M. Lin, W. He, G.-N. Chen and X. Chen, *Analyst*, 2011, **136**, 205-210.
30. M.-J. Li, Z. Chen, N. Zhu, V. W.-W. Yam and Y. Zu, *Inorg. Chem.*, 2008, **47**, 1218-1223.
31. S. Zanarini, E. Rampazzo, L. D. Ciana, M. Marcaccio, E. Marzocchi, M. Montalti, F. Paolucci and L. Prodi, *J. Am. Chem. Soc.*, 2009, **131**, 2260-2267.
32. S. Zanarini, E. Rampazzo, S. Bonacchi, R. Juris, M. Marcaccio, M. Montalti, F. Paolucci and L. Prodi, *J. Am. Chem. Soc.*, 2009, **131**, 14208-14209.
33. D. Mazzier, M. Favaro, S. Agnoli, S. Silvestrini, G. Granozzi, M. Maggini and A. Moretto, *Chem. Commun.*, 2014, **50**, 6592-6595.

CHAPTER 1

General Introduction

Abstract

We briefly introduce the most common diagnostic techniques for bioimaging, including magnetic resonance imaging (MRI), positron emission tomography (PET) and fluorescence imaging. Among these diagnostic methods, fluorescence imaging is getting very interesting, and especially, the design of luminescent labels. Three kind of luminescent labels, organic fluorophores, metal complexes and quantum dots, are presented and used for in vitro/vivo studies. Also an introduction on silicon nanoparticles gives insight into the properties of this material. Finally, an emerging imaging tool, electrochemiluminescence is introduced as well.

1.1 Introduction of diagnostic methods

With the rapid development of technology nowadays, the number of diagnostic tools have dramatically increased, finding a lot of improvement in accuracy and precision. As shown in Figure 1, the most common imaging technologies used in clinic are X-ray, ultrasound, computed tomography (CT) and magnetic resonance imaging (MRI), providing anatomical and physiological information.[1] Other techniques like positron emission tomography (PET) and fluorescence imaging are able to obtain molecular information. Here we present a description of the above mentioned techniques.

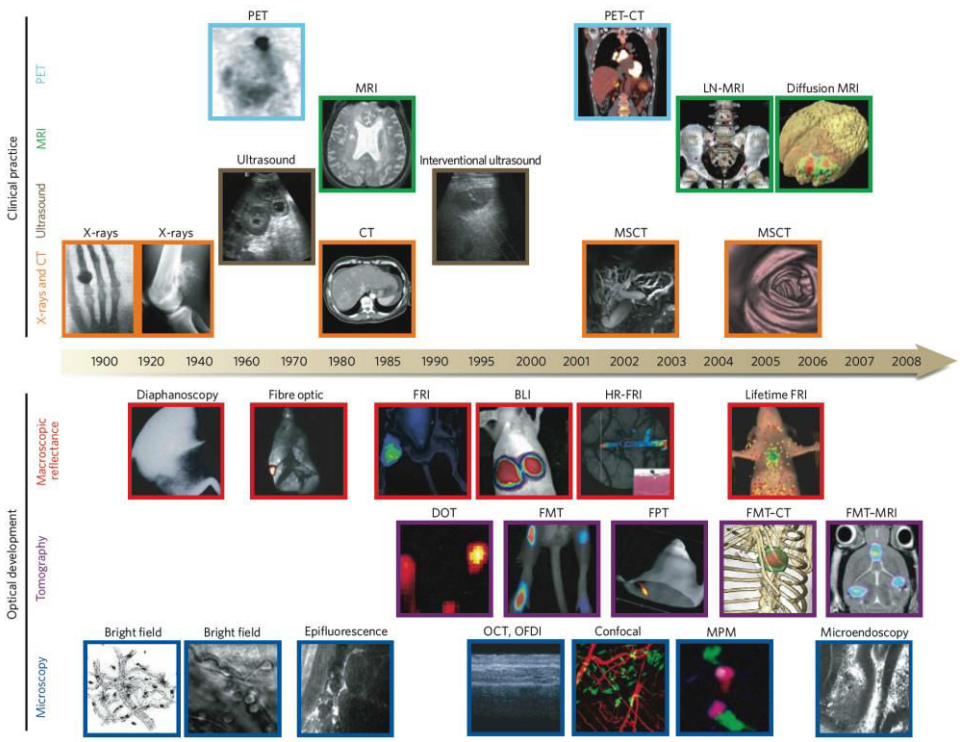

Figure 1. Imaging technologies. Reproduced from *Nature*, **2008**, *452*, 580-589 with permission from Nature Publishing Group.

MRI imaging

To perform MRI imaging, the patient is positioned inside a strong magnet field. The protons in water molecules in tissues (hydrogen nucleus, spin quantum number I = 1/2) can respond to an external magnetic field, splitting the spins into two states (2I +1 states), being the energy between two states proportional to the strength of the magnetic field. An external radio frequency pulse is applied at the same time and the nuclei absorb this specific energy, changing their spin orientation from +1/2 state to –1/2 state which, is called resonance. When the pulse is discontinued, the excited nuclei relax to the ground state. The radiofrequency (RF) signals from relaxation process can be recorded by the RF detector coils and convert to the MRI imaging.[2-4] This technique

has high resolution between 10 – 100 μm and no limited detection in depth. However, the low sensitivity (mM to μM), long time to acquire the data (minutes to hours) and high cost are still the drawbacks of this technique. Moreover, Table 1 shows the comparison of different imaging systems.

Table 1. Comparison of different imaging systems

Technique	Resolution	Depth	Time to acquire data	Sensitivity	Multi-channel	Cost
MRI	10–100 μm	No limit	Minutes to hours	mM to μM	No	***
CT	50 μm	No limit	Minutes	–	No	**
PET	1–2 mm	No limit	Minutes to hours	pM	No	***
Optical imaging	2–3 mm	<1cm	Seconds to minutes	nM to pM	Yes	*

PET imaging

To perform PET imaging, the patient is injected the radiopharmaceutical and placed on a special moveable bed which slides into a circular opening of detector. Positron emission tomography, PET, is a technique to detect high energy γ–rays generated by radioactive species. ^{15}O, ^{13}N, ^{11}C and ^{18}F are the common used positron emitting isotopes. When the radioactive species, ^{19}F for example, undergo a β decay,[5] a positron is generated. The emitted positron travels in a short distance and interacts with an electron. The annihilation of these counter particles, positron and electron, produce a pair of γ photons. Those γ–rays are collected on a radiation detector and generate the PET imaging.[6, 7] It has very high sensitivity at pM range and no limited depth detection. However, the experiment time takes minutes to hours and it also has high cost, being these important concerns.

Optical imaging

For the optical imaging, in vitro study for example, the cells were treated with fluorophores in certain incubation time for internalization and image the cells under microscopy. The principle of this method requires a luminophore which absorbs certain wavelength of light and emits light in longer wavelength. With different emission wavelength labels, multi-channel imaging can be performed at the same time. Besides, neither using high toxic gadolinium reagents, nor radiative species, fluorescence imaging can be seen as a safe and convenient tool. This method shows good sensitivity in nM to pM range and fast time to acquire the data (seconds to minutes).

However, the input light source and output signal are easily affected by the biological environment. Short wavelength light cannot penetrate the tissue more than 1 cm, and the incident or emission light is easy to be scattered or absorbed by the tissues leading to autofluorescence. To avoid this problem both, light absorption and scattering in tissues should be taken into account. The emission of chromophores should fit an optical window between 700 to 1100 nm.[8] As shown in Figure 2, water absorbs light both in UV and near IR regions, and many biological pigments and proteins such as melanin and haemoglobin (HbO_2) absorb visible light. Only in 700 to 1100 nm region lacks of efficient absorbers and is suitable for optical imaging.

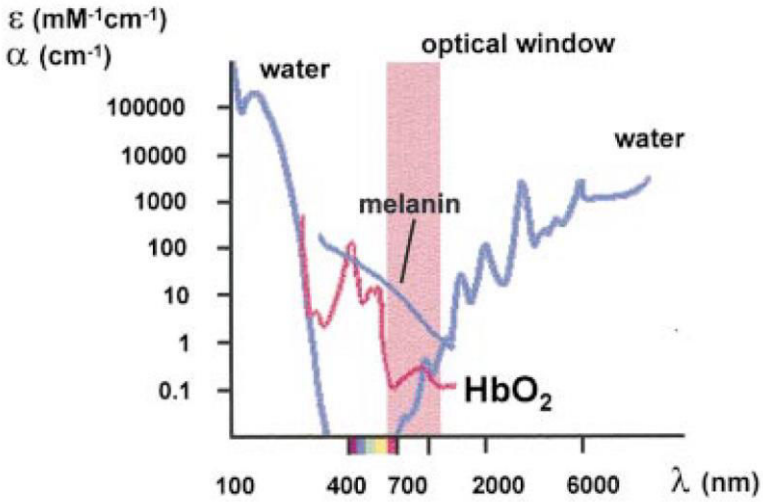

Figure 2. Absorption spectra of major intracellular absorbers. Reproduced from *Journal of Microscopy,* **2000***, 200,* 83–104 with permission from John Wiley and Sons.

1.2 Introduction of luminescent labels

Among these diagnostic tools, we would like to focus in optical imaging, especially in the design of the luminescent labels. One of the challenges is how to design the compounds with strong preferential localization. In order to target a specific cell or organelle, these luminescent chromophores are functionalized with bioactive molecules such as peptides, estradiol and vitamin conjugates.[9-13] With these specific biomolecules, the modified labels are able to selectively target particular cells or cellular structure. For example, folic acid modified luminophores can target HeLa cells which cell membrane contains lots of folate receptors (FR), while MCF-7 and NIH-3T3 cells are not labeled (FR negative).[14]

Besides being a good luminescent probe, there are many factors that need to be considered. According to Baggaley *et al.*,[15] in order to exploit the luminescent probes

and use then for bioimaging, the candidates should possess the following requirements:

(1) high extinction coefficient in the visible range
(2) high emission quantum yield
(3) solubility in water
(4) high cell permeability
(5) low cytotoxicity
(6) high chemical stability
(7) high photostability

However, in reality, it is hard to achieve all the conditions. Here, three type of luminescent probes are introduced: organic fluorophores, metal complexes and quantum dots, discussing their advantage and drawbacks.

1.2.1 Organic fluorophores

Organic fluorophores have been designed and selectively targeted to specific organelles over three decades.[16, 17] For instance, DAPI (4',6-diamidino-2-phenylindole) shows high emission quantum yield and high selectivity towards the cell nuclei.[18] Besides, other fluorescent labels such as fluorescein and rhodamine are also applied in many bioimaging because of the high quantum efficiency.[19] Recently, BODIPY (boron-dipyrromethene) received a lot of attention,[12, 13] due to its sharp fluorescence with high quantum yield, insensitivity to pH changes and tunable emission,[20, 21] it is used to label lipid membranes and proteins.[22, 23] However, the poor water solubility and difficult synthetic routes still need to be solved when applied in bioapplications.

1.2.2 Metal complexes

Other luminescent probes are metal complexes based on Ru, Ir, Re and Pt complexes The origin of emission can be explained by Jablonski diagram. (scheme 1) Upon light irradiation, the complex absorbs one photon and is excited from the ground state, S_0 (singlet ground state), to the higher excited states, S_n, $n \geq 1$ (singlet excited states). In these excited states, the energy is deactivated through different pathways. For example, internal conversion (IC) is a process through which the energy undergoes non-radiative deactivation though vibrational relaxation. The time scale of this process is in the picosecond range. Another process involves the deactivation from S_1 state to S_0 state through a radiative decay emiting a photon. This emission is called fluorescence and the time scale is of 10^{-9} to 10^{-7} s. Normally the molecules emit light from the lowest singlet excited state (S_1), and the emission wavelength is independent of the excitation wavelength (Kasha's rule). When heavy atoms, such as metal ions are present in the

system, a third deactivation process called intersystem crossing (ISC) can occur. It allows the excited molecules to cross from the lowest singlet excited state (S_1) to the lowest triplet excited state (T_1) (the time scale is 10^{-9} to 10^{-7} s) Then the T_1 state goes back to S_0 state through a radiactive decay called phosphorescence. This pathway is spin forbidden but it can happen in the case of increasing the spin-orbit coupling when heavy atoms are present. The time scale is relatively slow around 10^{-6} to 1 s.

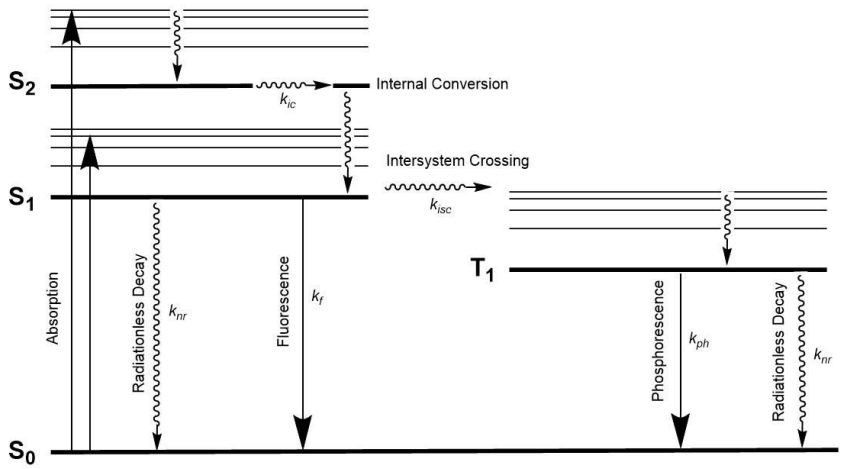

Scheme 1 Simplified Jablonski diagram

Pt complexes

d^8 electron configuration metal complexes are known to have high stacking tendency and change the photophysical properties.[24-26] For example, the famous linear chain structure in Krogmann salts[27] and platinum blue[28] show deeply colored crystals but no color in aqueous solution due to the d–d metal interactions in the solid state that do not exist in dilute system. In particular, square-planar Pt(II) complexes have strong tendency to stacking through non-covalent metal···metal and/or ligand π–π interactions.[29-31] As a result, the aggregated Pt complexes display a new electronic transition which is called metal-metal-to-ligand charge transfer (MMLCT). The mechanism can be illustrated in Scheme 2. When two Pt complexes are close enough (distance below 3.5Å), the d_z^2 orbitals of Pt metal have interaction with each other resulting a new excited state (MMLCT) and emission bathochromic shift.

This aggregation can be caused either by solid state polymorphism or solvent induced aggregation. Yam *et al* reported that[31], the Pt complex ([Pt(terpy)(C≡C–C≡CH)]OTf, OTf = trifluoromethanesulfonate), under different recrystalization conditions, yields two crystal structures, a dark green form with short Pt···Pt distance of 3.388 Å and a red form with long Pt···Pt distances of 3.394 and 3.648 Å. Mauro *et al* also reported that by drop casting Pt complexes can assemble into fibrous structure with

Pt···Pt distance of 3.28 Å.[26] In terms of solvent induced aggregation, Pt complexes tend to aggregate when adding unfavorable solvent into the Pt complex solution. Yam *et al.* exhibited the UV-Vis absorption of Pt complex changes (color form light yellow to green) upon adding diethyl ether into an acetonitrile solution containing the Pt complex [Pt(terpy)(C≡C–C≡CH)]OTf.[31] With such an interesting luminescent properties, Chang *et al.* presented tunable electroluminescence (EL) in OLED (Organic Light-Emitting Diode) devices using one Pt complex.[32] With increasing the dopant concentration in the device, the EL shift from 502 to 556 nm which is attributed to the π–π stacking interaction between the Pt complexes. Also Murphy *et al.* showed the white light OLED (WOLED) using a single Pt complex by controlling the ratio between the Pt monomer and excimer.[33]

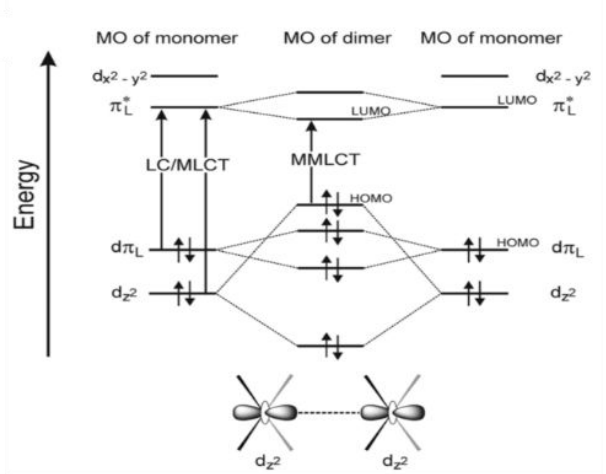

Scheme 2. Simplified MO diagram of two interacting square-planar platinum(II) complexes. Reproduced from *Chem. Soc. Rev.,* **2014**, *43*, 4144-4166 with permission from The Royal Society of Chemistry.

Moreover, Pt complexes present an interesting aggregation-induced emission (AIE) behavior.[34-37] By adding unfavorable solvent, Pt(II) complexes tend to aggregate and enhance the emission. The AIE mechanism in metal complex is still controversial due to the more complicated excited state properties. The most acceptable explanation for AIE effect is the restriction of intramolecular rotation (RIR).[38, 39] Generally, emission intensity is quenched when the organic compounds aggregate (aggregation caused-quenching, ACQ). However, by using appropriate ligand design to reduce the level of aggregation, the ACQ effect can be avoid and increase the emission. In the case of Pt complex, the enhanced emission could be also due to the formation of triplet metal-metal-to-ligand charge transfer (MMLCT) states and the aggregation protects the inner core from oxygen quenching.[40] Besides, decreasing the mobility of Pt complex in aggregated state can also enhance the emission intensity.[41]

Bioimaging in metal complexes

These materials have high quantum yield, large Stoke shift, long excited state lifetime, tunable emission and high resistance to photobleaching compared to the organic fluorophores, making them very suitable for bio-imaging. Figure 3 shows the localization of metal complexes inside the cells. We can observe that the uptaken compounds are mainly positively charged. It is due to the negative suface charge on living cells which allows the permeation of cations easily.[42] On the contrary, negatively charged or zwitterionic complex, cellular uptake is slower, even in long incubation time.[43] In addition, the hydrophobic/hydrophilic structure also influences the cellular uptake. Due to the phospholipid layer of cell membrane, certain hydrophobicity can assist the metal complex cross the cell membrane.

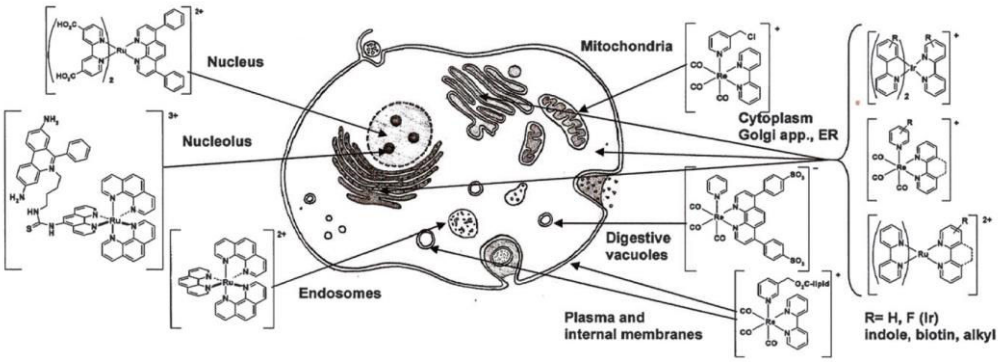

Figure 3. Localization of metal complexes in the cells. Reproduced from *Chem. Commun.*, **2010**, *46*, 186–202 with permission from The Royal Society of Chemistry.

Bioimaging in Ir complexes

Ir (III) complexes, with the general formula $[Ir(C^N)_2(N^N)]$, where C^N represents the cyclometalated ligand and N^N is a bipyridine based chelating ligand, are widely utilized in bioimaging. Ir(III) complexes exhibit tunable emission wavelength depending on the ligand design and long excited state lifetime with ligand centered (LC), metal-to-ligand charge transfer (MLCT) or mixed LC/MLCT emission character. In vitro studies show that biotinylated Ir(III) complexes present high binding affinity to the glycoprotein avidin and are uptaken into cells easily.[9-11]. Lo *et al.* reported the cellular uptake of three Ir(III) complexes with different alkyl chain length (C_nH_{2n+1}, n = 2, 10 and 18).[44] The lipophilicity of these complexes increase by elongating the alkyl chains. The C10 Ir complex shows the highest cellular uptake, however, the most lipophilic C18 Ir complex, the cellular uptake decreases dramatically. Indeed, prolonging the hydrophobic alkyl chains improves the cellular uptake, but the excess lipophilicity can also reduce the cellular uptake. Also most of Ir(III) complexes show cytoplasm localization without specific targeting.

Bioimaging in Pt complexes

Pt complexes are also investigated as potential luminescent probes for bioimaging.[45] Especially the self-assembled structures lead to changes in properties either in solution or in solid state. Zou *et al* reported that [Pt(thpy)(N^C)]OTf complex, thpy = 2-(thiophen-2-yl)pyridine and N^C = N,N-dimethyl-bis(imidazolium) shows emission in 562-605 nm with long excited state lifetime, and the compound presents cytotoxicity upon light irradiation that could be used for theranostics.[46] In a different study, Septiadi *et al.* presented the cellular uptake of the self-assembled Pt complex CF3-Pt-4OHpy by HeLa cells.[47] This Pt complex displays aggregation in DMSO:H_2O = 1:99 solution, enhancing the emission quantum yield to 36% (solution < 1%). After 4 hours incubation in HeLa cells, the assembled Pt complexes were uptaken by the cells and located into cytoplasm and nucleus.

1.2.3 Quantum dots

The advantage of using quantum dots (QDs) as bioimaging tools is that QDs have high photostability, high quantum yield, tunable emission wavelength, and long excited state lifetime, etc. The emission properties can be explained by quantum confinement effect.[48-50] As the dimensions of semiconductor nanocrystal decrease to the nanoscale, the size is comparable to the wavelength of electron and motion of the electron is confined into this nano-space. In this case, the behavior can be described as a particle in a box and the energy levels are discrete. The first excited energy can be shown as $E = h^2/8ma^2$, where h is the Planck constant, m is mass and a is the size of the particles. When the particle size decreases, the energy band gap increases, resulting a size-dependent emission. (Figure 4)

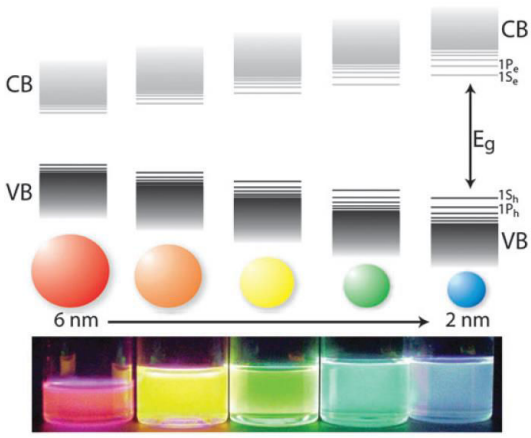

Figure 4. Quantum confinement effect and size-dependent emission of semiconductor materials. Reproduced from *Chem. Soc. Rev.,* **2011**, *40*, 1512–1546 with permission from The Royal Society of Chemistry.

Nowadays, II-VI semiconductor based quantum dots have been widely studied and the emission wavelength can cover almost the full spectrum. (Figure 5) This luminescent properties are interesting for biological applications. However, achieving water solubility is an issue. Bruchez *et al*. modified a layer of silica with CdSe QDs making a water soluble core-shell structure.[51] The CdSe-QDs modified silica are then functionalized with trimethoxysilylpropyl urea and acetate groups to target the cell nucleus. Chan *et al.* also modified a layer of water soluble carboxylate groups on the surface of CdSe@ZnS QDs and then used them for bioimaging of HeLa cells.[52] Besides, covered with biocompatible materials such as sugar and PEG can increase the cellular uptake.[53, 54] However, the releasing of fatal metal ions is still a big issue for using this nanomaterials.[55]

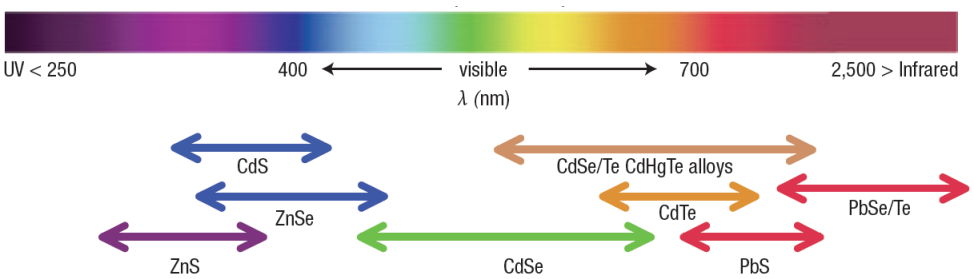

Figure 5. Category of quantum dots and their emission wavelength. Reproduced from *Nature materials*, **2005**, *4*, 435–446 with permission from Nature Publishing Group.

1.3 Silicon nanoparticles (Si NPs)

As a semiconductor material, bulk silicon has been widely utilized in electronic product. However, due to the indirect bandgap, to generate a photon it is necessary the assistance of a phonon across the bandgap, resulting in an inefficient emitter[56-58] (Figure 6). When the particle size reaches to nano scale, the optical properties change and Si NPs behave like quantum dots, exhibiting bright luminescence. The first study of Si NPs was reported in 1990 by the Canham group[59] showing the high quantum efficiency of red luminescent porous Si NPs. After this discovery, many more studies have been focused on the luminescent properties of silicon and in particular of nanoparticles.

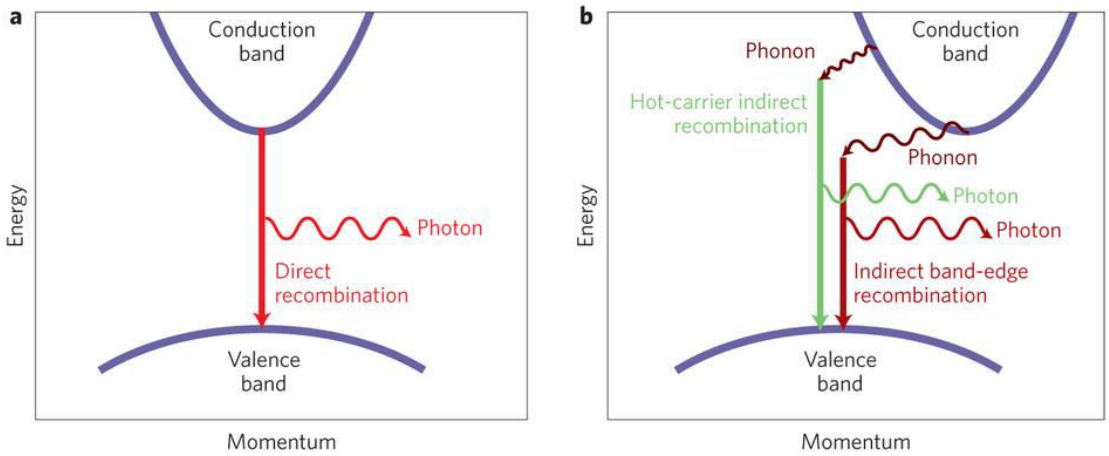

Figure 6. direct bandgap and indirect bandgap diagram. Reproduced from *Nature photonics*, **2013**, *7*, 264–265 with permission from Nature Publishing Group.

1.3.1 Si NPs synthetic methods

There are many different synthetic strategies to synthesize Si NPs in literature, including top-down and bottom-up techniques. Both approaches are useful to produce Si NPs but both lead to a variety of particle size, luminescent properties and surface modification. Below are summarized the most important synthetic methods described in the literature.

A. Top-Down approach

Mechanical methods

An intuitive way to synthesize Si NPs is by breaking a silicon wafer into small pieces. Heintz *et al.* used a technique called high energy ball milling (HEBM).[60, 61] By mixing silicon pieces and capping reagents in a stainless-steel milling vial, 4 nm Si NPs were produced displaying blue emission. In addition, the emission wavelength showed bathochromic shift upon increasing the excitation wavelength. It might due to the polydispersity of silicon nanoparticles. The emission energy can also change with different capping reagents. When high polar molecules such as 1-octaldehyde and 1-octanoic acid are used, the particles emitted at 522 nm and 518 nm, respectively. In contrast, using 1-octene and 1-octyne as capping molecules, the maximum emission were 394 nm and 435 nm, respectively.

Laser ablation

Okada *et al.* reported the synthesis of Si NPs by a pulse Nd:YAG laser at argon atmosphere in 1991.[62] The particles are spherical and possess a crystalline structure with diameter spanning from 20 to 500 nm. Few years later Werwa *et al.* used the same approach with low pressure (at 10^{-8} Torr), and 3 nm Si NPs showing red emission were

produced.[63] Furthermore, Orii *et al.* reported monodispersed Si NPs with different controllable size and tunable emission form 1.34 to 1.79 eV by using differential mobility analyzer (DMA) and postannealing process (PAP).[64] Recently, the laser ablation method also performed in the liquid phase.[65, 66]

Electrochemical etching

In 1990, Canham discovered luminescent Si nanowires by electrochemical etching of silicon wafers.[59] Following this process, Heinrich *et al.* obtained luminescent colloidal Si suspensions in 1992.[67] By controlling the current density and catalysts, Kang *et al.* were able to synthesize different structures from nanoparticles to nanowires.[68] Afterwards, Kang *et al.* published 3 nm Si NPs with tunable emission ranging from blue to red by changing the electrochemical etching times. With longer reaction time, the Si crystal core was reduced by etching and the emission of Si NPs were blue shifted.[69]

B. Bottom-Up approach

Thermolysis and pyrolysis of silane

This method consists on the reduction of SiH_4, the silicon source, through the dissociation of SiH_4 and nucleation of Si atoms to form Si NPs by either, high temperature treatment or laser irradiation. Brus *et al.* reported this method to obtain 7.5 nm Si@SiO_2 NPs with NIR emission at 970 nm.[70] Swihart *et al.* used CO_2 laser-induced pyrolysis of silane to produce 5 nm Si NPs.[71] Then the particles were etched via HF/HNO_3 to get different thickness of the SiO_2 shell and tune the luminescence from 500 nm to 800 nm. The emission shifted from red to blue because of the size reduction of the Si core, being the result consistent with quantum confinement effect.

Solution based micelle method

Wilcoxon *et al.* introduced an interesting way to control the formation of the nanoparticles by using micelles as reaction vessels for the synthesis of Si NPs[72, 73] (Figure 7). The silicon sources, SiX_4; X = Cl, Br or I, were dissolved into the hydrophilic center of inverse micelles, which is formed by an ammonium surfactant in octane. Then a reduction reagent, $LiAlH_4$, was added to reduce Si(IV) to Si(0). The particles are 1.8 – 10 nm and have high crystallinity and blue emission. Using micelles to control the particles size is a good strategy. However, the conditions the author used were not optimized. Later, Tilley *et al.* modified the method using tetraoctylammonium bromide (TOAB) as surfactant and toluene as solvent, resulting in monodisperse Si NPs (1.8 ± 0.2 nm) with amino groups on the surface.[74, 75] The particles exhibited blue emission, quantum yield of 10%, and they have been used for imaging HeLa cells. In

our group, we modified the micelle method and we have produced monodisperse Si NPs, in large scale with size of 1.57 ± 0.21 nm.[76] We have modified the Si NPs with water soluble amino groups, and they were employed for the cellular imaging of BV2 cells.[77]

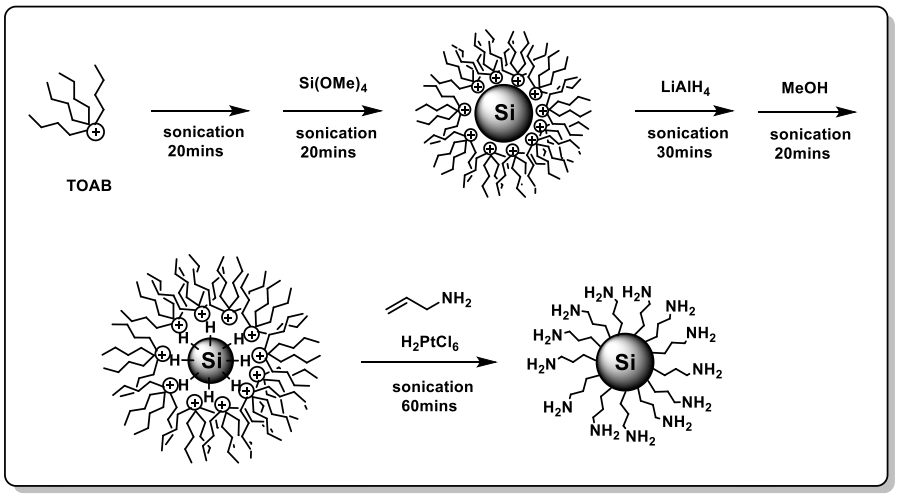

Figure 7. Example of micelle based synthesis of Si NPs.

Solution based reduction-oxidation method

Kauzlarich *et al.* developed interesting methodologies for the synthesis of Si NPs. Reduction of $SiCl_4$ with NaSi or Mg_2Si, resulted in chloro–terminated Si NPs and subsequent treatment with alkyllithium or Grignard reagents led to different funtionalizations. The UV-blue emissive (~350 nm) crystalline Si NPs were obtained in good yield and with size in the range of 2 – 5 nm.[78, 79] Later in 2002, the same group published a synthesis using bromine to oxidize Mg_2Si to form bromo–terminated Si NPs.[80] Moreover, Zuilhof *et al.* used the same approach and modified the surface by adding a Grignard reagent,[81] where the alkene groups were further conjugated with other molecules by thiol-ene click chemistry. The particles were 2.4 ± 0.5 nm and the emission maxium is 525 at an excitation wavelength of 430 nm.

Another interesting synthetic methodology is the so called Zintl salt reaction. Zintl salt, NaSi, is reacted with ammonium bromide to form hydrogen terminated Si NPs.[82] With different conditions, the particle size can range from 5 to 60 nm. Following the same approach, iron doped Si NPs were also prepared with Fe:Na_4Si_4 as the starting materials and further reacted with NH_4Br to obtain the iron–doped NPs used for bimodal imaging, optical and MRI imaging.[83] In addition, using Na(naphthalide) to reduce $SiCl_4$, 5.2 ± 1.9 nm Si NPs can be obtained with photoluminescence in the 410 – 430 nm range.[84]

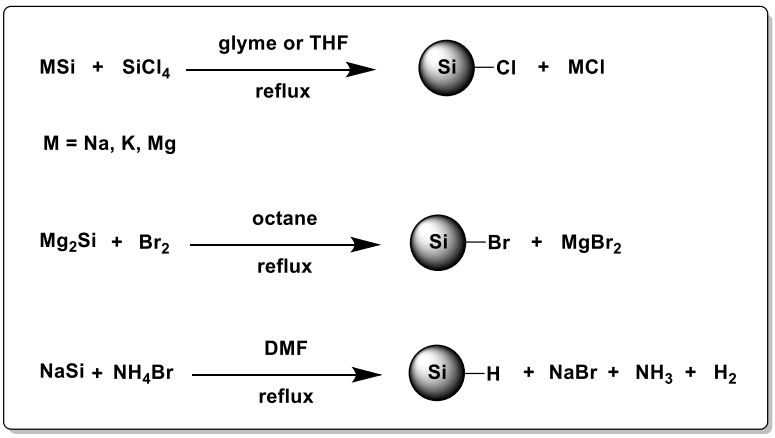

Figure 8. Examples of solution based synthesis of Si NPs.

1.3.2 Surface chemistry of Si NPs

Surface functionalization is an important step to exploit the materials for different applications. For many nanoparticles, the bare surface area must be protected by a shell of ligands since it is sensitive to oxygen and water. In particular the synthesis of Si NPs with hydrogen or halogen modified surfaces is very challenging. The Si–H or Si–X (X = I, Br or Cl) are very reactive and Si–O bonds can be formed in the presence of oxygen and water. Hence, we need to passivate the surface to avoid oxidation to silica and also use a stabilizer to avoid self-aggregation.

The surface groups of Si NPs have strong influence in the emission energy and excited state lifetime, and even the presence of silica (Si–O) can decrease the emission quantum efficiency.

The Si–X (X = I, Br or Cl) derivatives can be easily transformed in alkoxy groups (Si–OR) by adding alcohol. However, short alkoxy chains such as methoxy, shows low stability, and converts to hydroxyl (Si–OH) after adding water.[85] A simple way to increase the stability is to add long alkyl chains (Si–R) by using alkyllithium or Grignard reagent.[78, 79] By substitution of the halogen atoms by strong bases like alkyllithium or Grignard reagents, the long alkyl chain can be covalently bound on the Si NPs (Scheme 3A). The Si–H intermediates, can react with alkene or alkyne through Pt catalyzed reactions or UV irradiation to obtain Si–R chains (Scheme 3B). The Pt catalyst undergoes two oxidative addition reactions of alkene and Si–H and reductive elimination to form H_2 and the Si–R product (hydrosilylation). Allylamine is the most popular ligand to use in order to have amino terminated Si NPs, that can be further reacted to allow any possible functionalization. However, some studies showed that the

amino group can bind with silicon to form a Si–N bond,[86, 87] and therefore particular care or protection of the amino groups is necessary to avoid this side reaction.

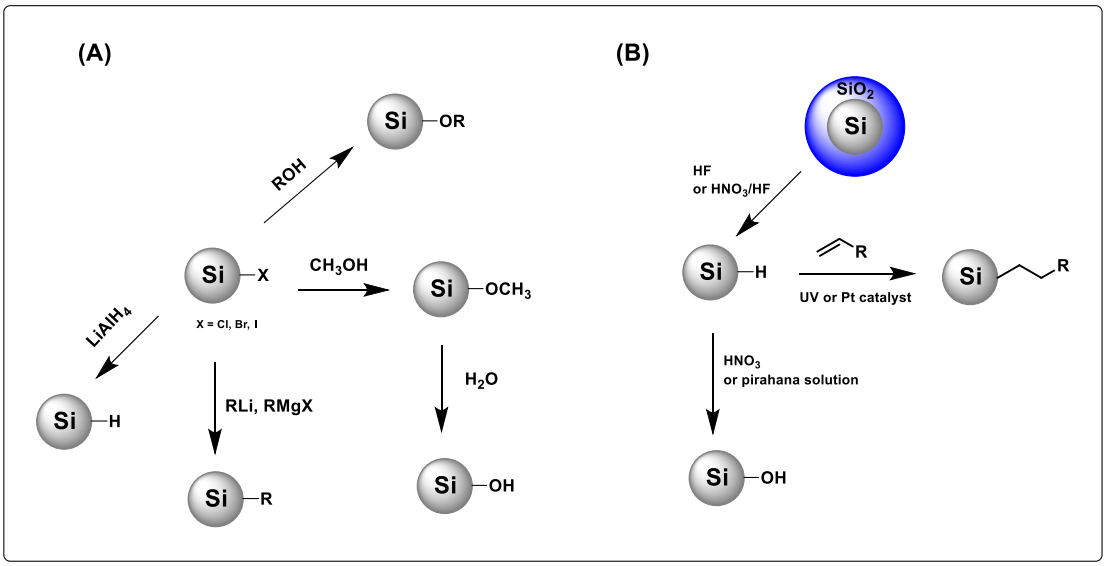

Scheme 3. Surface functionalization of Si NPs.

1.3.3 Luminescent properties of Si NPs

The mechanism of luminescence of Si NPs is still controversial. The most acceptable explanations are the quantum confinement effect and the surface states. Interestingly, Si NPs from different synthetic methods exhibit different emission color, emission quantum yields and excited state lifetimes. In the most cases, the red emitting Si NPs show microsecond lifetime decay while blue emitting Si NPs show nanosecond lifetime decay, indicating the difference in fundamental emission mechanisms.

The luminescence of Si NPs can be explained by the recombination of excitons in quantum confined space of silicon, dominated by quantum confinement effect. Brus *et al.* showed through DFT calculations that for small Si NPs (1.0 to 1.5 nm), the emission comes from direct band transition.[88] This prediction was proved few years later by the Kang group.[69] In their experiments, 3 nm Si NPs were treated with H_2O_2/EtOH to oxidize silicon to silica (SiO_2). With decreasing the thickness of the silicon core, they could tune the emission from red to blue. Also they confirmed that the blue emission is from the silicon core and does not change the color after etching in HF solution. On the other hand, Kim *et al.* suggested that the emission comes from the defects.[89] They observed that the oxidation of porous silicon does not change the emission peaks, and the emission is very stable even after exposing in ambient air for two months. Moreover, the surface states also play an important role in emission.[90] Upon modification of the surface, surface states are created in between the conduction band and valence band,

resulting in an emission shift.

We demonstrated the luminescent labels based on organic fluorophores, metal complexes and quantum dots. Those labels show very promising luminescent properties upon light irradiation. However, the luminescence can be also generated without an incident excitation light, such as electroluminescence,[91-93] chemiluminescence,[94] thermoluminescence[95] and electrochemiluminescence[96] etc. In particular, we are interested in using luminescent labels to generate light by electrochemical reactions and the general introduction of electrochemiluminescence (ECL) is discussed in 1.4.

1.4 Electrochemilumiescence (ECL)

Electrochemiluminescence (ECL) studies were firstly described by Hercules and Bard *et al.* in mid-1960s.[97-99] Bright electrochemiluminescence is observed when applying a voltage using Pt electrode in a solution containing aromatic hydrocarbon such as pyrene, perylene, rubrene etc. Nowadays ECL becomes a powerful analytical technique largely used in immunoassays, food and water testing, that combines simple equipment with high sensitivity, selectivity and reproducibility in the detection of different analysts at very low concentration.[96, 100] The luminescence is triggered not by means of an external light source but applying a voltage to a solution containing a luminophore. Without the incident light, the Raman band from the solvent and second-order diffraction band are not observed in this process, and also enhances the signal–to-noise ratio.

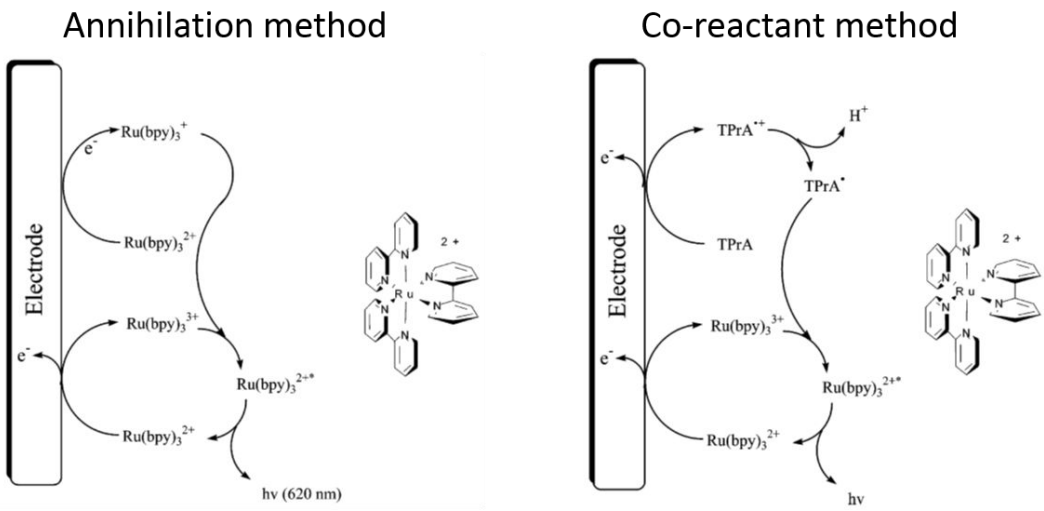

Figure 9. Mechanisms of ECL in annihilation and co-reactant methods. Reprinted with permission from *Chem. Rev.* **2004**, *104,* 3003-3036 Copyright (2004) American Chemical Society.

There are two main pathways to generate ECL: the annihilation and the co-reactant method. As shown in Figure 9, in the annihilation method, both the reduced and oxidized form of $[Ru(bpy)_3]^{2+}$ are generated at the electrodes when the applied voltage is swept from oxidation to reduction potentials of $[Ru(bpy)_3]^{2+}$. The newly formed radical cation and anion are annihilated to form the excited species and emits light. On the other hand, in the co-reactant method, the excited state luminophore is generated by the co-reactant at a fixed applied voltage. Take TPA co-reactant (tripropylamine) for example, at the oxidation potential of TPA, TPA• radical is formed (after extracting one proton from TPA•+ radical cation), and undergo one electron transfer to oxidized emitter, $[Ru(bpy)_3]^{3+}$, to form excited state species that emit light. The latter method has several advantages over the annihilation one, it allows the employment of emitters which are stable only in the $R^{\bullet+}$ (oxidized) or $R^{\bullet-}$ (reduced) form, that has only a reversible electrochemical reduction or oxidation, and also the use of solvents with narrow potential windows.[101]

Following the literature so far, the most used system in ECL is based on ruthenium trisbipyridine complex, $[Ru(bpy)_3]^{2+}$. This complex has been widely set up for many commercially available bio- and immunoassays mainly based on the co-reactant method[102] such as DNA sequences detection,[103] Aptamer and DNAzyme biosensor[104-106] or metal cations detection.[107, 108] However, due to the increasing demand for accuracy and multiplexing in diagnostics higher sensitivity of ECL assays and different emission colors are desirable. To answer this need, one promising strategy seems to be the replacement of $[Ru(bpy)_3]^{2+}$ by cyclometalated Ir(III) derivatives. Although many groups have been focusing on the development of ECL active iridium complexes with emission across the entire visible region, only few example of highly efficient compound have been reported.[109]

1.4.1 ECL in Ir(III) complexes

In the literature, cyclometalated Ir(III) complexes have been examined for ECL applications. Kim *et al.* reported a series of $Ir(pq)_2L$ complexes, in which pq is 2-phenylquinoline and L is monoanionic bidentate ligand such as acetylacetoneate (acac) and picolinate (pico) etc.[109, 110] Those complexes exhibit high intense ECL efficiency in three measured ways: annihilation, TPA co-reactant and $S_2O_8^{2-}$ co-reactant methods. As a result, $Ir(pq)_2(acac)$ displays ECL efficiency 77-fold higher than $Ru(bpy)_3^{2+}$ standard in TPA method, but only 3-fold higher than standard in annihilation method. That is due to the unstable anion species of $Ir(pq)_2(acac)$ which shows irreversible reduction process. The annihilation method requires combination of two oxidative and reductive species, and the unstable cation (or anion) can reduce the ECL efficiency. In contrast,

$Ir(pq)_2(pico)$ complex shows reversible redox process (stable redox species), resulting high efficient ECL in all three methods.

However, many Ir complexes display high efficient ECL only in nonaqueous solutions. In order to apply Ir complex in biological assay, water solubility is necessary to consider. Zanarini *et al.* published a series of charged cyclometalated Ir(III) complexes which are water soluble, high emission quantum yield and suitable for ECL application. Indeed, these Ir complexes show ECL active in PB/DBAE water solution (PB is aqueous phosphate buffer and DBAE is 2-dibutylaminoethanol, co-reactant), exhibiting ECL emission in blue and green regions that seldom ECL probes report in this emission wavelength.

1.4.2 ECL in nanomaterials

Nanomaterials are of considerable interest in this field, the first ECL study of semiconductor is reported in 2002. 2 to 4 nm silicon nanoparticles exhibited ECL at 640 nm both in annihilation and co-reactant methods.[111] Following this discovery, many semiconductors, Ge, CdSe, CdTe etc., are examined to perform ECL properties.[112-114] They exhibit red-shifted ECL compared to their photoluminescence, indicating the emission states are different. The photoluminescence (PL) of quantum dots is via the excitation and emission from the inner core of the nanoparticles, while the ECL is mainly influenced by the surface chemistry and the presence of the surface states.[115] Myung *et al*. gave an example of CdSe/ZnSe nanoparticles, the ECL exhibits two emission peaks: one is identical to the PL spectrum and another is with 200 nm red-shift emission which comes from the surface states of nanoparticles.[116] (Figure 10)

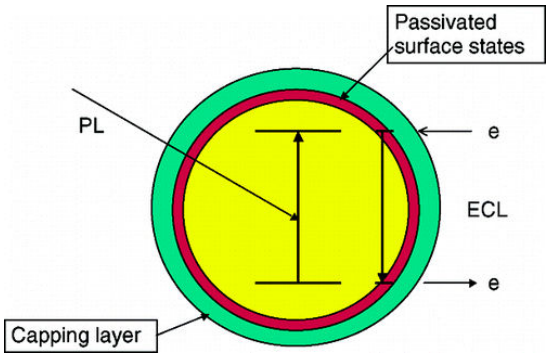

Figure 10. Schematic representation of PL and ECL in semiconductor NPs. Reprinted with permission from *Nano Lett.*, 2003, **3**, 1053-1055 Copyright (2003) American Chemical Society.

Recently the use of nanoparticles as platform for probes has also gained a lot of interest. In particular, the key of success for building highly sensitive ECL assay seems to be the combination of nanomaterials with metal complexes. The encapsulation of molecules into nanoparticles matrix ensure the protection from the surrounding environment, increase of photostability and signal enhancement due to an increase of active molecules number directly on the electrode. However it could also lead to lower rate of (electro)chemical processes as well as to low diffusion of the analytes and intermediates through the nanostructured material. Moreover leaking of labels from the material is often observed.[117-120]

1.5 Scope the thesis

Using nanotechnology to image, diagnose and therapize the diseases has become important issue nowadays. In this thesis, we have developed many imaging probes based on metal complexes, nanoparticles and metal complex modified nanomaterials for cellular imaging and electrochemiluminescence (ECL) applications.

Chapter 2 describes the synthesis of novel Ir(III) complexes and the applications for ECL. A series of Ir(III) complexes with one large π conjugated N^N ligand (1H-pyrazole[5,4-h]quinoline) and two ancillary ligands (C^N), C^N = 2-phenylpyridine (ppy) 2-(2, 4-difluorophenyl)pyridine (dfppy), 2-phenylquinoline (pq), 2-phenylisoquinoline (piq), are synthesized and as well as the photophysical properties are discussed. These Ir(III) complexes are examined as potential luminescent probes for electrochemiluminescence (ECL) applications.

Chapter 3 describes the synthesis and characterization of silicon nanoparticles (Si NPs). Si NPs are synthesized based on wet chemistry method (oxidation and zintl salt methods) and modified with different functional groups.

The chapter 4 is the bioapplication of Si NPs. Glucose modified Si NPs were synthesized and characterized. Further, two Si NPs, Si-COOH and Si-Glc NPs, are studied *in vitro* including the cellular uptake, localization, and the cytotoxicity.

Chapter 5 introduces Si NPs conjugated with the Pt(II) complexes. When the planar Pt(II) complexes are closed enough (Pt···Pt < 3.5Å), an interaction of the d_{z2} orbitals resulting a new transition band called metal-metal-to-ligand charge transfer (MMLCT) appears and the emission is bathochromic shifted. We synthesized two amino Pt(II) complexes and coupled with Si-COOH NPs. The photophysical properties are discussed and as well as the aggregation induced emission (AIE) effect. Furthermore, those nanoparticles are studied the cellular uptake in HeLa.

Chapter 6 describes the electrochemiluminescence using metal complexes conjugated nanoparticles. Nanoparticles contain large surface area that can be modified by different functional groups for multi-modal imaging, and the amino or carboxylate surface groups keep them in good water solubility. Two type nano-systems are introduced, ruthenium complex conjugated carbon dots and iridium complex conjugated silicon nanoparticles, and ECL measurement are performed in ProCell solution which is provided by Roche company.

1.6 Reference

1. R. Weissleder and M. J. Pittet, *Nature*, 2008, **452**, 580-589.
2. D. W. McRobbie, E. A. Moore, M. J. Graves and M. R. Prince, *MRI from picture to proton*, 2 edn., Cambridge University press, United Kindom, 2006.
3. D. L. Pavia, G. M. Lampman and G. S. Kriz, *Introduction to spectroscopy*, 3 edn., Thomson Learning, United States of America, 2001.
4. J. Cheon and J. H. Lee, *Acc. Chem. Res.*, 2008, **41**, 1630.
5. C. S. Wu, E. Ambler, R. W. Hayward, D. D. Hoppes and R. P. Hudson, *Physical Review*, 1957, **105**, 1413-1415.
6. C. Tassa, S. Y. Shaw and R. Weissleder, *Acc. Chem. Res.*, 2011, **44**, 842-852.
7. S. S. Gambhir, *Nat Rev Cancer*, 2002, **2**, 683-693.
8. K. König, *Journal of Microscopy*, 2000, **200**, 83-104.
9. K. K.-W. Lo, K. Y. Zhang, S.-K. Leung and M.-C. Tang, *Angew. Chem. Int. Ed.*, 2008, **47**, 2213-2216.
10. K. K.-W. Lo, J. S.-W. Chan, L.-H. Lui and C.-K. Chung, *Organometallics*, 2004, **23**, 3108-3116.
11. K. K.-W. Lo, C.-K. Li and J. S.-Y. Lau, *Organometallics*, 2005, **24**, 4594-4601.
12. K. B. Chalasani, G. J. Russell-Jones, A. K. Jain, P. V. Diwan and S. K. Jain, *J. Controlled Release*, 2007, **122**, 141-150.
13. Y. Zhang, J. Naleway, K. Larison, Z. Huang and R. Haugland, *The FASEB journal*, 1991, **5**, 3108-3113.
14. D. Feng, Y. Song, W. Shi, X. Li and H. Ma, *Anal. Chem.*, 2013, **85**, 6530-6535.
15. E. Baggaley, J. A. Weinstein and J. A. G. Williams, *Coord. Chem. Rev.*, 2012, **256**, 1762-1785.
16. I. Johnson, *Histochem J*, 1998, **30**, 123-140.
17. R. P. Haugland and K. D. Larison, *Handbook of Fluorescent Probes and Research Chemicals*, Molecular Probes, 1992.
18. F. Otto, *Methods in cell biology*, 1990, **33**, 105-110.
19. A. Minta, J. Kao and R. Y. Tsien, *J. Biol. Chem.*, 1989, **264**, 8171-8178.
20. R. Ziessel, G. Ulrich and A. Harriman, *New J. Chem.*, 2007, **31**, 496-501.
21. A. Loudet and K. Burgess, *Chem. Rev.*, 2007, **107**, 4891-4932.
22. M.-c. Yee, S. C. Fas, M. M. Stohlmeyer, T. J. Wandless and K. A. Cimprich, *J. Biol. Chem.*, 2005, **280**, 29053-29059.
23. J. Karolin, L. B.-A. Johansson, L. Strandberg and T. Ny, *J. Am. Chem. Soc.*, 1994, **116**, 7801-7806.
24. V. H. Houlding and V. M. Miskowski, *Coord. Chem. Rev.*, 1991, **111**, 145-152.
25. I. Fratoddi, C. Battocchio, A. Furlani, P. Mataloni, G. Polzonetti and M. V. Russo, *J. Organomet. Chem.*, 2003, **674**, 10-23.

26. M. Mauro, A. Aliprandi, C. Cebrian, D. Wang, C. Kubel and L. De Cola, *Chem. Commun.*, 2014, **50**, 7269-7272.
27. K. Krogmann, *Angewandte Chemie International Edition in English*, 1969, **8**, 35-42.
28. S. Lippard, *Science*, 1982, **218**, 1075-1082.
29. H.-K. Yip, L.-K. Cheng, K.-K. Cheung and C.-M. Che, *J. Chem. Soc., Dalton Trans.*, 1993, 2933-2938.
30. B.-C. Tzeng, W.-F. Fu, C.-M. Che, H.-Y. Chao, K.-K. Cheung and S.-M. Peng, *J. Chem. Soc., Dalton Trans.*, 1999, 1017-1024.
31. V. W.-W. Yam, K. M.-C. Wong and N. Zhu, *J. Am. Chem. Soc.*, 2002, **124**, 6506-6507.
32. S.-Y. Chang, J. Kavitha, S.-W. Li, C.-S. Hsu, Y. Chi, Y.-S. Yeh, P.-T. Chou, G.-H. Lee, A. J. Carty, Y.-T. Tao and C.-H. Chien, *Inorg. Chem.*, 2006, **45**, 137-146.
33. L. Murphy, P. Brulatti, V. Fattori, M. Cocchi and J. A. G. Williams, *Chem. Commun.*, 2012, **48**, 5817-5819.
34. W. Lu, Y. Chen, V. A. L. Roy, S. S.-Y. Chui and C.-M. Che, *Angew. Chem.*, 2009, **121**, 7757-7761.
35. N. Komiya, T. Muraoka, M. Iida, M. Miyanaga, K. Takahashi and T. Naota, *J. Am. Chem. Soc.*, 2011, **133**, 16054-16061.
36. K. M.-C. Wong and V. W.-W. Yam, *Acc. Chem. Res.*, 2011, **44**, 424-434.
37. H. Honda, Y. Ogawa, J. Kuwabara and T. Kanbara, *Eur. J. Inorg. Chem.*, 2014, **2014**, 1865-1869.
38. Y. Hong, J. W. Lam and B. Z. Tang, *Chem. Soc. Rev.*, 2011, **40**, 5361-5388.
39. M.-X. Zhu, W. Lu, N. Zhu and C.-M. Che, *Chemistry – A European Journal*, 2008, **14**, 9736-9746.
40. C. A. Strassert, C.-H. Chien, M. D. Galvez Lopez, D. Kourkoulos, D. Hertel, K. Meerholz and L. De Cola, *Angew. Chem. Int. Ed.*, 2011, **50**, 946-950.
41. N. Komiya, M. Okada, K. Fukumoto, D. Jomori and T. Naota, *J. Am. Chem. Soc.*, 2011, **133**, 6493-6496.
42. Q. Zhao, M. Yu, L. Shi, S. Liu, C. Li, M. Shi, Z. Zhou, C. Huang and F. Li, *Organometallics*, 2010, **29**, 1085-1091.
43. W. Jiang, Y. Gao, Y. Sun, F. Ding, Y. Xu, Z. Bian, F. Li, J. Bian and C. Huang, *Inorg. Chem.*, 2010, **49**, 3252-3260.
44. K. K.-W. Lo, P.-K. Lee and J. S.-Y. Lau, *Organometallics*, 2008, **27**, 2998-3006.
45. M. Mauro, A. Aliprandi, D. Septiadi, N. S. Kehr and L. De Cola, *Chem. Soc. Rev.*, 2014, **43**, 4144-4166.
46. T. Zou, C.-N. Lok, Y. M. E. Fung and C.-M. Che, *Chem. Commun.*, 2013, **49**, 5423-5425.

47. D. Septiadi, A. Aliprandi, M. Mauro and L. De Cola, *RSC Advances*, 2014, **4**, 25709-25718.
48. M. R. Krishna and R. Friesner, *The Journal of chemical physics*, 1991, **95**, 8309-8322.
49. C. de Mello Donega, *Chem. Soc. Rev.*, 2011, **40**, 1512-1546.
50. M. Nirmal and L. Brus, *Acc. Chem. Res.*, 1999, **32**, 407-414.
51. M. Bruchez, M. Moronne, P. Gin, S. Weiss and A. P. Alivisatos, *Science*, 1998, **281**, 2013-2016.
52. W. C. Chan and S. Nie, *Science*, 1998, **281**, 2016-2018.
53. Y. Chen, T. Ji and Z. Rosenzweig, *Nano Lett.*, 2003, **3**, 581-584.
54. J. Lee, J. Kim, E. Park, S. Jo and R. Song, *PCCP*, 2008, **10**, 1739-1742.
55. C. Kirchner, T. Liedl, S. Kudera, T. Pellegrino, A. Muñoz Javier, H. E. Gaub, S. Stölzle, N. Fertig and W. J. Parak, *Nano Lett.*, 2005, **5**, 331-338.
56. D. Kovalev, H. Heckler, G. Polisski and F. Koch, *physica status solidi (b)*, 1999, **215**, 871-932.
57. J. D. Holmes, K. J. Ziegler, R. C. Doty, L. E. Pell, K. P. Johnston and B. A. Korgel, *J. Am. Chem. Soc.*, 2001, **123**, 3743-3748.
58. L. Pavesi, L. Dal Negro, C. Mazzoleni, G. Franzo and F. Priolo, *Nature*, 2000, **408**, 440-444.
59. L. T. Canham, *Appl. Phys. Lett.*, 1990, **57**, 1046-1048.
60. A. S. Heintz, M. J. Fink and B. S. Mitchell, *Adv. Mater.*, 2007, **19**, 3984-3988.
61. A. S. Heintz, M. J. Fink and B. S. Mitchell, *Appl. Organomet. Chem.*, 2010, **24**, 236-240.
62. R. Okada and S. Iijima, *Appl. Phys. Lett.*, 1991, **58**, 1662-1663.
63. E. Werwa, A. A. Seraphin, L. A. Chiu, C. Zhou and K. D. Kolenbrander, *Appl. Phys. Lett.*, 1994, **64**, 1821-1823.
64. T. Orii, M. Hirasawa and T. Seto, *Appl. Phys. Lett.*, 2003, **83**, 3395-3397.
65. R. Intartaglia, A. Barchanski, K. Bagga, A. Genovese, G. Das, P. Wagener, E. Di Fabrizio, A. Diaspro, F. Brandi and S. Barcikowski, *Nanoscale*, 2012, **4**, 1271-1274.
66. N. Shirahata, M. R. Linford, S. Furumi, L. Pei, Y. Sakka, R. J. Gates and M. C. Asplund, *Chem. Commun.*, 2009, 4684-4686.
67. J. L. HEINRICH, C. L. CURTIS, G. M. CREDO, M. J. SAILOR and K. L. KAVANAGH, *Science*, 1992, **255**, 66-68.
68. Z. Kang, C. H. A. Tsang, Z. Zhang, M. Zhang, N.-b. Wong, J. A. Zapien, Y. Shan and S.-T. Lee, *J. Am. Chem. Soc.*, 2007, **129**, 5326-5327.
69. Z. Kang, Y. Liu, C. H. A. Tsang, D. D. D. Ma, X. Fan, N.-B. Wong and S.-T. Lee, *Adv. Mater.*, 2009, **21**, 661-664.

70. K. A. Littau, P. J. Szajowski, A. J. Muller, A. R. Kortan and L. E. Brus, *The Journal of Physical Chemistry*, 1993, **97**, 1224-1230.
71. X. Li, Y. He, S. S. Talukdar and M. T. Swihart, *Langmuir*, 2003, **19**, 8490-8496.
72. J. P. Wilcoxon and G. A. Samara, *App. Phys. Lett.*, 1999, **74**, 3164.
73. J. P. Wilcoxon, G. A. Samara and P. N. Provencio, *Phys. Rev. B*, 1999, **60**, 2704.
74. J. H. Warner, A. Hoshino, K. Yamamoto and R. D. Tilley, *Angew. Chem. Int. Ed.*, 2005, **117**, 4626-4630.
75. R. D. Tilley and K. Yamamoto, *Adv. Mater.*, 2006, **18**, 2053-2056.
76. M. Rosso-Vasic, E. Spruijt, B. van Lagen, L. De Cola and H. Zuilhof, *Small*, 2008, **4**, 1835-1841.
77. M. Rosso-Vasic, E. Spruijt, Z. Popovic, K. Overgaag, B. van Lagen, B. Grandidier, D. Vanmaekelbergh, D. Dominguez-Gutierrez, L. De Cola and H. Zuilhof, *J. Mater. Chem.*, 2009, **19**, 5926-5933.
78. C.-S. Yang, R. A. Bley, S. M. Kauzlarich, H. W. H. Lee and G. R. Delgado, *J. Am. Chem. Soc.*, 1999, **121**, 5191-5195.
79. D. Mayeri, B. L. Phillips, M. P. Augustine and S. M. Kauzlarich, *Chem. Mater.*, 2001, **13**, 765-770.
80. Q. Liu and S. M. Kauzlarich, *Mater. Sci. Eng. B*, 2002, **B96**, 72.
81. L. Ruizendaal, S. P. Pujari, V. Gevaerts, J. M. Paulusse and H. Zuilhof, *Chem Asian J*, 2011, **6**, 2776-2786.
82. D. Neiner and S. M. Kauzlarich, *Chem. Mater.*, 2010, **22**, 487-493.
83. M. P. Singh, T. M. Atkins, E. Muthuswamy, S. Kamali, C. Tu, A. Y. Louie and S. M. Kauzlarich, *ACS Nano*, 2012, **6**, 5596-5604.
84. R. K. Baldwin, K. A. Pettigrew, E. Ratai, M. P. Augustine and S. M. Kauzlarich, *Chem. Commun.*, 2002, 1822-1823.
85. J. Zou, R. K. Baldwin, K. A. Pettigrew and S. M. Kauzlarich, *Nano Lett.*, 2004, **4**, 1181-1186.
86. Y.-C. Liao and J. T. Roberts, *J. Am. Chem. Soc.*, 2006, **128**, 9061-9065.
87. M. Dasog, Z. Yang, S. Regli, T. M. Atkins, A. Faramus, M. P. Singh, E. Muthuswamy, S. M. Kauzlarich, R. D. Tilley and J. G. C. Veinot, *ACS Nano*, 2013, **7**, 2676-2685.
88. J. Zou, P. Sanelle, K. A. Pettigrew and S. M. Kauzlarich, *J. Cluster Sci.*, 2006, **17**, 565-578.
89. Y. S. Kim, K. Y. Suh, Hyunsik Yoon and H. H. Lee, *J. Electrochem. Soc.*, 2002, **149**, C50-C51.
90. W. Yu, Y. Xu, H. Li, X. Zhan and W. Lu, *Appl. Phys. A*, 2013, **111**, 501-507.
91. C.-H. Yang, M. Mauro, F. Polo, S. Watanabe, I. Muenster, R. Fröhlich and L. De Cola, *Chem. Mater.*, 2012, **24**, 3684-3695.

92. N. Darmawan, C.-H. Yang, M. Mauro, R. Frohlich, L. De Cola, C.-H. Chang, Z.-J. Wu and C.-W. Tai, *Journal of Materials Chemistry C*, 2014, **2**, 2569-2582.
93. T. Komine and M. Nakagawa, *Consumer Electronics, IEEE Transactions on*, 2004, **50**, 100-107.
94. A. Juris, V. Balzani, F. Barigelletti, S. Campagna, P. Belser and A. von Zelewsky, *Coord. Chem. Rev.*, 1988, **84**, 85-277.
95. A. G. Wintle, *Nature*, 1973, **245**, 143-144.
96. M. M. Richter, *Chem. Rev.*, 2004, **104**, 3003-3036.
97. D. M. Hercules, *Science*, 1964, **145**, 808-809.
98. R. E. Visco and E. A. Chandross, *J. Am. Chem. Soc.*, 1964, **86**, 5350-5351.
99. K. Santhanam and A. J. Bard, *J. Am. Chem. Soc.*, 1965, **87**, 139-140.
100. L. Hu and G. Xu, *Chem. Soc. Rev.*, 2010, **39**, 3275-3304.
101. W. Miao, *Chem. Rev.*, 2008, **108**, 2506-2553.
102. M.-J. Li, P. Jiao, M. Lin, W. He, G.-N. Chen and X. Chen, *Analyst*, 2011, **136**, 205-210.
103. C. Li, J. Lin, Y. Guo and S. Zhang, *Chem. Commun.*, 2011, **47**, 4442-4444.
104. M. Famulok, J. S. Hartig and G. Mayer, *Chem. Rev.*, 2007, **107**, 3715-3743.
105. J. Liu, Z. Cao and Y. Lu, *Chem. Rev.*, 2009, **109**, 1948-1998.
106. Y. Zhao, Y. Luo, T. Li and Q. Song, *RSC Advances*, 2014, **4**, 57709-57714.
107. H. Lin, M. E. Cinar and M. Schmittel, *Dalton Transactions*, 2010, **39**, 5130-5138.
108. M. Schmittel and H. Lin, *Inorg. Chem.*, 2007, **46**, 9139-9145.
109. J. I. Kim, I.-S. Shin, H. Kim and J.-K. Lee, *J. Am. Chem. Soc.*, 2005, **127**, 1614-1615.
110. I.-S. Shin, J. I. Kim, T.-H. Kwon, J.-I. Hong, J.-K. Lee and H. Kim, *The Journal of Physical Chemistry C*, 2007, **111**, 2280-2286.
111. Z. Ding, B. M. Quinn, S. K. Haram, L. E. Pell, B. A. Korgel and A. J. Bard, *Science*, 2002, **296**, 1293-1297.
112. Y. Bae, N. Myung and A. J. Bard, *Nano Lett.*, 2004, **4**, 1153-1161.
113. N. Myung, X. Lu, K. P. Johnston and A. J. Bard, *Nano Lett.*, 2004, **4**, 183-185.
114. N. Myung, Z. Ding and A. J. Bard, *Nano Lett.*, 2002, **2**, 1315-1319.
115. A. Bard, Z. Ding and N. Myung, in *Semiconductor Nanocrystals and Silicate Nanoparticles*, eds. X. Peng and D. M. P. Mingos, Springer Berlin Heidelberg, 2005, vol. 118, pp. 1-57.
116. N. Myung, Y. Bae and A. J. Bard, *Nano Lett.*, 2003, **3**, 1053-1055.
117. P. Bertoncello and R. J. Forster, *Biosens. Bioelectron.*, 2009, **24**, 3191-3200.
118. X. Hun and Z. Zhang, *Electroanalysis*, 2008, **20**, 874-880.
119. S. Zanarini, E. Rampazzo, L. D. Ciana, M. Marcaccio, E. Marzocchi, M.

Montalti, F. Paolucci and L. Prodi, *J. Am. Chem. Soc.*, 2009, **131**, 2260-2267.
120. Y. Liu and Q. Song, *Analytical Methods*, 2014, **6**, 5258-5263.

CHAPTER 2

Novel Ir(III) Complexes for ECL Application

Abstract

Electrochemiluminscence (ECL) based on $[Ru(bpy)_3]^{2+}$ system has been widely utilized for immunoassay. In order to extend the promising potential of ECL based immunoassays, Ir(III) complexes are chosen as new ECL probes because of their luminescent properties and tunable emission wavelength. In this chapter, we describe a series of novel Ir complexes using a large π conjugated ligand and different ancillary chelates and the complexes obtained have been fully characterized and used for ECL measurement.

2.1 Introduction

Iridium complexes have been widely used in many applications such as OLED, catalysis, water splitting and solar cells.[1-4] The remarkable luminescent properties originate from their high quantum efficiency, long excited state lifetime, large Stock shift and emission wavelength tunable from blue to red with suitable ligand design. In particular, research on blue emitting Ir(III) complexes plays a crucial role in OLED study nowadays.[5]

Recently electrochemiluminescence (ECL) has emerged in biological assays because of its highly sensitive detection.[6, 7] The signal of $[Ru(bpy)_3]^{2+}$ can be detected below 10^{-11} M. The luminescence is triggered by applied voltage without external light source, which enhances the signal–to-noise ratio. Moreover, the Raman band from solvent and second-order diffraction band are not be observed. Following the literature so far, the most used system is based on ruthenium trisbipyridine complex, $[Ru(bpy)_3]^{2+}$, with tri-n-propylamine (TPA) as co-reactant. This system has been widely set up for many commercially available bio- and immunoassays,[8] DNA sequences detection,[9] Aptamer and DNAzyme biosensor[10-12] , or metal cations detection.[13, 14] However, higher sensitivity of ECL assays and different emission colors are desirable due to the increasing demand for accuracy and multiplexing in diagnostics. One promising strategy is to replace $[Ru(bpy)_3]^{2+}$ by cyclometalated Ir(III) derivatives.

There are two main pathways to generate ECL (Figure 1), one is called annihilation method, in which the applied voltage is swept from oxidation to reduction potentials of $[Ru(bpy)_3]^{2+}$, resulting in formation of both oxidized and reduced species which after diffusion collision produce excited state of $[Ru(bpy)_3]^{2+*}$, which emits light; another commonly used pathway is called co-reactant mechanism[15], in which the reducing radicals co-reactant $TPA^{\bullet}$ give electron to oxidized $[Ru(bpy)_3]^{3+}$ to form $[Ru(bpy)_3]^{2+*}$ excited state which emits light, at a fixed applied voltage. In addition, Stringer *et al.* gave evidence that more negative free energy (ΔG) results in more efficient ECL.[16] The potential of TPA radicals, $E^0(TPA^{\bullet})$, must be higher than the reduction potential of metal complexes which allows the electron transfer from reducing radical co-reactant to the LUMO of electrochemiluminophores easily. Also some studies reported using different co-reactants to fit the energy levels.[17, 18]

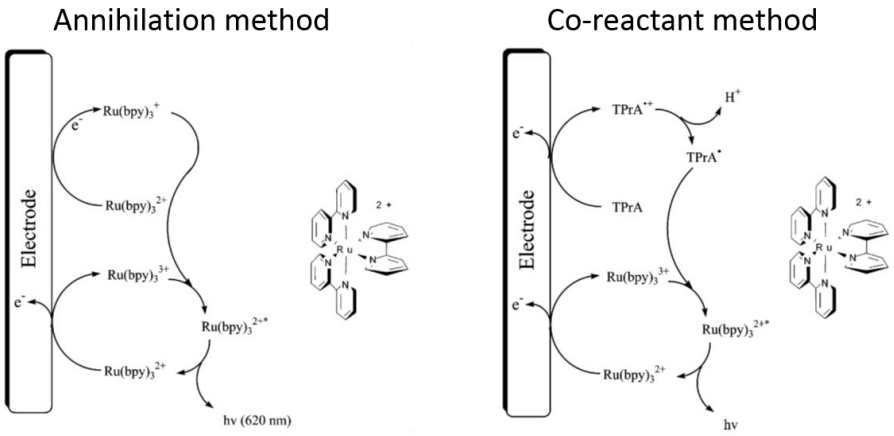

Figure 1. Mechanisms of ECL in annihilation and co-reactant methods. Reprinted with permission from *Chem. Rev.* **2004**, *104,* 3003-3036 Copyright (2004) American Chemical Society.

Kim *et al.* reported high red emitting ECL efficiency in $Ir(pq)_2L$ complexes, in which pq is 2-phenylquinoline and L is monoanionic bidentate ligand such as acetylacetoneate (acac) and picolinate (pico) etc in acetonitrile solution.[19, 20] However, high ECL efficiency in the blue and green color of the electromagnetic spectrum is still rare.[21] In order to contribute to the field with efficient and stable ECL probes that can satisfactorily fill the gap and emit at such high energies, we developed a series of novel Ir(III) complexes using a novel, large π conjugated ligand and different ancillary chelates, and we fully characterized the complexes obtained, and tested them for ECL assays.

2.2 Synthesis of complexes

The synthesis of Ir dimer was achieved by modification of a previous report.[22] As shown in scheme 1, the Ir dimer with two equivalent 1H-pyrazole[5,4-h]quinoline (N^N) and sodium carbonate in 2-methoxyethanol was refluxed for 15 hours. After column chromatography and recrystallization, yellow to red Ir complexes were obtained with 50% to 68% product yield, and characterized by ^{1}H NMR, ^{19}F NMR, mass spectrometry and elemental analysis. (See 2.4 Experimental Section for detail)

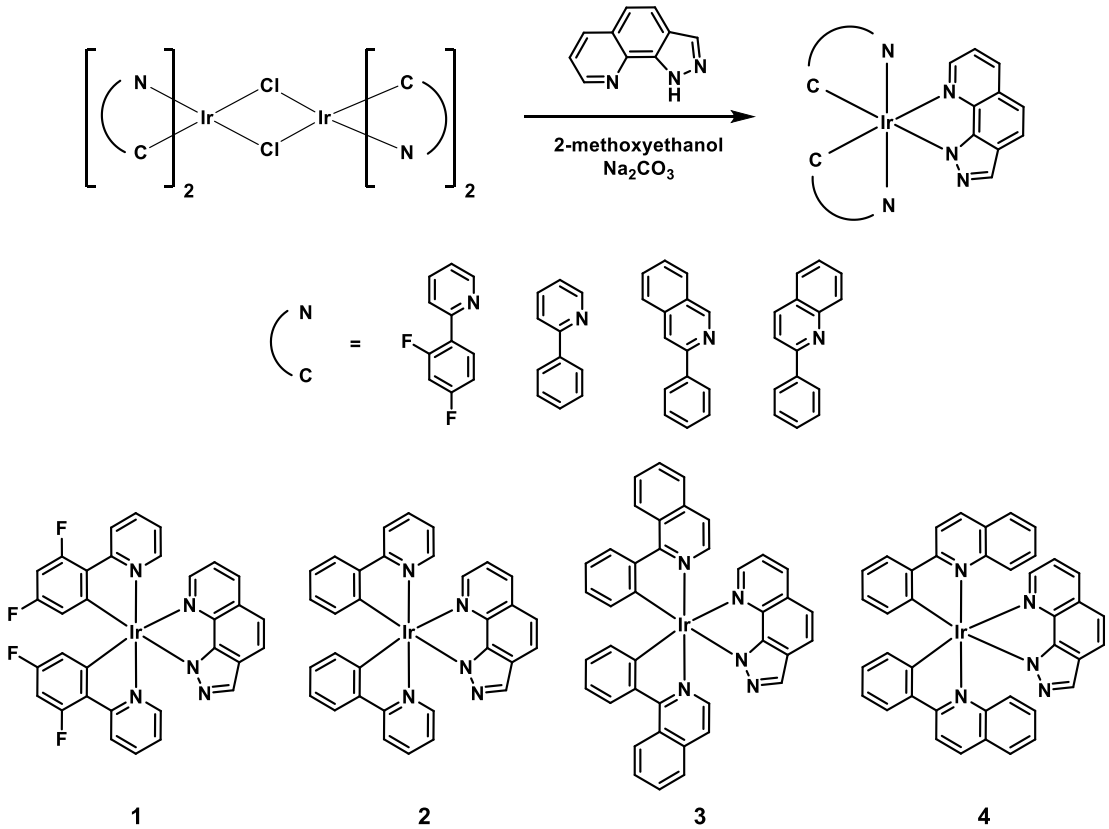

Scheme 1. Synthesis of Ir complexes

2.3 Crystal structure

Crystal of complex **3** was obtained by slow diffusion of hexane into dichloromethane solution. Table 1 and 2 reported the selected bond lengths and angles for the structure. Crystal structure of complex **3** (Figure 2) showed distorted octahedral geometry with two 2-phenylisoquinoline in the *trans* position and one pyrazole[5,4-h]quinoline coordinated. The bond length of Ir(1)-N(1) and Ir(1)-C(15) were 2.048(4) and 2.001(5) Å which is common for similar cyclometalated ligands chelated to Ir(III) complexes previously reported in literature.[23-25] Due to the *trans* effect caused by strong sigma donation of the carbon atoms,[26] the bond length of Ir(1)-N(3) and Ir(1)-N(5), 2.204(4) and 2.155(4) Å, are longer than cyclometalated ligands. Also the bite angle of pyrazole

ligand, 78.47(16)°, is bigger than normal pyridyl azolate ligand in the literature[26, 27] because of the rigid ligand structure.

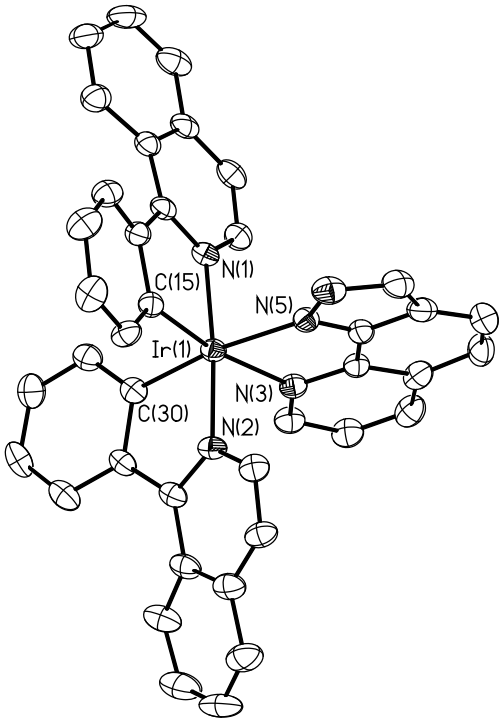

Figure 2. X-ray structure of complex **3**. Ellipsoids include 50% of the electron density.

Table 1. Selected bond length (Å) for Ir complex **3**

Ir(1)-N(1)	2.048(4)	Ir(1)-N(2)	2.050(4)
Ir(1)-N(3)	2.204(4)	Ir(1)-N(5)	2.155(4)
Ir(1)-C(15)	2.001(5)	Ir(1)-C(30)	2.014(5)

Table 2. Selected bond angle (°) for Ir complex **3**

N(1)-Ir(1)-C(15)	79.51(19)	N(2)-Ir(1)-C(30)	80.08(19)
N(3)-Ir(1)-N(5)	78.47(16)	C(15)-Ir(1)-C(30)	92.50(2)
C(30)-Ir(1)-N(1)	95.12(19)	C(15)-Ir(1)-N(2)	98.76(19)
C(15)-Ir(1)-N(5)	94.07(19)	C(30)-Ir(1)-N(5)	172.15(17)
C(15)-Ir(1)-N(3)	170.71(17)	C(30)-Ir(1)-N(3)	95.35(18)
N(1)-Ir(1)-N(2)	174.86(15)	N(1)-Ir(1)-N(5)	90.27(17)
N(2)-Ir(1)-N(5)	94.69(17)	N(1)-Ir(1)-N(3)	94.85(16)
N(2)-Ir(1)-N(3)	87.47(16)		

2.4 Absorption and emission spectroscopy

The UV-Vis absorption spectra of complex **1**-**4** are presented in Figure 3 and were measured at concentration of 10^{-5} M of CH_3CN solution at room temperature. The absorption band at wavelength below 300 nm ($\varepsilon > 10^4$ $M^{-1}cm^{-1}$) is assigned to the ligand centered (^{1}LC) $^1\pi$–π^* transition and the absorption band at λ = 300-400 nm is the mixture of singlet-manifold ligand-to-ligand charge transfer (^{1}LLCT) and metal-to-ligand charge transfer (^{1}MLCT) transitions. The lowest-lying bands at λ > 400 nm in complex **1** and **2** are attributed to both singlet and triplet metal to ligand charge transfer transition, ^{1}MLCT and ^{3}MLCT, respectively. Moreover bathochromic shift is observed in complex **3** and **4**, the absorption extinction coefficient increases and the lowest-lying absorption band extends to 550 nm due to the large π conjugated ligands (C^N) from phenylpyridium to phenylquinoline and phenylisoquinoline.

The emission spectra were recorded at concentration of 10^{-5} M of degassed CH_3CN solution in Figure 3 and Table 3. All the Ir(III) complexes exhibit yellow to red emission with λ_{max} at 534, 530, 612 and 607 nm. With large π conjugated ligands (C^N), the emission properties can be easily tuned by more than 70 nm.[28] The vibronic structured emission indicates that the emission excited states consist of two mixing transitions between ligand centered (^{3}LC) and ^{3}MLCT character.[29] And $Ir(piq)_2$(N^N) complex possesses larger radiative rate constant, 1.85×10^5, than $Ir(pq)_2$(N^N) complex, 2.24×10^4, resulting in high luminescent quantum yield (0.38) in acetonitrile. Solid state emission also displays in Figure 4, complexes **1**-**4** exhibit red shift emission λ_{max} than in solution due to the π–π stacking of the structure. Furthermore, upon cooling all the samples down to 77 K, the emission profile displays vibronic structure and hypsochromic shift, as expected due to the rigidochromic effect. (Figure 5 and Table 4)

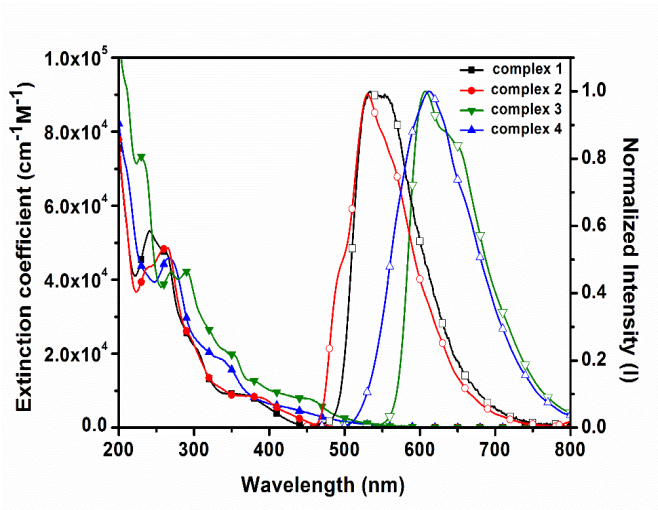

Figure 3. UV-Vis and emission spectra of Ir(III) complexes. The measurement was in acetonitrile at 10^{-5}M.

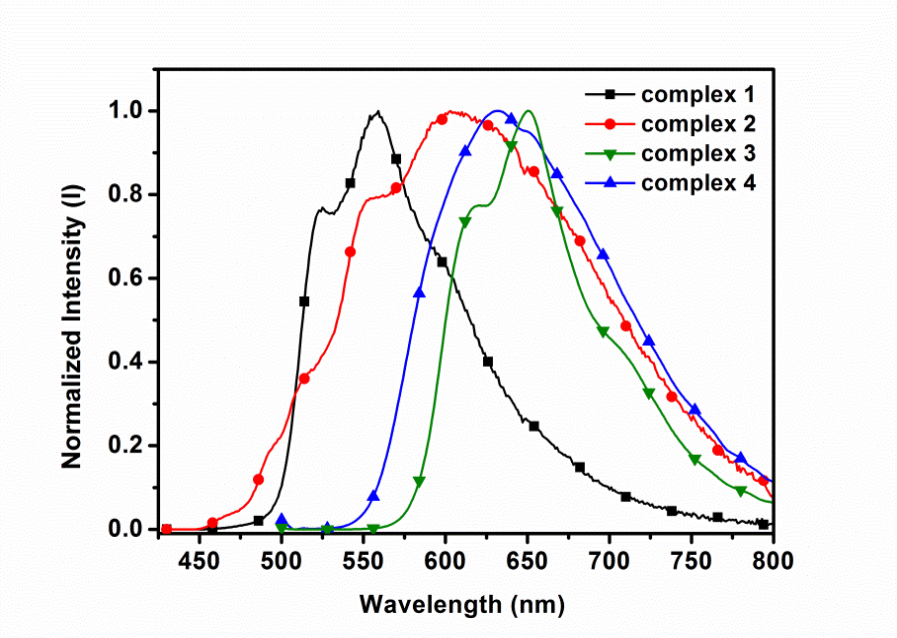

Figure 4. Emission spectra of Ir(III) complexes in solid state.

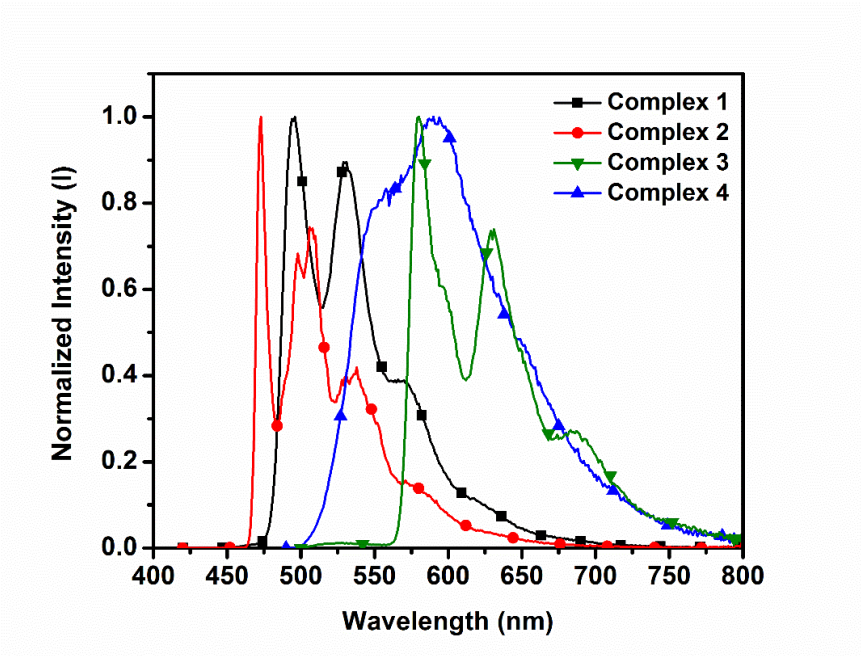

Figure 5. Emission spectra of Ir(III) complexes in 77K. The measurement was in 2-methylTHF at 10^{-5}M.

Table 3. Photophysical data for Ir(III) complexes in acetonitrile solution

	Absorption[1]	Emission, ACN, 298K[1]				
	λmax, nm	λmax[2], nm	τ[2], μs	ϕ	k_r, s^{-1}	k_{nr}, s^{-1}
1	241, 263, 305, 370	534, 553	69.8	0.42	6.02×10^3	8.31×10^3
2	238, 264, 300, 390	495, 530, 564	3.62	0.08	2.21×10^4	2.54×10^5
3	230, 269, 289, 354, 452	612	2.05	0.38	1.85×10^5	3.02×10^5
4	266, 338, 434	607, 645	0.82 (56.8%) 3.05 (43.2%)	0.04	2.24×10^4	5.38×10^5

1. Acetonitrile was used for UV-Vis and PL measurement in degassed. 2. λex = 400 nm. 3. Quantum yield was measured by integrating sphere.

Table 4. Photophysical data for Ir(III) complexes in solid state and 77K

	Emission, solid state, 298K			Emission, 77K[2]	
	λmax, nm[1]	τ, μs	ϕ[2]	λmax, nm[1]	τ, μs
1	523, 559	13.4 (66.2%) 25.7 (33.8%)	0.11	496, 531, 572	139.2 (84.4%) 215 (15.6%)
2	553, 603	3.32 (50.7%) 9.99 (47.6%) 33.0 (1.7%)	0.01	473, 498, 508, 538, 571	5.19 (72.6%) 8.24 (17.4%)
3	620, 651, 702	47.3 ns (56.9%) 145.4 ns (39.3%) 474.9 ns (3.8%)	0.03	580, 631, 685	7.13 (55.8%), 4.05 (44.2%)
4	632	8.1 ns (61.5%) 31.0 ns (34.8%) 179.1 ns (3.7%)	0.01	550, 590, 650	4.94 (78.2%), 1.19 (21.8%)

1. λex = 400 nm. 2. 77K measurement was measured in 2-methylTHF. 3. Quantum yield was measured by integrating sphere.

2.5 Computational calculation

The molecular structures of Ir(III) complexes **1**-**4** were optimized at their electronic ground state (S_0) by means of density function theory (DFT) at B3LYP/(6-31G(d,p) level. The optimized ground state (S_0) structure shows a distorted octahedral geometry, for complex **3**, the bond length of Ir-C(15) and Ir-C(30) are 2.007 and 2.016 Å, versus corresponding crystal structure values of 2.001 and 2.014 Å, respectively. Also according to previous literature, Ir-N(pyridine) bond distances are overestimated by the B3LYP functional, resulting a longer bond length of range 2–4%.[30, 31] Figure 6 shows the selected front orbitals and orbital transition of complexes **1**-**4**. Figure 7 displays the energy level diagram and the HOMO–LUMO gap of Ir complexes. In complex **2**, without any substituted group, the HOMO distributes over the d-orbital of Ir(t_{2g}) and π-orbital of pyrazole ring and cyclometalated phenyl rings lying at -5.335 eV. While adding the electron withdrawing groups, F atoms stabilized the HOMO of complex **1** lying at -5.498 eV, and with extension of π conjugation, the HOMO increase to -5.312 and -5.288 eV in complex **3** and **4**. The LUMOs of these four complexes locate at π* character of two ppy, dfppy, piq, or pq moieties, mainly on the pyridyl fragment, and minor contribution on the metal d-orbital. Besides, in complex **3** and **4**, the LUMO is stabilized by the long π conjugation lying at -2.080 and -2.030 eV compared to complex **2** (-1.549 eV).

To further gain further insight into the electronic transition, we performed the computational calculation by means of time dependent density function theory (TDDFT) in acetonitrile. The 50 singlet excited states ($S_0 \rightarrow S_n$, n = 1 to 50) were calculated and the most relevant transition involved along with their energy, oscillator strength, assignment are listed in Table 5. The lowest-energy singlet vertical excitation, $S_0 \rightarrow S_1$, for complex **2**, **3**, **4** are assigned to HOMO → LUMO which consists of the d(Ir)π(phenyl)π(pyrazole) → π*(ppy, piq or pq). For complex **1**, the $S_0 \rightarrow S_1$ is assigned to HOMO-1 → LUMO which is attributed to d(Ir)π(phenyl) → π*(dfppy). Moreover, from the transition assignments of the lowest-energy singlet excitation (S_1), the transition of Ir complexes can be possible to ascribe such process to a mixing singlet-manifold metal-to-ligand charge transfer, ^{1}MLCT, intraligand charge transfer, ^{1}ILCT, and ligand-to-ligand charge transfer, ^{1}LLCT. Also, those calculated values correspond well to the experimental absorption spectra. (See Figure 8)

To understand the emission properties of these Ir(III) complexes, 50 vertical excitations of singlet to triplet state ($S_0 \rightarrow T_n$, n = 1 to 50) were calculated at optimized S_0 geometry and first three transitions are showed at Table 6. The first triplet transition (T_1) for complex **1** is assigned to HOMO → LUMO+1 and HOMO → LUMO+2, and

for complex **2**, the T_1 is assigned to HOMO-1 → LUMO+1 which are attributed to the d(Ir)π(pyrazole) → π*(pyridine)π*(dfppy or ppy) with ^{3}MLCT, ^{3}ILCT and ^{3}LLCT character. For large π-conjugated complex **3** and **4**, the majority of $S_0 \rightarrow T_1$ transition is assigned to HOMO → LUMO which is attributed to d(Ir)π(phenyl) → π*(piq or pq) with ^{3}MLCT and ^{3}ILCT character. Summarizing, in complex **1** and **2**, the emission comes from the N^N ligand, but for complex **3** and **4**, the emission comes from phenylquinoline or phenylisoquinoline.

	Complex **1**	Complex **2**	Complex **3**	Complex **4**
HOMO-1	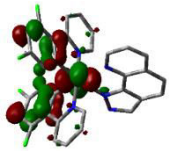	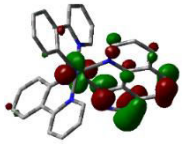	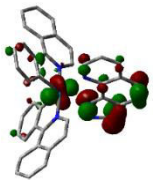	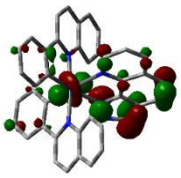
HOMO	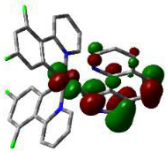	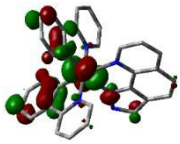	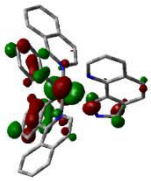	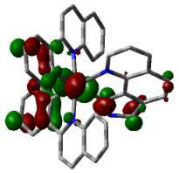
LUMO	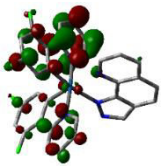	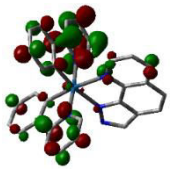	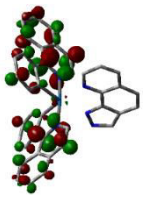	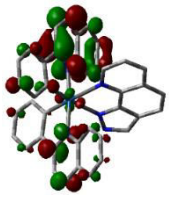
LUMO+1	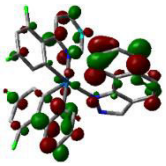		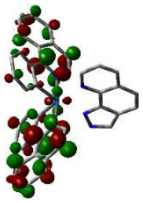	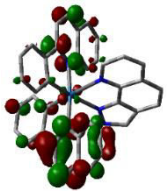
LUMO+2		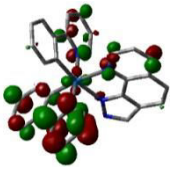	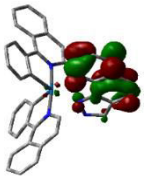	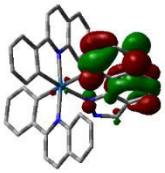

Fig. 6 Isodensity surface plots of some selected frontier molecular orbitals for complexes **1**–**4**, at their optimized S_0 geometry in CH_3CN. The isodensity value is 0.04 e bohr^{-3}.

Table 5. Calculated Energy Levels, Oscillator Strengths (*f*), and Orbital Transition Analyses for Selected Singlet Lower-Lying Transitions of Ir(III) complexes **1**-**4**.

	states	λ_{cal} (nm)	*f*	Assignments
Complex 1	S1	387.78	0.0144	HOMO → LUMO (18%)
				HOMO-1 → LUMO (76%)
	S2	382.20	0.0136	HOMO-1 → LUMO+1 (6%)
				HOMO-1 → LUMO+2 (4%)
				HOMO → LUMO+1 (69%)
				HOMO → LUMO+2 (14%)
	S3	376.32	0.0500	HOMO-1 → LUMO (54%)
				HOMO-1 → LUMO+1 (4%)
				HOMO → LUMO (17%)
				HOMO → LUMO+1 (8%)
				HOMO → LUMO+2 (13%)
	S4	374.31	0.0288	HOMO-1 → LUMO (17%)
				HOMO-1 → LUMO+1 (8%)
				HOMO-1 → LUMO+2 (7%)
				HOMO → LUMO+1 (15%)
				HOMO → LUMO+2 (49%)
	S5	364.04	0.0260	HOMO-1 → LUMO (5%)
				HOMO-1 → LUMO+1 (70%)
				HOMO-1 → LUMO+2 (5%)
				HOMO → LUMO+1 (3%)
				HOMO → LUMO+2 (14%)
Complex 2	S1	408.12	0.0435	HOMO → LUMO (84%)
				HOMO → LUMO+1 (7%)
				HOMO → LUMO+2 (4%)
	S2	398.36	0.0017	HOMO → LUMO+1 (41%)
				HOMO → LUMO+2 (55%)
	S3	390.33	0.0041	HOMO → LUMO (11%)
				HOMO → LUMO+1 (49%)
				HOMO → LUMO+2 (39%)
	S4	384.08	0.0079	HOMO-1 → LUMO (78%)
				HOMO-1 → LUMO+1 (12%)
				HOMO-1 → LUMO+2 (4%)
	S5	377.66	0.0690	HOMO-1 → LUMO (16%)
				HOMO-1 → LUMO+1 (78%)
				HOMO-1 → LUMO+2 (3%)
Complex 3	S1	486.69	0.0641	HOMO-1 → LUMO (3%)
				HOMO → LUMO (95%)
	S2	460.84	0.0022	HOMO → LUMO+1 (96%)
	S3	449.71	0.0341	HOMO-1 → LUMO (96%)
				HOMO-1 → LUMO+1 (3%)
				HOMO → LUMO (3%)
	S4	427.46	0.0372	HOMO-1 → LUMO (4%)
				HOMO-1 → LUMO+1 (93%)
	S5	392.84	0.0065	HOMO → LUMO+2 (98%)
Complex 4	S1	478.02	0.0064	HOMO → LUMO (96%)
	S2	472.74	0.0464	HOMO-1 → LUMO+1 (2%)
				HOMO → LUMO+1 (95%)
	S3	444.44	0.0219	HOMO-1 → LUMO (91%)
				HOMO-1 → LUMO+1 (3%)
	S4	431.95	0.0220	HOMO-1 → LUMO (4%)
				HOMO-1 → LUMO+1 (93%)
	S5	390.66	0.0058	HOMO → LUMO+2 (98%)

Table 6. Calculated Energy Levels, Oscillator Strengths (*f*), and Orbital Transition Analyses for Selected Triplet Lower-Lying Transitions of Ir(III) complexes **1**-**4**.

	states	λ_{cal} (nm)	*f*	Assignments
Complex 1	T1	471.64	0	HOMO → LUMO+1 (38.9%) HOMO → LUMO+2 (39.2%)
	T2	433.51	0	HOMO-4 → LUMO (8.0%) HOMO-3 → LUMO+1 (10.2%) HOMO-3 → LUMO+2 (7.8%) HOMO-1 → LUMO (43.0%) HOMO → LUMO (6.4%)
	T3	429.80	0	HOMO-3 → LUMO (24.4%) HOMO-1 → LUMO (5.3%) HOMO-1 → LUMO+1 (20.6%) HOMO-1 → LUMO+2 (13.1%) HOMO → LUMO+2 (5.6%)
Complex 2	T1	472.60	0	HOMO-2 → LUMO+1 (5.4%) HOMO-1→ LUMO (7.4%) HOMO-1 → LUMO+1 (49.2%) HOMO-1 → LUMO+2 (9.0%) HOMO → LUMO+1 (8.9%)
	T2	457.14	0	HOMO-3 → LUMO+2 (8.7%) HOMO-1 → LUMO (4.8%) HOMO → LUMO (57.3%) HOMO → LUMO+2 (4.9%)
	T3	450.66	0	HOMO-3 → LUMO (15.5%) HOMO → LUMO+1 (13.7%) HOMO → LUMO+2 (47.5%)
Complex 3	T1	568.59	0	HOMO-3 → LUMO (5.8%) HOMO-3 → LUMO+1 (5.4%) HOMO-2 → LUMO+1 (15.1%) HOMO → LUMO (51.3%) HOMO → LUMO+1 (5.3%)
	T2	557.96	0	HOMO-4 → LUMO+1 (5.2%) HOMO-2 → LUMO (31.0%) HOMO-1 → LUMO (7.7%) HOMO → LUMO+1 (34.9%)
	T3	477.77	0	HOMO-4→ LUMO (8.0%) HOMO-3 → LUMO (8.0%) HOMO-2 → LUMO (9.2%) HOMO-2 → LUMO+1 (10.2%) HOMO-1 → LUMO (5.9%) HOMO-1 → LUMO+1 (10.1%) HOMO → LUMO (30.5%)
Complex 4	T1	529.07	0	HOMO-2 → LUMO+1 (7.7%) HOMO-1 → LUMO (11.1%) HOMO → LUMO (62.8%)
	T2	523.39	0	HOMO-4 → LUMO+1 (7.6%) HOMO-3 → LUMO (11.5%) HOMO-1 → LUMO+1 (6.2%) HOMO→ LUMO (55.8%)
	T3	490.28	0	HOMO-4 → LUMO (6.6%) HOMO-2 → LUMO (5.2%) HOMO-1 → LUMO (15.2%) HOMO-1 → LUMO+2 (5.7%) HOMO → LUMO (23.9%) HOMO → LUMO+1 (13.2%)

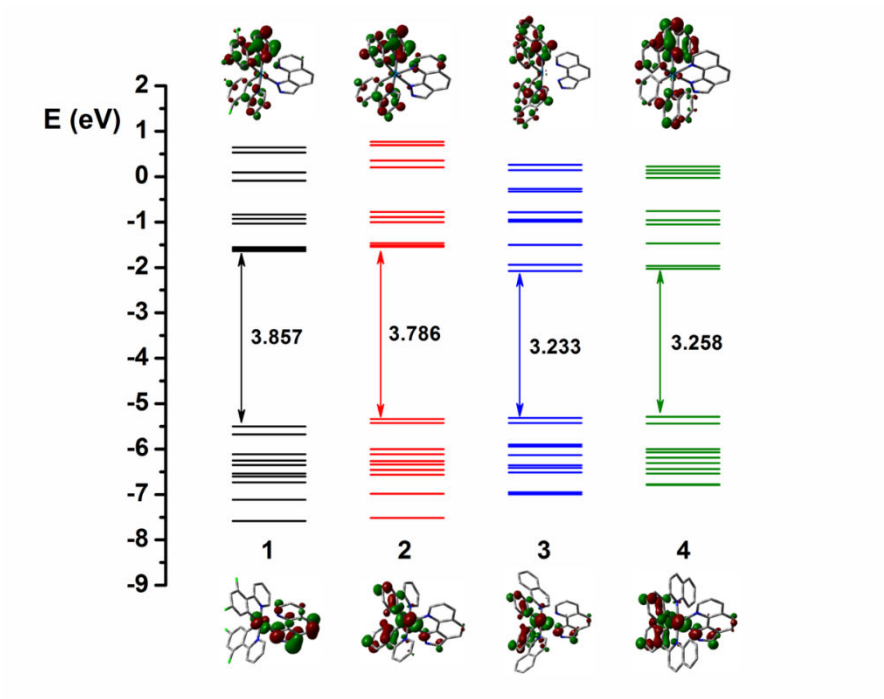

Figure 7. Partial molecular orbital diagram for Ir(III) complexes **1−4**. The arrows are intended to highlight the HOMO−LUMO energy gaps

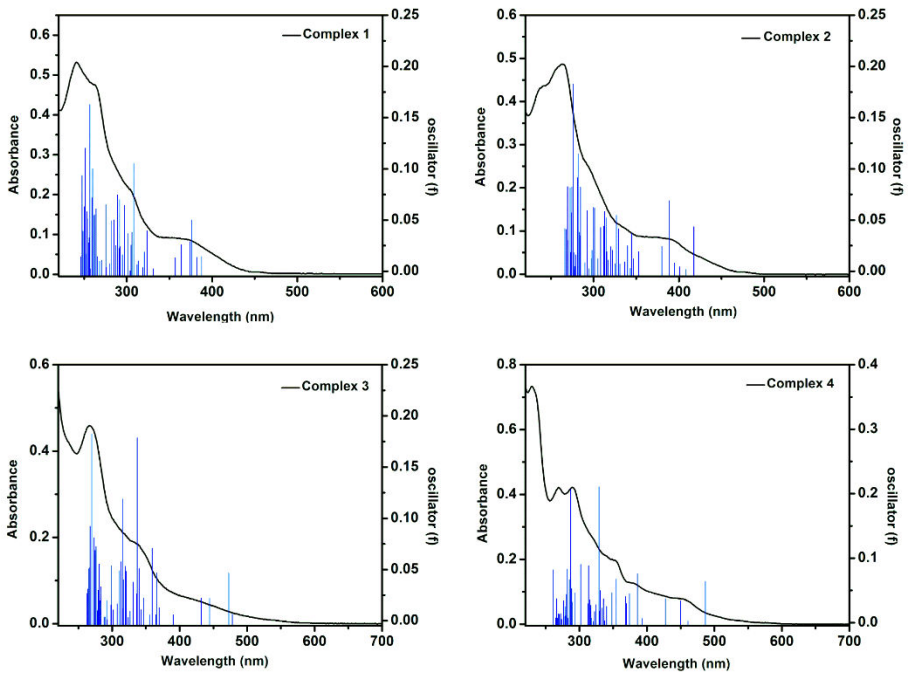

Figure 8. Comparison of singlet excitations from TDDFT with absorption spectra at 10^{-5} M Ir complexes in acetonitrile.

2.6 Electrochemistry

The electrochemical behavior of the iridium(III) complexes was investigated by cyclic voltammetry, dissolving the compounds in freshly distilled and dry acetonitrile, containing 0.1 M of supporting electrolyte tetrabutylammonium hexafluorophosphate ($TBAPF_6$). The analytic solutions have concentration at 10^{-3} M and ferrocene was used as internal reference.[32] All the potential values shown in Table 7 are versus SCE. The values of the first oxidation potentials and the first reduction potentials were used to calculate the values of the frontier orbitals, HOMO and LUMO of the Ir(III) complexes.

Electrochemical measurement of these four Ir complexes were performed in acetonitrile solutions. All the Ir complexes showed irreversible process in oxidation, complex **1** and **2** also showed irreversible process in reduction when applied Cyclic voltammetry (CV) as shown in Figure 9. The $E_{1/2}$ potential of oxidation and reduction were taken from Differential Pulse Voltammetry (DPV) measurement in Figure 10. Table 7 shows the oxidation potential which is 1.16, 1.00, 0.98, 0.96 V (vs SCE), and reduction potential which is -1.91, -1.97, -1.65, -1.65 V (vs SCE) for **1**, **2**, **3**, **4**, respectively. In complex **1**, fluorine atoms stabilize the HOMO resulting in a higher oxidation potential than the other complexes. For the large π-conjugated ligand the stabilization of the LUMO results in a lower reduction potential in complex **3** and **4**.

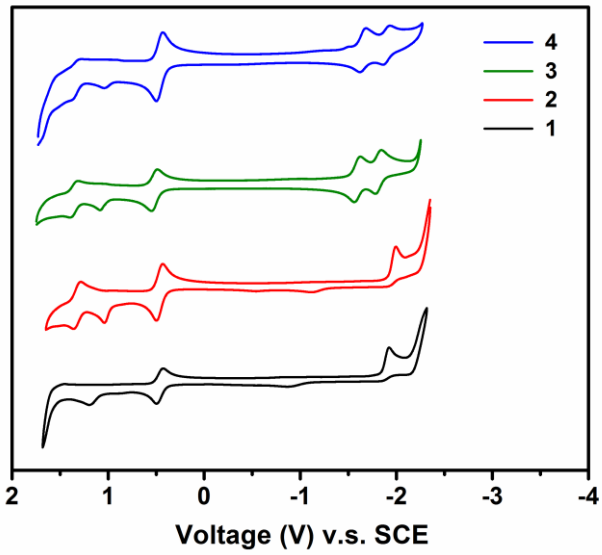

Figure 9. Cyclic voltammetry (CV) measurements of Iridium(III) complexes. Ferrocene as internal standard is 0.46 V vs SCE.

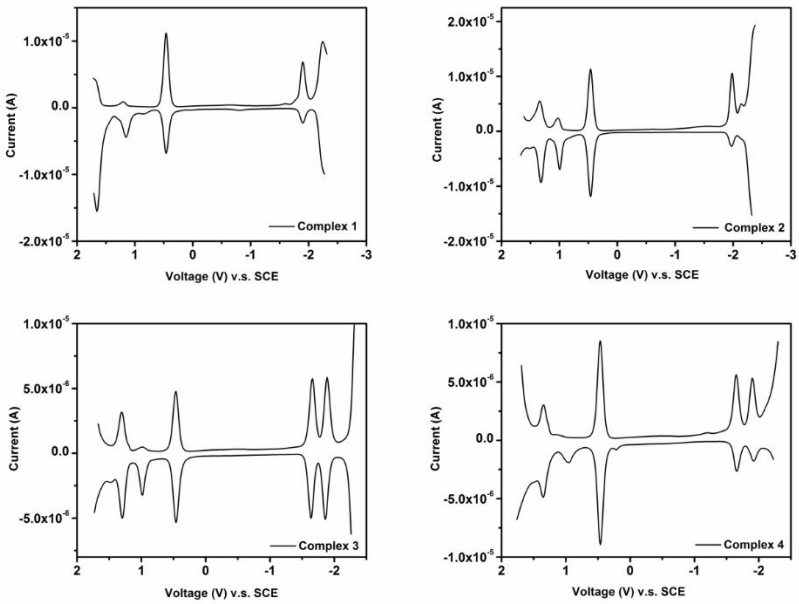

Figure 10. Differential Pulse Voltammetry (DPV) measurements of Iridium(III) complexes. Ferrocene as internal standard is 0.46 V vs SCE.

Table 7. Electrochemical properties of Ir(III) complexes

Complex	$E_{1/2}^{ox}$, V	$E_{1/2}^{red}$, V
1	1.16	-1.91
2	1.00	-1.97
3	0.98	-1.65, -1.89
4	0.96	-1.65, -1.90
$[Ru(bpy)_3]^{2+}$	1.35[d]	-1.33,[d] -1.52,[d]-1.76[d]

a. $E_{1/2}$ determined through Differential Pulse Voltammetry (vs SCE). b. CH_3CN was used as solvent. c. Ferrocene as internal standard for each measurement. d. literature report from *J. Am. Chem. Soc.* **1973**, *95*, 6582

2.7. Electrochemiluminescence

For ECL studies, the compounds were prepared at a concentration 0.2 mM of dry acetonitrile with 0.1 M tetra-butylammonium hexafluorophosphate ($TBAPF_6$). The solution was purged with argon for 15 minutes prior every measurement. Co-reactant ECL was generated additionally adding to the solution 10 mM of tripropylamine (TPA) or 5 mM of benzoyl peroxide (BPO).[17] In the annihilation method the ECL/voltage curves were recorded by scanning the potential 0.1 V beyond the oxidation and reduction potential of the compounds, to ensure the generation of 1^+ and 1^- forms of the Ir(III) complexes. In the TPA oxidative reduction method since for all the complexes only one oxidation process is observed, the potential was scanned from 0 to

1.5 V. In the BPO reductive oxidation method, instead, the potential was scanned from 0 to 0.1 V beyond the reduction potential of the compounds. The ECL spectra for the calculation of the efficiencies were recorded in a pulsing for 1.0 s at 1.5 V for the TPA method; a pulse at an overpotential of 0.1 V for the reduction potential; a sequentially stepping at 0.1 V beyond the oxidation and reduction potential of the compounds for the annihilation method. In each case an integration time of 20 seconds was used. The relative ECL efficiencies Φ_{ECL} were obtained by comparison of the ECL spectra with that of $[Ru(bpy)_3]^{2+}$under the same conditions.

In the annihilation method (Figure 11 and Table 8), complex **1**, **2** and **4** show very low ECL intensity. Only complex **3** has better efficiency around 81% compared to $[Ru(bpy)_3]^{2+}$ as 100%. As shown before, the oxidation potential of all complexes reveal irreversible process in cyclic voltammetry, indicating that Ir(IV) species are unstable. The unstable $[Ir(C^\wedge N)_2(N^\wedge N)]^+$ decomposes before it reacts to $[Ir(C^\wedge N)_2(N^\wedge N)]^-$, resulting in a low ECL efficiency. For example, in Figure 11, the CV profile of complex **2** shows two unknown peaks at -1.1 and -0.6 V, possibly due to the decomposition of unstable Ir complexes.

In the case of co-reactant method using TPA, the reaction mechanism is shown below:

$$TPA \rightarrow TPA^{\bullet+} + e^-$$

$$TPA^{\bullet+} \rightarrow (C_3H_7)_2N(\bullet CHC_2H_5) + H^+$$

$$[Ir(C^\wedge N)_2(N^\wedge N)] \rightarrow [Ir(C^\wedge N)_2(N^\wedge N)]^+ + e^-$$

$$[Ir(C^\wedge N)_2(N^\wedge N)]^+ + (C_3H_7)_2N(\bullet CHC_2H_5) \rightarrow [Ir(C^\wedge N)_2(N^\wedge N)]^* + [(C_3H_7)_2N{=}CHC_2H_5]^+$$

$$[Ir(C^\wedge N)_2(N^\wedge N)]^* \rightarrow [Ir(C^\wedge N)_2(N^\wedge N)] + h\nu$$

However, the TPA co-reactant method (presents in Figure 12 and Table 8) also results in poor ECL efficiency in complex **1**, **2** and **4**. The reduction potential of TPA• radicals is -1.64 V vs SCE[15] and the reduction potential of Ir complexes are above -1.64 V, resulting unfavorable electron transfer from TPA• radicals to the LUMO of Ir complex. Stringer *et al.*[16] gave insight about the ECL efficiency by calculating the free energy (ΔG) in the process of electron transfer between TPA• radical and the LUMO of Ir complex by followed equation:

$$\Delta G = E^0(TPA^\bullet) - E^0_{ox} + E_{MLCT}$$

If the $\Delta G < 0$, the probe shows ECL activity. We used the above equation to elucidate the relation between oxidation potential and MLCT emission of the proposed Ir complexes. In Figure 15, complex **1** and **2** are on the $\Delta G = 0$ line or close to this line,

which indicates insufficient driving force and results in no or low ECL efficiency.

The third method is using BPO as co-reactant and it shows higher ECL efficiency than previous two methods. The mechanism of BPO co-reactant is shown below:

$$BPO + e^- \rightarrow BPO^{\bullet-}$$
$$BPO^{\bullet-} \rightarrow C_6H_5CO_2^{\bullet} + C_6H_5CO_2^-$$
$$C_6H_5CO_2^{\bullet} + [Ir(C^\wedge N)_2(N^\wedge N)] \rightarrow [Ir(C^\wedge N)_2(N^\wedge N)]^{+\bullet} + C_6H_5CO_2^-$$
$$[Ir(C^\wedge N)_2(N^\wedge N)]^{+\bullet} + BPO^{\bullet-} \rightarrow [Ir(C^\wedge N)_2(N^\wedge N)]^* + BPO$$
$$[Ir(C^\wedge N)_2(N^\wedge N)]^* \rightarrow [Ir(C^\wedge N)_2(N^\wedge N)] + h\upsilon$$

By applying a negative potential, 0.1 V overpotential which respect to the reduction potential of the label, the complex and BPO were simultaneously reduced at the working electrode, the formed $BPO^{\bullet-}$ then decompose to form a strong oxidizing intermediate radical that upon reaction with the complex generated its oxidized species. Then, the oxidized iridium complex react directly with $BPO^{\bullet-}$ to form the excited state, with this mechanism the light is generated before the reduction potential of the complex, right after the reduction of the BPO.

As shown in Figure 13 and Table 8, the complex **1**, **2** and **4** show lower ECL intensity than $[Ru(bpy)_3]^{2+}$ standard, 28%, 47% and 33% respectively. However, in complex **3**, the ECL efficiency is two times (218%) higher than $[Ru(bpy)_3]^{2+}$ standard. Figure 14 exhibit the ECL spectra of these three method, complex **1** and **2** show the emission is in yellow region, and complex **3** and **4** are emitting at red. To a summary, blue-yellow emitting Ir complexes have low efficiency with TPA co-reactant due to unmatched potential levels, but with BPO one complex displays a very high efficiency (compared to Rubpy), which proves that the approach we used is promising and can give very interesting results in terms of both efficiency and color tuning.

Table 8. ECL efficiency with different methods

	Relative ECL efficiencies Φ_{ECL} (%)[a]		
Compound	Annihilation method	TPA co-reactant method	BPO co-reactant method
1	<1	<1	28
2	<1	<1	47
3	81	74	218
4	4	10	33

a. Efficiences are relative to $[Ru(bpy)_3]^{2+}$ taken as 100% in acetonitrile in the same condition

(concentration 0.2mM).

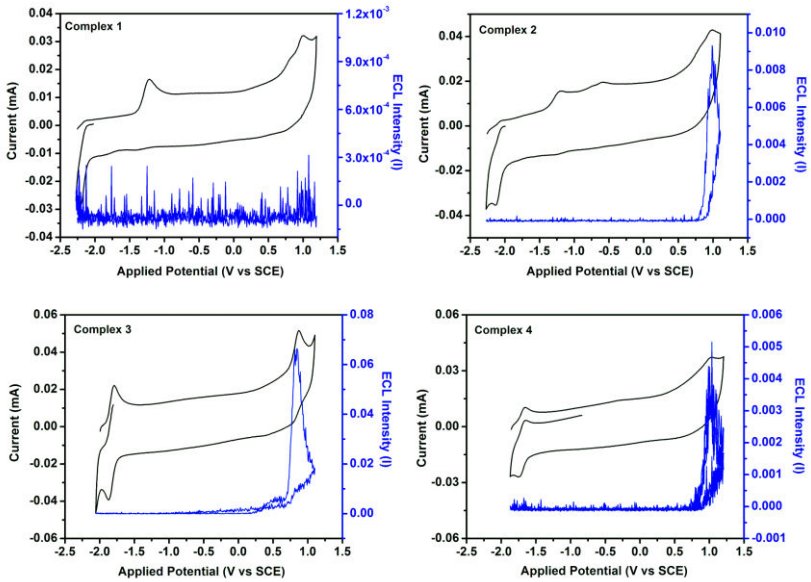

Figure 11. Cyclic voltammetry and corresponding ECL intensity upon scanning between the first reduction and oxidation potential.

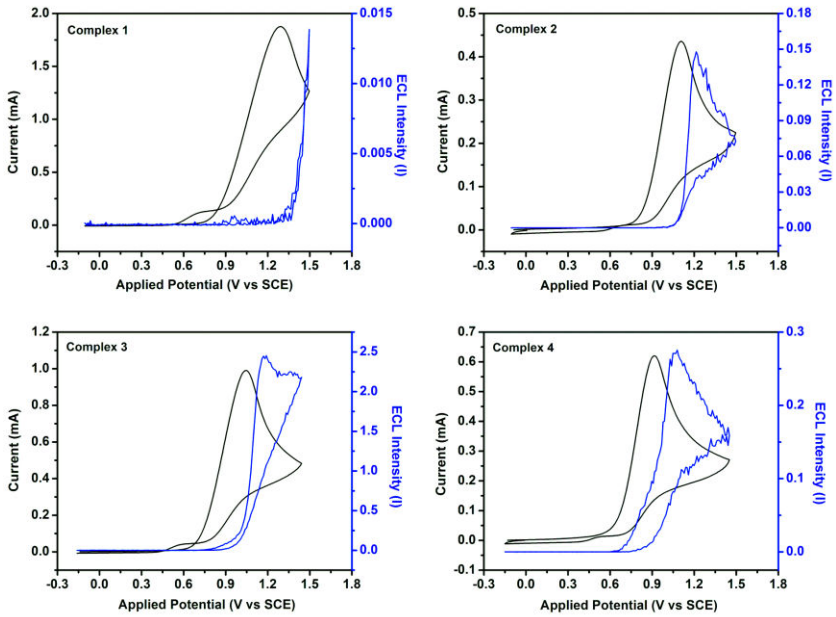

Figure 12. Cyclic voltammetry and corresponding ECL intensity presenting TPA co-reactant.

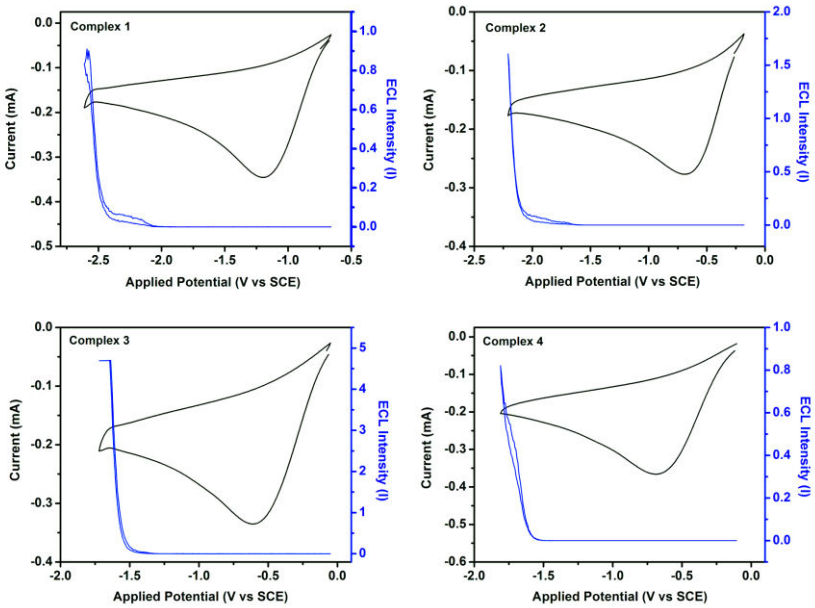

Figure 13. Cyclic voltammetry and corresponding ECL intensity presenting BPO co-reactant.

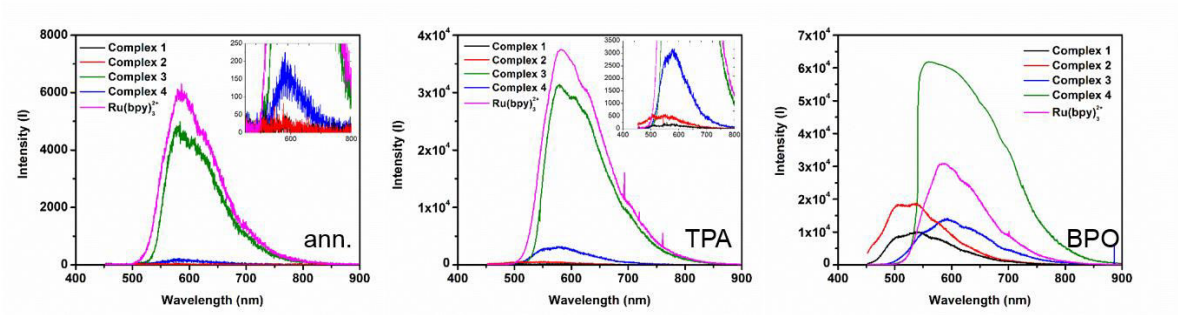

Figure 14. Electrochemiluminescence spectra of Ir complexes **1**-**4** in different method. (Left) annihilation method (middle) TPA co-reactant method (right) BPO co-reactant

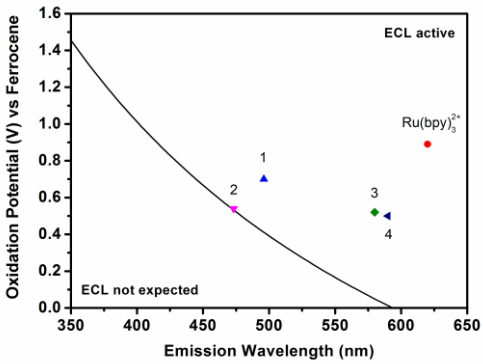

Figure 15. ECL prediction with oxidation potential and emission wavelength

2.8 Cell imaging of Ir(III) complex 2

In addition, we tested complex **2** for bioimaging applications by an *in vitro* study. HeLa cells were incubated with 50 μM complex **2** in PBS with less than 1% DMSO for 2 hours. After incubation time, cells were washed with PBS to remove excess non-uptaken materials and finally fixed by using paraformaldehyde solution. Fluorescence confocal microscopy experiments were carried out by exciting the sample at wavelength 405 nm and the emission signal was collected by a PMT detector in the range 450 to 650 nm. Figure 16 shows that complex **2** was uptaken into HeLa cells and inside all the cytoplasm and organelle except cell nucleus.

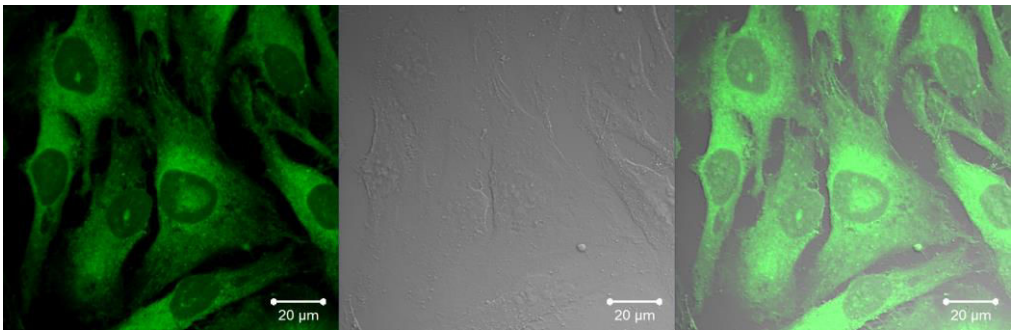

Figure 16. Cell imaging of complex **2** in Hela cells for incubation time 2 hours.

2.9 Conclusion

A series of novel Ir(III) complexes were synthesized with a large π-conjugated pyrazole ligand. By changing different ancillary ligands, we designed four Ir(III) complexes with tunable emission from yellow to red. All complexes were fully characterized and crystal structure of complex **3** was obtained. In electrochemistry study, all complexes showed irreversible oxidation; complex **1** and **2** exhibited irreversible reduction as well. For electrochemiluminescence (ECL), three methods were performed, annihilation, TPA co-reactant and BPO co-reactant. Complex **1** and **2** showed very poor ECL with annihilation and TPA co-reactant methods, due to the irreversible behavior in oxidation and reduction, and also the reduction potential close to TPA radicals potential results in poor electron transfer. BPO co-reactant method gives the best results, and in particular complex **3** exhibited two times higher ECL intensity than $[Ru(bpy)_3]^{2+}$ standard. Still, the redox potential of metal complex is crucial point to exploit the better ECL fluorophore and it might be tuned by different ligand design in the future work.

2.10 Experimental Section

General information and materials

All reagents were purchased from Sigma-Aldrich and Alfa and used without any further purification unless specified notice. Solvents were purified according to the standard procedure.[33] All air and water sensitive experiments were carried out in standard glassware under an inert nitrogen or argon atmosphere using schlenk line techniques. ^{1}H and ^{19}F NMR were acquired on a Bruker AV400 (400 MHz) at 25 °C with the deuterated solvent as the lock and residual solvent as the internal reference. Mass spectrometry measurements and element analysis measurements were performed in the Department of Chemistry, University of Strasbourg. NMR measurements were performed in Institut de Science et d'Ingénierie Supramoléculaires (ISIS), University of Strasbourg.

Photophysical measurement

Steady-state emission spectra were recorded on a HORIBA Jobin-Yvon IBH FL-322 Fluorolog 3 spectrometer equipped with a 450 W xenon arc lamp as the excitation source, double-grating excitation and emission monochromators (2.1 nm mm^{-1} of dispersion; 1200 grooves mm^{-1}), and a TBX-04 single-photon-counting device as the detector. Emission and excitation spectra were corrected for source intensity (lamp and grating) and emission spectral response (detector and grating) by standard correction curves. Time-resolved measurements were performed using the PicoHarp 300 equipped with time correlated single photon counting (TCSPC) system on the Fluoro Time 300 (PicoQuant), where a laser source 375 nm was applied to excite the samples. The laser was mounted directly on the sample chamber at 90° to a Czerny-Turner type emission monochromator (2.7 nm mm^{-1} of dispersion; 1200 grooves mm^{-1}) and collected by a PMA-C 192M single-photon- counting detector. Signals were collected using EasyTau software, and data analysis was performed using FluoFit software (PicoQuant). The quality of the fit was assessed by minimizing the reduced $\chi 2$ function and by visual inspection of the weighted residuals. Luminescence quantum yield was performed with integrating sphere (Hamamatsu, C11347-11).

Electrochemistry

The electrochemical characterization was performed using a CHI750C Electrochemical Workstation (CH Instruments, Inc., Austin, TX, USA). A conventional three electrode

cell configuration was used consisting of a silver wire as quasi-reference electrode (QRE), a platinum wire as counter electrode and a 3 mm diameter glassy-carbon disk , GC (66-EE047 Cypress Systems) as working electrode. Both Cyclic voltammetry (CV) and Differential Pulse Voltammetry (DPV) were applied for all Ir complexes.

The ECL studies were performed using an Autolab electrochemical workstation PGSTAT101 (Metrohm, The Netherlands). For measuring the ECL/voltage curves the system was coupled with a photosensor module with photomultiplier tube (PMT, Hamamatsu, H10723-01, Japan). The transients and the faradic currents were managed by using the software NOVA provided with the Autolab. The ECL spectra were acquired using a calibrated electron multiplying charge couple device (EM-CCD) camera (A-DU971N-BV Andor technology, Newton EM-CCD) coupled with a spectrograph (Andor Technology, Shamrock 163). The camera was cooled to -70 °C prior to use, and controlled by Andor Technology software (Andor Solis). A three electrode cell configuration was used, consisting of a silver wire as quasi-reference electrode (QRE), a platinum wire as counter electrode and a home-made 3 mm diameter glassy-carbon disk (Tokai Inc.), as working electrode. The working electrode was closely facing (a few millimetres) the PMT or the optic fibre connetted to the CCD.

Computational calculation

The theoretical calculation was performed with a Gaussian 09 program. The geometries of ground state (S_0) was optimized by density function theory (DFT) with the exchange correlation hybrid functional B3LYP in the solvent of acetonitrile. A double-ζ polarized basis set 6-31G(d,p) was used for C, H, N and F atoms, and for the Ir(III) metal the LANL2DZ basis set with the pseudo potential LANL was applied. Time-dependent density function theory (TDDFT) calculation using B3LYP functional was performed on the optimized S_0 geometry in the solvent of acetonitrile. 50 singlet and triplet excitations ($S_0 \rightarrow S_n$ and $S_0 \rightarrow T_n$, n = 1 to 50) were calculated for all Ir complexes.

Cell experiment

HeLa cells were cultured inside media which contain 88 % Dulbecco's Modified Eagle Medium (DMEM), 10 % Fetal Bovine Serum, 1 % Penicillin-Streptomycin and 1 % L-Glutamine 200mM (all material was purchased from Gibco) under 37ºC and 5% of CO_2 condition for 48 hours until reaching 70 to 80 % cell confluency. Subsequently, the cells were washed twice with Phosphate Buffer Solution (PBS, Gibco), trypsinated and approximately 50,000 cells were reseeded on the monolayer glass cover slip inside 6

well plate culture dish. New culture media (2 ml) were added gently and the cells were grown overnight.

Synthetic Procedure

Ir Precursor

[Ir(dfppy)$_2$Cl]$_2$

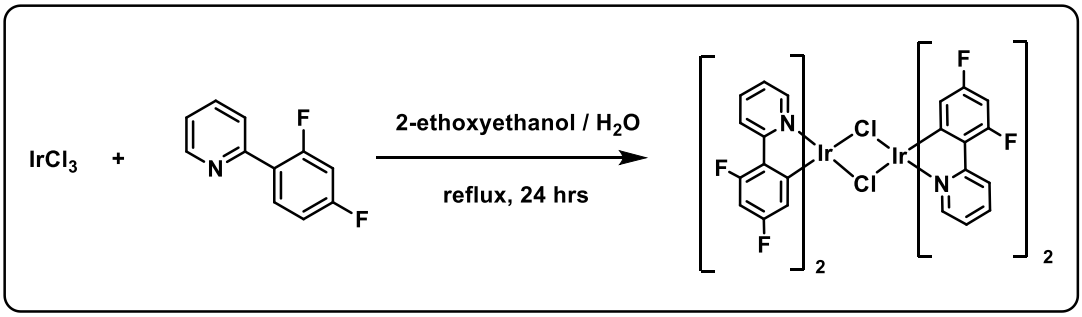

To a 100 mL round bottle with $IrCl_3$ (250 mg, 0.71 mmol) and 2-(2,4-difluorophenyl)pyridine (609.9 mg, 3.19 mmol), solvent pair 2-ethoxyethanol : H_2O = 30 : 10 mL were added. All the mixture was refluxed for 24 hours under N_2. After cooling down to room temperature, collect the precipitation by filtration. The yellow solid was washed by cool ethanol and ether three times. Then use the chemical without further purification. (371.3 mg, yield 86.0%)

[Ir(ppy)$_2$Cl]$_2$

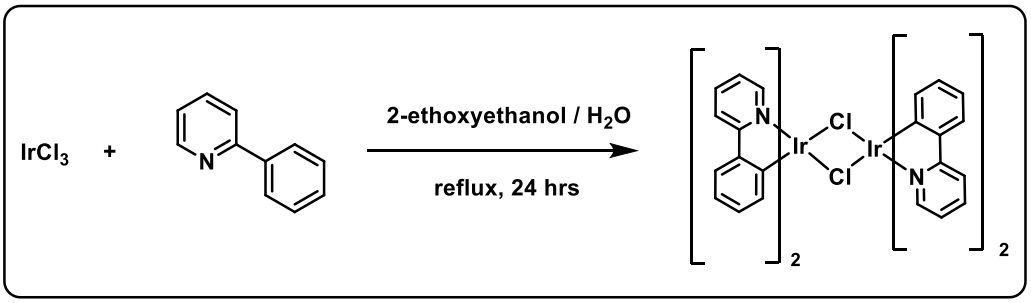

To a 100 mL round bottle with $IrCl_3$ (500 mg, 1.42 mmol) and 2-phenylpyridine (990.3 mg, 6.38 mmol), solvent pair 2-ethoxyethanol : H_2O = 30 : 10 mL were added. All the mixture was refluxed for 24 hours under N_2. After cooling down to room temperature, collect the precipitation by filtration. The yellow solid was washed by cool ethanol and ether three times. Then use the chemical without further purification. (750 mg, yield 98.9%)

[Ir(phenylisoquinoline)$_2$Cl]$_2$

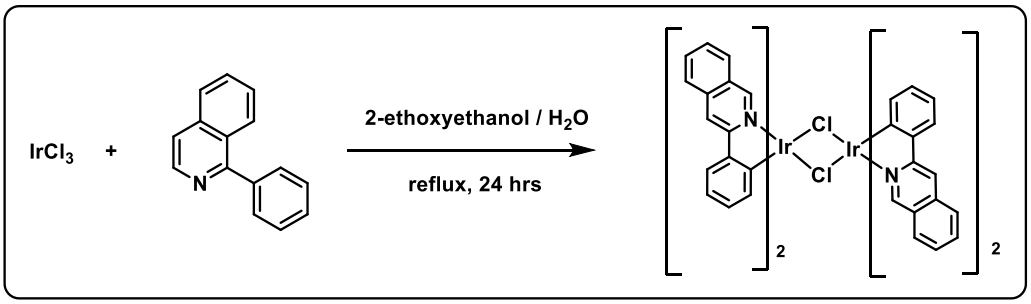

To a 50 mL round bottle with $IrCl_3$ (200 mg, 0.56 mmol) and 2-phenylisoquinoline (523.8 mg, 2.56 mmol), solvent pair 2-ethoxyethanol : H_2O = 15 : 5 mL were added. All the mixture was refluxed for 24 hours under N_2. After cooling down to room temperature, collect the precipitation by filtration. The red solid was washed by cool ethanol and ether three times. Then use the chemical without further purification. (320 mg, yield 88.7%)

[Ir(phenylquinoline)$_2$Cl]$_2$

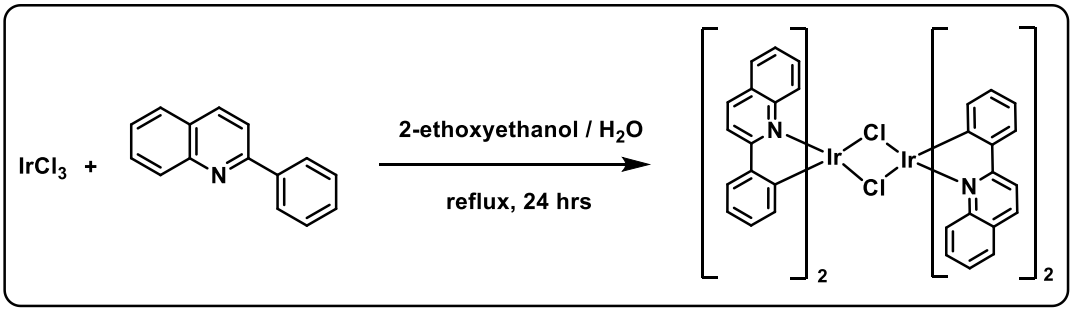

To a 50 mL round bottle with $IrCl_3$ (200 mg, 0.56 mmol) and 2-phenylquinoline (523.8 mg, 2.56 mmol), solvent pair 2-ethoxyethanol : H_2O = 15 : 5 mL were added. All the mixture was refluxed for 24 hours under N_2. After cooling down to room temperature, collect the precipitation by filtration. The red solid was washed by cool ethanol and ether three times. Then use the chemical without further purification. (302 mg, yield 83.7%)

Ir(III) Complex

Ir complex 1

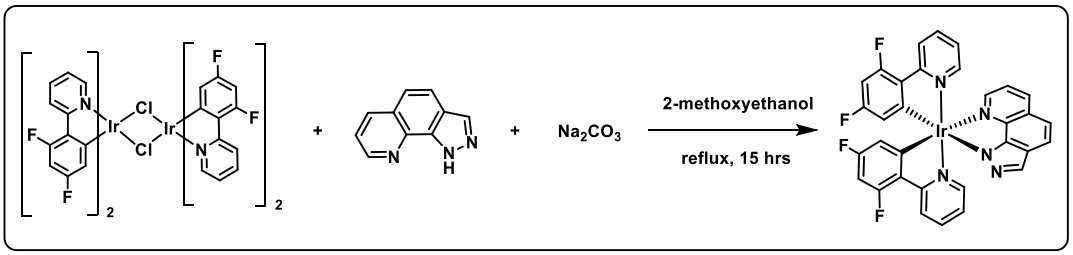

To a 50 mL round-bottomed flask was added Ir-dimer (100 mg, 0.08 mmol), N^N ligand (27.8 mg, 0.16 mmol), and Na_2CO_3 (43.6 mg, 0.41 mmol), followed by addition of 15 mL 2-methoxyethanol under nitrogen atmosphere. The reaction was stirred under reflux for 15 h. The resulting mixture was cooled to room temperature, then remove the solvent in vacuum. The crude product was purified by column chromatography on silica gel (CH_2Cl_2 : ethyl acetate = 1 : 1) providing yellow powder. Then recrystallize (CH_2Cl_2/Hexane) to get yellow solid (83.8 mg, 68.4 %)

Spectral data of **1**: ^{1}H NMR (400 MHz, CD_2Cl_2, 298K): δ 8.40 (dd, J_{HH} = 11.2, 1.6 Hz, 1H), 8.27 (t, J_{HH} = 11.6 Hz, 2H), (d, J_{HH} = 8.0 Hz, 1H) 8.00 (s, 1H), 7.90 – 7.80 (m, 5H), 7.50 (dd, J_{HH} = 10.8, 6.8 Hz, 1H), 7.41 (d, J_{HH} = 8.0 Hz, 1H), 7.33 (d, J_{HH} = 11.6 Hz, 1H), 7.02 (t, J_{HH} = 8.0 Hz, 2H), 6.72 – 6.56 (m, 2H), 6.00 (d, J_{HH} = 11.6, 3.2 Hz, 1H), 5.84 (dd, J_{HH} = 11.6, 3.2 Hz, 1H). HRMS calcd for $C_{32}H_{18}F_9IrN_5$ 742.12071 ([M+H]$^+$); found 742.12063. Elemental analysis calcd for $C_{32}H_{18}F_9IrN_5$: C, 51.89; H, 2.45; N, 9.45, found : C, 52.11; H, 2.80; N, 9.11.

Ir complex 2

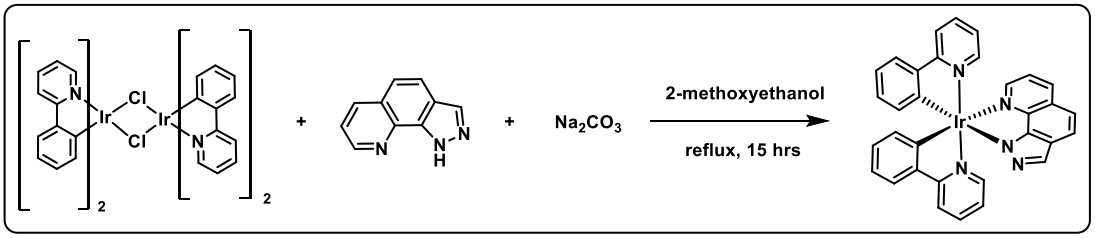

To a 50 mL round-bottomed flask was added Ir-dimer (100 mg, 0.09 mmol), N^N ligand (31.6 mg, 0.19 mmol), and Na_2CO_3 (49.4 mg, 0.47 mmol), followed by addition of 15 mL 2-methoxyethanol under nitrogen atmosphere. The reaction was stirred under reflux for 15 h. The resulting mixture was cooled to room temperature, then remove the solvent in vacuum. The crude product was purified by column chromatography on silica gel (CH_2Cl_2 : MeOH = 10 : 1) providing yellow powder (81.1 mg, 65 %)

Spectral data of **2**: ^{1}H NMR (400 MHz, $CDCl_3$, 298K): δ 8.20 (s, 1H), 8.13 (d, J_{HH} = 8.0 Hz, 1H), 7.84 (d, J_{HH} = 8.8 Hz, 2H), 7.76 (d, J_{HH} = 8.0 Hz, 1H), 7.72 (d, J_{HH} = 5.2 Hz, 1H), 7.64 (t, J_{HH} = 7.6 Hz, 2H), 7.58 – 7.53 (m, 4H), 7.25 (t, J_{HH} = 8.8 Hz, 2H), 7.00 – 6.88 (m, 4H), 6.73 – 6.70 (m, 2H), 6.54 – 6.49 (m, 2H). MS(ESI+) calcd for $C_{32}H_{22}IrN_5$ 670.16 ([M+H]$^+$); found 670.16. Elemental analysis calcd for $C_{32}H_{22}IrN_5$ · 1/2H_2O: C, 56.71; H, 3.42; N, 10.33, found: C, 56.64; H, 3.32; N, 10.29.

Ir complex 3

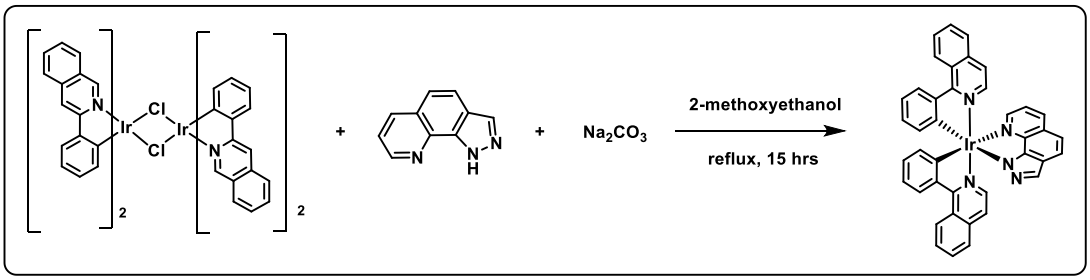

To a 50 mL round-bottomed flask was added Ir-dimer (100 mg, 0.08 mmol), N^N ligand (26.6 mg, 0.16 mmol), and Na_2CO_3 (41.7 mg, 0.39 mmol), followed by addition of 15 mL 2-methoxyethanol under nitrogen atmosphere. The reaction was stirred under reflux for 15 h. The resulting mixture was cooled to room temperature, then remove the solvent in vacuum. The crude product was purified by column chromatography on silica gel (CH_2Cl_2 : MeOH = 10 : 1) providing yellow powder (77.3 mg, 64 %)

Spectral data of **3**: ^{1}H NMR (400 MHz, CD_2Cl_2) δ 9.01 (d, J_{HH} = 8.1 Hz, 1H), 8.95 (d, J_{HH} = 8.6 Hz, 1H), 8.31 (dd, J_{HH} = 18.0, 8.0 Hz, 2H), 8.16 (d, J_{HH} = 8.1 Hz, 1H), 8.09 (s, 1H), 7.84 (d, J_{HH} = 8.6 Hz, 1H), 7.79 (t, J_{HH} = 7.3 Hz, 2H), 7.75 – 7.63 (m, 4H), 7.60 (d, J_{HH} = 4.9 Hz, 1H), 7.54 (d, J_{HH} = 6.5 Hz, 1H), 7.40 (d, J_{HH} = 6.4 Hz, 1H), 7.33 – 7.20 (m, 2H), 7.18 – 7.02 (m, 4H), 6.91 (t, J_{HH} = 7.3 Hz, 1H), 6.83 (t, J_{HH} = 7.4 Hz, 1H), 6.58 (d, J_{HH} = 7.6 Hz, 1H), 6.50 (d, J_{HH} = 7.6 Hz, 1H). MS(ESI+) calcd for $C_{40}H_{26}IrN_5$ 770.19 ($[M+H]^+$); found 770.19. Elemental analysis calcd for $C_{40}H_{26}IrN_5 \cdot H_2O$: C, 61.05; H, 3.59; N, 8.90, found : C, 60.82; H, 3.09; N, 8.85.

Selected crystal data for **3**. $C_{40}H_{26}IrN_5CH_2Cl_2$, M = 853.78, triclinic, space group P1, T = 173(2) K, a = 10.8915(2), b = 11.7095(3), c = 14.3745(4) Å, α = 109.1430(10)°, β = 104.619(2)°, γ = 92.671(2)°, V = 1658.93(7) Å^3, Z = 2, Fcalcd = 1.709 mg/m^3 , F(000) = 840, λ(Mo Kα) = 0.7107 Å, μ = 4.225 mm^{-1}, crystal size = 0.26 × 0.18 × 0.08 mm^3, GOF = 1.184, final $R_1[I > 2\sigma(I)]$ = 0.0346, wR_2(all data) = 0.1150.

Ir complex 4

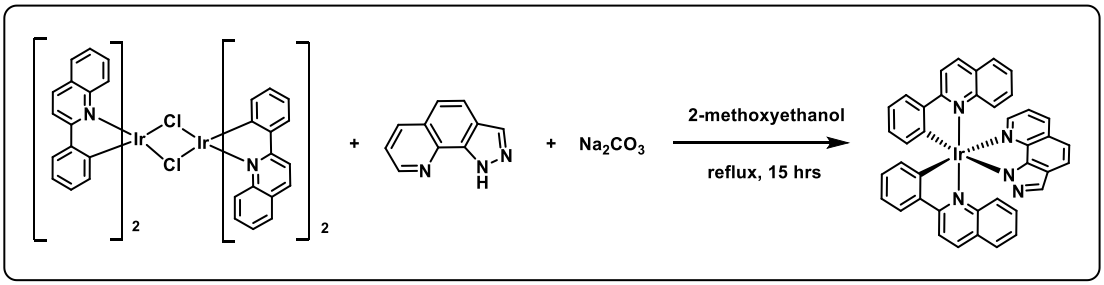

To a 50 mL round-bottomed flask was added Ir-dimer (100 mg, 0.08 mmol), N^N ligand (26.6 mg, 0.16 mmol), and Na_2CO_3 (41.7 mg, 0.39 mmol), followed by addition of 15

mL 2-methoxyethanol under nitrogen atmosphere. The reaction was stirred under reflux for 15 h. The resulting mixture was cooled to room temperature, then remove the solvent in vacuum. The crude product was purified by column chromatography on silica gel (CH_2Cl_2 : MeOH = 10 : 1) providing yellow powder (60.2 mg, 50 %)

Spectral data of **4**: ^{1}H NMR (400 MHz, CD_2Cl_2, 298K): δ 8.20 - 8.02 (m, 5H), 8.01 - 7.84 (m, 5H), 7.63 (d, J_{HH} = 8.7 Hz, 1H), 7.57 (d, J_{HH} = 7.8 Hz, 1H), 7.51 (d, J_{HH} = 8.7 Hz, 2H), 7.25 (dd, J_{HH} = 7.9, 5.3 Hz, 1H), 7.21 – 7.05 (m, 4H), 6.92 (t, J_{HH} = 6.6 Hz, 2H), 6.88 – 6.79 (m, 2H), 6.75 (t, J_{HH} = 6.8 Hz, 2H), 6.58 (d, J_{HH} = 7.6 Hz, 1H). MS (ESI+) calcd for $C_{40}H_{26}IrN_5$ 770.1892 ($[M+H]^+$); found 770.1923. Elemental analysis calcd for $C_{40}H_{26}IrN_5 \cdot 2H_2O$: C, 59.69; H, 3.76; N, 8.70, found: C, 59.67; H, 3.44; N, 8.41.

2.11 Reference

1. K. K.-W. Lo, M.-W. Louie and K. Y. Zhang, *Coord. Chem. Rev.*, 2010, **254**, 2603-2622.
2. L. V. Mattos, G. Jacobs, B. H. Davis and F. B. Noronha, *Chem. Rev.*, 2012, **112**, 4094-4123.
3. R. Lalrempuia, N. D. McDaniel, H. Müller-Bunz, S. Bernhard and M. Albrecht, *Angew. Chem. Int. Ed.*, 2010, **49**, 9765-9768.
4. Z. Ning, Q. Zhang, W. Wu and H. Tian, *J. Organomet. Chem.*, 2009, **694**, 2705-2711.
5. N. Darmawan, C.-H. Yang, M. Mauro, M. Raynal, S. Heun, J. Pan, H. Buchholz, P. Braunstein and L. De Cola, *Inorg. Chem.*, 2013, **52**, 10756-10765.
6. L. Hu and G. Xu, *Chem. Soc. Rev.*, 2010, **39**, 3275-3304.
7. M. M. Richter, *Chem. Rev.*, 2004, **104**, 3003-3036.
8. M.-J. Li, P. Jiao, M. Lin, W. He, G.-N. Chen and X. Chen, *Analyst*, 2011, **136**, 205-210.
9. C. Li, J. Lin, Y. Guo and S. Zhang, *Chem. Commun.*, 2011, **47**, 4442-4444.
10. M. Famulok, J. S. Hartig and G. Mayer, *Chem. Rev.*, 2007, **107**, 3715-3743.
11. J. Liu, Z. Cao and Y. Lu, *Chem. Rev.*, 2009, **109**, 1948-1998.
12. Y. Zhao, Y. Luo, T. Li and Q. Song, *RSC Advances*, 2014, **4**, 57709-57714.
13. H. Lin, M. E. Cinar and M. Schmittel, *Dalton Transactions*, 2010, **39**, 5130-5138.
14. M. Schmittel and H. Lin, *Inorg. Chem.*, 2007, **46**, 9139-9145.
15. W. Miao, J.-P. Choi and A. J. Bard, *J. Am. Chem. Soc.*, 2002, **124**, 14478-14485.
16. B. D. Stringer, L. M. Quan, P. J. Barnard, D. J. D. Wilson and C. F. Hogan, *Organometallics*, 2014, **33**, 4860-4872.
17. K. N. Swanick, S. Ladouceur, E. Zysman-Colman and Z. Ding, *Angew. Chem. Int. Ed.*, 2012, **51**, 11079-11082.
18. M.-M. Chang, T. Saji and A. J. Bard, *J. Am. Chem. Soc.*, 1977, **99**, 5399-5403.
19. I.-S. Shin, J. I. Kim, T.-H. Kwon, J.-I. Hong, J.-K. Lee and H. Kim, *The Journal of Physical Chemistry C*, 2007, **111**, 2280-2286.
20. J. I. Kim, I.-S. Shin, H. Kim and J.-K. Lee, *J. Am. Chem. Soc.*, 2005, **127**, 1614-1615.
21. S. Zanarini, M. Felici, G. Valenti, M. Marcaccio, L. Prodi, S. Bonacchi, P. Contreras-Carballada, R. M. Williams, M. C. Feiters, R. J. M. Nolte, L. De Cola and F. Paolucci, *Chem. Eur. J.*, 2011, **17**, 4640-4647.
22. A. B. Tamayo, B. D. Alleyne, P. I. Djurovich, S. Lamansky, I. Tsyba, N. N. Ho, R. Bau and M. E. Thompson, *J. Am. Chem. Soc.*, 2003, **125**, 7377-7387.
23. N. Darmawan, C.-H. Yang, M. Mauro, R. Frohlich, L. De Cola, C.-H. Chang, Z.-J. Wu and C.-W. Tai, *Journal of Materials Chemistry C*, 2014, **2**, 2569-2582.
24. C.-H. Yang, M. Mauro, F. Polo, S. Watanabe, I. Muenster, R. Fröhlich and L. De

Cola, *Chem. Mater.*, 2012, **24**, 3684-3695.
25. C.-H. Yang, J. Beltran, V. Lemaur, J. Cornil, D. Hartmann, W. Sarfert, R. Fröhlich, C. Bizzarri and L. De Cola, *Inorg. Chem.*, 2010, **49**, 9891-9901.
26. E. Orselli, R. Q. Albuquerque, P. M. Fransen, R. Frohlich, H. M. Janssen and L. De Cola, *J. Mater. Chem.*, 2008, **18**, 4579-4590.
27. C.-H. Lin, Y. Chi, M.-W. Chung, Y.-J. Chen, K.-W. Wang, G.-H. Lee, P.-T. Chou, W.-Y. Hung and H.-C. Chiu, *Dalton Transactions*, 2011, **40**, 1132-1143.
28. S. Lamansky, P. Djurovich, D. Murphy, F. Abdel-Razzaq, R. Kwong, I. Tsyba, M. Bortz, B. Mui, R. Bau and M. E. Thompson, *Inorg. Chem.*, 2001, **40**, 1704-1711.
29. S. Lamansky, P. Djurovich, D. Murphy, F. Abdel-Razzaq, H.-E. Lee, C. Adachi, P. E. Burrows, S. R. Forrest and M. E. Thompson, *J. Am. Chem. Soc.*, 2001, **123**, 4304-4312.
30. K. Nozaki, K. Takamori, Y. Nakatsugawa and T. Ohno, *Inorg. Chem.*, 2006, **45**, 6161-6178.
31. P. J. Hay, *The Journal of Physical Chemistry A*, 2002, **106**, 1634-1641.
32. G. Gritzner and J. Kuta, *Pure Appl. Chem.*, 1984, **56**, 461-466.
33. W. L. F. Armarego and C. L. L. Chai, *Purification of laboratory chemicals*, 5th edn., Butterworth-Heinemann, Amsterdam, 2003.

CHAPTER 3

Synthesis and Characterization of Silicon Nanoparticles

Abstract

Silicon chemistry plays an important role in semiconductor industry and high-tech electronic product. Reducing the size from bulk silicon to small nanoparticles leads to luminescent properties, easy functionalization, biocompatibility and therefore interesting development in bio-and nanomedicine. In this chapter, are presented two wet chemistry methods to synthesize ultrasmall silicon nanoparticles – oxidation method and the use of Zintl salt reaction. The particles were characterized by FT-IR, XPS, TEM/STEM and photophysical properties.

3.1 Introduction

Silicon based materials are highly interesting in development of electronic devices nowadays. In the nanoscale, silicon nanoparticles (Si NPs) also get more attention of their photoluminescent properties. Although the origin of the emission is still controversial, there are two most acceptable explanations, quantum confinement effect and surface state.[1] Due to the quantum confinement effect, the Si NPs exhibit bright luminescence at size below 5 nm. Besides, the emission can also originate from the surface states caused by the surface modifications and the defect sites inside the nanoparticles. The major interests for these nanoparticles (NPs), rely in their biocompatibility, intrinsic luminescence as well as photo- and electro- stability, that have highly potential to apply in many fields such as solar cells,[2] in vitro and in vivo imaging,[3-6] and light emitting diode (LED).[7, 8]

To obtain such small size nanoparticles (< 5 nm), there are plenty of synthetic methods form top-down to bottom-up approaches in the literatures such as mechanical process (high energy ball milling),[9, 10] laser ablation,[11-13] electrochemical etching,[14-16] solution based micelle method[3, 17-19] and solution based reduction–oxidation method[20, 21], etc. Among these methods, solution based micelle method provide a nice approach to control the particle size using surfactant. Tilley *et al.* reported monodisperse Si NPs (1.8 ± 0.2 nm) with amino groups using tetraoctylammonium bromide (TOAB) as surfactant and toluene as solvent.[3] Following this method, in our group, we also modified the micelle method and produced in large scale monodisperse Si NPs with sized of 1.57 ± 0.21 nm.[19] Modified with water soluble amino groups, the blue emitting particles were further employed for the cellular imaging of BV2 cells.[22] However, it is difficult to remove all the surfactant during the purification and the remains of surfactant can cause cytotoxicity to cells.

Therefore, in this chapter, we introduce two synthetic methods without using surfactant, which are bromine oxidation method and zintl salt reaction. By controlling the adding reagents and the reaction time, we can still get quite good monodisperse nanoparticles without using the surfactants. In addition, by means of solution based reduction–oxidation methods, the surface of Si NPs are facile to functionalize by using Grignard reagent or alkyllithium for halogen terminated Si NPs, and hydrosilylation for hydrogen terminated Si NPs. Here, we report the synthesis of Si NPs with two functional groups on the surface, amino and carboxylate. Besides, TEM/STEM, FT-IR and XPS are performed to characterize this materials. Photophysical measurement is also discussed in the chapter.

3.2 Synthesis and Characterization of Si NPs

Synthesis

Si NPs were synthesized from wet chemistry processes. Two different strategies were used: the first methodology was the oxidation method employing Br_2 to oxidize Mg_2Si[23] (Scheme 1A); the second approach was the Zintl salt reaction[24] (Scheme 1B). The reaction detail is showing below.

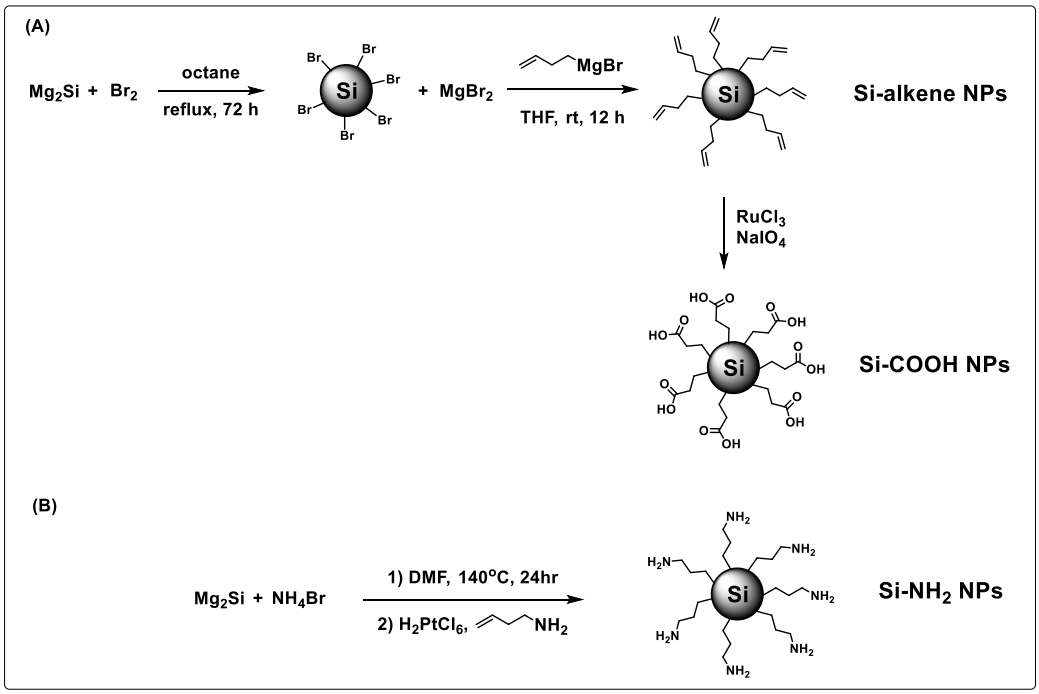

Scheme 1. Synthesis of Si NPs through different methodologies.

For the first synthetic method, Mg_2Si was oxidized by Br_2 in octane to form bromo-terminated Si NPs. The reaction was refluxed for 72 hours. After the reaction, octane was removed by distillation, and fresh dried octane was added. Then Grignard reagent (3-butenylmagnesium bromide) was added to form a capping species, to prevent surface oxidation to silica, leading to alkene terminated Si NPs. However, following the literature procedure, we observed a large amount of white precipitate after adding Grignard reagent. The precipitate is unreacted Grignard reagent because of its poor solubility in octane solution. Therefore fresh dried THF was used to replace the octane to increase the solubility and reactivity of Grignard reagent. The reaction was stirred at room temperature overnight and the final product was as expected the Si-alkene NPs. The NPs were purified by size exclusion chromatography (QX-1) and the final product as a brownish wax.

Without further purification the alkene groups were oxidized to carboxylic acid group by the ruthenium catalyst, $RuCl_3$, and sodium periodate. According to the literature,[25] the best condition is in the solvent mixture acetonitrile : ethylacetate : H_2O = 2 : 2: 3 and stirring at room temperature for 2.5 hours. In our case, however, the optimal reaction time was 4 to 6 hours. Stirring for more than 12 hours, caused a dramatic reduction of the emission properties. Finally the Si-COOH NPs were purified by size exclusion chromatography (LH-20) and MeOH as eluent to get yellow-brown wax.

The second method is called Zintl salt method, 1 equivalent of Mg_2Si was reacted with 4 equivalent of NH_4Br at 130ºC for 24 hours to form hydrogen terminated Si NPs under Ar atmosphere. Then allylamine and Pt catalyst, H_2PtCl_6, were added, alkene group was coupling to Si NPs to obtain the amino-terminated Si NPs. The brown oil like Si nanoparticles were purified by size exclusion chromatography (LH-20) and MeOH as eluent.

In summary, from the oxidation method, we obtained carboxylate functionalized Si NPs (Si-COOH NPs) and from the Zintl salt method, we acquired amino functionalized Si NPs (Si-NH_2 NPs).

FT-IR spectra

Si NPs from the two synthetic methods were characterized by FT-IR in attenuated total reflection (ATR) mode and the spectra are shown in Figure 4. In the oxidation method, the Si-alkene NPs, typical alkene stretching (sp^2C–H) at 3076 cm^{-1} and C=C bond stretching at 1640 cm^{-1} are observed. The other peaks at 2960, 2926, 1456 and 1375 cm^{-1} are attributed to the vibrations of the alkyl chain. However we observed large vibration in between 1000 – 1100 cm^{-1} which is the vibration of Si–O bond. After the reaction to Si-COOH NPs, the broad band in between 2500 – 3600 $cm^{-1}$is the stretching of carboxylic acid group. The carbonyl group of carboxylic acid vibrates at 1730 cm^{-1}. Other peaks at 2789, 1570, and 1375 cm^{-1} are belonged to the alkyl chains. Besides, the peak at 1260 cm^{-1} is assigned to Si-C bond vibration according to literature.[3] Moreover, we still observe Si-O vibration in 1000 – 1100 cm^{-1}, but much less intense than for the alkyl derivatives. In the Zintl salt method, Si-NH_2 NPs, amine N–H bending is at 1604 cm^{-1} and the vibration of alkyl chain are at 2951, 2926, 1454 and 1398 cm^{-1}.

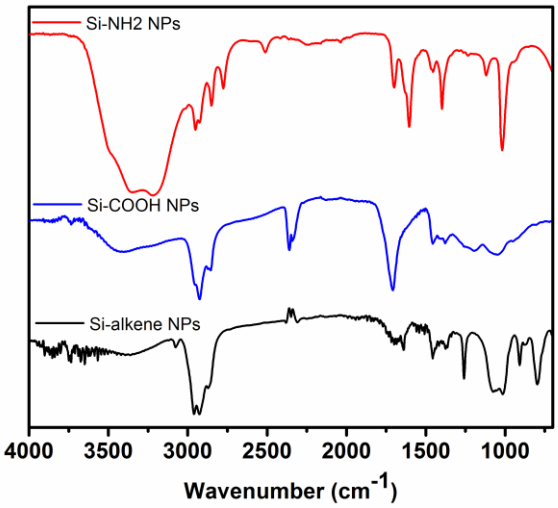

Figure 1. The FT-IR spectra of the Si NPs synthesized.

TEM/STEM imaging

Three nanoparticles, Si-alkene, Si-COOH and Si-NH_2 NPs, were observed by TEM or STEM. For Si-alkene NPs, Figure 2, the particles show polydisperse distribution and size are around 3 ~ 6 nm. After further modification and purification from alkene to carboxylate, the Si-COOH NPs reveal more monodispersity, Figure 3, and the particle size is around 3.9 ± 0.8 nm. Also the particles composition is confirmed by the energy dispersive X-ray spectroscopy (EDX) in Figure 4. The analysis shows that the particles contain mainly Si, C and O elements and we do not observe the Ru catalyst used for functionalization of the nanoparticles. For the Si-NH_2 NPs, we performed the STEM measurement in dark field and the images are depicted in Figure 5. The bright (white) dots are the Si-NH_2 NPs and the particle size is around 3.1 nm. Figure 6 shows the EDX spectrum of Si-NH_2 NPs that confirm that the particles mainly consist of Si element.

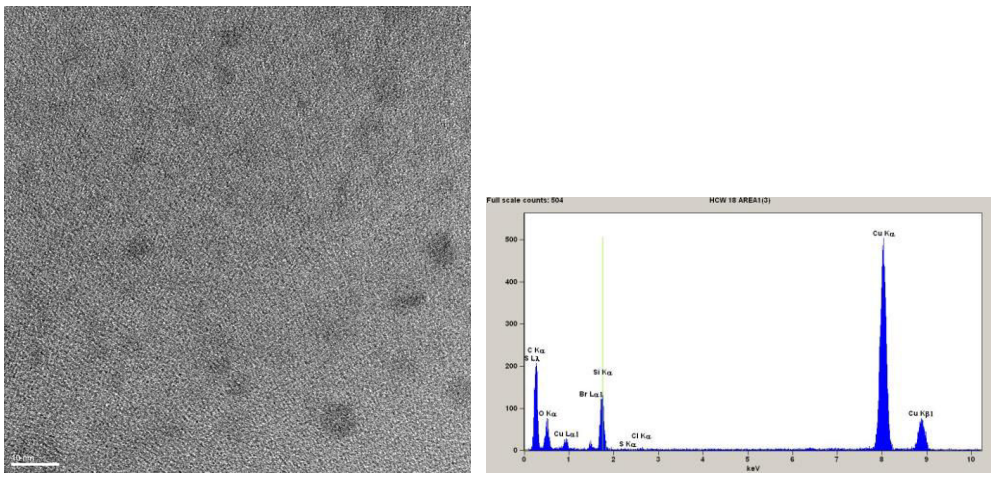

Figure 2. (left) TEM imaging of Si-alkene NPs. Scale bar: 10 nm. (right) EDX analysis of Si-alkene NPs.

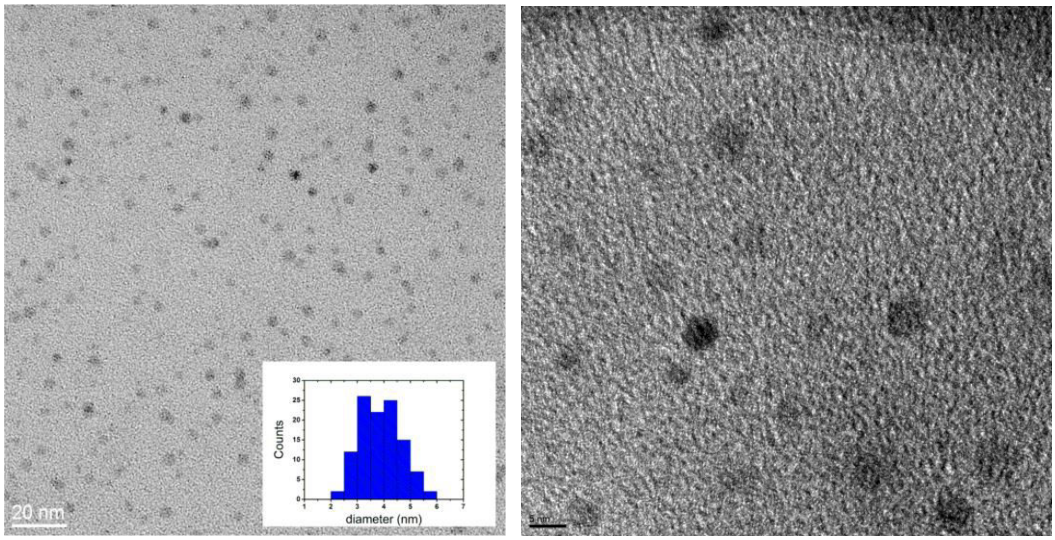

Figure 3. TEM imaging of Si-COOH NPs. Scale bar: 20 nm (left), 5 nm (right).

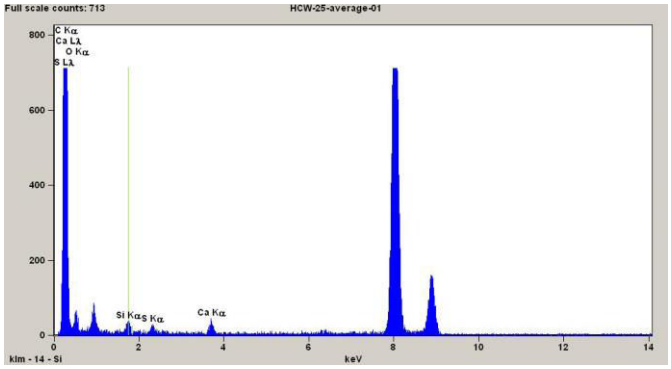

Figure 4. EDX analysis of Si-COOH NPs.

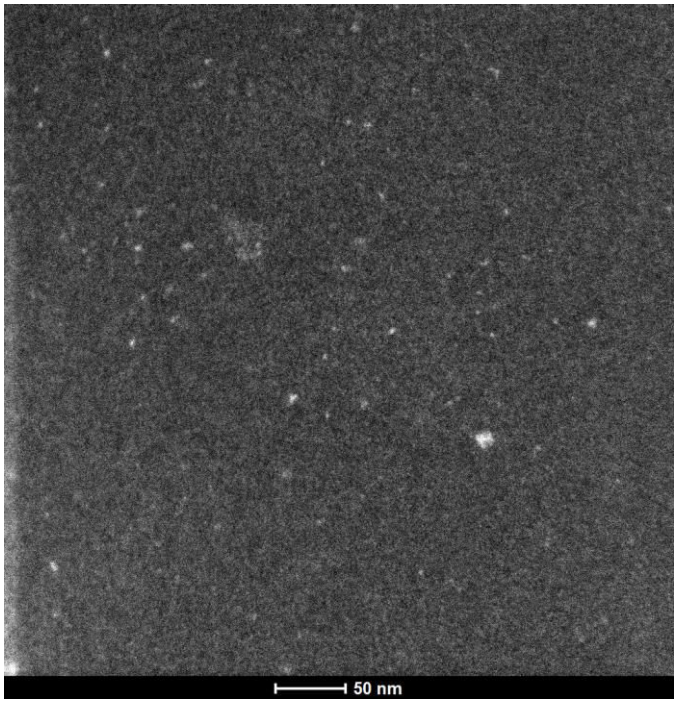

Figure 5. STEM imaging of Si-NH_2 NPs. Scale bar: 50 nm.

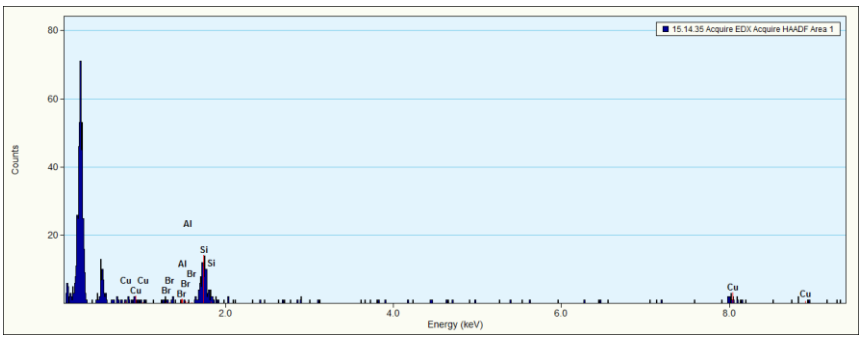

Figure 6. EDX analysis of Si-NH_2 NPs.

XPS measurement

X-ray photoelectron spectroscopy (XPS) measurements were performed to study the elemental composition of Si NPs and all the signals were calibrated with the binding energy of C1s at 284.80 eV. Figure 7a, of the Si-COOH NPs, shows the existence of Si, C and O elements. Besides, in the elemental scan, Si2p electron displayed one peak at 102.08 eV which corresponds to the binding energy of Si–C composition. (Table 1) This value is consistent with the other Si NPs reported in the literature and prepared following the same synthesis.[26, 27] C1s binding energy at 284.80 eV revealed the C-C composition and the small shoulder at 288 eV was the carbon of carboxylic acid. XPS analysis for Si-NH_2 NPs is shown in Figure 8 and listed in Table 2, the particles contain Si, C, O and N elements, and the O atom might also due to the CO_2 adsorption on the surface of thin film. Moreover, Si2p binding energy was detected at 101.61 eV which is attributed to the Si–C group, and there is no signal indicating the silica formation (104 eV).

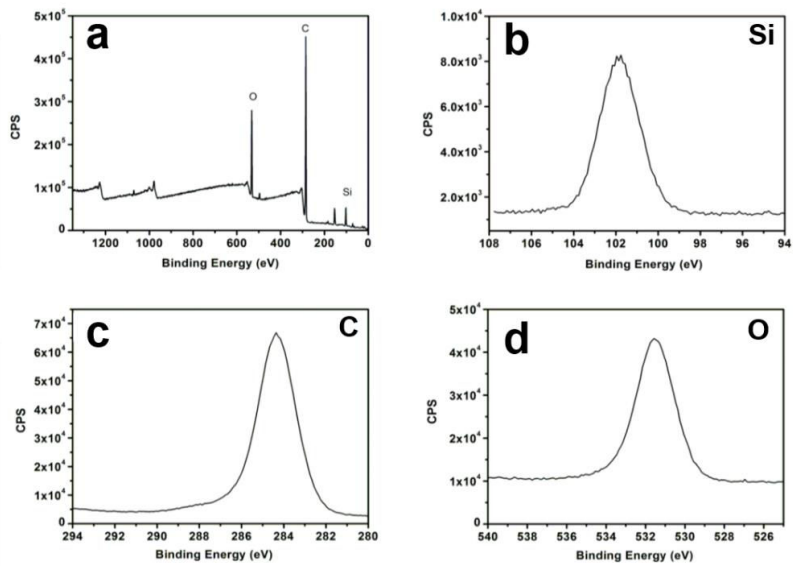

Figure 7. XPS spectra of Si-COOH NPs. (a) survey scan (b) Si 2p elemental scan (c) C 1s elemental scan (d) O 1s elemental scan.

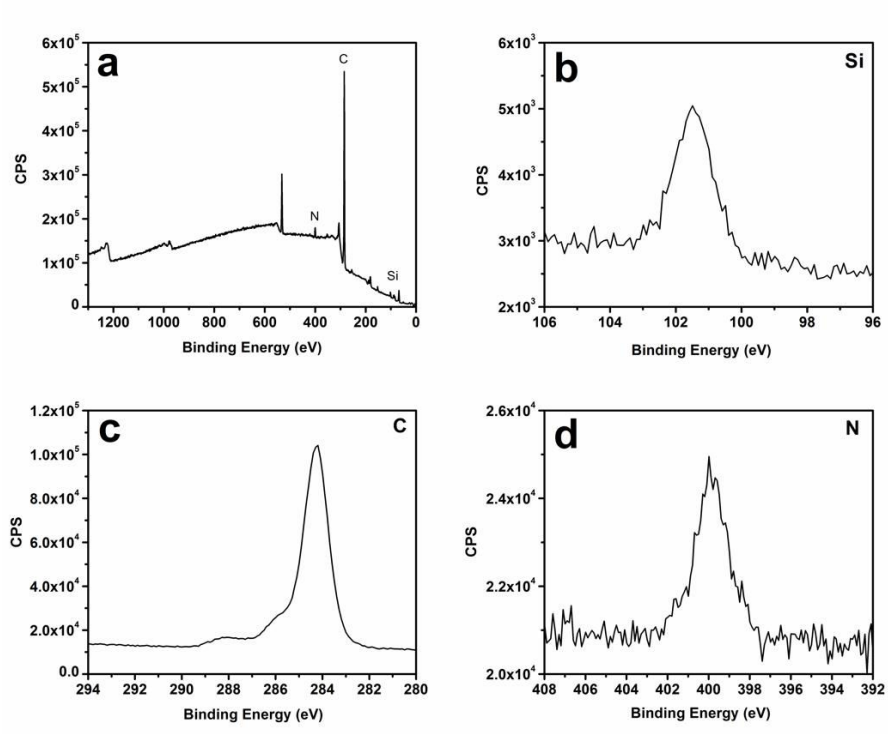

Figure 8. XPS spectra of Si-NH_2 NPs. (a) survey scan (b) Si 2p elemental scan (c) C 1s elemental scan (d) N 1s elemental scan.

Table 1. XPS data for Si-COOH NPs

Element	Peak, eV	FWHM, eV	Atomic ration, %
C1s	284.80	2.88	75.66
O1s	531.95	3.02	16.01
Si2p	102.09	1.87	8.33

Table 2. XPS data for Si-NH_2 NPs

Element	Peak, eV	FWHM, eV	Atomic ratio, %
C1s	284.80	2.61	81.35
O1s	531.99	2.95	10.86
N1s	400.13	3.02	3.24
Si2p	101.61	2.63	2.11

Molecular weight estimation of Si-COOH NP by analytical ultracentrifugation (AUC) method

AUC measurements were performed in an Optima Max-E centrifuge (Beckman-Coulter) equipped with a ML-80 fixed angle rotor. The sample was dispersed in EtOH and spun (45000 rmp) for 18 – 20 hours at 20 °C. The hydrodynamic Stokes' diameter was obtained from Svedberg equation and Stoke-Einstein relation, giving the well-known expression for Stoke-equivalent spherical diameters in AUC[28] which is shown below.

$$\rho_p = \rho_s + 18\eta_s s\left(\frac{1}{D}\frac{k_b T}{3\pi\eta_s}\right)^{-2}$$

$$\mathrm{M} = \frac{sRT}{D}\left(1 - \frac{\rho_s}{\rho_p}\right)^{-1}$$

$$d_p = \sqrt{\frac{18\eta_s s}{(\rho_p - \rho_s)}}$$

where ρ_P is the particle density, ρ_s is the solvent density, η_S is the viscosity of the liquid, M is the molecular weight, d_P is the diameter of NPs, k_b is the Boltzmann's constant, T is the temperature, D is the diffusion coefficient and S is the sedimentation coefficient. In Figure 9, the most intense point (cross line), the diffusion coefficient and sedimentation coefficient were 1.1×10^{-10} m^2 sec^{-1} and S = 0.9, respectively. The size of the particles was calculated from the above equation, and the diameter of Si-COOH NP resulted 3.25 nm, the molecular weight 10546 Dalton, and the density 973 kg m^{-3}.

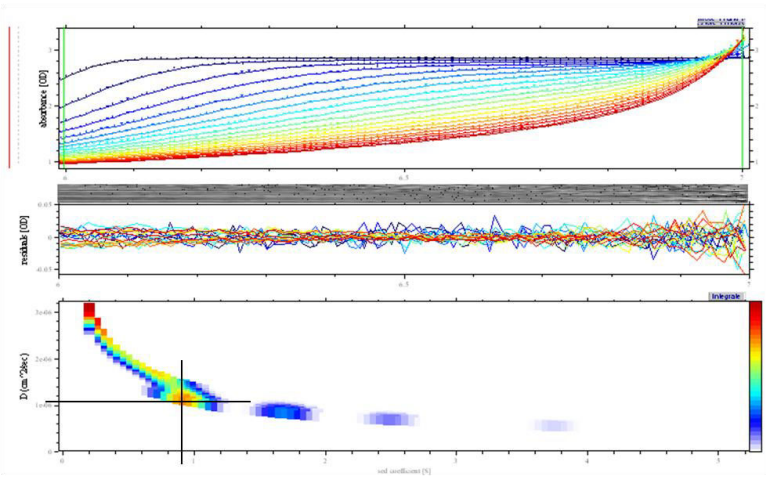

Figure 9. The analytical ultracentrifugation data.

Quantification of –COOH on Si-COOH NPs

The amount of carboxylic acid group was quantified by acid-base titration. The NaOH aqueous solution (5×10^{-3} M) was added dropwise into the solution of Si-COOH NPs (20.0 mg), waiting for 30 seconds after each addition and monitoring the pH change till end point of titration. From the titration curve, Figure 10, the equivalent point was calculated from the second derivative which was 5.0 mL. Therefore the amount of carboxylic acid groups was 1.17 μmol –COOH / 1 mg Si NPs. Considering the particles size and the molecular weight obtained from the analytical ultracentrigugation (AUC) measurements, 15 carboxylic acid groups were obtained on a single Si-COOH NPs.

It is interesting to note that the pKa of Si-COOH NPs is above 7. Wang *et al.* reported that the pKa of carboxylic acid on nanoparticles presents a large deviation from the free acid ligand.[29] The pKa of carboxylic acid on the nanoparticles varies with the particle size, the amount of carboxylic acid on the surface and the ions concentration in the solution. The 4.1 nm of 11-mercaptoundecanoic acid (MUA) modified Au NPs showed pKa at 6.8 in 0.2 M of TMACl (tetramethylammonium chloride) and 8.5 without salt concentration, while the pKa of free acid ligand is 4.8. That change of the pKa without the TMACl is due to the electrostatic repulsions between the charged carboxylic acid that make dissociation harder. Even in the literature, the pKa of MUA within monolayer on the flat gold surface is around 10, much higher than the free ligand.[30, 31]

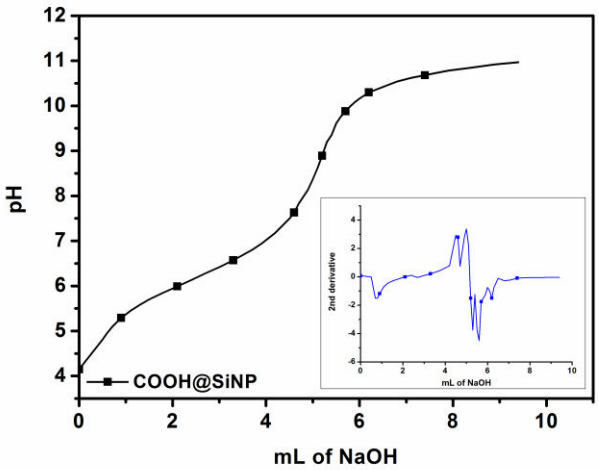

Figure 10. The acid-base titration curve for Si-COOH NPs.

3.3 Photophysical properties

The photophysical properties of the Si-COOH and Si-NH_2 NPs were studied in EtOH solution and all the measurements were performed without degassing and at room temperature. The concentration of Si-COOH and Si-NH2 NPs is 0.05 mg/mL.

UV-Vis absorption

UV-Vis absorption of the Si-COOH and Si-NH_2 NPs are shown in Figure 11. Both nanoparticles were dispersed in EtOH at the concentration of 0.05 mg/mL. The Si-COOH NPs show broad and continuous absorption profile, with the exception of a shoulder absorption around 270 nm. This absorption at 270 nm is consistent with the absorption of bulk Si which is attributed to the direct L–L transition.[32] In the sample of Si-NH_2 NPs, the absorption peaks are observed at 270 and 310 nm which are consistent with the direct band transition in the bulk Si as well.[32]

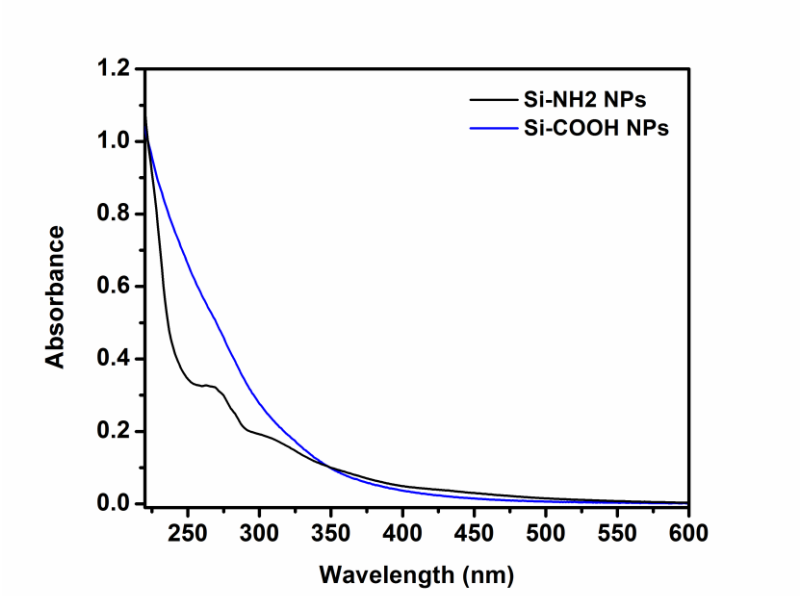

Figure 11. UV-Vis absorption spectra for Si-COOH and Si-NH_2 NPs.

Emission properties

The emission spectra of the different functionalized Si NPs are shown in Figure 12 and the photophysical data is listed in Table 3. Both particles exhibit emission that shift upon changing the excitation wavelength. Figure 12A shows the Si-COOH NPs emission in EtOH (0.05 mg/mL) upon λ_{ex} exciting between 340 – 400 nm and the corresponding emission red shift from 435 to 490 nm. A similar behavior is obtained for the amino terminated particles (Figure 12B). This phenomenon was also reported in the literature[27, 33] and it is attributed to either the polydisperse size of Si NPs or existing many surface states, resulting in broad and wavelength-dependent emission. For the Si-

COOH NPs the excited state lifetime shows multi-exponential decay with value of 1.40 ns (50.9%), 3.67 ns (42.7%), 10.88 ns (6.4%), indicating that the structure contain defect sites or surface states as also reported for similar wet chemistry preparation of SiNPs in the literature.[27] The luminescent excited state of Si-NH_2 also show multi-exponential decay with value of 0.17 ns (73.8%), 1.73 ns (21.8%) and 5.45 ns (4.4 %). The quantum efficiency for both particles was measured using integrating sphere, and the quantum yield of these Si NPs are 3~4% in aerated ethanol upon λ_{exc} exciting at 375 nm. From the multi-channel of excited state lifetime, the emission probably mixes with the direct band and surface states emission of Si NPs.

The excitation spectra were recorded in EtOH solution at concentration of 0.05 mg/mL shown in Figure 13. The excitation spectra of Si-COOH and Si-NH_2 NPs show different from the absorption spectra and exhibit one significant band at 365 and 369 nm, respectively. Compared with bulk Si, this band is consistent with the direct Γ–Γ transition of silicon, and in the case of Si-COOH NPs, a small band at 272 nm which corresponds to direct L–L transition.[17, 32, 34] The excitation spectra of our Si NPs also match with the literature data reported by Kauzlarich *et al*. using Zintl salt reaction.[35]

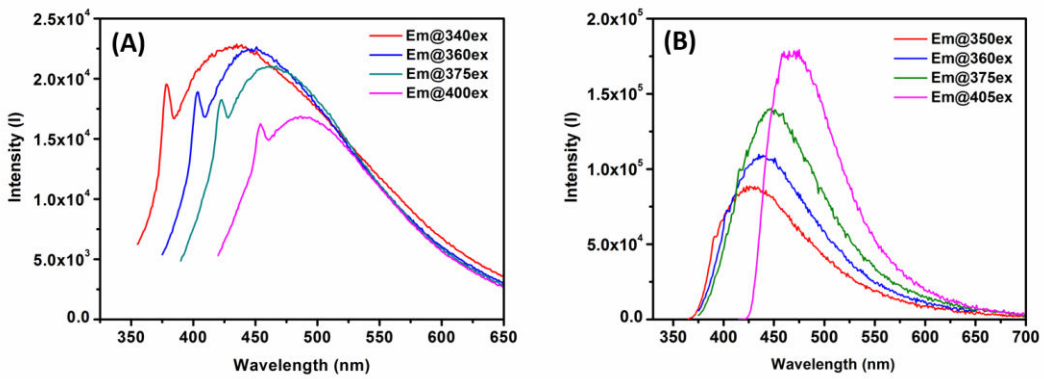

Figure 12. Emission spectra of (A) Si-COOH and (B) Si-NH_2 NPs with different excitation.

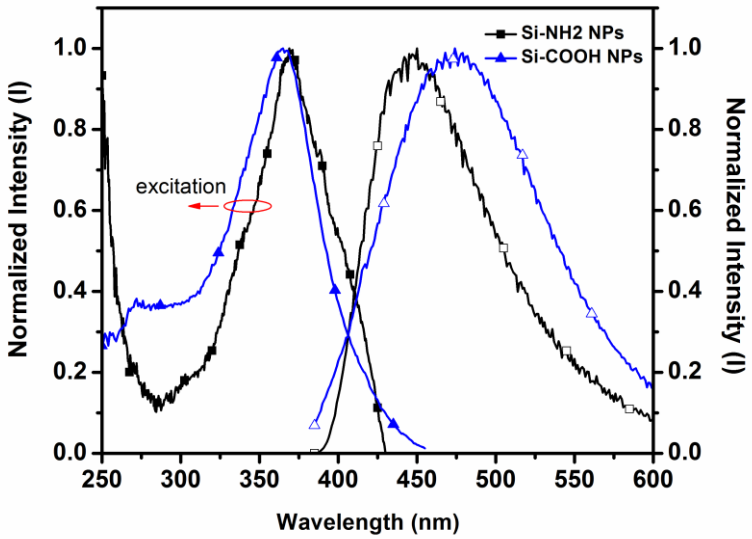

Figure 13. The emission and excitation spectra of Si-COOH and Si-NH_2 NPs.

Table 3. Photophysical data for Si-COOH NPs and Si-NH_2 NPs in EtOH

Sample	Excitation, nm[a]	Emission, nm[b]	Lifetime, ns[b]	Q.Y., %[c]
Si-COOH NPs	365	474	1.40 (50.9%) 3.67 (42.7%) 10.88 (6.4 %)	3
Si-NH_2 NPs	369	447	0.17 (73.8%) 1.73 (21.8%) 5.45 (4.4 %)	4

a. excitation spectra were collected at λ_{em} max. b. λ_{ex} = 370 nm. c. absolute quantum yield measurement was performed using integrating sphere.

3.4 Conclusions

Silicon nanoparticles have attracted a lot of attention in the last 10 years because of their biocompatibility, excellent stability, covalent functionalization of their surfaces, luminescence properties. In this chapter we describe the synthesis of silicon nanoparticles via wet chemistry method and their surface functionalization with amino and carboxylic acid groups in order to exploit their possible use in bio-medicine. The Si NPs were characterized by FT-IR, TEM/STEM and XPS techniques to confirm that the structure consist of silicon (and not silica) and the particles size was determined for both type of particles: 3.9 nm for Si-COOH NPs, 3.1 nm for Si-NH_2 NPs. These Si NPs exhibit luminescence in the blue region and excited state lifetime in the nanosecond time scale. In order to perform further coupling reaction with other labels, we calculated the mass by analytical ultracentrifugation (AUC) and the amount of carboxylic acid group on the surface by acid-base titration. These particles have a very low photobleaching upon light irradiation and are therefore suitable for further bioimaging. (See Chapter 4)

3.5 Experimental Section

General information and materials

All reagents were purchased from Sigma-Aldrich and Alfa and used without any further purification unless specified notice. Solvents were purified according to the standard procedure.[36] All air and water sensitive experiments were carried out in standard glassware under an inert argon atmosphere using schlenk line techniques.

Optical Measurement

Steady-state emission spectra were recorded on a HORIBA Jobin-Yvon IBH FL-322 Fluorolog 3 spectrometer equipped with a 450 W xenon arc lamp as the excitation source, double-grating excitation and emission monochromators (2.1 nm mm^{-1} of dispersion; 1200 grooves mm^{-1}), and a TBX-04 single-photon-counting device as the detector. Emission and excitation spectra were corrected for source intensity (lamp and grating) and emission spectral response (detector and grating) by standard correction curves. Time-resolved measurements were performed using the Time-Correlated Single Photon Counting (TCSPC) on the FT-300 (PicoQuant), where a polarized laser source 375 nm used for exciting the samples. The excitation sources were mounted directly on the sample chamber at 90° to a Czerny-Turner type emission monochromator (2.7 nm mm^{-1} of dispersion; 1200 grooves mm^{-1}) and collected by a PMA-C 192M single-photon- counting detector. Signals were collected using EasyTau software, and data analysis was performed using FluoFit software (PicoQuant). The quality of the fit was assessed by minimizing the reduced $\chi 2$ function and by visual inspection of the weighted residuals. Luminescence quantum yield was performed with integrating sphere (Hamamatsu, C11347-11).

Synthetic procedure

3-Butenylmagnesium bromide

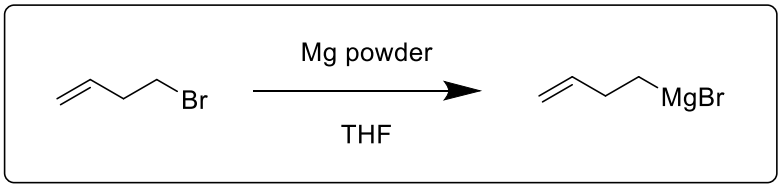

Magnesium powder (1.8 g, 75 mmol) was added into a 100 mL flask and heated to 100ºC for 15 minutes to remove all the H_2O. 4-bromobutene (5.6 mL, 57.7 mmol) was dissolved into 41 mL dried THF and placed in an additional funnel. Firstly, 5 mL of 4-

bromobutene in THF solution was added and heated by heat gun. Once the H_2 bubbles were observed, the reaction started to work and stopped heating. Then the rest of 4-bromobutene in THF solution was added slowly. During the addition, the H_2 bubbles were still continuously appeared. Then the reaction was stirred at room temperature for 4 hours and the product was used without further purification.

Quantification of ***3-Butenylmagnesium bromide***

8 mL dried THF with 0.1 mL 2-butanol and 2 mg 1,10-phenanthroline was prepared in 25 mL flask. Fresh 3-Butenylmagnesium bromide was added slowly and purple color was appeared and disappeared upon adding. To the end point of the titration, the purple color was stayed still more than 1 minute. Then followed the equation below, we could get the concentration of 3-Butenylmagnesium bromide was 0.95 M.

$$[Grignard\ reagent] = \frac{mmol\ of\ 2-butanol}{volumn\ of\ RMgX\ in\ mL}$$

Si-alkene NPs

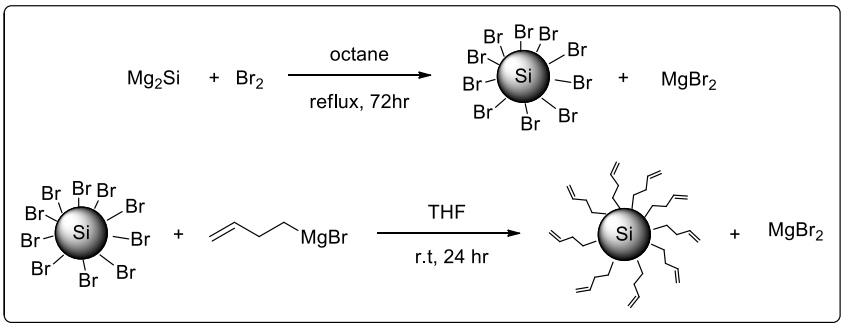

The synthesis of silicon nanoparticles was modified from previous literature by Kauzlarich *et al.*[23] 300 mL dried octane was added into 500 mL flask with Mg_2Si (1.0 g, 7.8 mmol). Then Br_2 (3.2 mL, 62 mmol) was added slowly, and stirred at room temperature for 2 hours. Following the reaction was refluxing for 72 hours. After cooling down to room temperature, octane was removed by vacuum and new 100 mL dried THF was added. To the solution, 3-butenylmagnesium bromide (0.5 M, 100 mL, 50 mmol) was added slowly and stirred at room temperature overnight. Quench with $NH_4Cl_{(aq)}$ and then wash with DI water two times. Collect all organic layers and dried with $MgSO_4$. Finally the nanoparticles were purified by size exclusion chromatography (biobeads S-X1) to get yellow wax.

Si-COOH NPs

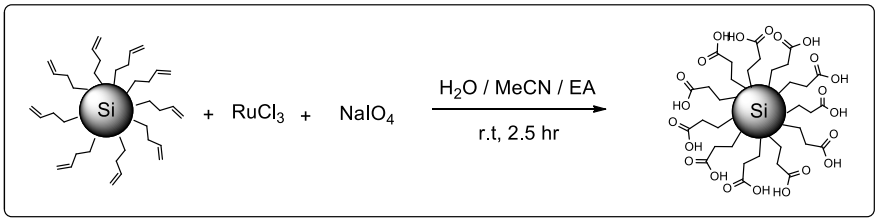

$NaIO_4$ (877 mg, 4.1 mmol) was dissolved into solvent pair of CH_3CN : ethyl acetate : H_2O = 6 : 6 : 9 mL. Then alkene terminated silicon nanoparticles and $RuCl_3$ (5 mg, 0.02 mmol) were added. The solution was stirred at room temperature for 3 hours. After reaction, ethyl acetate was added and washed with DI water twice. Collect all organic layers and dried with $MgSO_4$. Final product was purified by size exclusion chromatography (LH-20) to get yellow wax.

Si-NH2 NPs

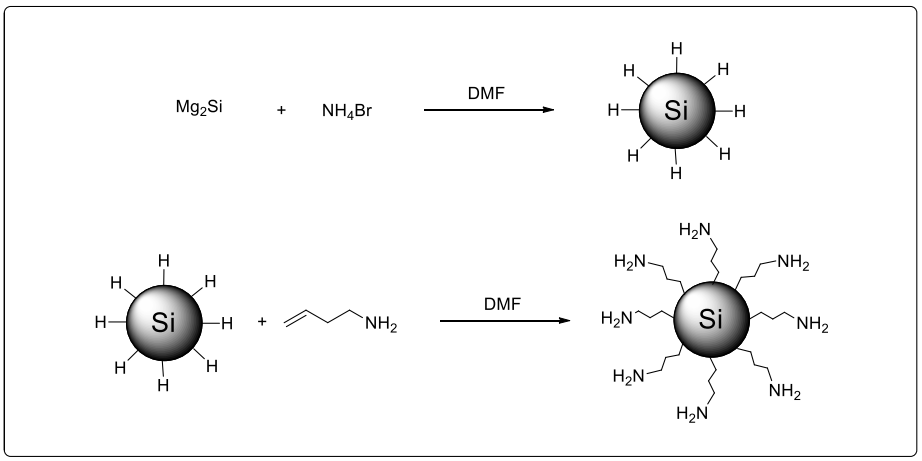

To a 250 mL flask with Mg_2Si (0.6 g, 4.7 mmol) and NH_4Br (1.83 g, 18.7 mmol), 200 mL dried DMF was added and the reaction was heated to reflux for 24 hours. After cooling down to room temperature, allylamine (10.2 mL, 233 mmol) was added. Then the reaction was heated to 110°C for overnight. Removed the solvent by rotavapor and purified by size exclusive chromatography (LH-20) to yield yellow wax.

3.6 Reference

1. B. Ghosh and N. Shirahata, *Science and Technology of Advanced Materials*, 2014, **15**, 014207.
2. M. S. Islam, M. E. Karim, H. Baerwolff and A. B. Md Ismail, Advances in Electrical Engineering (ICAEE), 2013 International Conference on, 2013.
3. J. H. Warner, A. Hoshino, K. Yamamoto and R. D. Tilley, *Angew. Chem. Int. Ed.*, 2005, **117**, 4626-4630.
4. F. Erogbogbo, K.-T. Yong, R. Hu, W.-C. Law, H. Ding, C.-W. Chang, P. N. Prasad and M. T. Swihart, *ACS Nano*, 2010, **4**, 5131-5138.
5. F. Erogbogbo, K.-T. Yong, I. Roy, R. Hu, W.-C. Law, W. Zhao, H. Ding, F. Wu, R. Kumar, M. T. Swihart and P. N. Prasad, *ACS Nano*, 2011, **5**, 413-423.
6. F. Erogbogbo, C. A. Tien, C. W. Chang, K. T. Yong, W. C. Law, H. Ding, I. Roy, M. T. Swihart and P. N. Prasad, *Bioconjug Chem*, 2011, **22**, 1081-1088.
7. M. L. Mastronardi, E. J. Henderson, D. P. Puzzo, Y. Chang, Z. B. Wang, M. G. Helander, J. Jeong, N. P. Kherani, Z. Lu and G. A. Ozin, *Small*, 2012, **8**, 3647-3654.
8. D. P. Puzzo, E. J. Henderson, M. G. Helander, Z. Wang, G. A. Ozin and Z. Lu, *Nano Lett.*, 2011, **11**, 1585-1590.
9. A. S. Heintz, M. J. Fink and B. S. Mitchell, *Adv. Mater.*, 2007, **19**, 3984-3988.
10. A. S. Heintz, M. J. Fink and B. S. Mitchell, *Appl. Organomet. Chem.*, 2010, **24**, 236-240.
11. R. Okada and S. Iijima, *Appl. Phys. Lett.*, 1991, **58**, 1662-1663.
12. E. Werwa, A. A. Seraphin, L. A. Chiu, C. Zhou and K. D. Kolenbrander, *Appl. Phys. Lett.*, 1994, **64**, 1821-1823.
13. T. Orii, M. Hirasawa and T. Seto, *Appl. Phys. Lett.*, 2003, **83**, 3395-3397.
14. L. T. Canham, *Appl. Phys. Lett.*, 1990, **57**, 1046-1048.
15. J. L. Heinrich, C. L. Curtis, G. M. Credo, K. L. Kavanagh and M. J. Sailor, *Science*, 1992, **255**, 66.
16. Z. Kang, C. H. A. Tsang, Z. Zhang, M. Zhang, N.-b. Wong, J. A. Zapien, Y. Shan and S.-T. Lee, *J. Am. Chem. Soc.*, 2007, **129**, 5326-5327.
17. J. P. Wilcoxon, G. A. Samara and P. N. Provencio, *Phys. Rev. B*, 1999, **60**, 2704.
18. R. D. Tilley and K. Yamamoto, *Adv. Mater.*, 2006, **18**, 2053-2056.
19. M. Rosso-Vasic, E. Spruijt, B. van Lagen, L. De Cola and H. Zuilhof, *Small*, 2008, **4**, 1835-1841.
20. C.-S. Yang, R. A. Bley, S. M. Kauzlarich, H. W. H. Lee and G. R. Delgado, *J. Am. Chem. Soc.*, 1999, **121**, 5191-5195.
21. D. Mayeri, B. L. Phillips, M. P. Augustine and S. M. Kauzlarich, *Chem. Mater.*, 2001, **13**, 765-770.

22. M. Rosso-Vasic, E. Spruijt, Z. Popovic, K. Overgaag, B. van Lagen, B. Grandidier, D. Vanmaekelbergh, D. Dominguez-Gutierrez, L. De Cola and H. Zuilhof, *J. Mater. Chem.*, 2009, **19**, 5926-5933.
23. Q. Liu and S. M. Kauzlarich, *Mater. Sci. Eng. B*, 2002, **B96**, 72.
24. D. Neiner and S. M. Kauzlarich, *Chem. Mater.*, 2010, **22**, 487-493.
25. F. Zimmermann, E. Meux, J.-L. Mieloszynski, J.-M. Lecuire and N. Oget, *Tetrahedron Lett.*, 2005, **46**, 3201-3203.
26. M. Dasog, Z. Yang, S. Regli, T. M. Atkins, A. Faramus, M. P. Singh, E. Muthuswamy, S. M. Kauzlarich, R. D. Tilley and J. G. C. Veinot, *ACS Nano*, 2013, **7**, 2676-2685.
27. L. Ruizendaal, S. P. Pujari, V. Gevaerts, J. M. Paulusse and H. Zuilhof, *Chem Asian J*, 2011, **6**, 2776-2786.
28. R. P. Carney, J. Y. Kim, H. Qian, R. Jin, H. Mehenni, F. Stellacci and O. M. Bakr, *Nat Commun*, 2011, **2**, 335.
29. D. Wang, R. J. Nap, I. Lagzi, B. Kowalczyk, S. Han, B. A. Grzybowski and I. Szleifer, *J. Am. Chem. Soc.*, 2011, **133**, 2192-2197.
30. T. Kakiuchi, M. Iida, S.-i. Imabayashi and K. Niki, *Langmuir*, 2000, **16**, 5397-5401.
31. M. C. Leopold and E. F. Bowden, *Langmuir*, 2002, **18**, 2239-2245.
32. J. D. Holmes, K. J. Ziegler, R. C. Doty, L. E. Pell, K. P. Johnston and B. A. Korgel, *J. Am. Chem. Soc.*, 2001, **123**, 3743-3748.
33. A. Shiohara, S. Prabakar, A. Faramus, C. Y. Hsu, P. S. Lai, P. T. Northcote and R. D. Tilley, *Nanoscale*, 2011, **3**, 3364-3370.
34. K. A. Littau, P. J. Szajowski, A. J. Muller, A. R. Kortan and L. E. Brus, *The Journal of Physical Chemistry*, 1993, **97**, 1224-1230.
35. D. Neiner, H. W. Chiu and S. M. Kauzlarich, *J. Am. Chem. Soc.*, 2006, **128**, 11016.
36. W. L. F. Armarego and C. L. L. Chai, *Purification of laboratory chemicals*, 5th edn., Butterworth-Heinemann, Amsterdam, 2003.

CHAPTER 4

Silicon Nanoparticles for Bio-imaging

Abstract

Luminescent silicon nanoparticles have received more attention in the field of nanotechnology, due to their remarkable and tunable photoemission properties. Thanks to their features of biocompatibility, non-toxicity, and facility of surface functionalization, recently, they have also been shown as a very good candidate to be used as a cellular probe in the field of bioimaging. Tailoring the surface of the particles with active biomolecules, such as sugar moiety, can be a good strategy to increase the kinetics of internalization of the materials into living cells. In this study, we synthesized and modified silicon nanoparticles with different quantities of glucose attached on the surface. *In vitro* studies using HeLa cells show the uptake of the particles inside the cells. Different localization and kinetic uptake of glucose-modified particles compared to unmodified ones were observed.

4.1 Introduction

Nanomaterials based on semiconductors, such as II-VI or III-V quantum dots (QDs), have been developed for photoelectron and medical applications for decades. Due to the high quantum yield, tunable emission wavelength, high photobleaching threshold, high electro- and chemical stability, these QDs are of higher interest than organic fluorescent dyes for cell imaging. However, biocompatibility and cytotoxicity are still the biggest restrictions in developing QDs as nano-medicine. Although coating with a ZnS layer or modification with biocompatible materials on the surface can afford good stability and high cell uptake, the risk of releasing fatal ions still remains.[1-4]

Recently, silicon nanoparticles (Si NPs) have received plenty of attention in bio-application because of their luminescent properties and non-cytotoxicity to cells.[5-8] Tilley *et al.* presented the amino functionalized Si NPs as a good candidate for cell imaging with HeLa[5, 9] and MCF-7[10] cell lines. Li and Ruckenstein showed poly(acrylic acid) coated Si NPs are a good label for the CHO cell line.[11] Prasad *et al*. modified different biomolecules, such as lysine, folic acid and antimesothelin, on Si NPs for cell imaging of the Panc-1 cell line.[12] Those particles are taken into Panc-1 cells and the 50% cell viability (IC_{50}) is more than 500 μg/mL. However, rare literature reports the detail of the cellular localization of Si NPs.

On the other hand, Prasad *et al*. have shown *in vivo* studies of Si NPs, which are able to locate inside tumor cells by direct injection and remain for 24 hours.[1] The Si and Fe_3O_4 nanoparticles were encapsulated with phospholipid (DSPE-PEG-2000) to form 50 to 100 nm micelle structures and exhibited both luminescent properties and MRI response. 24 hours after injection to the tumor sites, the luminescence is still observed inside the tumor and the signal even increases 20% higher than the intensity 0 hour after injection. This might be due to the acidic environment of tumor, as the silicon luminescence intensity typically rises with decreasing pH. With same idea, they modified the surface of micelle encapsulated Si nanoparticles with biomolecule (Arginylglycylaspartic acid, RGD peptides) to target neoplastic sites.[13] Indeed, they showed the successful tumor targeting and sentinel lymph node (SLN) mapping with these nanopartilces, and nontoxic *in vivo* at the dosage of 380 mg/kg which is 10 times higher than the highest dose of CdSe/ZnSe NPs. Kauzlarich *et al*. have developed bimodal imaging systems of Si NPs by doping iron into silicon nanoparticles for both MRI and luminescent probes.[14] With a small concentration of iron (5%), the iron-doped silicon nanoparticles still keep luminescent properties and a significant T_2 contrast. The particles also exhibit low toxicity at concentrations as high as 5 mM with cell viability ≥85%. Also by linking the radioactive ^{64}Cu complex, it can be used for PET imaging.

Tu *et al*. showed the bio-distribution of ^{64}Cu modified Si NPs in mouse.[15] Smaller Si NPs were easily excreted from the urinary system, while the bigger particles accumulated inside the liver. In addition, surface functionalization also plays an important role in the cell targeting and toxicity[16-18], generally speaking, amino groups and positive charge groups presented more toxic than carboxylic acid groups, dextran-coated or PEG-coated Si NPs.

Carbohydrates are the essential biomolecules in human life. Carbohydrates can be used for energy storage and also play important roles in many biological events. These kind of carbohydrate-protein interactions (CPIs) include cell-cell recognition, signalling, immune response, cell growth regulation, bacterial and viral infections.[19] Besides, CPIs on normal cells and their malignant counterparts show significant difference. For example glucose transporters (GLUT) have shown observed overexpression in HeLa cells and other tumor cells.[20] Many glyconanoparticles have been designed for medical examination for many years.[21-26] Penades *et al.* have modified various oligosaccharides on Au NPs in order to investigate the carbohydrate-carbohydrate interaction.[27] Lately high-mannose (HM) oligosaccharides showed anti-HIV activity by binding with gp120.[28] Kauzlarich *et al*. published dextran coated Si NPs for macrophage targeting by using dextran sulfate (DS) ligand to target SR-A receptor.[29] Without sulfate groups, dextran coated Si NPs showed non-specific target to cells. Jayshree H. Ahire *et al.* showed mannose coated Si NPs had high affinity binding with ConA and were uptaken by MCF-7 human breast cancerous cells.[30] Moreover, some of carbohydrates moiety modified NPs could be easily taken into cells, increasing cell uptake.[31-35]

Here we reported the synthesis and characterization of glucose modified Si NPs. Furthermore, the *in vitro* study including cell uptake, cellular localization, and cell viability test also give us a tool to understand these materials for further nanomedicine research.

4.2 Synthesis and Characterization

Synthesis of Si-COOH and Si-Glc NPs

Si-COOH NPs were synthesized by modified previous literature.[36] (See scheme 1) Magnesium silicide (grind to powder before using) was oxidized by bromine to get bromo-terminated Si NPs under Ar. Then 3-butenylmagnesium bromide was added slowly as capping reagent to prevent forming silica. THF was using instead of octane in order to increase the reactivity of Grignard reagent. Further step, alkenes groups were transverted to carboxylic acid by ruthenium catalyst and sodium periodate.[37] The optimal reaction time for this step is 4 to 6 hours. The emission properties, unfortunately, totally disappeared if the reaction time is more than 12 hours. Si-COOH NPs were further purified by size exclusive chromatography (Sephadex LH-20) using MeOH as eluent to get yellow wax. Then different equivalents of amino functionalized glucose were coupling to Si-COOH NPs forming glucose modified Si NPs (Si-Glc NPs). Note that this coupling reaction is a heterogeneous reaction, the reactants should keep in high concentration by reducing the volume of solvent. After size exclusive chromatography (Sephadex LH-20, MeOH as eluent), the sample was dried using freeze dry technique to get yellow powder but hydroscopic.

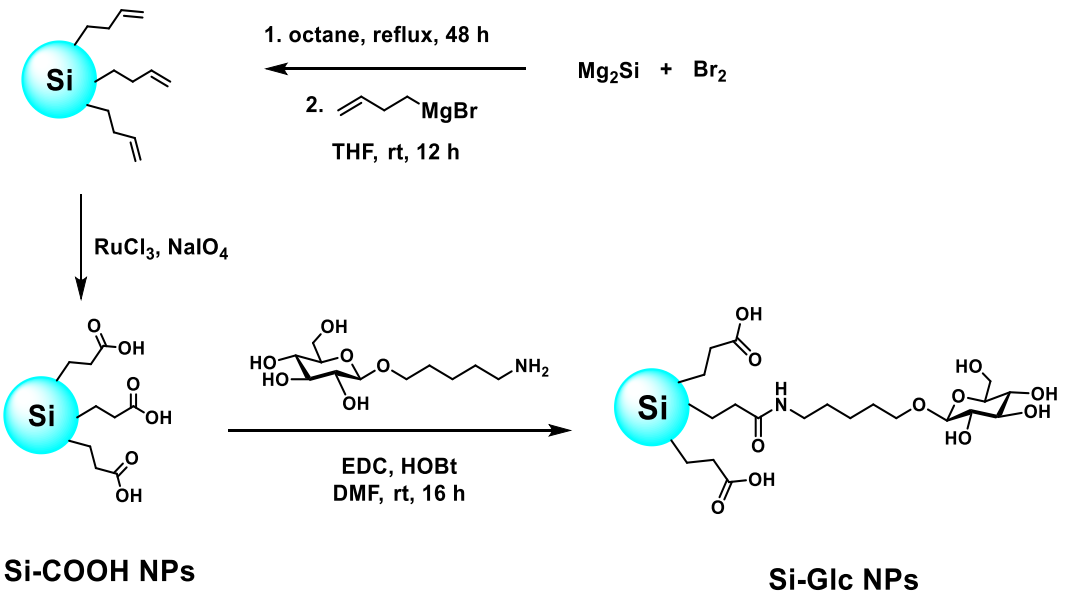

Scheme 1. Synthesis of Si-COOH NPs and Si-Glc NPs

In the ^{1}H NMR spectra, Figure 1, amino-glucose ligand shows the chemical shift in between 1 to 4.5 ppm, and the chemical shift at 2.63 ppm (triplet) is assigned to the proton which is next to the amino group. When coupling to Si-COOH NPs, it shifts downfield and proves that the amide bond formation works. Also the disappearance of peak at 2.63 ppm presents no free glucose ligand after purification. Moreover, ^{13}C NMR is performed in Figure 2, the carbon signals of glucose are presented in the Si-Glc NPs sample, and the chemical shift at 161.6 and 172.95 ppm are assigned to the amide and carboxylic acid groups. With adding two different equivalents of glucose ligand, 1 eq. and 0.5 eq., we could have different sugar coverage on the Si NPs and quantified the amount with ^{1}H NMR. By using $CDCl_3$ as internal standard, the integration of proton gives us the ratio between $CHCl_3$ and glucose to calculate the amount of glucose, 0.84 and 0.38 μmol per 1 mg of Si-Glc NPs, respectively. Then comparison of the amount of glucose and carboxylic acid, we can acquire 71.8% and 32.6% coverage by adding 1 and 0.5 equivalents of glucose.

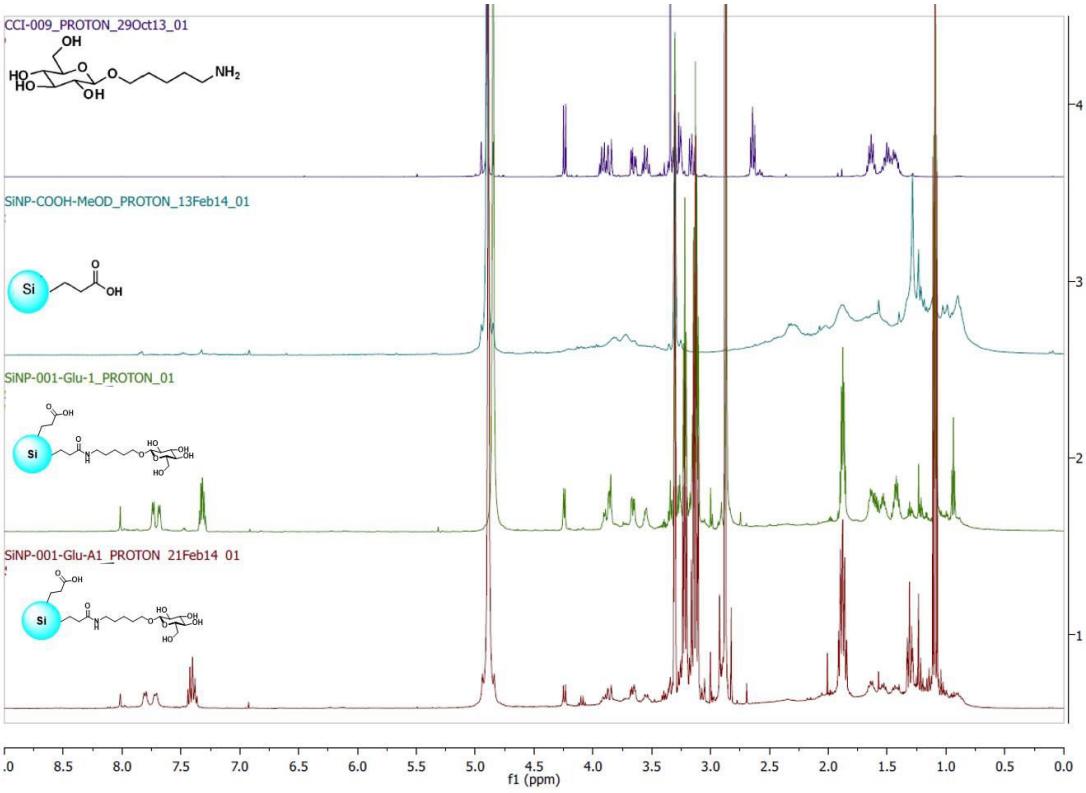

Figure 1. ^{1}H NMR of glucose ligand, Si-COOH NPs and Si-Glc NPs.

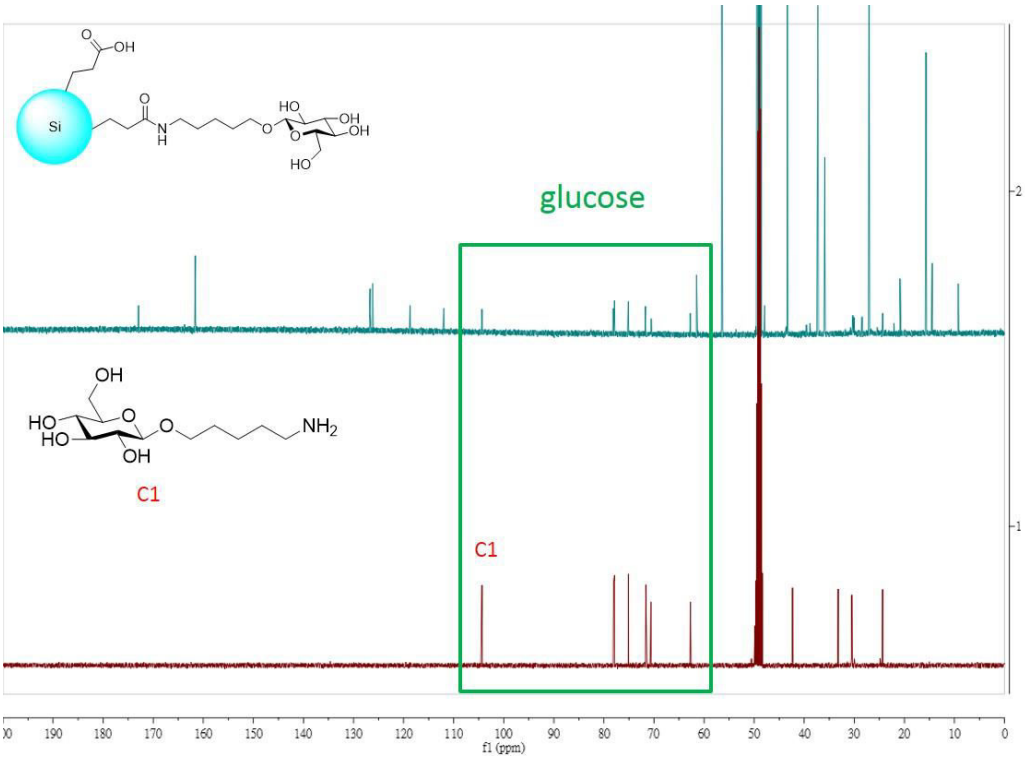

Figure 2. ^{13}C NMR of Si-Glc NPs and glucose ligand.

FT-IR spectra

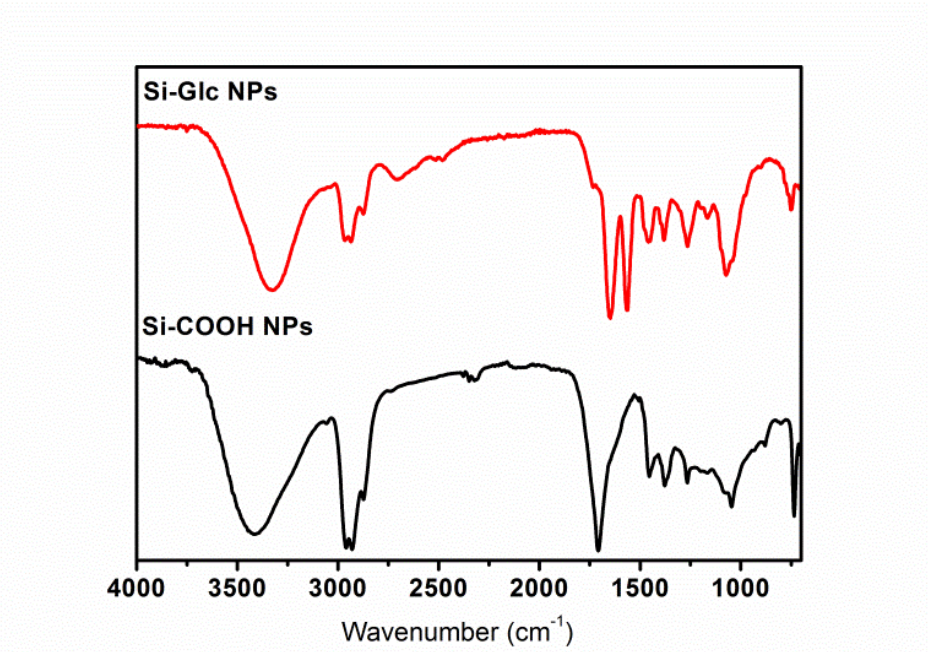

Figure 3. FT-IR-ATR spectra of Si-COOH and Si-Glc NPs

In order to identify the surface functional groups, FT-IR spectra were studied for Si NPs using attenuated total reflection (ATR) mode (Figure 3). In Si-COOH NPs, carboxylic groups show very broad band at 2500 ~ 3600 cm^{-1} which corresponds to –

OH stretching of carboxylic acid. And the carbonyl group stretching is at 1730 cm^{-1}. The peaks at 2789, 1570, and 1375 cm^{-1} are attributed to the stretching and bending of alkyl chains. 1260 cm^{-1} is assigned to Si–C bond vibration according to literature.[5] Moreover, we still observe Si-O vibration in 1000 – 1100 cm^{-1}, indicating some silica forming on the surface. Both Si-Glc NPs with different glucose coverage show amide bond vibration at 1648 cm^{-1} (C=O stretching) and 1565 cm^{-1} (N-H bending). The other peaks, 2935, 1458, 1381, 1264 cm^{-1}, are assigned as stretching and bending of alkyl chains. Besides, the peak at 1734 cm^{-1} is the remains of carboxylic acid group.

STEM imaging

Because the atomic number of Si and C are too close and light, TEM images show low contrast between silicon and carbon film and it is hard to acquire the images. However, with STEM mode, we can observe better contrast and acquire the images. In Figure 4, STEM imaging shows the Si-COOH NPs size around 4 nm and EDX spectrum confirms those particles consist of silicon element. For Si-Glc NPs, the particles aggregate to form larger sizes, around 10 to 20 nm, which is due to the carbohydrate-carbohydrate interaction.[38] Those particles also consist of silicon element by EDX measurement.

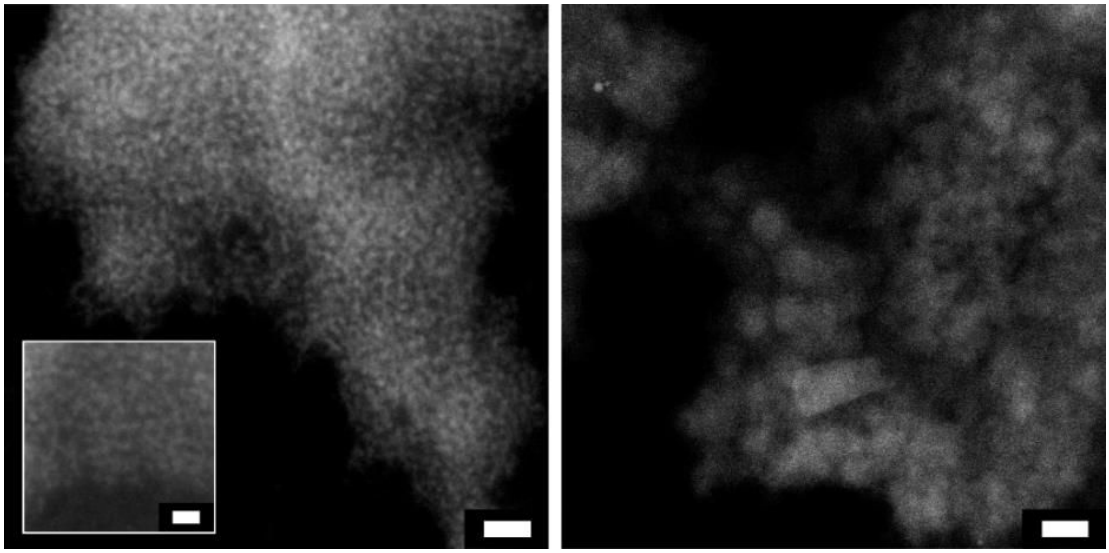

Figure 4. STEM of Si-COOH (left) and Si-Glc NPs (right). Scale bar: 20 nm (inset: 10 nm).

Zeta potential measurement

Zeta potential measurement (Figure 5) was performed to obtain the surface charge before and after the surface functionalization. The samples were prepared in pH = 10 water solution. Before coupling, Si-COOH NPs show very negative value at –37.60 ±

1.9 mV. Then the zeta potential of glucose coated Si NPs move to –15.38 ± 2.8 mV and –12.9 ± 1.6 mV, giving an evidence of successful coupling reaction.

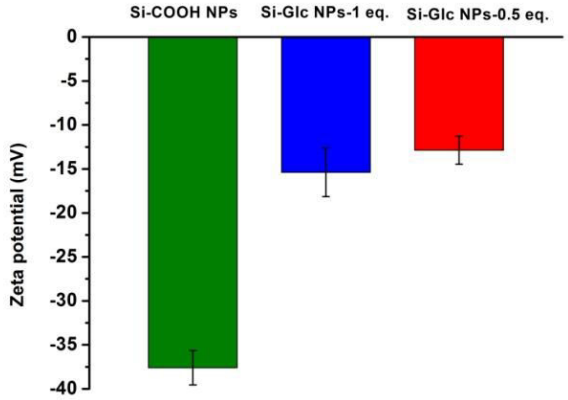

	Si-COOH	Si-Glc (70%)	Si-Glc (30%)
Zeta potential (mV)	-37.6 ± 1.9	-15.4 ± 2.8	-12.9 ± 1.6

Figure 5. Zeta potential of Si-COOH NPs, Si-Glc NPs-1 eq., and Si-Glc NPs-0.5eq.

X-ray photoelectron spectroscopy (XPS) measurement

Si NPs were further characterized by x-ray photoelectron spectroscopy (XPS) to understand the elemental composition and all the signals were calibrated with binding energy of C1s = 284.80 eV. In Figure 6, the survey scan of Si-COOH NPs displays the existence of Si, C and O elements. In the elemental scan, Si2p electrons display only one peak at 102.08 eV which corresponds to the binding energy of Si-C composition and it is in the same range with the other Si NPs reported from the literature.[39, 40] C1s binding energy at 284.80 eV reveals the C-C composition and a small shoulder at 288 eV is the carbon of carboxylic acid. In the sample with glucose modified, Figure 7, the Si-Glc NPs contain Si, C, O and N elements, and the new appearing nitrogen atoms come from the glucose ligands. Besides, Si2p binding energy is detected at 101.68 eV (Si-C composition) and there is no signal indicating Si-O (104 eV) formation.

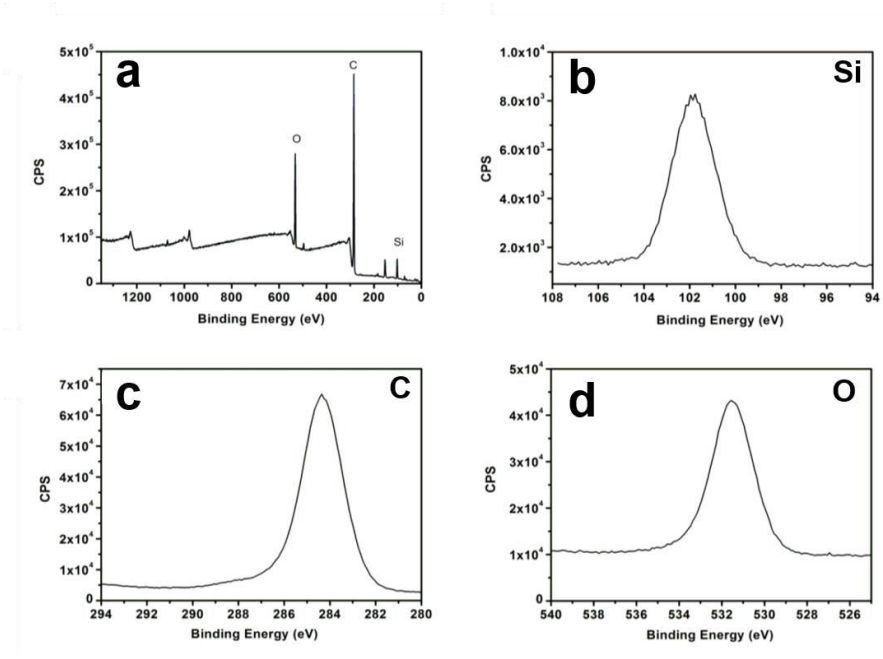

Figure 6. XPS spectra of Si-COOH NPs. (a) survey scan (b) Si 2p elemental scan (c) C 1s elemental scan (d) O 1s elemental scan.

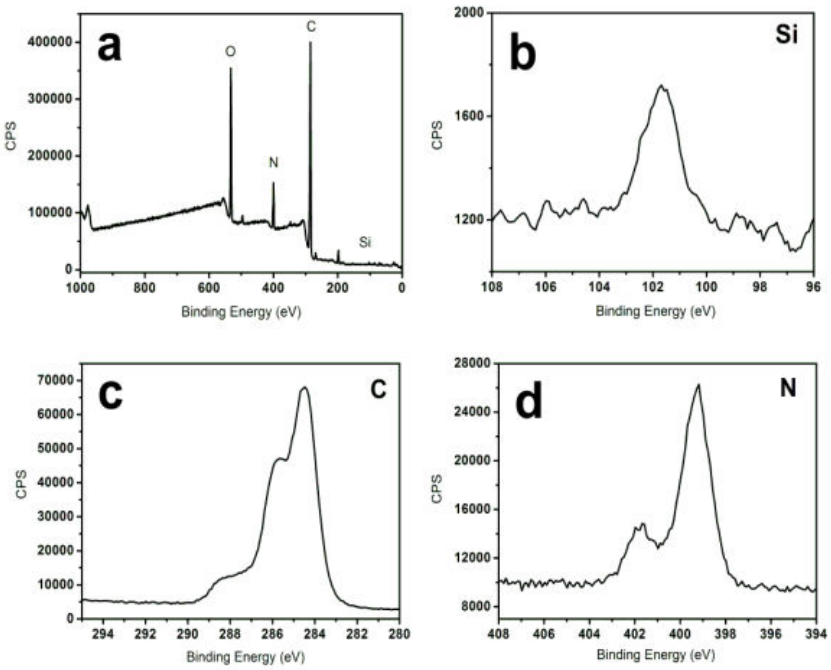

Figure 7. XPS spectra of Si-Glc NPs. (a) survey scan (b) Si 2p elemental scan (c) C 1s elemental scan (d) N 2p elemental scan.

Table 1. XPS data for Si-COOH NPs

Element	Peak, eV	FWHM, eV	Atomic ratio, %
C1s	284.80	2.88	75.66
O1s	531.95	3.02	16.01
Si2p	102.09	1.87	8.33

Table 2. XPS data for Si-Glc NPs

Element	Peak, eV	FWHM, eV	Atomic ratio, %
C1s	284.80	3.12	69.68
O1s	531.66	2.88	18.03
N1s	399.55	3.11	8.63
Si2p	101.66	2.37	0.96

4.3 Photophysical properties

Absorption and emission properties

The absorption spectra presents in Figure 8. Si-COOH and Si-Glc NPs were dispersed in EtOH solution at concentration of 0.05 mg/mL. Due to the indirect band gap of silicon, the UV-Vis absorption spectrum showed no significant absorption band in Si-COOH NPs. For the luminescent properties, Si-COOH NPs emitted at 474 nm and excited state lifetime showed multi-exponential decay with value 1.40 ns (50.9%), 3.67 ns (42.7%), 10.88 ns (6.4%), indicating the structure contained defect or surface states. For the other two glucose modified Si NPs, Si-Glc-1 and Si-Glc-0.5 NPs, the Si-Glc-1 NPs emitted at 465 nm and excited state lifetime was 0.26 ns (67.5%), 3.03 ns (26.9%) and 8.95 ns (5.6%). Similarly, Si-Glc-0.5 NPs showed emission at 470 nm and excited state lifetime was 0.35 ns (70.1%), 3.25 ns (24.9%) and 9.24 ns (5.0%). The emission properties are nearly the same for both Si-COOH and Si-Glc NPs which make sense that the glucose doesn't influence the photophysical properties. The quantum efficiency was measured using integrating sphere, and the quantum yield of these Si NPs are 3% at aerated ethanol upon light irradiation λ_{exc} at 375 nm.

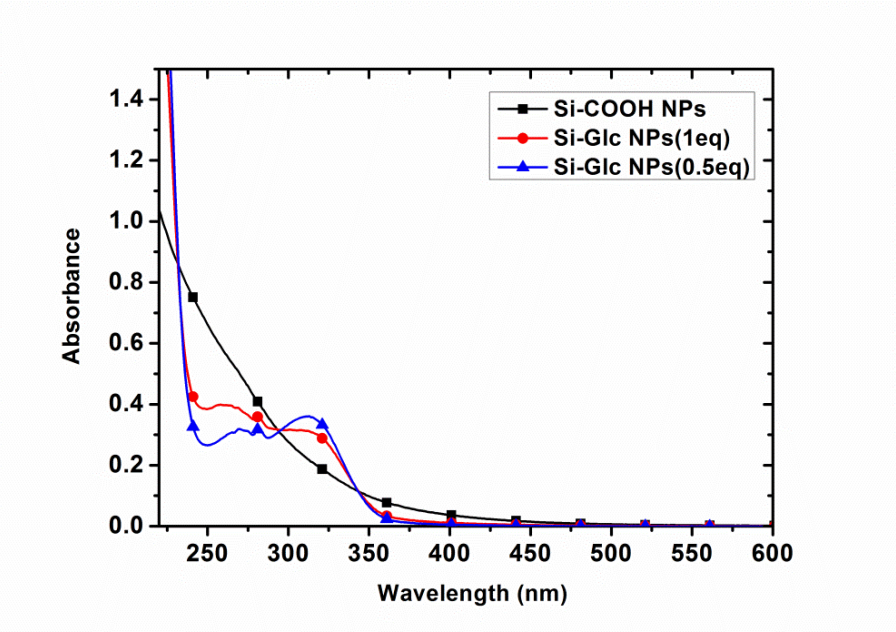

Figure 8. UV-Vis absorption spectra of Si-COOH and Si-Glc NPs in EtOH solution.

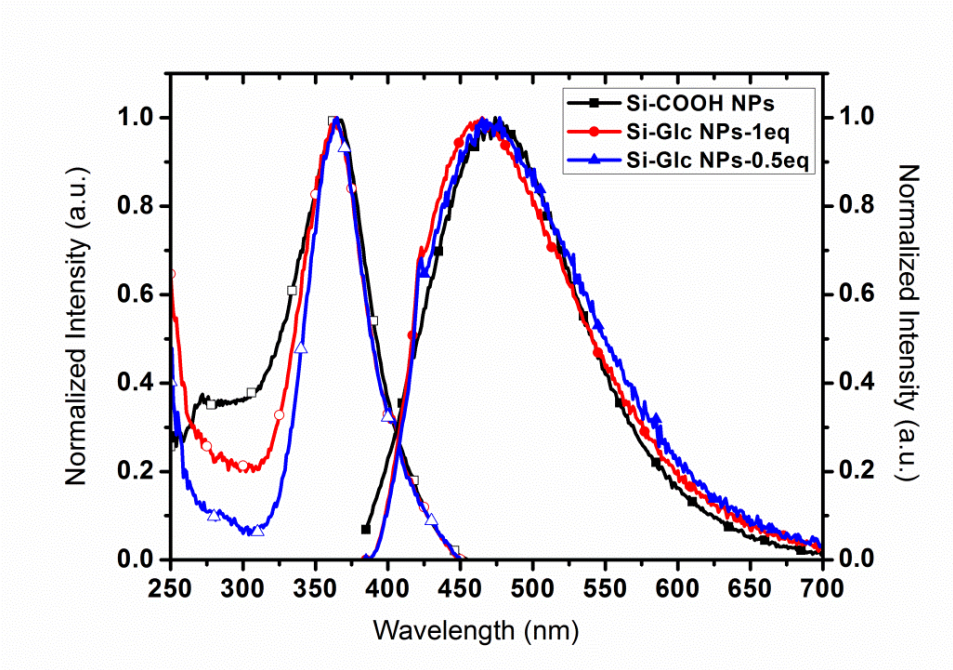

Figure 9. Emission spectra of Si-COOH and Si-Glc NPs in EtOH solution.

Table 3. Photophysical data for Si-COOH and Si-Glc NPs

Sample	λ_{ex}, nm[b]	λ_{em}, nm[c]	Lifetime τ,ns	Q.Y., %
Si-COOH NPs	365	474	1.40 (50.9%) 3.67 (42.7%) 10.88 (6.4 %)	3
Si-Glc NPs-1	365	465	0.26 (67.5%) 3.03 (26.9%) 8.95 (5.6%)	3
Si-Glc NPs-0.5	365	470	0.35 (70.1%) 3.25 (24.9%) 9.24 (5.0%)	3

a. All the samples were prepared in aerated EtOH solution. b. excitation spectra were collected at λ_{em} maximum. c. λ_{ex} = 370 nm.

Anisotropy decay

In addition, anisotropy decay measurement gives us information regarding to the rotation rate of nanoparticles and the formula of anisotropy decay describes as

$$r(\mathrm{t}) = r_0 e^{-(t/\theta)}$$

where r_0 is the anisotropy at t = 0, t is the excited state lifetime and θ is the rotational correlation time. The rotation of a molecule is described by its rotational correlation time θ, which can be presented in following equation

$$\theta = \frac{\eta V f C}{k_B T}$$

where η is the viscosity of the solvent, V is the volume of the nanoparticles, f is shape factor, C is the solute-solvent coupling parameter, k_B is the Boltzmann constant, and T is the absolute temperature. Figure 10 shows the anisotropy decay spectra of Si-COOH and Si-Glc NPs in different solvent and temperature. In Table 4, the anisotropy decay of Si-COOH and Si-Glc NPs has same decay profile in ethanol solution at room temperature, 0.52 ns and 0.55 ns, respectively. Using high viscous solvent, ethylene glycol, the anisotropy decay of Si-Glc NPs shows slightly longer than Si-COOH NPs. When the temperature is down to 0°C, however, the Si-Glc NPs exhibits longer anisotropy decay (6.12 ns) than Si-COOH NPs (3.67 ns). The reason might due to the hydrogen bond interaction of glucose and ethylene glycol is higher than carboxylic acid and ethylene glycol which enhances the solute-solvent coupling and increases the anisotropy decay time. By means of this, it also proves that in Si-Glc NPs, glucose is indeed binding on the surface of Si NPs.

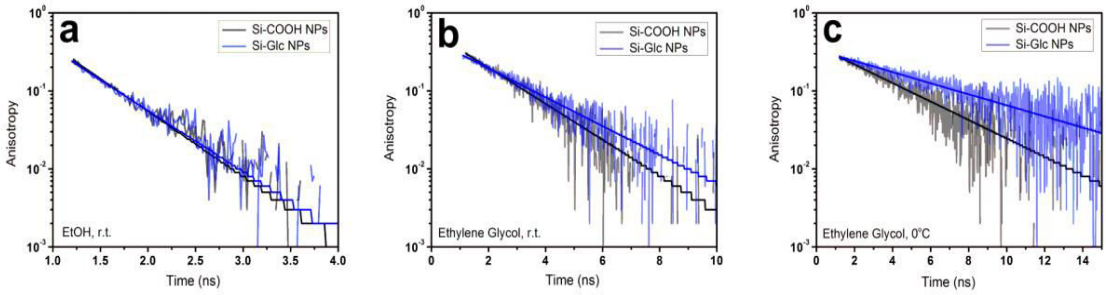

Figure 10. Anisotropy decay spectra of Si-COOH and Si-Glc NPs in different solvent and temperature.

Table 4. Anisotropy decay data

	Si-COOH NPs			Si-Glc NPs		
	EtOH	Ethylene Glycol	Ethylene Glycol, 0°C	EtOH	Ethylene Glycol	Ethylene Glycol, 0°C
r_0	0.247	0.300	0.270	0.237	0.285	0.274
θ, ns	0.52	1.91	3.67	0.55	2.36	6.12
G factor	1.81	1.91	2.22	1.72	1.97	2.11

4.4 *In vitro* imaging

To address the ability of the synthesized nanomaterials to be used as a bioimaging agent, cellular uptake experiments using HeLa cells were carried out. To be more specific, the objectives of these experiments are: (a) to prove the cellular internalization and to compare the kinetic uptake of the two systems, (b) to understand the specific distribution of the materials inside the cells by means of co-localization study, and (c) to understand the possible toxicity effect that will reduce the percentage of cellular viability.

Living HeLa cells were incubated with the particles dispersion at the final concentration 100 μg/mL in less than 1% DMSO/culture media and the incubation times were set at 1, 4, and 24 hours. After the incubation finished, the cells were washed out from the access of non-uptaken materials and finally fixed by using paraformaldehyde solution. Fluorescence confocal microscopy experiments were carried out by exciting the sample at lambda 405 nm and the emission signals were collected by detector at lambda 412 to 600 nm, respectively. As can be seen from Figure 11, the uptake of Si-COOH particles was found very rapid and it was already observed even after short incubation time, i.e. 1 hour (see z-stack in Figure 13). Moreover, the amounts of materials uptaken by the cells increased linearly by the incubation time, proven by growth of intensity profile in Figure 11.

Sugar is an active biomolecule, and its presence on the surface of any nanomaterials indeed has been already confirmed as a successful strategy to increase the uptake kinetic of particles by the cells. The reason might be the fact that the interaction between saccharides moiety and cell receptor is favourable thus increasing the uptake. De Farias *et al*. reported that the rapid cellular uptake of glucose capped nanoparticles less than 10 minutes in yeast cells which contain high-affinity glucose transporters.[32] In addition, the expression of GLUT1 and GLUT3 glucose transporters has been observed in HeLa cells and other tumor cells.[20]

As it is been demonstrated from its predecessor, Si-Glc NPs was also internalized by living HeLa cells (see z-stack in Figure 14). Thanks to the saccharides, the cellular response towards the glucose-modified silicon particles at the same concentration were found slightly faster after short period of incubation compared to the mother systems as can be seen from different level of emission intensity collected from the cells. Furthermore, the same trend also can be monitored at longer incubation times, i.e. 4 and 24 hours, respectively. (Figure 12)

Specific distribution of the two particles inside the cells was further studied. Co-localization experiments were carried out by using commercially available dyes named ER-Tracker™ Red, LysoTracker® Red DND-99, and Alexa Fluor® 647 Phalloidin as the endoplasmic reticulum, the lysosome and the f-actin/membrane staining agents. The corresponding microscopy images after 24 hours of incubation time are depicted in Figure 13 and 14. Both particles were distributed inside the lysosome (overlap coefficient 0.86 for Si-COOH and 0.84 for Si-Glc, respectively), a common phenomenon that has been commonly observed in the most cases of nanoparticles uptake experiments.[41-43] The Si-COOH particles were also found distributed inside endoplasmic reticulum (overlap coefficient 0.87), but very interestingly, lower distribution were observed for the case of glucose-modified system (overlap coefficient 0.62). The cellular co-localization of Si NPs in endoplasmic reticulum could be due to the chelation of metal ions and carboxylate group which it has been shown that endoplasmic reticulum contains Zn^{2+} ions, ca. 0.9 pM in HeLa cells.[44] Besides, the regulation of glucose is related to G6P-phosphatase which is also located in the endoplasmic reticulum.[45]

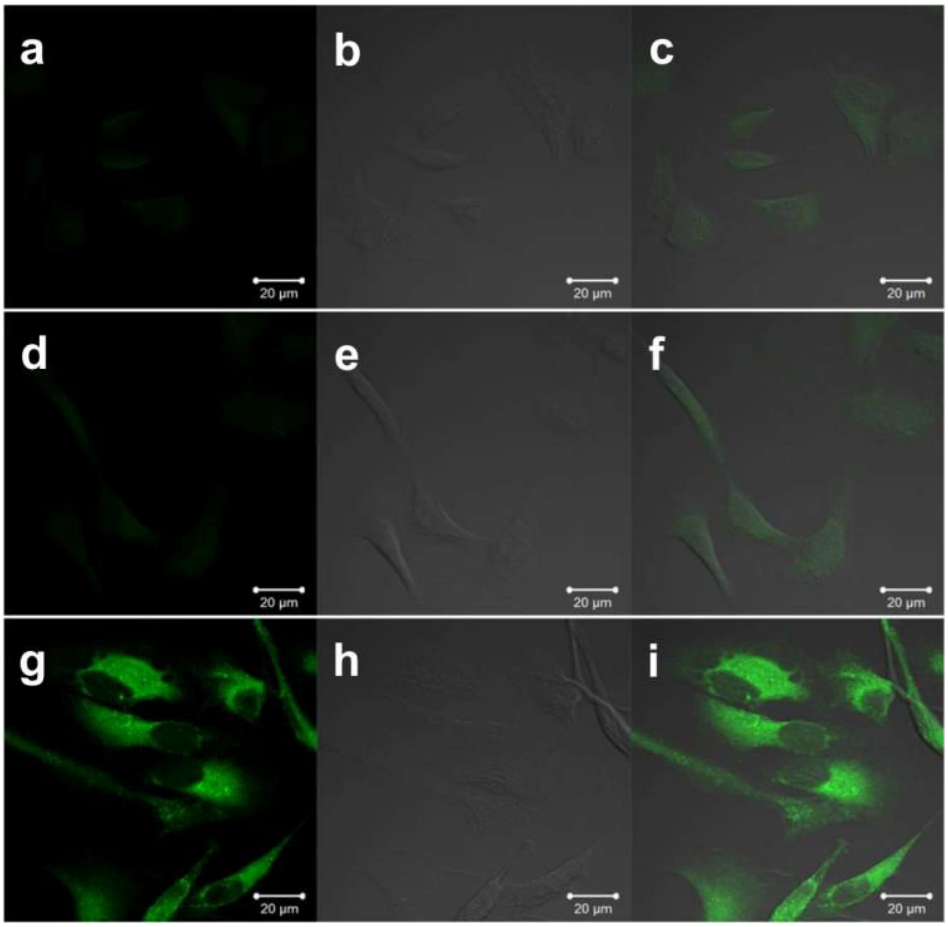

Figure 11. Confocal imaging of 100 µg/ mL Si-COOH NPs in HeLa cells for (a) – (c) 1 hour, (d) – (f) 4 hours, (g) – (i) 24 hours incubation time. (a), (d) and (g) are luminescence images, (b), (e) and (h) are transmission images, and (c), (f) and (i) are overlay of the two images. Scale bar: 20 µm. The emissions are false colors.

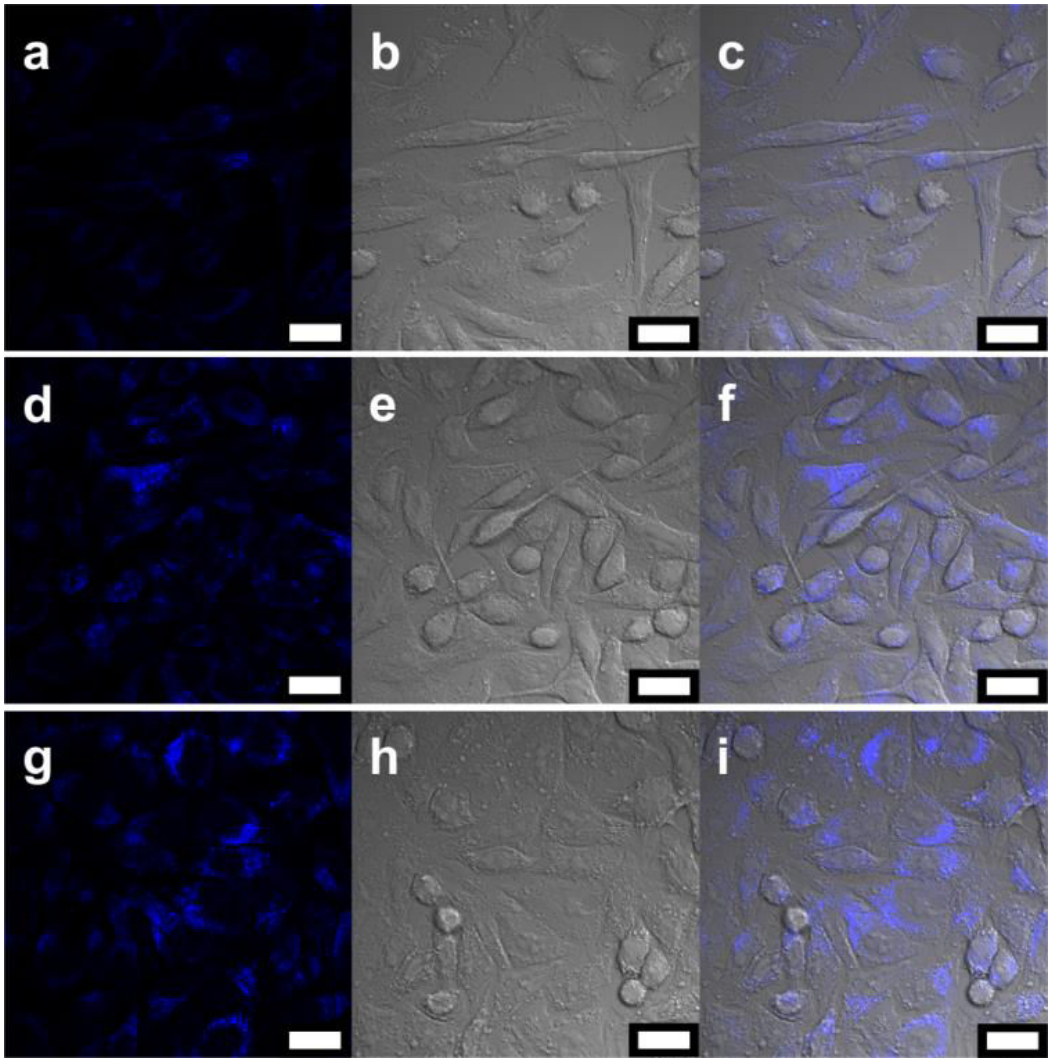

Figure 12. Confocal imaging of 100 μg/ mL Si-Glc NPs in HeLa cells for (a) – (c) 1 hour, (d) – (f) 4 hours, (g) – (i) 24 hours incubation time. (a), (d) and (g) are luminescence images, (b), (e) and (h) are transmission images, and (c), (f) and (i) are overlay of the two images. Scale bar: 20 μm. The emissions are false colors.

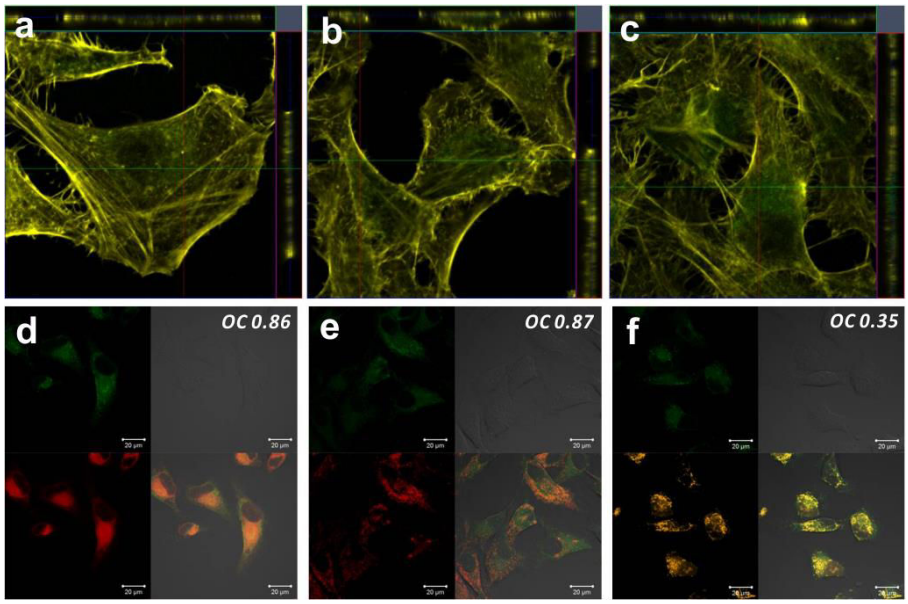

Figure 13. Confocal imaging of Si-COOH NPs (a) – (c) Z stack of Si-COOH in 1, 4 and 24 hours. (d) Cellular localization of Si-COOH in ER. (e) Cellular localization of Si-COOH in lysosome. (f) Cellular localization of Si-COOH in mitochondria. Scale bar: 5 μm for (a) – (c); 20 μm for (d) – (f).

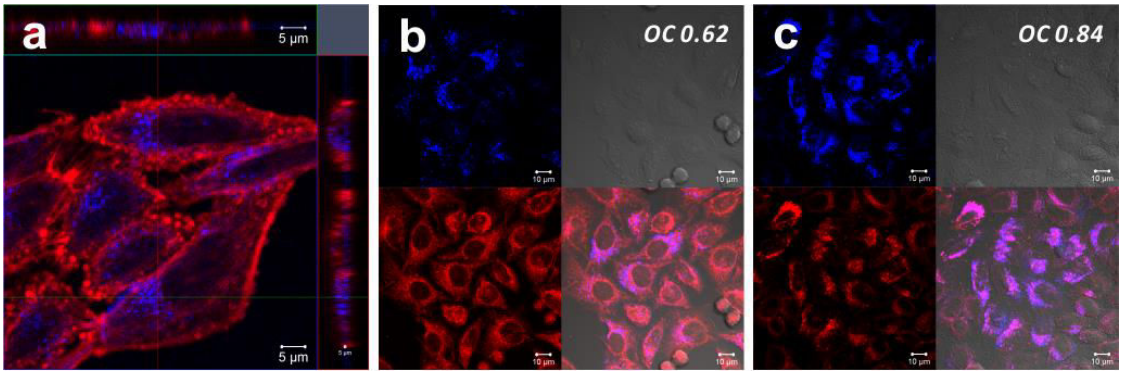

Figure 14. Confocal imaging of Si-Glc NPs (a) Z stack of Si-Glc in 24 hours. (b) Cellular localization of Si-Glc in ER. (c) Cellular localization of Si-Glc in lysosome. Scale bar: 5 μm for (a); 10 μm for (b) and (c).

Furthermore, the numbers of viable cells after 24 hours incubation of the two nanomaterials at concentration up to 100 μg/mL are found to be close to the control experiments. (Figure 15) As previous report[16], carboxylic acid modified Si NPs exhibited high cell viability. Although many literatures have shown that glyconanoparticles have non-toxicity or could lower the cytotoxicity after modified sugars,[33, 46-48] this is the first time we report in silicon NPs. Indeed this is strongly demonstrating the low cytotoxicity of the complexes and their suitability as efficient staining agents for bio-imaging application.

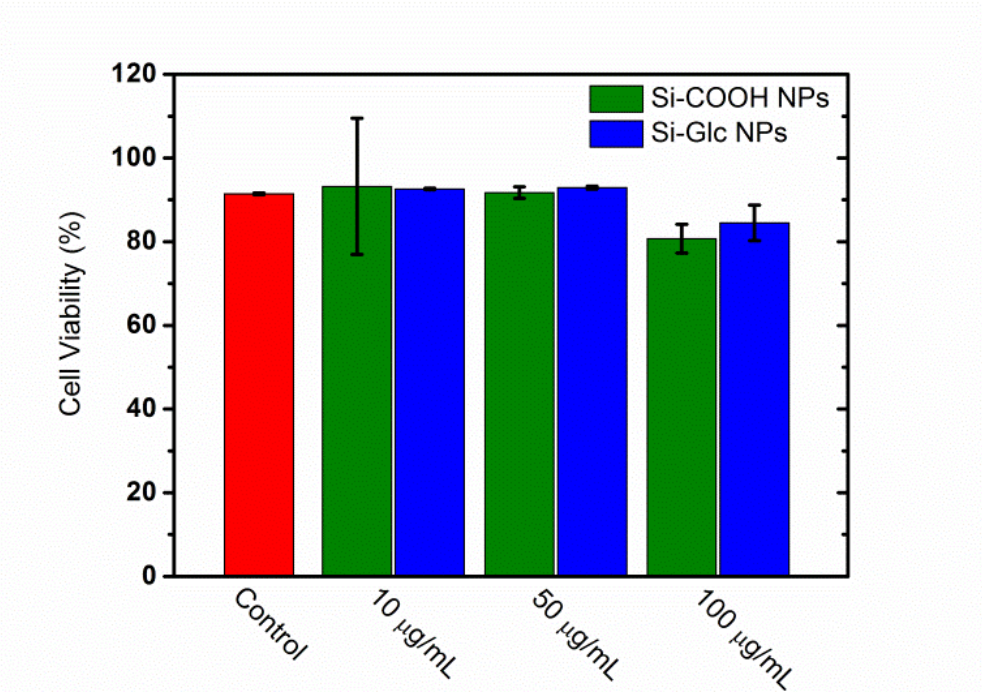

Figure 15. Cell viability test of HeLa cells after 24 hours incubation.

4.5 Conclusion

Ultrasmall silicon nanoparticles namely Si-COOH (diameter ca. 4 nm) were successfully synthesized and later, chemically modified by attaching glucose moiety on the surface (Si-Glc). The amount of the sugar on the surface was well controlled by varying the ratio of the capping groups. FT-IR, zeta potential measurement, and anisotropy decay analysis show proof of the attachment of glucose to the nanoparticles. By analyzing rotational correlation time, we observed strong interaction between glucose-modified particles and ethylene glycol resulting longer anisotropy decay time. Remarkably, photophysical measurements don't show any significant change in emission features upon the binding. *In vitro* and viability study using HeLa cells show the uptake of both particles inside the cells with high cellular viability. Different localization and kinetic uptake of glucose-modified particles compared to unmodified ones were observed. Glucose-modified Si NPs demonstrated rapid cellular uptake compared to Si-COOH NPs. This result suggests silicon based nanomaterials is a better choice than using conventional CdSe quantum dot, and it can open a possibility to be used as a new staining probe with high interest and potential for bioimaging application.

4.6 Experimental Section

General information and materials

All reagents were purchased from Sigma-Aldrich and Alfa and used without any further purification unless specified notice. The glucose was provided by Group of Prof. Peter Seeberger. Solvents were purified according to the standard procedure.[49] All air and water sensitive experiments were carried out in standard glassware under an inert argon atmosphere using schlenk line techniques. ^{1}H and ^{13}C NMR were acquired on a Bruker AV400 (400 MHz) at 25°C with the deuterated solvent as the internal reference. NMR measurements were performed in Institut de Science et d'Ingénierie Supramoléculaires (ISIS), University of Strasbourg.

Optical measurement

Steady-state emission spectra were recorded on a HORIBA Jobin-Yvon IBH FL-322 Fluorolog 3 spectrometer equipped with a 450 W xenon arc lamp as the excitation source, double-grating excitation and emission monochromators (2.1 nm mm^{-1} of dispersion; 1200 grooves mm^{-1}), and a TBX-04 single-photon-counting device as the detector. Emission and excitation spectra were corrected for source intensity (lamp and grating) and emission spectral response (detector and grating) by standard correction curves. Time-resolved measurements were performed using the PicoHarp 300 equipped with time correlated single photon counting (TCSPC) system on the Fluoro Time 300 (PicoQuant), where a laser source 375 nm was applied to excite the samples. The laser was mounted directly on the sample chamber at 90° to a Czerny-Turner type emission monochromator (2.7 nm mm^{-1} of dispersion; 1200 grooves mm^{-1}) and collected by a PMA-C 192M single-photon- counting detector. Signals were collected using EasyTau software, and data analysis was performed using FluoFit software (PicoQuant). The quality of the fit was assessed by minimizing the reduced $\chi 2$ function and by visual inspection of the weighted residuals. Luminescence quantum yield was performed with integrating sphere (Hamamatsu, C11347-11). Anisotropy decay was measured by Fluoro Time 300 (PicoQuant) in room temperature and 0°C with laser excited at 375 nm, and collected the data after 30 seconds. FT-IR spectra were measured in attenuated total reflectance (ATR) method with Shimadzu IRAffinity-1.

XPS measurement

All the X–ray Photoelectron Spectroscopic (XPS) measurements were done by a Thermo Scientific K-Alpha X-ray Photoelectron Spectrometer using a monochromatic AlKα radiation (hυ = 1486.6 eV). Survey measurements were performed with a 200 eV analyzer pass energy and a 1 eV energy step size to calculate the atomic concentrations. Element scans were performed with a 50 eV analyzer pass energy and a 0.1 eV energy step size obtain the chemical state information. All the obtained binding energies were referenced to carbon 1s peak at 284.8 eV.

Cell experiments

HeLa cells were cultured inside media which contain 88 % Dulbecco's Modified Eagle Medium (DMEM), 10 % Fetal Bovine Serum, 1 % Penicillin-Streptomycin and 1 % L-Glutamine 200mM (all material was purchased from Gibco) under 37ºC and 5% of CO_2 condition for 48 hours until reaching 70 to 80 % cell confluency. Subsequently, the cells were washed twice with Phosphate Buffer Solution (PBS, Gibco), trypsinated and approximately 50,000 cells were reseeded on the monolayer glass cover slip inside 6 well plate culture dish. New culture media (2 mL) were added gently and the cells were grown overnight.

Cell viability was measured by an automatic cell counter CASY (Roche Innovatis AG, Bielefeld, Germany). 50,000 cells were grown in 2 mL of culture media inside 6 well plates at 37ºC, 5 % CO_2 environment for 24 hours. Culture media were removed and replaced by solution containing 0.01, 0.05 and 0.1 mg/mL of Si-COOH NPs or Si-Glc NPs, followed by cell incubation. After 24 hours of incubation, the culture media we removed to an eppendorf tube and 0.5 mL of trypsin were added. In order to detach the cell from the surface of the plate, cells were incubated for the next 10 minutes. Subsequently, 1.5 mL of new culture media were added to neutralize trypsin. Cell suspension together with first solution collected were removed into 10 mL eppendorf tube and centrifuged at 1000 rpm for 5 minutes. Supernatant were removed and cell palates were suspended into 1 mL of new culture media. 200 µL of the cell suspension was dissolved in 10 mL of CASY solution and measurement was performed. To add negative control experiment, the exact same procedure was performed by incubating cells in 30% of DMSO in culture media while for positive control, cells were incubated only with culture media.

Synthetic procedure

Please see chapter 3 for the detail synthesis of Si-COOH NPs.

Si-Glc NPs

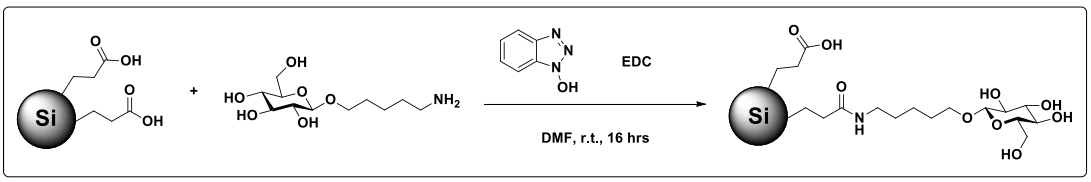

Carboxylic acid terminated Si NPs (13 mg), EDC (5.83 mg, 30.4 μmol), and HOBt (4.66 mg, 30.4 μmol) were dissolved into 2 mL dried DMF. Glucose ligand (4.03 mg, 15.2 μmol or 2.02 mg, 7.6 μmol) and Et_3N (10 μL, 71.7 μmol) were added and stirred at room temperature for 16 hours at Ar atmosphere. After reaction, DMF was removed by vacuum and purified by size exclusion chromatography (LH-20) to get yellow solid.

4.7 Reference

1. F. Erogbogbo, K.-T. Yong, R. Hu, W.-C. Law, H. Ding, C.-W. Chang, P. N. Prasad and M. T. Swihart, *ACS Nano*, 2010, **4**, 5131-5138.
2. C. Kirchner, T. Liedl, S. Kudera, T. Pellegrino, A. Muñoz Javier, H. E. Gaub, S. Stölzle, N. Fertig and W. J. Parak, *Nano Lett.*, 2005, **5**, 331-338.
3. N. Lewinski, V. Colvin and R. Drezek, *Small*, 2008, **4**, 26-49.
4. L. Wang, D. K. Nagesha, S. Selvarasah, M. R. Dokmeci and R. L. Carrier, *J Nanobiotechnology*, 2008, **6**, 11.
5. J. H. Warner, A. Hoshino, K. Yamamoto and R. D. Tilley, *Angew. Chem. Int. Ed.*, 2005, **117**, 4626-4630.
6. M. Rosso-Vasic, E. Spruijt, Z. Popovic, K. Overgaag, B. van Lagen, B. Grandidier, D. Vanmaekelbergh, D. Dominguez-Gutierrez, L. De Cola and H. Zuilhof, *J. Mater. Chem.*, 2009, **19**, 5926-5933.
7. M. Rosso-Vasic, E. Spruijt, B. van Lagen, L. De Cola and H. Zuilhof, *Small*, 2008, **4**, 1835-1841.
8. M. Rosso-Vasic, L. De Cola and H. Zuilhof, *The Journal of Physical Chemistry C*, 2009, **113**, 2235-2240.
9. R. D. Tilley and K. Yamamoto, *Adv. Mater.*, 2006, **18**, 2053-2056.
10. A. Shiohara, S. Prabakar, A. Faramus, C. Y. Hsu, P. S. Lai, P. T. Northcote and R. D. Tilley, *Nanoscale*, 2011, **3**, 3364-3370.
11. Z. F. Li and E. Ruckenstein, *Nano Lett.*, 2004, **4**, 1463.
12. F. Erogbogbo, C. A. Tien, C. W. Chang, K. T. Yong, W. C. Law, H. Ding, I. Roy, M. T. Swihart and P. N. Prasad, *Bioconjug Chem*, 2011, **22**, 1081-1088.
13. F. Erogbogbo, K.-T. Yong, I. Roy, R. Hu, W.-C. Law, W. Zhao, H. Ding, F. Wu, R. Kumar, M. T. Swihart and P. N. Prasad, *ACS Nano*, 2011, **5**, 413-423.
14. M. P. Singh, T. M. Atkins, E. Muthuswamy, S. Kamali, C. Tu, A. Y. Louie and S. M. Kauzlarich, *ACS Nano*, 2012, **6**, 5596-5604.
15. C. Tu, X. Ma, A. House, S. M. Kauzlarich and A. Y. Louie, *ACS Med Chem Lett*, 2011, **2**, 285-288.
16. S. Bhattacharjee, I. M. Rietjens, M. P. Singh, T. M. Atkins, T. K. Purkait, Z. Xu, S. Regli, A. Shukaliak, R. J. Clark, B. S. Mitchell, G. M. Alink, A. T. Marcelis, M. J. Fink, J. G. Veinot, S. M. Kauzlarich and H. Zuilhof, *Nanoscale*, 2013, **5**, 4870-4883.
17. L. Ruizendaal, S. Bhattacharjee, K. Pournazari, M. Rosso-Vasic, L. H. J. de Haan, G. M. Alink, A. T. M. Marcelis and H. Zuilhof, *Nanotoxicology*, 2009, **3**, 339.
18. A. Shiohara, S. Hanada, S. Prabakar, K. Fujioka, T. H. Lim, K. Yamamoto, P. T. Northcote and R. D. Tilley, *J. Am. Chem. Soc.*, 2010, **132**, 248-253.

19. A. Varki, R. D. Cummings, J. D. Esko, H. H. Freeze, P. Stanley, C. R. Bertozzi, G. W. Hart and M. E. Etzler, *Essentials of Glycobiology*, 2nd edn., Cold Spring Harbor Laboratory Press, 2009.
20. T. Suzuki, A. Iwazaki, H. Katagiri, Y. Oka, J. L. Redpath, E. J. Stanbridge and T. Kitagawa, *Eur. J. Biochem.*, 1999, **262**, 534-540.
21. A. Bernardi, J. Jimenez-Barbero, A. Casnati, C. De Castro, T. Darbre, F. Fieschi, J. Finne, H. Funken, K.-E. Jaeger, M. Lahmann, T. K. Lindhorst, M. Marradi, P. Messner, A. Molinaro, P. V. Murphy, C. Nativi, S. Oscarson, S. Penades, F. Peri, R. J. Pieters, O. Renaudet, J.-L. Reymond, B. Richichi, J. Rojo, F. Sansone, C. Schaffer, W. B. Turnbull, T. Velasco-Torrijos, S. Vidal, S. Vincent, T. Wennekes, H. Zuilhof and A. Imberty, *Chem. Soc. Rev.*, 2013, **42**, 4709-4727.
22. J. M. de la Fuente and S. Penades, *Biochim. Biophys. Acta*, 2006, **1760**, 636-651.
23. T. D. Farr, C.-H. Lai, D. Grünstein, G. Orts-Gil, C.-C. Wang, P. Boehm-Sturm, P. H. Seeberger and C. Harms, *Nano Lett.*, 2014, **14**, 2130-2134.
24. C.-H. Lai, T.-C. Chang, Y.-J. Chuang, D.-L. Tzou and C.-C. Lin, *Bioconjugate Chem.*, 2013, **24**, 1698-1709.
25. C.-H. Lai, N.-C. Lai, Y.-J. Chuang, F.-I. Chou, C.-M. Yang and C.-C. Lin, *Nanoscale*, 2013, **5**, 9412-9418.
26. D. C. Kennedy, D. Grünstein, C.-H. Lai and P. H. Seeberger, *Chemistry – A European Journal*, 2013, **19**, 3794-3800.
27. Á. G. Barrientos, J. M. de la Fuente, T. C. Rojas, A. Fernández and S. Penadés, *Chemistry – A European Journal*, 2003, **9**, 1909-1921.
28. X. Wang, E. Matei, L. Deng, O. Ramstrom, A. M. Gronenborn and M. Yan, *Chem. Commun.*, 2011, **47**, 8620-8622.
29. C. Tu, X. Ma, P. Pantazis, S. M. Kauzlarich and A. Y. Louie, *J. Am. Chem. Soc.*, 2010, **132**, 2016-2023.
30. J. H. Ahire, I. Chambrier, A. Mueller, Y. Bao and Y. Chao, *ACS Applied Materials & Interfaces*, 2013, **5**, 7384-7391.
31. M. Ahmed, Z. Deng, S. Liu, R. Lafrenie, A. Kumar and R. Narain, *Bioconjugate Chem.*, 2009, **20**, 2169-2176.
32. P. M. A. de Farias, B. S. Santos, F. D. Menezes, A. G. Brasil Jr, R. Ferreira, M. A. Motta, A. G. Castro-Neto, A. A. S. Vieira, D. C. N. Silva, A. Fontes and C. L. Cesar, *Appl. Phys. A*, 2007, **89**, 957-961.
33. M. Moros, B. Hernáez, E. Garet, J. T. Dias, B. Sáez, V. Grazú, Á. González-Fernández, C. Alonso and J. M. de la Fuente, *ACS Nano*, 2012, **6**, 1565-1577.
34. C.-H. Lai, C.-Y. Lin, H.-T. Wu, H.-S. Chan, Y.-J. Chuang, C.-T. Chen and C.-C. Lin, *Adv. Funct. Mater.*, 2010, **20**, 3948-3958.
35. R. Kikkeri, B. Lepenies, A. Adibekian, P. Laurino and P. H. Seeberger, *J. Am.*

Chem. Soc., 2009, **131**, 2110-2112.
36. Q. Liu and S. M. Kauzlarich, *Mater. Sci. Eng. B*, 2002, **B96**, 72.
37. F. Zimmermann, E. Meux, J.-L. Mieloszynski, J.-M. Lecuire and N. Oget, *Tetrahedron Lett.*, 2005, **46**, 3201-3203.
38. C. Q. Tu, X. C. Ma, P. Pantazis, S. M. Kauzlarich and A. Y. Louie, *J. Am. Chem. Soc.*, 2010, **132**, 2016.
39. M. Dasog, Z. Yang, S. Regli, T. M. Atkins, A. Faramus, M. P. Singh, E. Muthuswamy, S. M. Kauzlarich, R. D. Tilley and J. G. C. Veinot, *ACS Nano*, 2013, **7**, 2676-2685.
40. L. Ruizendaal, S. P. Pujari, V. Gevaerts, J. M. Paulusse and H. Zuilhof, *Chem Asian J*, 2011, **6**, 2776-2786.
41. X. Jiang, C. Röcker, M. Hafner, S. Brandholt, R. M. Dörlich and G. U. Nienhaus, *ACS Nano*, 2010, **4**, 6787-6797.
42. A. D. Lehmann, W. J. Parak, F. Zhang, Z. Ali, C. Röcker, G. U. Nienhaus, P. Gehr and B. Rothen-Rutishauser, *Small*, 2010, **6**, 753-762.
43. L. W. Zhang and N. A. Monteiro-Riviere, *Toxicol. Sci.*, 2009, **110**, 138-155.
44. Y. Qin, P. J. Dittmer, J. G. Park, K. B. Jansen and A. E. Palmer, *Proceedings of the National Academy of Sciences*, 2011, **108**, 7351-7356.
45. M. Fehr, H. Takanaga, D. W. Ehrhardt and W. B. Frommer, *Molecular and Cellular Biology*, 2005, **25**, 11102-11112.
46. M. Yu, Y. Yang, R. Han, Q. Zheng, L. Wang, Y. Hong, Z. Li and Y. Sha, *Langmuir*, 2010, **26**, 8534-8539.
47. B. Mehravi, M. Ahmadi, M. Amanlou, A. Mostaar, M. S. Ardestani and N. Ghalandarlaki, *Int. J. Nanomedicine*, 2013, **8**, 3209-3216.
48. X. Jiang, M. Ahmed, Z. Deng and R. Narain, *Bioconjugate Chem.*, 2009, **20**, 994-1001.
49. W. L. F. Armarego and C. L. L. Chai, *Purification of laboratory chemicals*, 5th edn., Butterworth-Heinemann, Amsterdam, 2003.

CHAPTER 5

Nano-system of Si NPs and Pt(II) Complexes

Abstract

Pt(II) complexes, possessing square planar geometry, when coordinated to aromatic ligands can undergo π–π stacking and eventually, Pt–Pt interactions, leading to the formation of aggregates. In fact, if the distance is lower than 3.5 Å, the d_{z^2} orbitals can electronically interact generating new excited states named metal-metal-to-ligand charge transfer (MMLCT). The self-assembly process protects the metal core from dioxygen quenching, causes a bathochromic shift of the luminescence and in some cases can lead to an enhancement of the emission intensity. In this chapter, we report the synthesis of two Pt(II) complexes and their conjugation with silicon nanoparticles. The photophysical properties are discussed as well as the aggregation induced emission (AIE) effect. Both nanoparticles and the metal complexes were further incubated with HeLa cells for *in vitro* imaging studies.

5.1 Introduction

In the last few decades, luminescent metal complexes have received a lot of attention and have been applied in many opto-electro applications. With different ligand design, the emission wavelength of metal complexes such as Ir(III), Re(I), Ru(II) and Pt(II) can be tuned form blue to near infrared red.[1-4] Due to the heavy metal, the intersystem crossing (ISC) from singlet to triplet excited state is strongly promoted, and, when luminescent, the emitted light is a phosphorescence through radiative decay from triplet excited state to ground state. To the nature of the emission the excited state lifetime is often long lived in deaerated solution or in the solid state. Also some of the Pt(II) complexes can have high emission quantum yield, tunable emission, upon changing the coordinated ligands.

d^8 electron configuration metal complexes have known to aggregate in linear chain or oligomeric structure in solid state and change the photophysical properties.[5-8] For example, in 1969, Krogmann[9] found out the $M[Pt(CN)_4]$ complexes (M = alkali or alkaline earth metal), known as Krogmann salts, are colorless in aqueous solution, but form deeply colored crystals. Also in the crystal structure, the complexes grew along in one dimension with Pt···Pt distance less than 3.2 Å. Same phenomenon is also observed in polypyridine system. Palmans reported the bis(2,2'-bipyridyl)platinum(I) complex forms a linear chain structure with Pt···Pt distance of 3.563 Å in crystal and absorbs light in a range of 500 to 2500 nm, while this absorption disappears when complex dissolves in aqueous solution.[10] As a result, the new formation of absorption band indicates the existence of the d–d interaction of metals. Moreover, with appropriate ligands, square planar Pt(II) complexes have interesting luminescent properties that in some cases can be modulated by their tendency to aggregate. Owing to the planar structure, Pt(II) complexes easily form π–π stacking through Pt–Pt interactions. Indeed the aggregation can be stabilized by the interaction of the d_{z2} orbitals (if the distance between two Pt complexes < 3.5 Å) resulting in new excited state named metal-metal-to-ligand charge transfer (MMLCT). The process is simplified in scheme 1. Such finding has been exploited for white light OLEDs (Organic light–emitting diodes) by controlling the ratio between the monomer and excimer, using a single molecule.[11] Moreover, assembled Pt(II) complexes can form fibers and gels that have been also exploited for OLEDs applications and exhibited anisotropic emission upon excitation with polarized light.[7, 12, 13] Also recently for bioimaging[14-16] since the luminescence can be very intense and the excited state lifetime as long as hundreds nanoseconds.

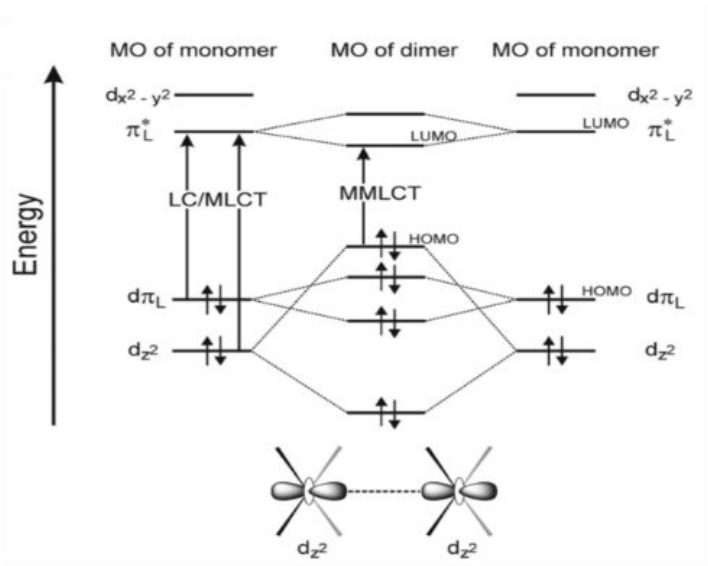

Scheme 1. Simplified MO diagram of two interacting square-planar platinum(II) complexes. Reproduced from *Chem. Soc. Rev.,* **2014**, *43*, 4144-4166 with permission from The Royal Society of Chemistry.

Recently aggregation-induced emission (AIE) is observed in organic compounds.[17-19] The phenomenon can be explained by the restriction of intramolecular rotation (RIR).[20, 21] Generally, emission intensity is quenched when the compounds aggregate, resulting aggregation caused-quenching (ACQ). However, by using appropriate ligand design to reduce the level of aggregation, the ACQ effect can be avoid and increase the emission. In addition, metal complex systems are also observe this AIE effect such as in Ir and Pt complexes.[12, 22-26] In the case of Pt complex, by adding unfavorable solvent, Pt(II) complexes tend to aggregate and enhance the emission. The enhanced luminescence could be due to the formation of triplet metal-metal-to-ligand charge transfer (MMLCT) states and the aggregation protects the inner core from oxygen quenching.[13] Besides, decreasing the mobility of Pt complex in aggregated state can also enhance the emission intensity.[27]

In this chapter we have synthesized some Pt(II) complexes that can undergo self-assembly and derivatized them with amino groups in order to couple them to carboxylic acid modified Si NPs. The photophysical properties have been s studied as well as the aggregation induced emission (AIE) effect. In addition, both the nanoparticles decorated with the complexes and the compounds alone were incubated with living HeLa cells for a possible application in bioimaging.

5.2 Synthesis and characterization

Synthesis

Synthesis of Pt(II) complexes

The synthesis of Pt(II) complexes was achieved following a general procedure published by our group.[7] However, from our previous experience, undesired Pt(II) complex was obtained when using triethylamine as a base, resulting to a Pt–triethylamine complex. (Scheme 2) Therefore, we decided to employ a more bulky amine, diisopropylethylamine, instead of trimethylamine. We also protected the amino group of 4-ethylaminopyridine with t-Boc to prevent the undesired Pt–amine chelation. $PtCl_2(DMSO)_2$ precursor synthesized according to literature methods,[28] was stirred with bis-triazole (N^N^N) ligand, 2,6-bis(3-(trifluoromethyl)-1H-1,2,4-triazol-5-yl)pyridine and 2,6-bis(3-(trimethoxyphenyl)-1H-1,2,4-triazol-5-yl)pyridine, and diisopropylethylamine was added to deprotonate the triazole units, in acetonitrile solution. After 10 minutes stirred at room temperature, t-Boc protected pyridine was added and heated at 70°C for 15 hours. After column chromatography, a yellow solid was obtained with 60 to 70% yield. For deprotecting the t-Boc group, 15% of trifluoroacetic acid (TFA) in CH_2Cl_2 solution was used and the reaction was monitored by TLC until no starting material was present. (Scheme 3) The Pt(II) complexes were further characterized by ^{1}H NMR, ^{19}F NMR and mass spectrometer.

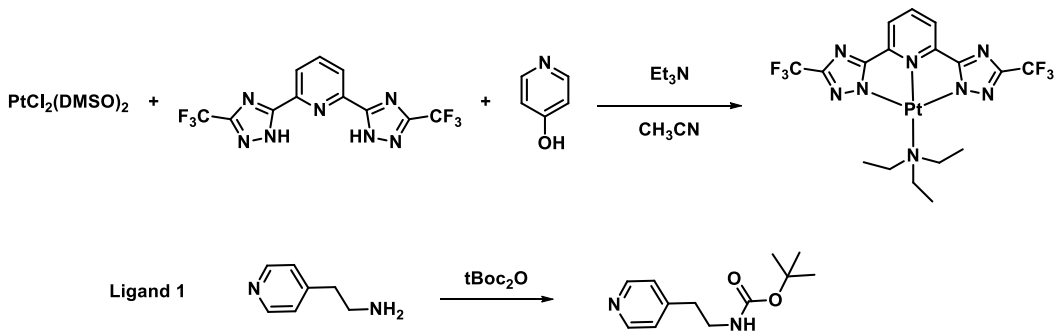

Scheme 2. Synthesis of the Pt(II) complex when the trimethylamine was added as a base and below the reaction for the protection of the amine.

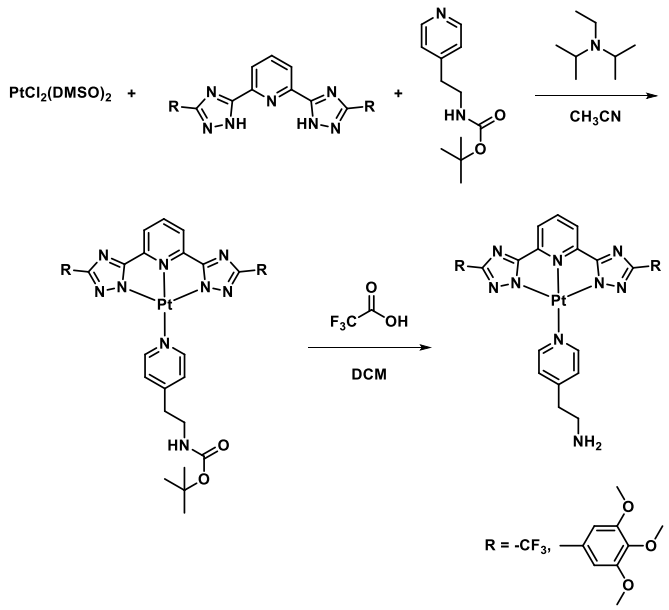

Scheme 3. Synthesis of the Pt(II) complexes

Synthesis and characterization of Si-[Pt] nanoparticles

The amino Pt(II) complexes were further coupled with carboxylate terminated Si NPs by amide bond coupling and obtained two nanoparticles, Si-[PtCF3] and Si-[Pttmp] NPs. (Scheme 4) In order to increase the reactivity in the heterogeneous phase, was used only 2 mL of solvent. Also by changing the number of equivalents of Pt(II) complex (0.2, 0.5 and 1 eq.), different Pt complex coverage of Si NPs were obtained, i.e. Si-[PtCF3]-1 (with 17 Pt complexes), Si-[Pt-CF3]-2 (with 63 Pt complexes) and Si-[PtCF3]-3 (with 5 Pt complexes). After purification by size exclusion chromatography, three Si-[PtCF3] NPs and one Si-[Pttmp] NPs of yellow solid were obtained and characterized by FT-IR and XPS.

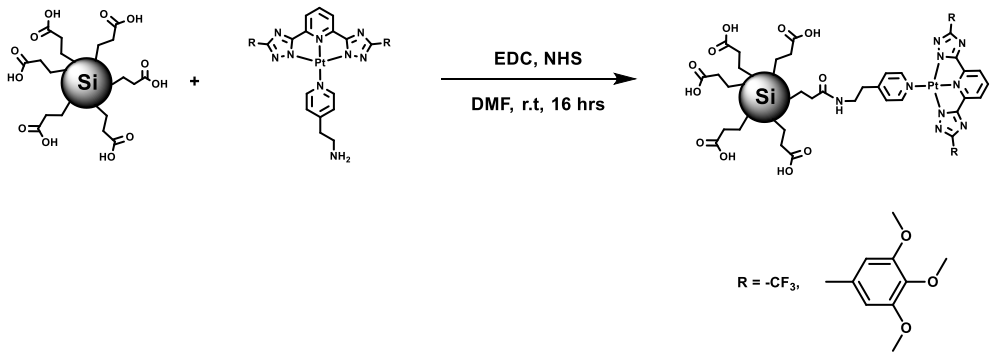

Scheme 4. Synthesis of Si-Pt nanoparticles coupled with platinum complexes

Characterization

FT-IR spectra

FT-IR measurements were performed to identify the surface functional groups and the attenuated total reflection (ATR) mode was operated for all the samples. Figure 1 presents the FT-IR spectra of Si-[PtCF3] NPs. Before coupling, PtCF3 complex shows FT-IR peak at 1629 cm^{-1} which corresponds to the N–H bending of amine. Once coupled to the NPs all the Si-[PtCF3] NPs display amide bond vibration at 1678 cm^{-1} (C=O stretch) and 1559 ~1563 cm^{-1} (N–H bending). Also the aromatic rings, C=C bond vibration, display bands at 1650 ~ 1655 cm^{-1}. The other peaks, 2940, 2873, 1463, 1374 cm^{-1}, are assigned to the vibrations of the alkyl chains. The peak at 1260 cm^{-1} is assigned to Si-C bond vibration according to literature reports.[29] We still observe the peak at 1702 ~ 1709 cm^{-1} which indicates that there are free carboxylic acid groups unreacted, after the coupling. Si-[Pttmp] NPs show the amide bond vibration at 1633 cm^{-1}, alkyl chain vibration are at 2926, 2854, 1458 and 1375 cm^{-1}. The vibration peak at 1716 cm^{-1} is the remains of carboxylic acid groups. (Figure 2)

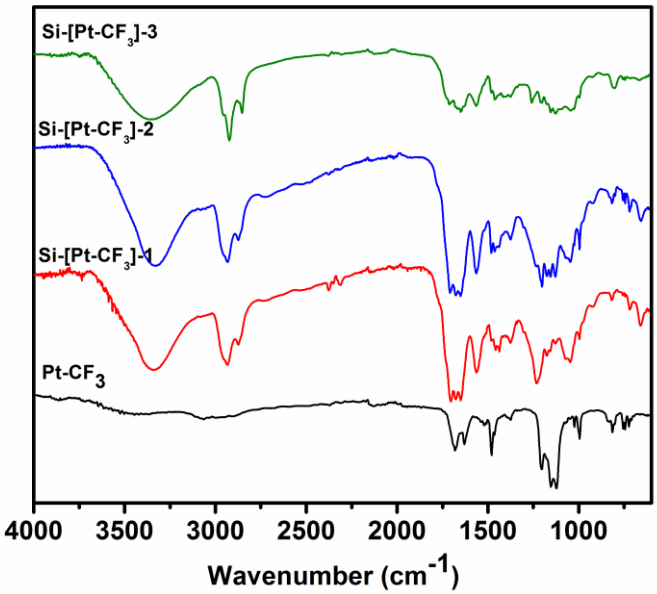

Figure 1. FT-IR spectra for Pt-CF3 complex and Si-[Pt-CF3] NPs

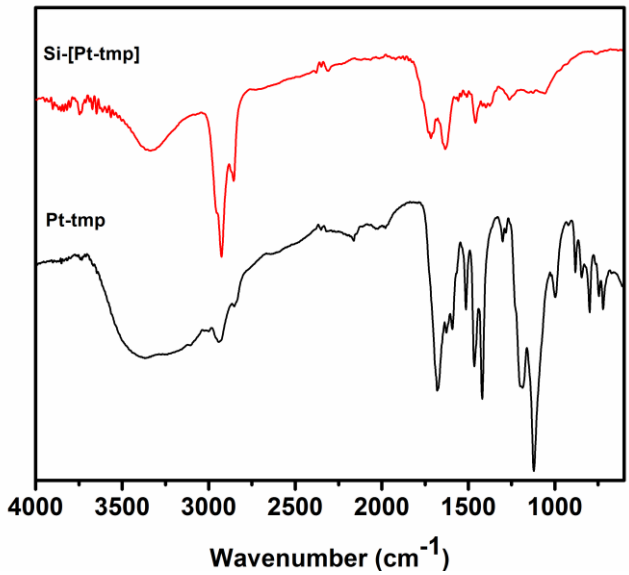

Figure 2. FT-IR spectra for Pt-tmp complex and Si-[Pt-tmp] NPs

X-ray photoelectron spectroscopy (XPS) measurement

XPS measurements were performed to acquire the chemical composition and to calculate the coverage of Pt complexes on Si NPs. The spectra were calibrated using C1s binding energy (284.80 eV) as standard. As shown in Figure 3 to 6, four nanoparticles, Si-[PtCF3]-1, Si-[PtCF3]-2, Si-[PtCF3]-3 and Si-[Pttmp], were examined and all particles consist of silicon, carbon, nitrogen, oxygen and platinum elements. The binding energy of Si2p is between 101.69 ~ 102.33 eV which corresponds to Si–C composition, and no sign of silica formation (104 eV). With increasing the equivalent of Pt complex, the Pt atom ratio increases as well. Changing from 0.2 to 1 equivalent, the Pt atom % / Si atom % ration is 0.045 for Si-[PtCF3]-1, 0.168 for Si-[PtCF3]-2 and 0.012 for Si-[PtCF3]-3. Considering that the mass of the silicon particle is 10546 Dalton from analytical ultracentrifugation (AUC) measurement (See chapter 3) and the molecule weight of silicon is 28, an estimate of 376 atoms in one single Si NPs is calculated. Combining the XPS data with these information, we can determine the amount of Pt complexes per nanoparticle, i.e. 17 Pt complexes per Si NP for Si-[PtCF3]-1, 63 Pt complexes per Si NP for Si-[PtCF3]-2 and 5 Pt complexes per Si NP for Si-[PtCF3]-3. It is quite surprising that only 5 Pt complexes per particle are calculated when applying 1 equivalent of Pt complexes. This might be due to the strong aggregation of Pt complexes in the reaction conditions, containing high concentration (2 mL solvent and 1 equivalent of Pt complex), resulting to a low coupling yield. For Si-[Pttmp] NPs, we estimated 75 Pt complexes per nanoparticles. All the XPS data are listed in Table 1 to 4.

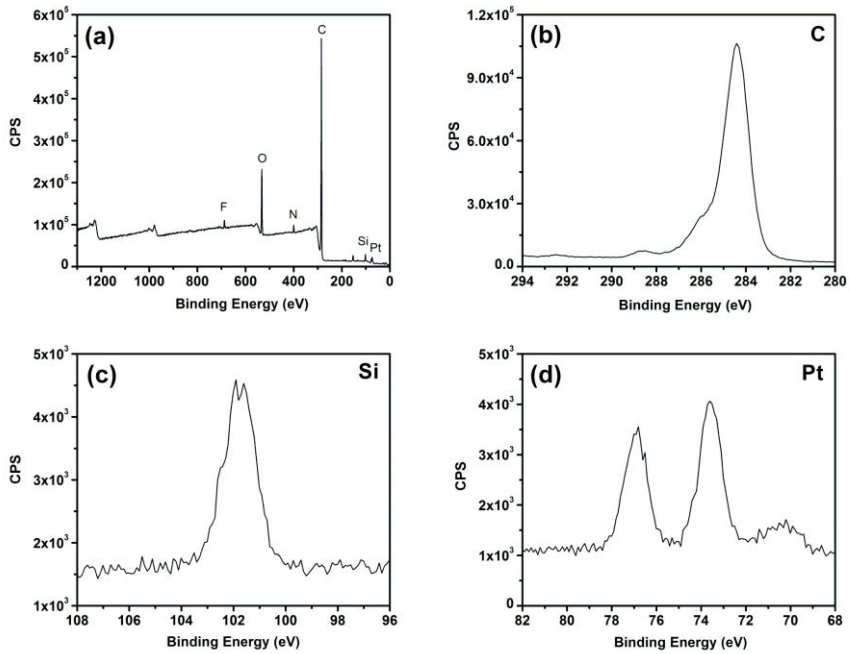

Figure 3. XPS data of Si-[Pt-CF3]-1 NPs. (a) survey scan (b) element scan of C atom (c) element scan of Si atom (d) element scan of Pt atom.

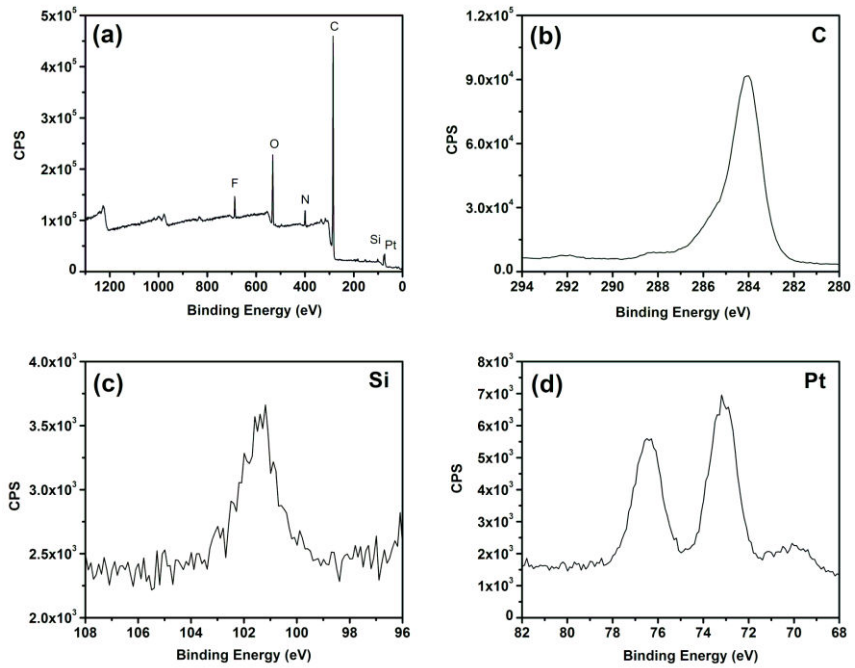

Figure 4. XPS data of Si-[Pt-CF3]-2 NPs (a) survey scan (b) element scan of C atom (c) element scan of Si atom (d) element scan of Pt atom.

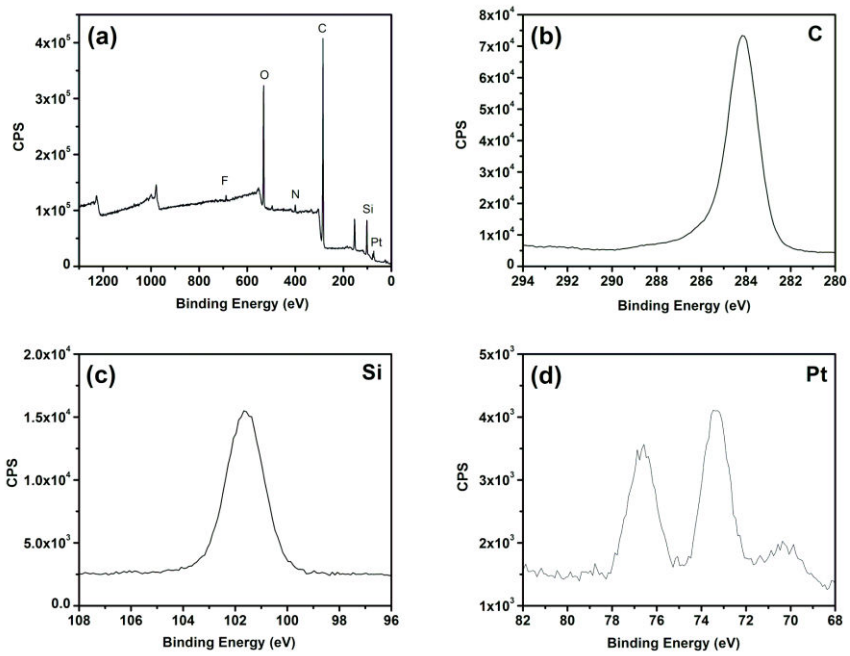

Figure 5. XPS data of Si-[Pt-CF3]-3 NPs. (a) survey scan (b) element scan of C atom (c) element scan of Si atom (d) element scan of Pt atom.

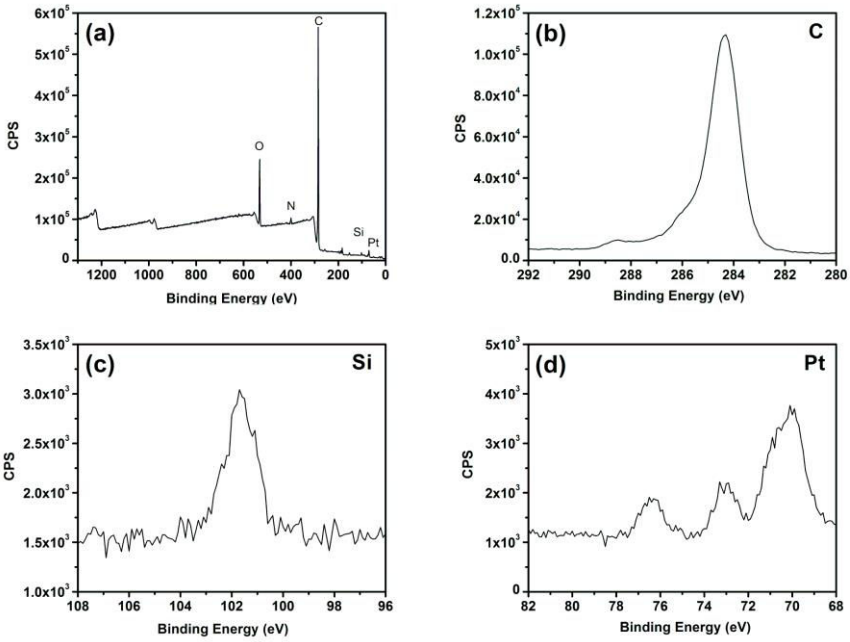

Figure 6. XPS data of Si-[Pt-tmp] NPs. (a) survey scan (b) element scan of C atom (c) element scan of Si atom (d) element scan of Pt atom.

Table 1. XPS data for Si-[Pt-CF3]-1 NPs

Name	Peak, eV	FWHM, eV	Area (P) CPS.eV	Atomic ratio, %
C1s	284.80	2.68	1330396	81.35
O1s	532.57	2.97	470729.4	11.92
N1s	399.85	2.91	60975.86	2.40
Si2p	101.90	2.61	51415.2	3.13
F1s	688.13	1.62	52177.68	1.06
Pt4f	73.92	2.62	43092.24	0.14

Table 2. XPS data for Si-[Pt-CF3]-2 NPs

Name	Peak, eV	FWHM, eV	Area (P) CPS.eV	Atomic ratio, %
C1s	284.80	2.80	1277150	79.91
O1s	532.12	3.21	449146.4	11.63
N1s	399.38	1.97	108361	4.37
F1s	687.73	2.49	99697.2	2.06
Si2p	101.69	3.18	27833.49	1.73
Pt4f	74.12	3.41	88400.78	0.29

Table 3. XPS data for Si-[Pt-CF3]-3 NPs

Name	Peak, eV	FWHM, eV	Area (P) CPS.eV	Atomic ratio, %
C1s	284.80	2.82	1052819.75	66.84
O1s	531.99	1.83	653612.33	17.17
N1s	399.97	3.30	56109.10	2.30
F1s	688.40	2.95	44762.48	0.94
Si2p	102.33	1.76	199308.88	12.60
Pt4f	73.80	2.19	44759.36	0.15

Table 4. XPS data for Si-[Pt-tmp] NPs

Name	Peak, eV	FWHM, eV	Area (P) CPS.eV	Atomic ratio, %
C1s	285.08	2.69	1409191	84.07
O1s	532.44	1.88	506186.7	12.29
N1s	400.31	3.91	61688.72	2.21
Si2p	102.19	2.47	18330.75	1.20
Pt4f	70.94	3.26	70616.24	0.24

5.3 Photophysical properties

UV-Vis absorption and emission properties of Pt(II) complexes

In Figure 7a, are shown the UV-Vis absorption spectra, measured in MeOH at 10^{-5} M. Pt-CF_3 complex exhibits ligand ππ* band at 252 and 298 nm ($\varepsilon = 1.8 \times 10^4$ and 1.1×10^4 $cm^{-1}M^1$) and broad bands in the region 350–450 nm ($\varepsilon = 0.5 \times 10^3$ $cm^{-1}M^{-1}$) which are attributed to the metal-to-ligand charge transfer (^{1,3}MLCT) transitions. Pt-tmp complex exhibits an intense band at 282 nm ($\varepsilon = 1.6 \times 10^4$ $cm^{-1}M^{-1}$) which is assigned to the ligand centered transition of the terdentate chelate and broad bands in the region 385–500 nm ($\varepsilon = 0.9 \times 10^3$ $cm^{-1}M^{-1}$) which are attributed to the ^{1,3}MLCT transitions. The emission spectra were record in aerated MeOH at 10^{-5} M. Figure 7b depicts the luminescence of Pt-CF3 complex. It shows a structured emission at λ_{em} = 461, 491 and 525 nm with multiexponential excited stated lifetime, 0.90 (85%), 3.6 (12%) and 13.8 (3%) ns. This vibronic emission structure reveals that the luminescence is dominated by a ligand charge transfer (^{3}LC) character. For Pt-tmp complex, the emission spectrum displays Gaussian distribution with λ_{em} centered at 545 nm, and longer excited state lifetimes which decay with multiexponential kinetics: 95.6 (56%), 11.7 (28%), 310.7 (16%) ns, indicating an aggregation formation. The solid state emission of these two Pt(II) complexes is centered at 570 nm for Pt-CF_3 and 592 nm for Pt-tmp, respectively. The emission in the solid is attributed to aggregates formation. Excited state lifetime in the solid state for Pt-CF_3 complex show a multiexponential decay with lifetimes of 0.42 (48.8%), 0.12 (27.5%), 0.88 (23.7%) μs, while for Pt-tmp complex are 0.83 (44.6%), 0.18 (35.7%), 2.37 (19.7%) μs. Solid state emission quantum yield were measured using an integrating sphere and are 30% for Pt-CF_3 and 6% for Pt-tmp, respectively. The photophysical data is presented in Table 5 and 6.

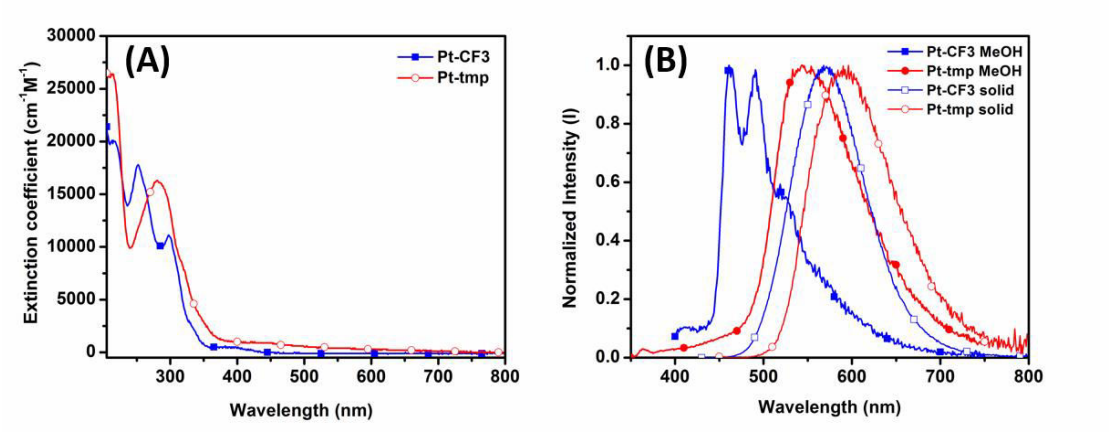

Figure 7. (A) UV-Vis absorption spectra for Pt-CF3 and Pt-tmp complexes in MeOH at a concentration of 10^{-5}M. (B) Emission spectra for Pt-CF3 and Pt-tmp complexes in MeOH (10^{-5}M) and solid state. λ_{ex} = 325 nm in MeOH and λ_{ex} = 400 nm in solid state.

UV-Vis absorption and emission properties of Si-[Pt] NPs

After characterizing the complexes the Si-[Pt] NPs were investigated and the main photophysical measurements and shown in Figure 8 and 9. Both Pt@nanoparticle systems, Si-[PtCF3] and Si-[Pttmp], are dispersed in MeOH solution in a concentration of 0.05 mg/mL. The UV-Vis absorption spectra, Figure 8a and 9a, suggest that the absorption of Si-[PtCF3] and Si-[Pttmp] NPs are similar to the sum of the individual components: Si NPs and Pt complexes. The absorption of Si-[Pttmp] NPs shows a hypsochromic shift compared to Pt-tmp complex alone, which could indicate that the degree of aggregation of the platinum units is less on the NPs than when the complex alone in solution. Both emission spectra in MeOH solution, Figure 8b and 9b, show broad luminescence from 350 to 750 nm which is mixing Si NPs and Pt complexes. The solid state emission of these two Si-[Pt] NPs is centered at 575 nm for Si-[PtCF3] NPs and 550 nm for Si-[Pttmp] NPs, respectively. The emission is strongly red shifted compared to the solution experiments and it is attributed to the ^{3}MMLCT of Pt complexes. The luminescence has an emission quantum yield of 28% for Si-[PtCF3] and 5% for Si-[Pttmp], respectively. Due to the strongly enhanced emission, we observe only a very weak luminescence of Si NPs in the 400 – 500 nm region. Excited state lifetime in the solid state for Si-[PtCF3] NPs show a multiexponential decay with lifetimes of 114 (43.3%), 14 (33.7%), 343 (23.0%) ns, while for Si-[Pttmp] NPs τ are 192 (72.2%), 1395 (27.8%) ns. The photophysical data are presented in Table 5 and 6.

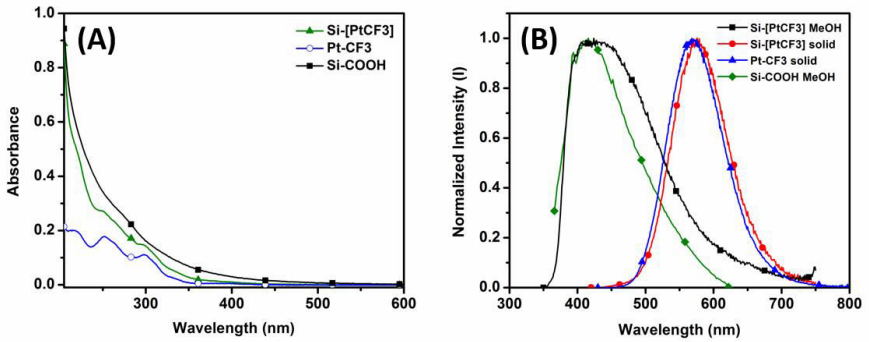

Figure 8. (A) UV-Vis absorption spectra for Pt-CF3 complex (10^{-5}M), Si-[PtCF3] and Si-COOH NPs (0.05mg/mL) in MeOH. (B) Emission spectra for Si-[PtCF3] in MeOH and solid state, and for comparison the Pt-CF3 in solid state is also depicted.

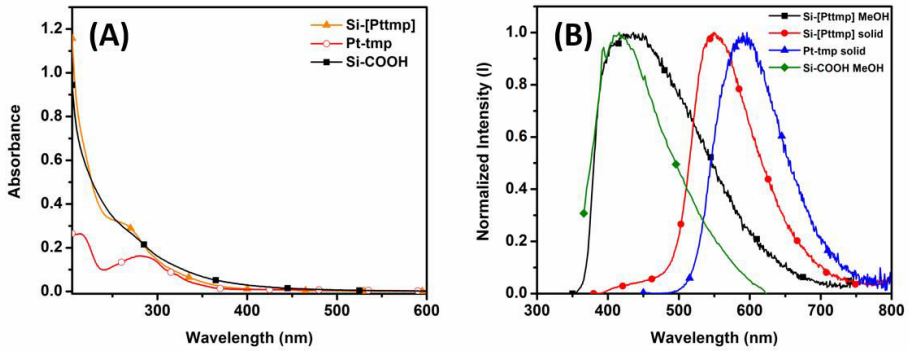

Figure 9. (A) UV-Vis absorption spectra for Pt-tmp complex (10^{-5}M), Si-[Pttmp] and Si-COOH NPs (0.05mg/mL) in MeOH. (B) Emission spectra for Si-[Pttmp] in MeOH and solid state, and for comparison Pt-tmp in solid state.

Table 5. Photophysical data for Pt complexes and Si-[Pt] NPs in MeOH solution

	Absorption[a]	Emission, MeOH, 298K[a]		
	λmax, nm	λmax[b], nm	τ[c], ns	ϕ[d]
Pt-CF3	252, 298	461, 491,525	0.90 (84.6%), 3.64 (12.8%) 13.76 (2.6%)	< 0.01
Pt-tmp	282	545	95.60 (55.9%), 11.71 (27.8%) 310.72 (16.3%)	< 0.01
Si-[PtCF3]	250, 298	425	1.16 (47.3%), 4.28 (45.6%) 11.50 (7.1%)	0.03
Si-[Pttmp]	262	430	1.31 (48.4%), 4.26 (45.0%) 11.83 (6.6%)	0.03

[a] UV-Vis and PL measurements were performed in aerated MeOH solution. [b] λex = 325 nm. [c] λex = 375 nm. [d] Quantum yield was measured by integrating sphere.

Table 6. Photophysical data for Pt complexes and Si-[Pt] NPs in solid state

	Emission, solid state, 298K[a]		
	λmax[a], nm	τ[a], ns	ϕ[b]
Pt-CF3	570	421.55 (48.8%) 120.76 (27.5%) 877.90 (23.7%)	0.30
Pt-tmp	592	832.10 (44.6%) 182.80 (35.7%) 2372.6 (19.7%)	0.06
Si-[PtCF3]	575	114.05 (43.3%) 14.04 (33.7%) 343.62 (23.0%)	0.28
Si-[Pttmp]	550	192.70 (72.2%) 1395 (27.8%)	0.05

[a]λ_{ex} = 400 nm for Pt complexes and λ_{ex} = 325 nm for Si-[Pt] NPs. [b]Emission quantum yields were measured using an integrating sphere.

Aggregation induced emission effect (AIE effect)

These nanoparticles show intense yellow emission in solid state but weakly emission in MeOH solution. From this observation, we expect these particles to display aggregation induced emission (AIE) behavior. To investigate the AIE effect, 2 mg of Si-[PtCF3]-2 or Si-[Pttmp] were dispersed in MeOH and up to 2 mL water were added as poor solvent. Different amount of water fraction (f_{water} = 0–90%) were used in order to keep the final concentration constant at 0.5 mg/mL. For Si-[PtCF3] NPs, Figure 10, the emission intensity increases and the emission maximum wavelength shifts to yellow with increasing f_{water}. At MeOH/H_2O = 50/50 ratio we observe an interesting white emission. The maximum emission intensity is observed with f_{water} = 90%. The enhanced emission is due to the stacking of the Pt(II) complexes due to interparticles aggregation, causing the formation a new excited states and protection towards dioxygen quenching.. Indeed due to the assembly process the Pt–Pt interactions can become very strong, and the new metal-metal-to-ligand charge transfer (MMLCT) states, are formed. The emission is bathochromic shift to 580 nm and the emission intensity is strongly enhanced. In order to check the morphology of these particles, SEM images were taken and are shown in Figure 11. With 100% of MeOH, the Si-[PtCF3] NPs show a covered organic layer without specific structure. Increasing the water fraction to 50%, the small nanoparticles tend to aggregate to form 150 nm nanoparticles. In 90% water fraction sample, those big nanoparticles aggregate (~120 nm) to form amorphous structure. In the case of Si-[Pttmp] NPs, the emission spectrum changes just slightly adding water

to the methanol solution. In Figure 12, are shown the changes upon increasing the f_{water}, and a small shoulder at lower energy appears. Such behavior is not surprising since the Pt complex with trimethoxyphenyl groups shows a much higher steric hindrance and therefore is less prone to aggregate. SEM images show an amorphous layer without any structure in all f_{water} of samples.

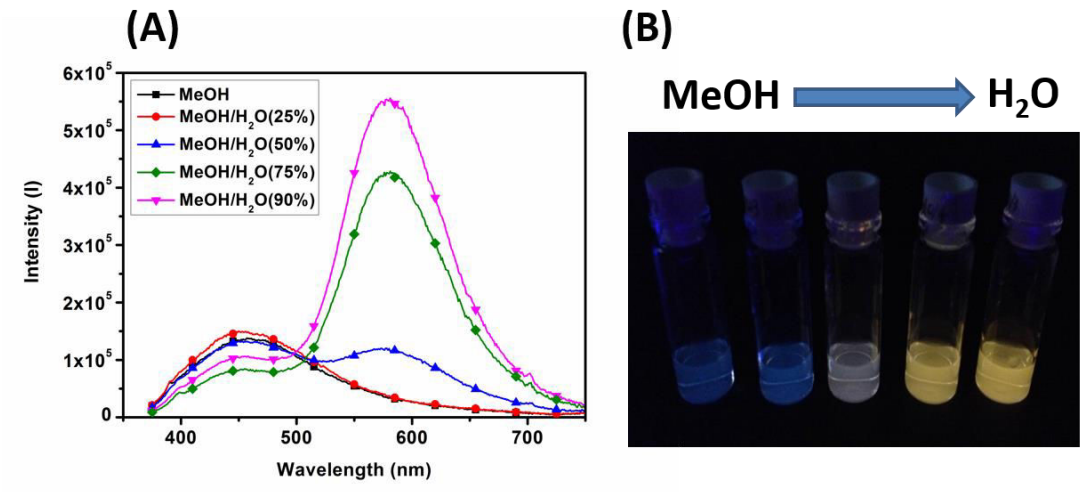

Figure 10. (A) Emission spectra of Si-[PtCF3]-2 NPs in MeOH/water mixed solvent with different fraction of water with excitation at 340 nm. (B) Samples with different amount of water fraction under UV lamp.

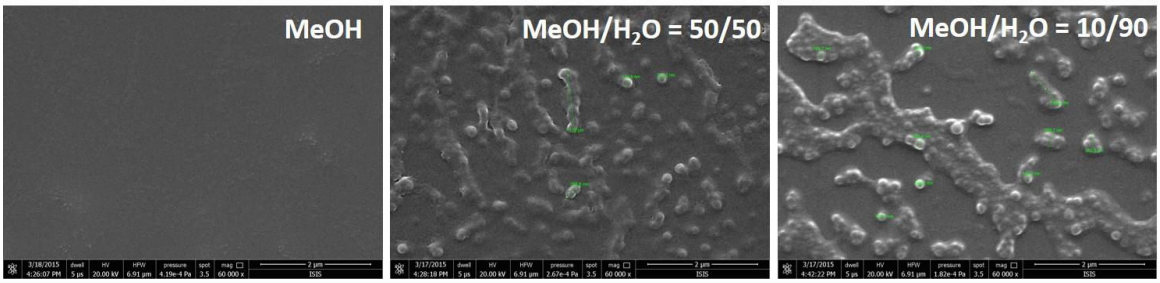

Figure 11. SEM imaging of Si-[Pt-CF3] NPs in different solvent pair. Scale bar: 2 μm.

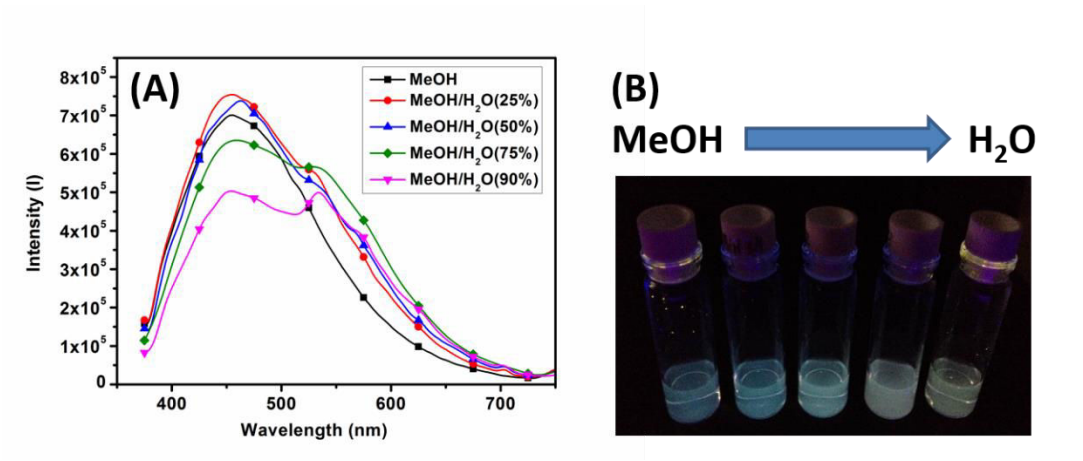

Figure 12. (A) Emission spectra of Si-[Pttmp] NPs in MeOH/water mixed solvent with different fraction of water with excitation at 340 nm. (B) Samples with different amount of water fraction under UV lamp.

5.4 *In vitro* study

Pt complexes and Si-[Pt] NPs were further investigated as a possible label for optical cellular imaging. Living HeLa cells were incubated with the Pt complexes or Si-[Pt] NPs separately in less than 1% DMSO/culture media. For the Pt complexes, 50 μM concentration was used and incubated for 30 minutes. For Si-[Pt] NPs, different concentration, 0.01, 0.05 and 0.1 mg/mL, were used and incubated for 1, 4 and 24 hours. After the incubation period, the cells were washed with PBS in order to remove excess of non-uptaken materials and finally fixed by using paraformaldehyde solution. Then fluorescence confocal microscopy experiments were carried out by exciting the sample at 405 nm, and the emission signals were collected by a detector between 412 and 600 nm.

As can be seen from Figure 13, the uptake of the Pt complexes is very rapid and it is already observed after 30 minutes incubation time. Interestingly, Pt-tmp complex is not internalized into cells, but resides on the cellular membrane, staining them (See Z-stack in Figure 14). However, after coupling the Pt complex with the nanoparticles, the Si-[Pt-tmp] NPs are taken into cells. (Figure 16) Moreover, the amounts of materials uptaken by the cells increases by the incubation time. Also the concentration of materials influence the cellular uptake, Si-[PtCF3] NPs showed increased fluorescent intensity when the material concentration increases from 0.01 to 0.1 mg/mL. (Figure 15)

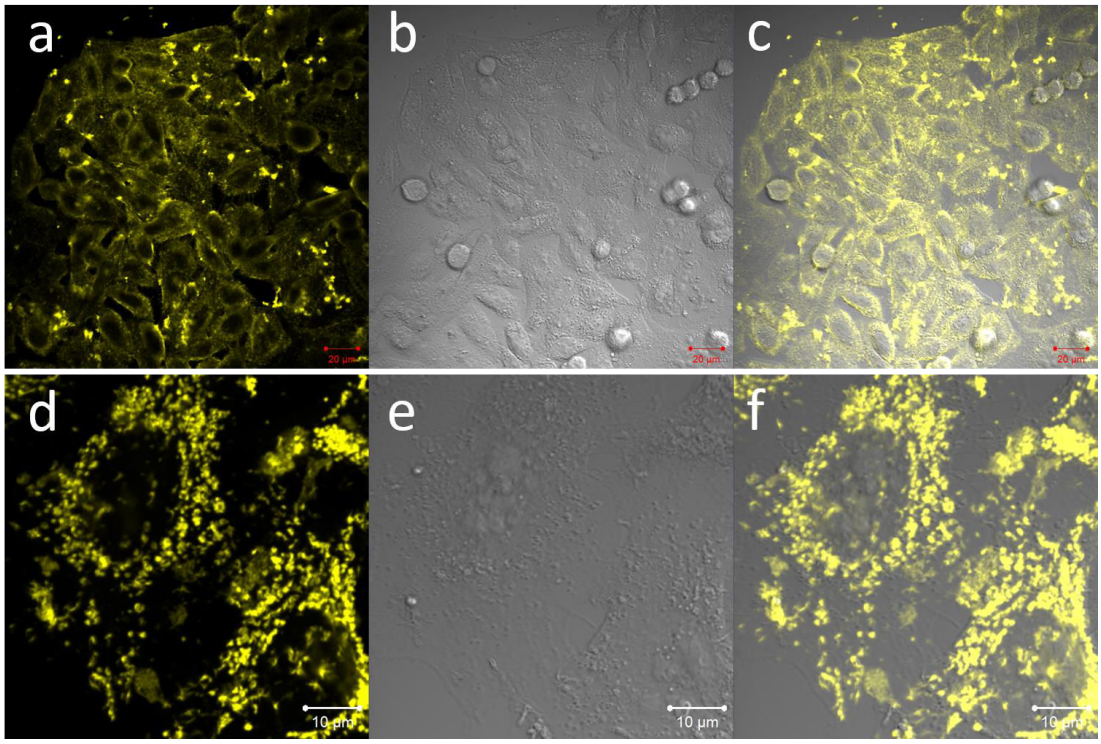

Figure 13. Confocal images of 50 µM Pt-tmp complex (a) – (c) and 50 µM Pt-CF3 complex (d) – (f) in HeLa cells for 30 minutes incubation time. (a) and (d) are luminescence images, (b) and (e) are transmission images, and (c) and (f) are overlay of the two images. Scale bar: (a)–(c) 20 µm, (d)–(f) 10 µm. The emissions are false colors.

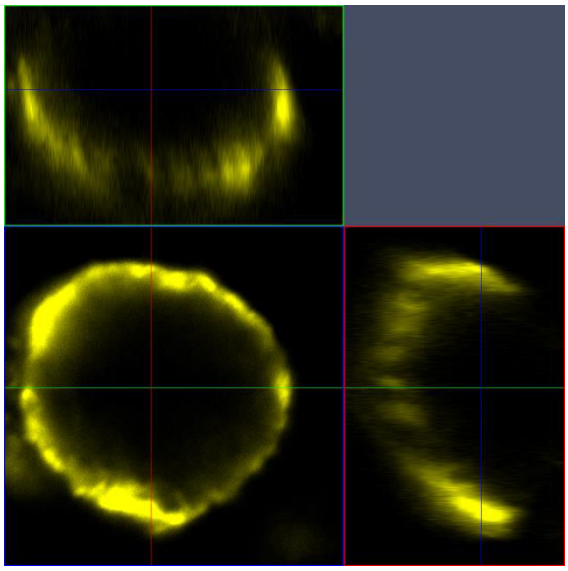

Figure 14. Confocal imaging of Pt-tmp complex in Z stack scan after 30 minutes incubation time. The emission is false color.

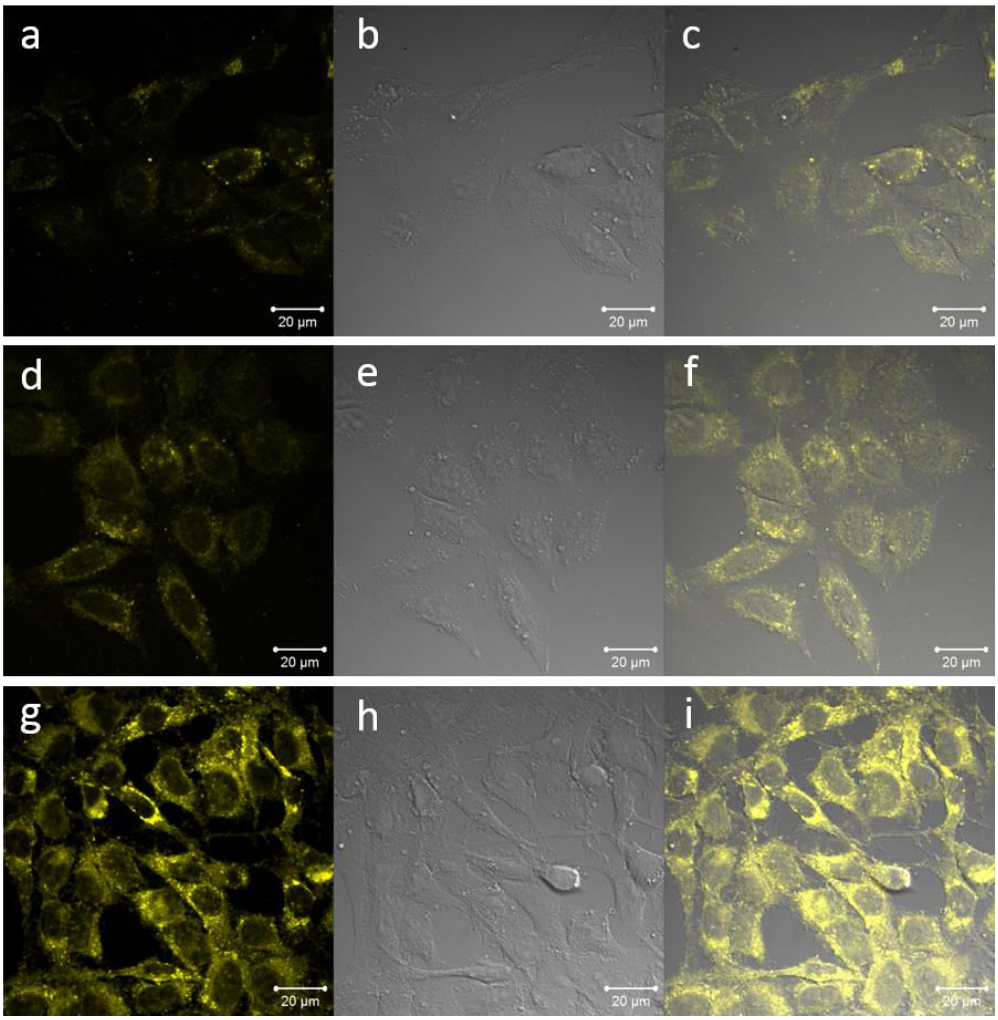

Figure 15. Confocal imaging of (a) – (c) 10 µg/ mL, (d) – (f) 50 µg/ mL, and (g) – (i) 100 µg/ mL Si-[PtCF3] NPs in HeLa cells for 24 hours incubation time. (a), (d) and (g) are luminescence images, (b), (e) and (h) are transmission images, and (c), (f) and (i) are overlay of the two images. Scale bar: 20 µm. The emissions are false colors.

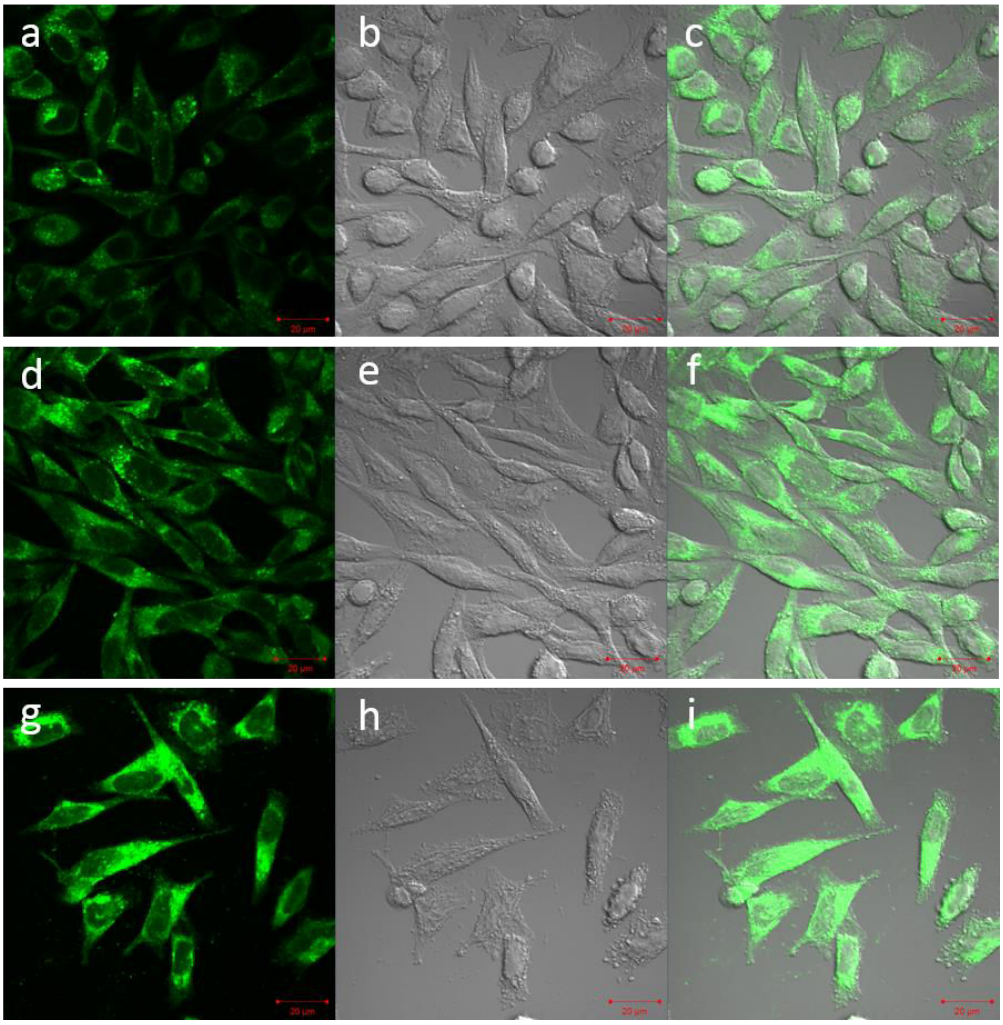

Figure 16. Confocal imaging of 100 μg/ mL Si-[Pttmp] NPs in HeLa cells for (a) – (c) 1 hour, (d) – (f) 4 hours, (g) – (i) 24 hours incubation time. (a), (d) and (g) are luminescence images, (b), (e) and (h) are transmission images, and (c), (f) and (i) are overlay of the two images. Scale bar: 20 μm. The emissions are false colors.

5.5 Conclusion

We synthesized two amino group functionalized Pt complexes, Pt-CF3 and Pt-tmp, and coupled them with Si-COOH NPs to get the hybrid nanosystems: Si-[PtCF3] and Si-[Pttmp] NPs. By controlling the equivalent of Pt complex in the reaction conditions, different amount of Pt complex loading can be achieved. These NPs were further characterized by FT-IR, XPS measurements and their photophysical properties were measured in solution and in solid state. Both Si-[Pt] NPs show greenish blue emission in MeOH solution and bathochromic shift to yellow emission in solid state which is due to the aggregation of Pt complexes, resulting in new MMLCT emission. An interesting aggregation induced emission (AIE) is also observed in this hybrid nanosystem. In the different ratio of MeOH/water solution, Si-[PtCF3] NPs display an emission shift from blue to yellow and enhance emission intensity upon increasing the water fraction in the solution. Interestingly, in the 50/50 ratio of MeOH/water solution, we observed white light emission in this system. Finally the Pt complexes and the Si-[Pt] NPs were investigated as possible luminescent labels. We performed the cellular imaging using HeLa cells. Surprisingly, the Pt-tmp complex only stained on the cell membrane, while the Si-[Pttmp] NPs were internalized into HeLa cells.

5.6 Experimental Section

General information and materials

All reagents were purchased from Sigma-Aldrich and Alfa and used without any further purification unless specified notice. Solvents were purified according to the standard procedure.[30] All air and water sensitive experiments were carried out in standard glassware under an inert nitrogen or argon atmosphere using schlenk line techniques. ^{1}H and ^{19}F NMR were acquired on a Bruker AV400 (400 MHz) at 25 °C with the deuterated solvent as the lock and residual solvent as the internal reference. Mass spectrometry measurements and element analysis measurements were performed in the Department of Chemistry, University of Strasbourg. NMR measurements were performed in Institut de Science et d'Ingénierie Supramoléculaires (ISIS), University of Strasbourg.

Photophysical measurement

Steady-state emission spectra were recorded on a HORIBA Jobin-Yvon IBH FL-322 Fluorolog 3 spectrometer equipped with a 450 W xenon arc lamp as the excitation source, double-grating excitation and emission monochromators (2.1 nm mm^{-1} of dispersion; 1200 grooves mm^{-1}), and a TBX-04 single-photon-counting device as the detector. Emission and excitation spectra were corrected for source intensity (lamp and grating) and emission spectral response (detector and grating) by standard correction curves. Time-resolved measurements were performed using the PicoHarp 300 equipped with time correlated single photon counting (TCSPC) system on the Fluoro Time 300 (PicoQuant), where a laser source 375 nm was applied to excite the samples. The laser was mounted directly on the sample chamber at 90° to a Czerny-Turner type emission monochromator (2.7 nm mm^{-1} of dispersion; 1200 grooves mm^{-1}) and collected by a PMA-C 192M single-photon- counting detector. Signals were collected using EasyTau software, and data analysis was performed using FluoFit software (PicoQuant). The quality of the fit was assessed by minimizing the reduced $\chi 2$ function and by visual inspection of the weighted residuals. Luminescence quantum yield was performed with integrating sphere (Hamamatsu, C11347-11). Anisotropy decay was measured by Fluoro Time 300 (PicoQuant) in room temperature and 0ºC with laser excited at 375 nm, and collected the data after 30 seconds. FT-IR spectra were measured in attenuated total reflectance (ATR) method with Shimadzu IRAffinity-1.

Cell experiment

HeLa cells were cultured inside media which contain 88 % Dulbecco's Modified Eagle Medium (DMEM), 10 % Fetal Bovine Serum, 1 % Penicillin-Streptomycin and 1 % L-Glutamine 200mM (all material was purchased from Gibco) under 37°C and 5% of CO_2 condition for 48 hours until reaching 70 to 80 % cell confluency. Subsequently, the cells were washed twice with Phosphate Buffer Solution (PBS, Gibco), trypsinated and approximately 50,000 cells were reseeded on the monolayer glass cover slip inside 6 well plate culture dish. New culture media (2 mL) were added gently and the cells were grown overnight.

Synthetic Procedure

<u>*Ligands*</u>

Ligand 1

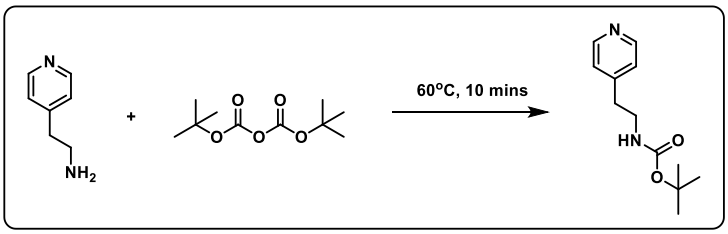

To a 25 mL flask, 4-ethylaminopyridine (2.0 g, 16.4 mmol) was added into Di-*t*-butyl dicarbonate (3.93 g, 18.0 mmol). Then the reaction was heated to 80°C for 10 minutes. After cooling down, added some DCM and the reaction was washed with DI water three times. The crude product was purified by column chromatography on silica gel (ethyl acetate) providing colorless oil (2.5 g, 68.9%).

Spectral data of **Ligand 1**: ^{1}H NMR (400 MHz, $CDCl_3$, 298K): δ 8.53 (d, J_{HH} = 5.8 Hz, 2H), 7.17 (d, J_{HH} = 5.0 Hz, 2H), 4.58 (br, 1H), 3.41 (dt, J_{HH} = 6.8, 6.8 Hz, 2H), 2.83 (d, J_{HH} = 6.7 Hz, 2H), 1.42 (s, 9H).

Pt(II) complexes

Pt-CF3-tBoc

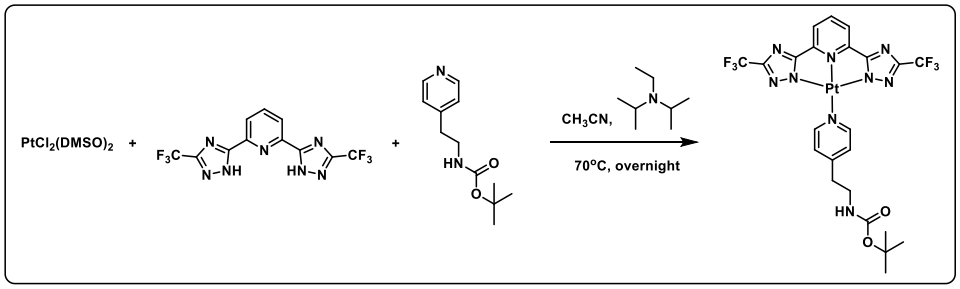

$PtCl_2(DMSO)_2$ (250 mg, 0.59 mmol), bistriazole-CF_3 (206 mg, 0.59 mmol), and 30 mL CH_3CN solvent were added into a 100 mL round bottle. Diisopropylethylamine (0.22 mL, 1.30 mmol) was added and stirred for 10 mins. Ligand 1 (144 mg, 0.65 mmol) was dissolved in 10 mL CH_3CN, and then added into above solution. The reaction was heated at 70°C for 12 hrs under nitrogen. After cooling down the reaction, washed by DI water twice, collected all the organic layer, and removed the solvent by rotavapor. The crude product was dissolved by few THF and put into 4°C refrigerator overnight. The final product was obtained by collecting the yellow precipitate (279 mg, 61.7%).

Spectral data of **Pt-CF3-tBoc** : ^{1}H NMR (400 MHz, CD_2Cl_2, 298K): δ 9.47 (d, J_{HH} = 6.6 Hz, 2H), 8.07 (t, J_{HH} = 7.9 Hz, 1H), 7.82 (d, J_{HH} = 7.9 Hz, 2H), 7.44 (d, J_{HH} = 6.8 Hz, 2H), 5.04 (br, 1H), 3.51 (dt, J_{HH} = 6.9, 6.9 Hz, 2H), 2.97 (t, J_{HH} = 6.8 Hz, 2H), 1.44 (s, 9H). ^{19}F NMR (376 MHz, CD_2Cl_2, 298K): δ -64.6 (s, 6F).

Pt-CF3

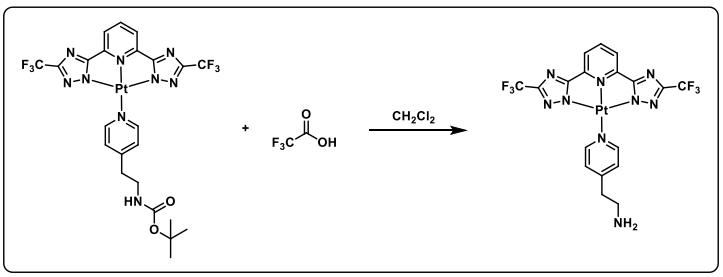

50 mg of Pt-CF_3-tBoc was dissolved into 20 mL dried CH_2Cl_2. Then 4 mL trifluoroacetic acid was added slowly at 0°C. All the reaction was monitored by TLC till no starting materials. Removed the solvent and wash with Na_2CO_3 solution to get yellow powder.

Spectral data of **Pt-CF3** : ^{1}H NMR (400 MHz, CD_2Cl_2, 298K): δ 9.19 (d, J_{HH} = 6.9 Hz, 2H), 8.31 (t, J_{HH} = 8.0 Hz, 1H), 7.98 (d, J_{HH} = 7.8 Hz, 2H), 7.72 (d, J_{HH} = 6.3 Hz, 2H), 3.04 – 2.96 (m, 2H), 2.89 (t, J_{HH} = 6.0 Hz, 2H). ^{19}F NMR (376 MHz, CD_2Cl_2,

298K): δ -64.3 (s, 6F). MS(ESI+) calcd for $C_{18}H_{14}N_9F_6Pt$ 665.09 ($[M+H]^+$); found 665.09.

Pt-tmp-tBoc

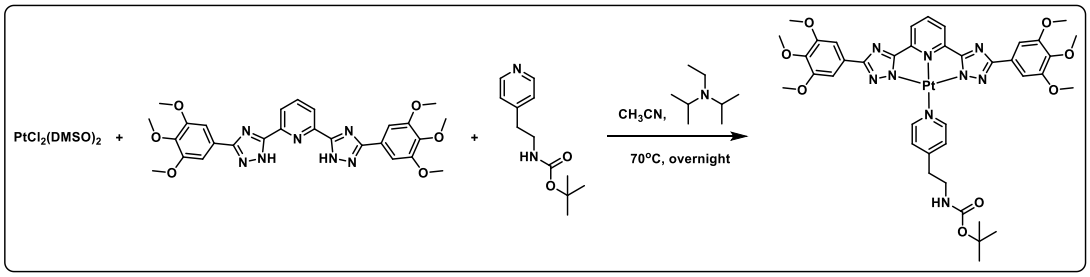

$PtCl_2(DMSO)_2$ (155 mg, 0.37 mmol), bistriazole-trimethoxy (200 mg, 0.37 mmol), and 30 mL CH_3CN solvent were added into a 100 mL round bottle. Diisopropylethylamine (0.13 mL, 0.81 mmol) was added and stirred for 10 mins. Ligand 1 (95 mg, 0.40 mmol) was dissolved in 10 mL CH_3CN, and then added into above solution. The reaction was heated at 70°C for 12 hrs under nitrogen. After cooling down the reaction, washed by DI water twice, collected all the organic layer, and removed the solvent by rotavapor. The crude product was purified by column chromatography on silica gel (CH_2Cl_2 : MeOH = 10 : 1) to get yellow powder.

Spectral data of **Pt-tmp-tBoc** : ^{1}H NMR (400 MHz, CD_2Cl_2, 298K): δ 9.91 (d, J_{HH} = 5.1 Hz, 2H), 7.78 (t, J_{HH} = 7.6 Hz, 1H), 7.55 (d, J_{HH} = 7.7 Hz, 2H), 7.42 (s, 4H), 7.24 (d, J_{HH} = 5.1 Hz, 2H), 3.98 (s, 12H), 3.87 (s, 6H), 3.41 (dt, J_{HH} = 6.2 Hz, 2H), 2.82 (d, J_{HH} = 6.2 Hz, 2H), 1.46 (s, 9H).

Pt-tmp

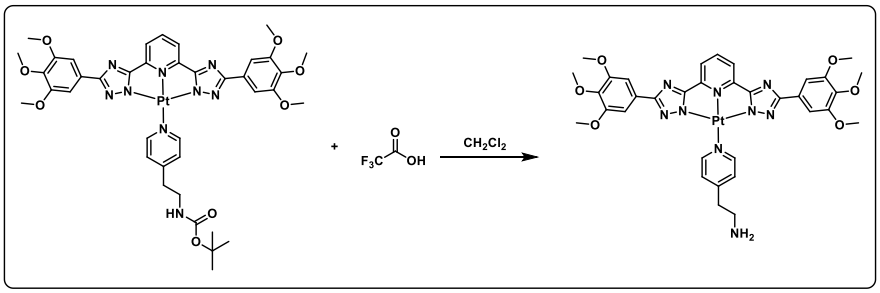

50 mg of Pt-trimethoxy-tBoc was dissolved into 20 mL dried CH_2Cl_2. Then 4 mL trifluoroacetic acid was added slowly at 0°C. All the reaction was monitored by TLC till no starting materials. Removed the solvent and wash with Na_2CO_3 solution to get yellow powder.

Spectral data of **Pt-tmp**: ^{1}H NMR (400 MHz, CD_2Cl_2, 298K): δ 9.38 (d, J_{HH} = 5.1 Hz,

2H), 7.24 (t, J_{HH} = 7.6 Hz, 1H), 7.15 – 6.90 (m, 8H), 3.85 (s, 12H), 3.83 (s, 6H), 2.95 (t, J_{HH} = 7.6 Hz, 2H), 2.52 (d, J_{HH} = 8.0 Hz, 2H). MS(ESI+) calcd for $C_{34}H_{36}N_9O_6Pt$ 861.24 ($[M+H]^+$); found 861.24.

Si-[Pt] nanoparticles

Si-[Pt-CF3] nanoparticles

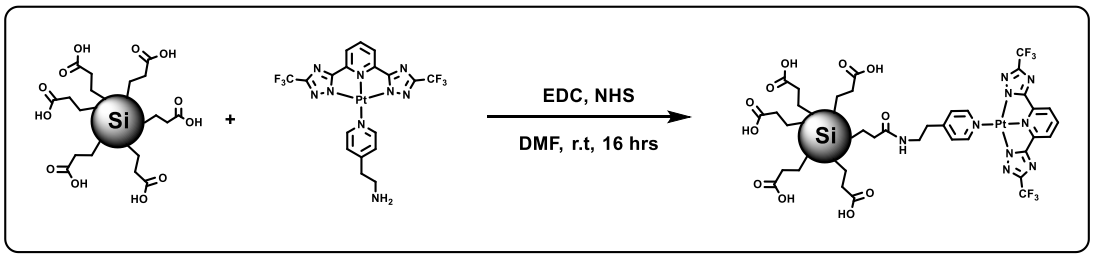

Carboxylic acid terminated Si NPs (13 mg), EDC (5.83 mg, 30.4 μmol), and NHS (4.66 mg, 30.4 μmol) were dissolved into 2 mL dried DMF. Pt((II) complexes (4.03 mg, 15.2 μmol or 2.02 mg, 7.6 μmol) and Et_3N (10 μL, 71.7 μmol) were added and stirred at room temperature for 16 hours at Ar atmosphere. After reaction, DMF was removed by vacuum and purified by size exclusion chromatography (LH-20) to get yellow solid.

Si-[Pt-tmp] nanoparticles

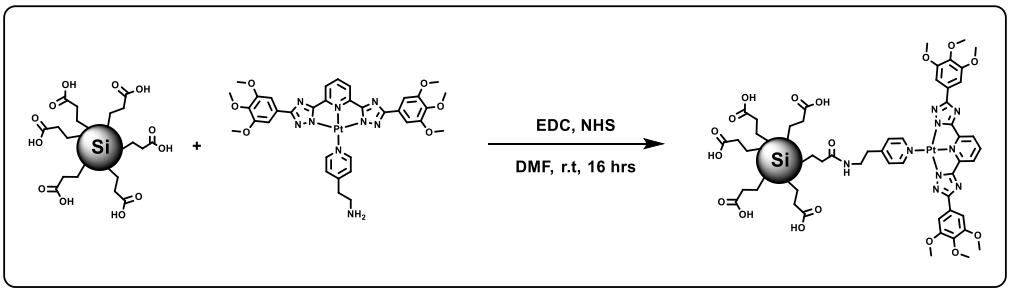

Carboxylic acid terminated Si NPs (13 mg), EDC (5.83 mg, 30.4 μmol), and HOBt (4.66 mg, 30.4 μmol) were dissolved into 2 mL dried DMF. Pt(II) complexes (4.03 mg, 15.2 μmol or 2.02 mg, 7.6 μmol) and Et_3N (10 μL, 71.7 μmol) were added and stirred at room temperature for 16 hours at Ar atmosphere. After reaction, DMF was removed by vacuum and purified by size exclusion chromatography (LH-20) to get yellow solid.

5.7 Reference

1. A. Tsuboyama, H. Iwawaki, M. Furugori, T. Mukaide, J. Kamatani, S. Igawa, T. Moriyama, S. Miura, T. Takiguchi, S. Okada, M. Hoshino and K. Ueno, *J. Am. Chem. Soc.*, 2003, **125**, 12971-12979.
2. H. Xiang, J. Cheng, X. Ma, X. Zhou and J. J. Chruma, *Chem. Soc. Rev.*, 2013, **42**, 6128-6185.
3. Q. Zhao, C. Huang and F. Li, *Chem. Soc. Rev.*, 2011, **40**, 2508-2524.
4. M. Mauro, A. Aliprandi, D. Septiadi, N. S. Kehr and L. De Cola, *Chem. Soc. Rev.*, 2014, **43**, 4144-4166.
5. V. H. Houlding and V. M. Miskowski, *Coord. Chem. Rev.*, 1991, **111**, 145-152.
6. I. Fratoddi, C. Battocchio, A. Furlani, P. Mataloni, G. Polzonetti and M. V. Russo, *J. Organomet. Chem.*, 2003, **674**, 10-23.
7. M. Mauro, A. Aliprandi, C. Cebrian, D. Wang, C. Kubel and L. De Cola, *Chem. Commun.*, 2014, **50**, 7269-7272.
8. S. Lippard, *Science*, 1982, **218**, 1075-1082.
9. K. Krogmann, *Angewandte Chemie International Edition in English*, 1969, **8**, 35-42.
10. R. Palmans, D. B. MacQueen, C. G. Pierpont and A. J. Frank, *J. Am. Chem. Soc.*, 1996, **118**, 12647-12653.
11. L. Murphy, P. Brulatti, V. Fattori, M. Cocchi and J. A. G. Williams, *Chem. Commun.*, 2012, **48**, 5817-5819.
12. W. Lu, Y. Chen, V. A. L. Roy, S. S.-Y. Chui and C.-M. Che, *Angew. Chem.*, 2009, **121**, 7757-7761.
13. C. A. Strassert, C.-H. Chien, M. D. Galvez Lopez, D. Kourkoulos, D. Hertel, K. Meerholz and L. De Cola, *Angew. Chem. Int. Ed.*, 2011, **50**, 946-950.
14. D. Septiadi, A. Aliprandi, M. Mauro and L. De Cola, *RSC Advances*, 2014, **4**, 25709-25718.
15. T. Zou, C.-N. Lok, Y. M. E. Fung and C.-M. Che, *Chem. Commun.*, 2013, **49**, 5423-5425.
16. S. Liu, H. Sun, Y. Ma, S. Ye, X. Liu, X. Zhou, X. Mou, L. Wang, Q. Zhao and W. Huang, *J. Mater. Chem.*, 2012, **22**, 22167-22173.
17. B. ZhongáTang and P. P. Lee, *J. Mater. Chem.*, 2001, **11**, 2974-2978.
18. J. Luo, Z. Xie, J. W. Lam, L. Cheng, H. Chen, C. Qiu, H. S. Kwok, X. Zhan, Y. Liu and D. Zhu, *Chem. Commun.*, 2001, 1740-1741.
19. S. Chen, Y. Hong, Y. Liu, J. Liu, C. W. Leung, M. Li, R. T. Kwok, E. Zhao, J. W. Lam and Y. Yu, *J. Am. Chem. Soc.*, 2013, **135**, 4926-4929.
20. Y. Hong, J. W. Lam and B. Z. Tang, *Chem. Soc. Rev.*, 2011, **40**, 5361-5388.
21. M.-X. Zhu, W. Lu, N. Zhu and C.-M. Che, *Chemistry – A European Journal*,

2008, **14**, 9736-9746.
22. N. Komiya, T. Muraoka, M. Iida, M. Miyanaga, K. Takahashi and T. Naota, *J. Am. Chem. Soc.*, 2011, **133**, 16054-16061.
23. K. M.-C. Wong and V. W.-W. Yam, *Acc. Chem. Res.*, 2011, **44**, 424-434.
24. H. Honda, Y. Ogawa, J. Kuwabara and T. Kanbara, *Eur. J. Inorg. Chem.*, 2014, **2014**, 1865-1869.
25. Q. Zhao, L. Li, F. Li, M. Yu, Z. Liu, T. Yi and C. Huang, *Chem. Commun.*, 2008, 685-687.
26. P. Alam, M. Karanam, A. R. Choudhury and I. R. Laskar, *Dalton Transactions*, 2012, **41**, 9276-9279.
27. N. Komiya, M. Okada, K. Fukumoto, D. Jomori and T. Naota, *J. Am. Chem. Soc.*, 2011, **133**, 6493-6496.
28. R. Melanson and F. D. Rochon, *Can. J. Chem.*, 1975, **53**, 2371-2374.
29. J. H. Warner, A. Hoshino, K. Yamamoto and R. D. Tilley, *Angew. Chem. Int. Ed.*, 2005, **117**, 4626-4630.
30. W. L. F. Armarego and C. L. L. Chai, *Purification of laboratory chemicals*, 5th edn., Butterworth-Heinemann, Amsterdam, 2003.

CHAPTER 6

Nanoparticle-Metal Complex Hybrid Nanosystems for ECL Applications

Abstract

Using electroluminescence (ECL) to light up luminophores is a very attractivestrategy for bioapplications. Many research works are focused in $[Ru(bpy)_3]^{2+}$derivatives, while hybrid nanoparticle systems are rarely reported. We have developed metal complex coated carbon dots and silicon nanoparticles for ECL applications. Due to the ultrasmall size and electrochemical properties of such nanoparticles, we expect these nano-systems to assist in the ECL process and increase the performance.

6.1 Introduction

Electrochemiluminescence (ECL) is the most sensitive assay utilized for the detection of many biomolecules at the subpicomolar concentration. The sensitivity of ECL is mostly related to the lack of photo excitation to create the excited state of the labeled analyte and lower background noise, due to the selective excitation of the labels.[1, 2] ECL requires the use of a luminophore, being $[Ru(bpy)_3]^{2+}$ derivatives the standard used up to now. However, other metal complexes based on Ru and Ir have shown higher efficiency in ECL than the standard luminophores.[3-5] Recently, metal complexes encapsulated in silica nanoparticles have shown ECL.[6, 7] Interestingly, the silica shell shields the water-insoluble metal complex from the water solution and are able to apply in the biological system. However, the weak emission of these encapsulated complexes compared to the simple labels normally used and the large size of the silica particles (~50 nm) are the drawbacks in this system. Li *et al.* proposed a way to solve the problem of low ECL efficiency by using magnetic nanoparticles.[8] By modifying the gold electrode with a magnet, the magnetic nanoparticles are attractively attached on the electrode surface and exhibit high ECL efficiency. In our idea, an attractive strategy to solve these problems and increase ECL efficiency is to use ultrasmall nanomaterials, such as carbon dots or silicon nanoparticles, which present very interesting electronic properties.[9-12]

Luminescent carbon dots (CDs) were discovered accidently by Xu *et al.* in 2004.[13] During the purification of single-walled carbon nanotubes (SWNTs) by gel electrophoresis, they found one of the separated materials exhibited very bright emission under UV light irradiation. Following the discovery of luminescent properties, many researchers have devoted to develop new synthetic routes and to understand the origin of the photophysical behaviors.[14-17] (Figure 1) In their studies, the evidences from HR-TEM, ^{13}C NMR and Raman spectroscopy reveal the CDs are sp^2 graphite structure,[18-20] and the PL emission shows strong excitation wavelength dependent which may due to a distribution of different emission states and surface functional groups.[14, 21] In addition, the environment friendly, low cytotoxicity, facility to surface modification and water solubility, the CDs are considered as imaging tools for *in vitro* and *in vivo* studies. [22-25] Besides, the electroluminescent properties also make them apply in a new type of light emitting diodes (LED).[26, 27]

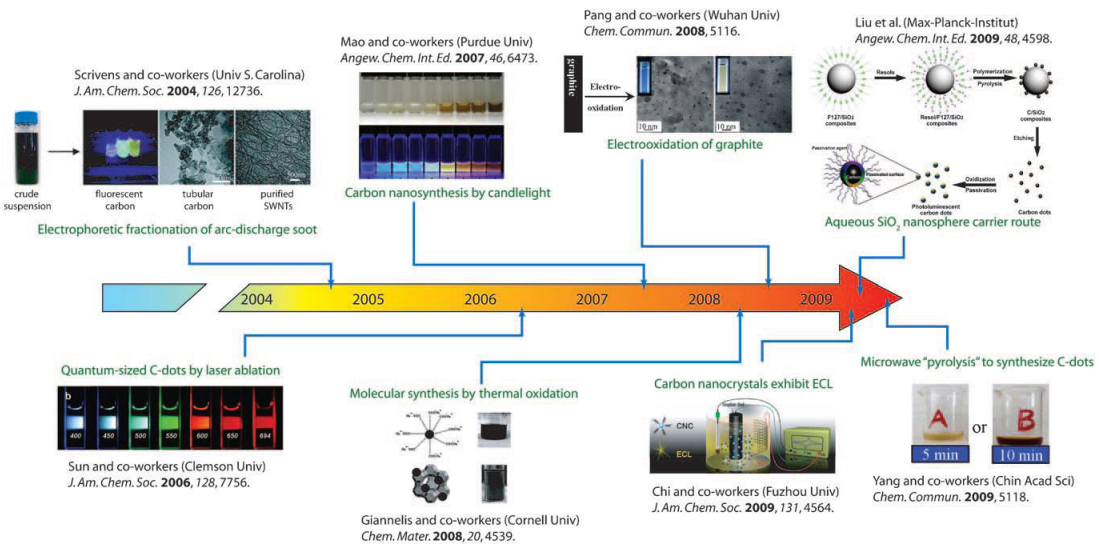

Figure 1. Recent progress in carbon dots. Reproduced from *Angew. Chem. Int. Ed.* **2010**, *49*, 6726 – 6744 with permission from Wiley-VCH.

Lately CDs have been introduced as luminophores for ECL applications.[28] Ultrasmall carbon quantum dots of approximately 3–4 nm in diameter exhibited strong ECL activity using co-reactant $K_2S_2O_8$. Other authors like Long *et al*. have shown that benzyl alcohol modified CDs can activate the ECL reaction acting as a co-reactant.[29] They proposed a mechanism in which benzyl alcohol can be converted to the reductive radical species $[C_6H_5CHOH]^{\bullet}$ through one electron abstraction by $[Ru(bpy)_3]^{3+}$, further oxidating to form benzaldehyde, C_6H_5CHO.

Here we show novel systems composed of carbon dots and silicon nanoparticles coated with iridium and ruthenium complexes. In this nano-system, combining the water solubility and good electronic properties of ultrasmall nanoparticles, we investigate the ECL performance and influence of ECL when nanoparticles are presented in the system.

6.2 Ruthenium complexes- Carbon dots nanosystems

6.2.1 Synthesis

Carbon dots (CDs) were provided by the group of Prof. Michele Maggini from Padova University. They are functionalized with both amino and carboxylate groups on the surface making them water soluble and facilitating their further functionalization. C-[Ru] NPs (Scheme 1) were synthesized by reacting amino-functionalized CDs and a NHS (N-hydroxysulfosuccinimide) activated Rubpy complex in phosphate-buffered saline, PBS, (pH = 7.4) at room temperature. for 12 hours. The reaction crude was washed with dichloromethane (CH_2Cl_2) to remove uncoupled Ru complexes. A red powder was obtained after size exclusion chromatography (LH-20). The detail is written in experimental section (6.5)

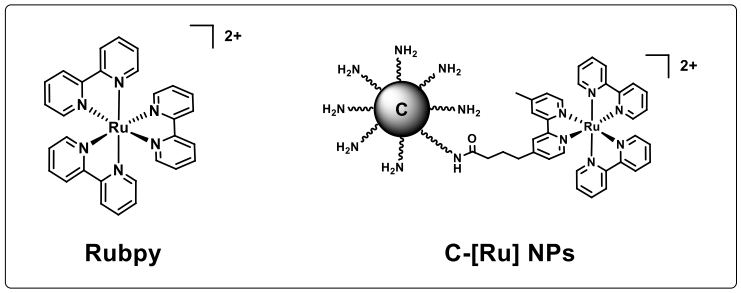

Scheme 1. Stucture of Rubpy and C-[Ru] NPs

6.2.2 Characterization

TEM imaging

The Rubpy modified carbon dots, C-[Ru], were characterized by TEM and are shown in Figure 2 and 3. From the TEM imaging, the nanoparticles aggregate inside a matrix, however, we can still observe the particles as draw with yellow circle. The size of round shape C-[Ru] NPs is around 4 nm.

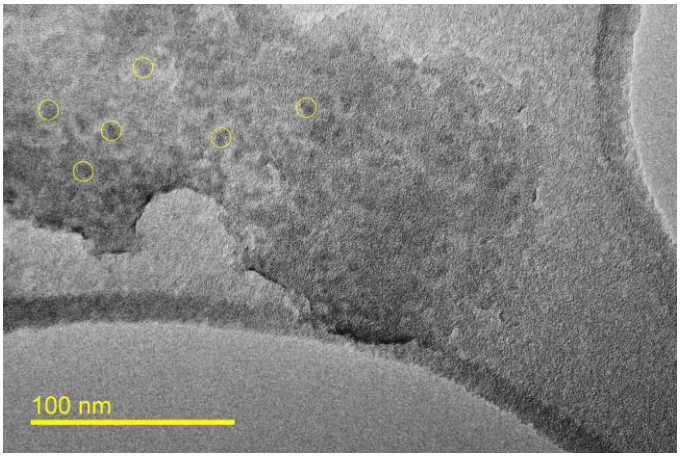

Figure 2. TEM imaging of C-[Ru] NPs

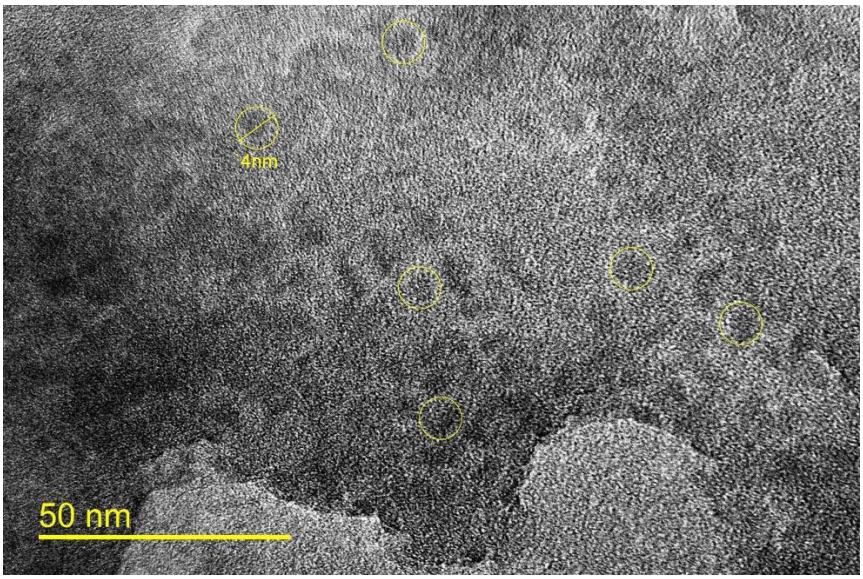

Figure 3. TEM imaging of C-[Ru] NPs

FT-IR spectra

The C-[Ru] NPs synthesized were characterized by FT-IR using attenuated total reflection (ATR) mode to identify the surface groups. In Figure 4, the FT-IR spectrum of C-[Ru] shows the vibration peaks at 1664 cm^{-1} and 1548 cm^{-1}, which are assigned to the carbonyl stretch and N–H bending of amide bond. The peaks at 2956, 2924 and 2854 cm^{-1} represent the stretch and bending modes of the alkyl chains, $C(sp^3)$–H. The $C(sp^2)$–H vibrations appear at 3066 cm^{-1}. The vanished vibration band at 1735 cm^{-1} corresponds to the succinimide group and can be interpreted as a proof of the successful coupling reaction. On the contrary, the CDs alone, amine reveals broad N–H stretch around 3400 cm^{-1} and the N–H bending (~ 1651 cm^{-1}).

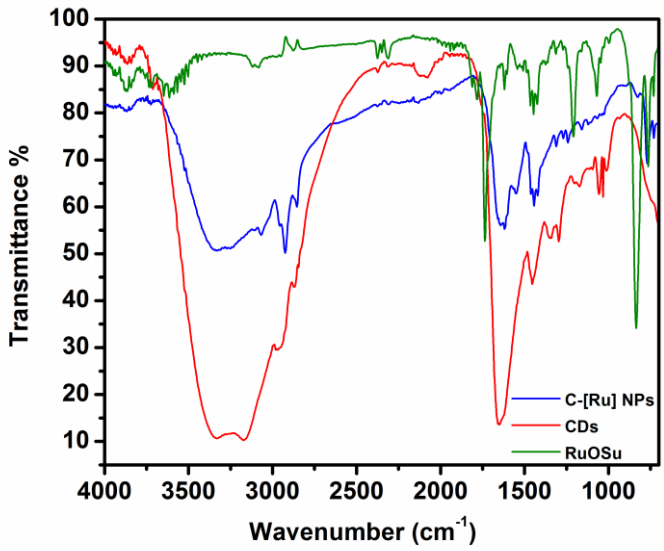

Figure 4. FT-IR spectra of CDs (red), RuOSu (green) and C-[Ru] NPs (blue).

X–ray Photoelectron Spectroscopy (XPS) measurements

C-[Ru] NPs were characterized by X–ray photoelectron spectroscopy (XPS) to acquire the elemental composition. As shown in Figures 5 and 6 and Table 1, the results of the survey scan and the element scan show the presence of C, N, O, P, F and Ru atoms inside the samples. In the element scan of the N atom (Figure 7), the N signal can be reassembled by many specific peaks which represent different chemical states such as amine, amide, pyridine, etc. In our studies, C-[Ru] NPs show XPS peaks at 399.58, 399.66 and 400.70 eV, corresponding to the binding energies of pyridine, aliphatic amine and amide groups respectively. In addition, the atomic ratio gives an evidence of the coverage of Ru complex on the CDs surface. Compared the atomic ratio data of the nitrogen atom in table 2, the nitrogen ratio of amide and amine is 5.3% and 61.6%. Therefore, the total amine groups are 66.9% before coupling and 61.6% remained after coupling, which indicates 8% of amine groups are successfully bound to the Ru complexes forming the amide bond. The CDs from Prof. Maggini group, in the literature report[21], show 8 to 10 amine groups were present on the particles surface. Then combined with the XPS data, we obtain only one ruthenium complex is coupling with CDs.

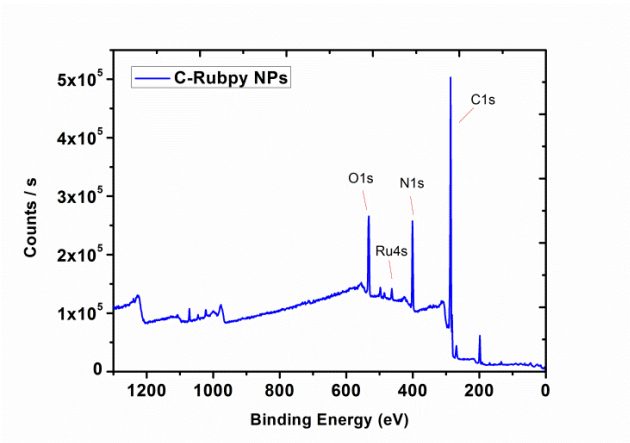

Figure 5. XPS spectrum of C-[Ru] NPs in the survey scan.

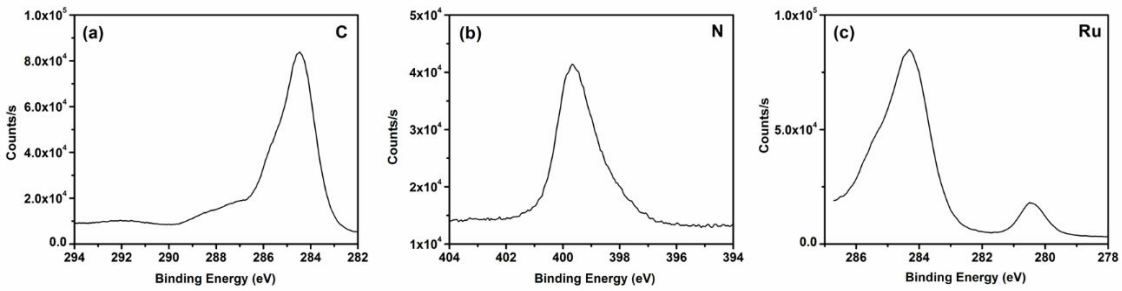

Figure 6. XPS spectra of C-[Ru] NPs in the element scan. (a) C atom (b) N atom (c) Ru atom.

Table 1. The XPS data for C-[Ru] NPs in survey scan.

	Peak, eV	FWHM, eV	Atomic ratio, %
C1s	284.80	2.91	71.18
N1s	399.48	2.71	13.31
O1s	531.15	3.78	10.75
P2p	132.50	2.83	0.68
Ru3p	461.79	3.47	0.54
F1s	689.55	0.44	0.21

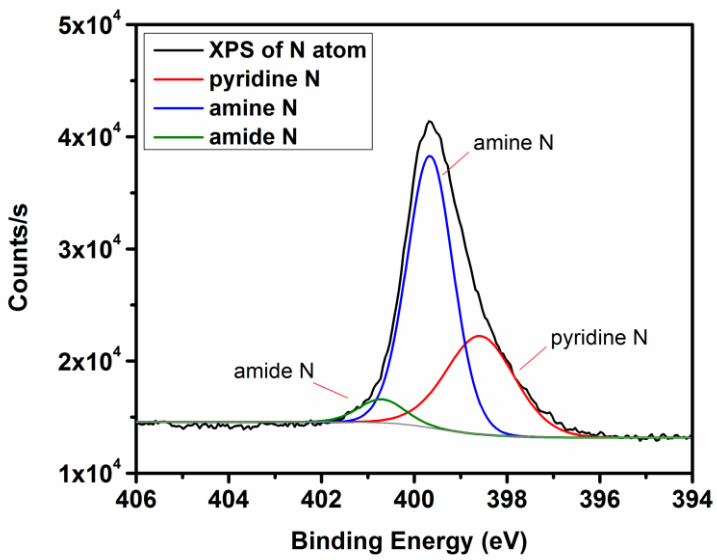

Figure 7. N atom scan of XPS spectrum of C-[Ru] NPs.

Table 2. XPS data for N atom scan.

	Peak, eV	FWHM, eV	Atomic ratio, %
pyridine N	398.58	1.74	33.03
amine N	399.66	1.17	61.64
amide N	400.70	1.17	5.33

6.2.3 Photophysical properties

The photophysical measurements were performed both in the aerated water and ProCell solution. The ProCell solution is a water solution mixing with amines and surfactants (the chemical formula is confidential) and was provided by Roche Company which used for immunoassays. As shown in Figure 8 and Table 3, CDs exhibit a broad absorption band between 250 ~ 400 nm in water solution. The Rubpy complex shows two absorption bands at 244 and 280 nm and are assigned to the $\pi\pi^*$ transitions and an

additional band at 460 nm assigned to the ^{1}MLCT transition. In order to compare the ECL efficiency of the C-[Ru] NPs to the Rubpy standard, the concentration of C-[Ru] NPs was tuned and made equal to the concentration of Rubpy used. For this purpose, the concentration of C-[Ru] NPs used was the one proportional to the absorption of a solution of Rubpy of 10^{-5} M concentration at 460 nm (λ_{max} of MLCT absorption band).

Table 3 shows the photophysical data of C-[Ru] NPs, the Rubpy complex and naked CDs. C-[Ru] NPs present dual emission when exciting at λ_{ex} of 350 nm, a blue emission band at 400 nm that is originated from the CDs and a red emission band at 627 nm that is attributed to the Rubpy. The excited state lifetime (detection at 630 nm) is of 331.6 ns for the Rubpy complex and 334.4 ns for the C-[Ru] NPs, having luminescent quantum yield (PLQY) both of 4% in aerated water solution. Changing the system to a ProCell solution, no significant blue/red shift in the UV-Vis absorption spectra was observed (Figures 9) Figure 10 shows the emission spectra of the Rubpy complex and the C-[Ru] NPs and the data is listed in Table 4. Particles display the same emission profile as in the water solution, being the emission intensity at 630 nm the same as Rubpy at 10^{-5} M. The Excited state lifetime (detection at 630 nm) is 358.0 ns for the ruthenium complex and 353.3 ns for C-[Ru] NPs, and luminescent quantum yield both are 4%.

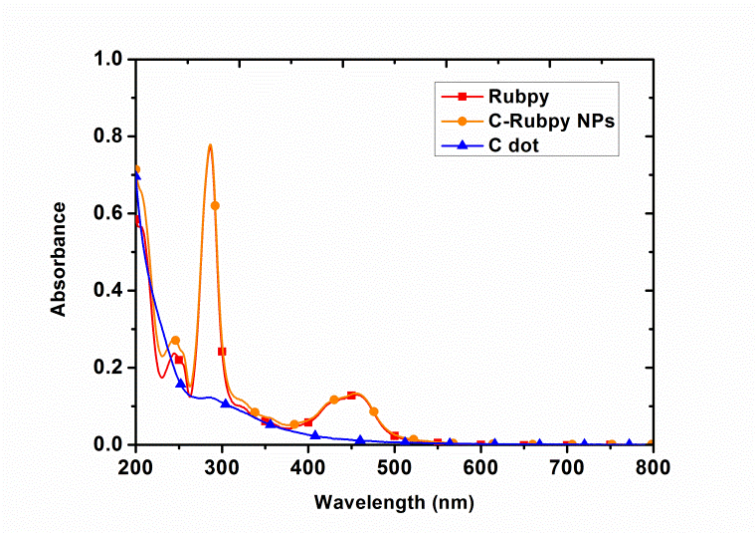

Figure 8. UV-Vis absorption spectra of CDs (blue), Rubpy (red) and C-[Ru] NPs (orange) in aerated water solution. [Ru complex] =10^{-5}M.

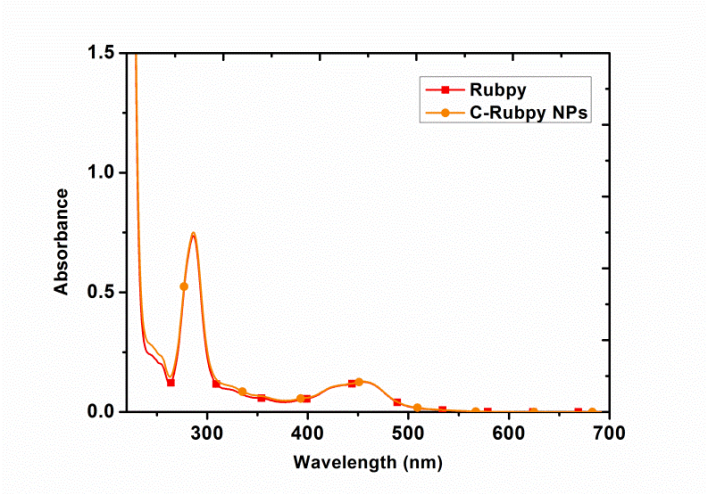

Figure 9. UV-Vis absorption spectra of Rubpy (red) and C-[Ru] NPs (orange) in aerated ProCell solution. [Ru complex] =10^{-5}M.

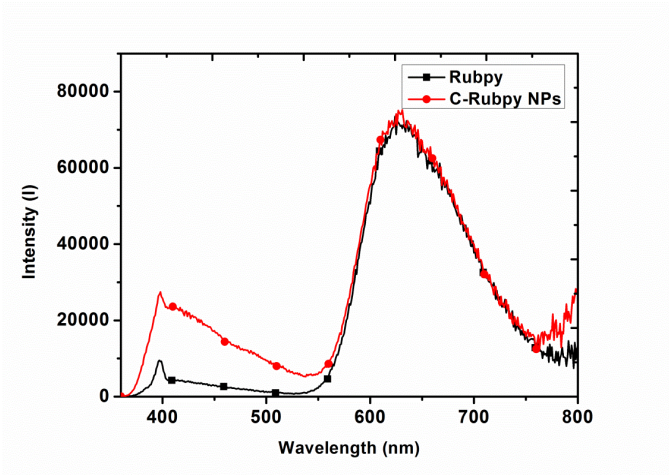

Figure 10. Emission spectra of Rubpy (black) and C-[Ru] NPs (red) in aerated ProCell solution. [Ru complex] =10^{-5}M.

Table 3. The photophysical data for CD, Ru complex and C-[Ru] in H_2O.

	$\lambda_{Absorption}$, nm	$\lambda_{Emission}$, nm	Lifetime τ, ns
CDs	286	418[b]	2.30 (66.2%), 6.18 (30.1%), 13.61 (3.7%)[c]
C-[Ru] NPs	244, 286, 456	393, 627[b]	2.33 (65.2%), 5.80 (31.0%), 14.09 (3.8%)[c]
			331.6[d]
Ru complex	244, 286, 456	631[b]	334.4[d]

a. All the measurements were in H_2O solution without degassing. b. λ_{ex} = 350 nm. c. λ_{ex} = 375 nm and collected at 410 nm. d. λ_{ex} = 440 nm and collected at 630 nm.

Table 4. Photophysical data for Rubpy and C-[Ru] in ProCell.

	$\lambda_{Absorption}$, nm	$\lambda_{Emission}$, nm	Lifetime τ, ns
C-[Ru] NPs	286, 456	411, 627[b]	1.55 (62.4%), 4.21 (32.9%), 11.13 (4.9%)[c]
			358.0[d]
Ru complex	286, 456	626[b]	353.3[d]

a. All the measurements were performed in aerated ProCell solution. b. λ_{ex} = 350 nm. c. λ_{ex} = 375 nm and collected at 410 nm. d. λ_{ex} = 440 nm and collected at 630 nm.

6.2.4 Electrochemiluminescence (ECL)

Electrochemiluminescence (ECL) measurements were performed using the C-[Ru] NPs synthesized and Rubpy as a control. Rubpy and C-[Ru] NPs were studied in Procell solution at a concentration of 10^{-5} M. The concentration of the C-[Ru] NPs solution in ProCell was evaluated through the absorbance of the sample in the UV-Vis absorption toward the same absorbance of Rubpy sample at 10^{-5} M. The device setup consists of a home-made glassy carbon disk electrode (3 mm diameter) as working electrode, an Ag/AgCl (1M KCl) electrode as reference electrode and a platinum wire as counter electrode.

In Figure 11 shows the ECL intensity during a cyclic voltammetry scan (0.1 Vs^{-1}) of Rubpy and C-[Ru] NPs in ProCell. Two peaks at +0.93 and +1.18 V vs Ag/AgCl (1M KCl) were observed for Rubpy. These values are in agreement with those reported by Bard *et al*. for the system $[Ru(bpy)_3](PF_6)_2$/TPA in aqueous solution containing Rubpy in low concentration and TPA in micro molar range to 0.1 M.[30-32] Both waves are associated with the generation of the excited state of Rubpy. However, the first wave occurs when the TPA radical cation ($TPA^{\bullet+}$) is formed and oxidizes $Rubpy^+$ to generate the excited state of Rubpy*. The second wave is assigned to the classic co-reactant mechanism for ProCell, which is described in scheme 2. For C-[Ru] NPs, the intensity profile is similar to Rubpy, however, the first peak (+0.93 V) is obscure and the second peak (+1.18 V) is more pronounced. It corresponds to the mechanism mentioned in scheme 1 where the first peak corresponds to the oxidation of TPA and the second peak is correlated to the potential of direct $Ru(bpy)_3^{2+}$ oxidation.

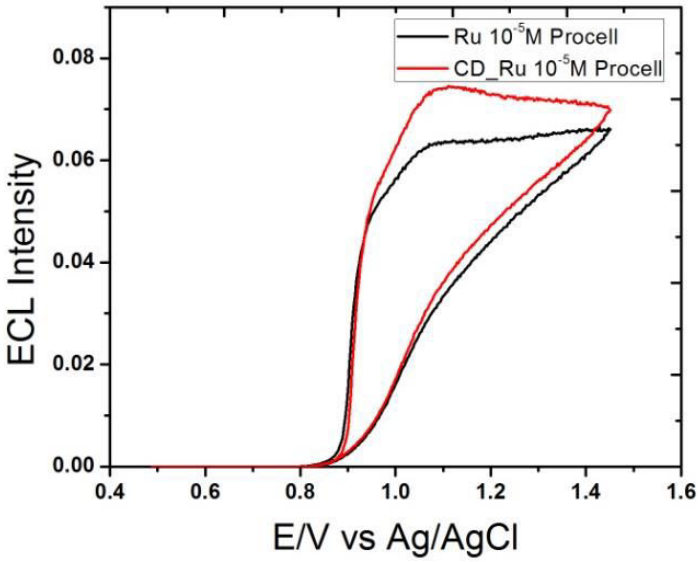

Figure 11. ECL intensities of Rubpy (black) and C-[Ru] NPs (red)in Procell using GC as working electrode. Potential scan rate 100 mV s^{-1}.

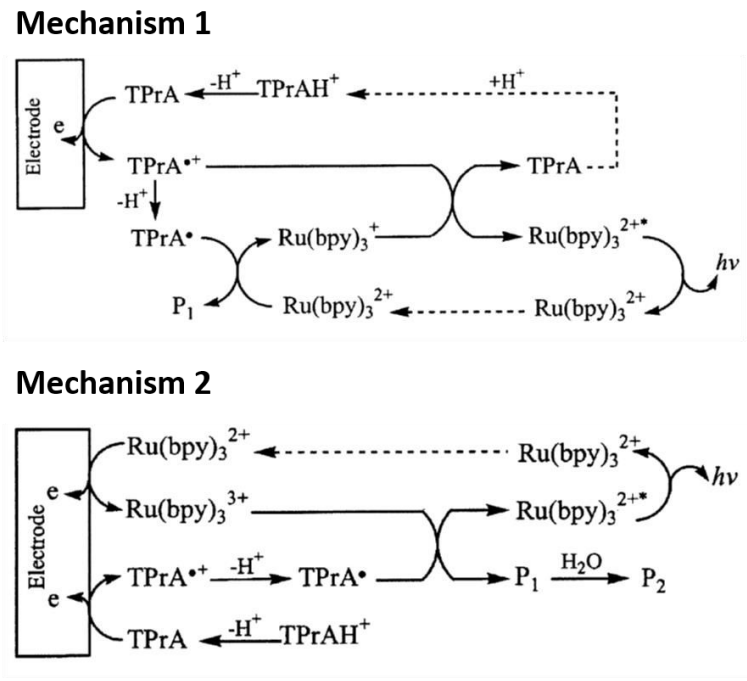

Scheme 2. Mechanisms reported by Bard *et al*. for the system $[Ru(bpy)_3](PF_6)$ /TPA in aqueous solution containing Rubpy in low concentration.[32] Reprinted with permission from *J. Am. Chem. Soc.,* **2002**, *124,* 14478-14485 Copyright (2004) American Chemical Society.

To evaluate the ECL efficiency of this new system, chronoamperometry measurements were performed. In this experiment, ECL was generated by a chronoamperometry pulse at +1.4 V for 1 s in a fresh prepared solution. (performed in 3 different days and repeated 3 times for each day, totally 9 experiments). The calculated ECL efficiency is the average of these 9 measurements with a relative standard deviation below 10%. Figure 12 shows one of the chronoamperometry experiment. Notably the ECL efficiency of C-[Ru] NPs (0.90) is almost same as Rubpy alone (1.00), shown in Table 5.

ECL emission spectra were also measured to evaluate the nature of the emissive excited state generated by this process and calculate the ECL efficiency. As mentioned before, the measurements were performed in 3 different days and repeated 3 times for each day (totally 9 experiments). Figure 13 shows the ECL emission spectrum of one experiment. As it can be seen the emission of C-[Ru] NPs is centered at 604 nm and the emission profile is same as the Rubpy, both ECL emission spectra are identical to the emission spectra observed upon photoexcitation (PL spectra). The ECL efficiency of C-[Ru] NPs is slightly higher (1.07) than Rubpy standard (1.00). The data is consistent with the chronoamperometry method and this is a really encouraging result for an ECL active nanoparticle system which means that the complexes linked to the CDs surface maintain the ECL activity and they are not affected by parasite quenching phenomena. Moreover, we still need to investigate the relation between the mass diffusion and the ECL efficiency in our system and it will be performed in the future work.

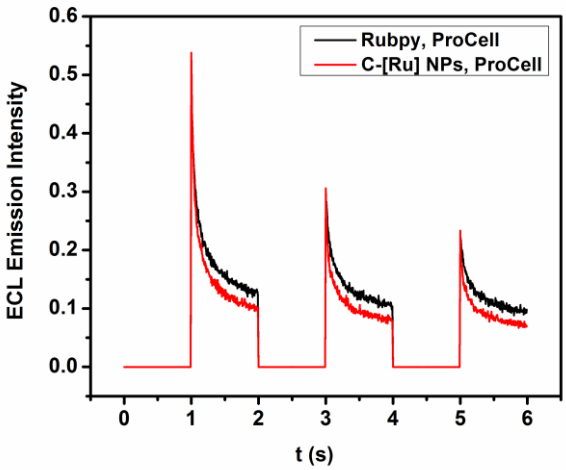

Figure 12. ECL Intensities in time of Rubpy (black) and C-[Ru] NPs (red) in ProCell.

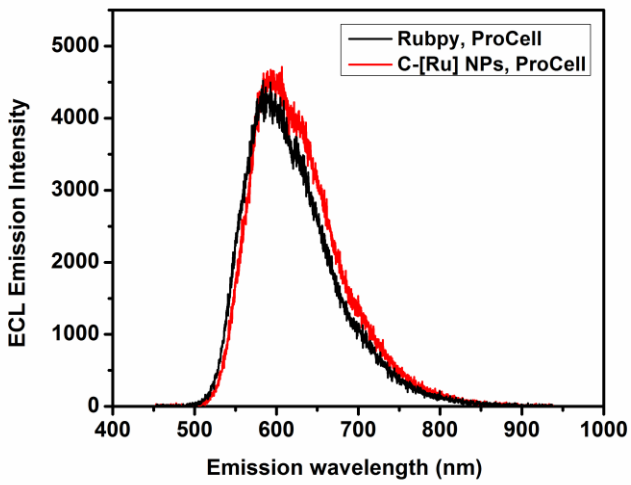

Figure 13. ECL emission spectra of Rubpy (black) and C-[Ru] NPs (red) in ProCell.

Table 5. ECL Efficiencies of C-[Ru] NPs in ProCell on GC electrode.

	ECL efficiency ($I_{C\text{-}[Ru]}/I_{Rubpy}$) on GC
C-[Ru] from Chrono	0.90
C-[Ru] from ECL Spectra	1.07

a. Rubpy was used as reference considering that its ECL efficiency is 100%

6.3 Iridium complexes-Silicon nanoparticles nanosystems

6.3.1 Synthesis

Silicon nanoparticles were functionalized with substituents containing carboxylic acids (Si-COOH). They were prepared using the method described in chapter 3. Two more reaction steps were needed to achieve the coupling of the Ir complexes to the Si nanoparticles. First, a coupling reaction was done between 1, 6-hexanediamine and the carboxylic acid functionalized Si-NPs in order to achieve amino functional groups on the Si-NPs surface. Subsequently, another coupling reaction was performed between the Ir complex chosen (Scheme 3) and the Si-COOH NPs in presenting 1-Ethyl-3- (3-dimethylaminopropyl)carbodiimide (EDC) and N-hydroxysulfosuccinimide (NHS) condition. Si-[Ir] NPs were obtained as red powder after purification by size exclusion chromatography (LH-20).

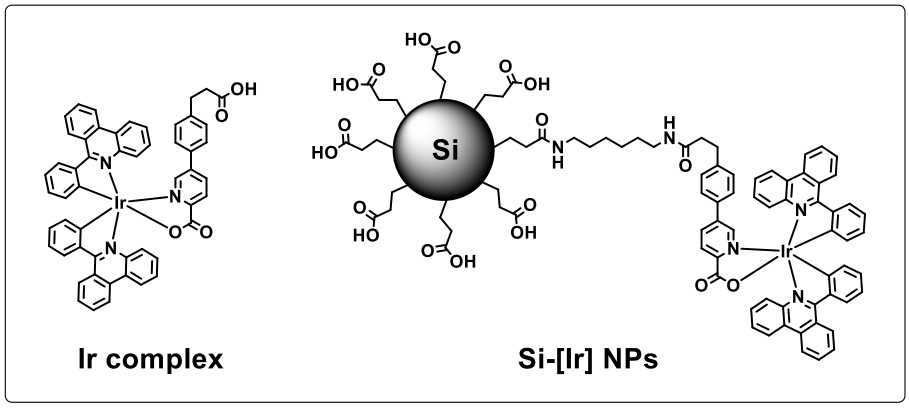

Scheme 3. Structure of Ir complex and Si-[Ir] NPs

6.3.2 Characterization

FT-IR spectra

Si-COOH and Si-[Ir] NPs were both characterized by FT-IR using attenuated total reflection (ATR) and the spectra show in Figure 14. Before coupling, Si-COOH NPs showed a very strong stretch band at 1707 cm^{-1}, which corresponds to the carbonyl group. After the coupling reaction, Si-[Ir] NPs, the uncoupled carboxylate groups still present the vibration at 1712 cm^{-1}. Besides, the new amide bond exhibits the carbonyl stretch at 1641 cm^{-1} and N–H bending at 1564 cm^{-1}. Other peaks at 2927, 2873, 1462 and 1379 cm^{-1} represent the stretch and bending bands of the alkyl chain, $C(sp^3)$–H.

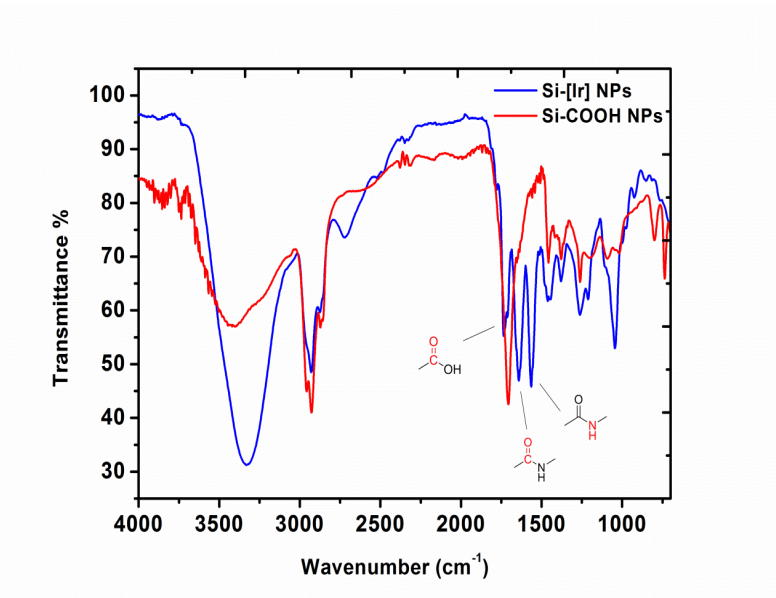

Figure 14. FT-IR spectra of Si-COOH NPs and Si-[Ir] NPs

X-ray photoelectron spectroscopy (XPS)

The XPS survey and element scans show the presence of C, Si, N, O and Ir atoms in the Si-[Ir] NPs (Figure 15, 16 and Table 6). As shown in Figure 17, different chemical compositions can be observed by analyzing the nitrogen atom in the element scan mode. The XPS peaks of the nitrogen appear at 401.47 and 399.28 eV (Table 7), which correspond to the binding energies of amide and pyridine nitrogen, respectively. Besides, the atomic ratio of amide and pyridine is 37.96% and 62.04%, which is consistent with the Si-[Ir] structure having two amide bonds and three pyridine moieties.

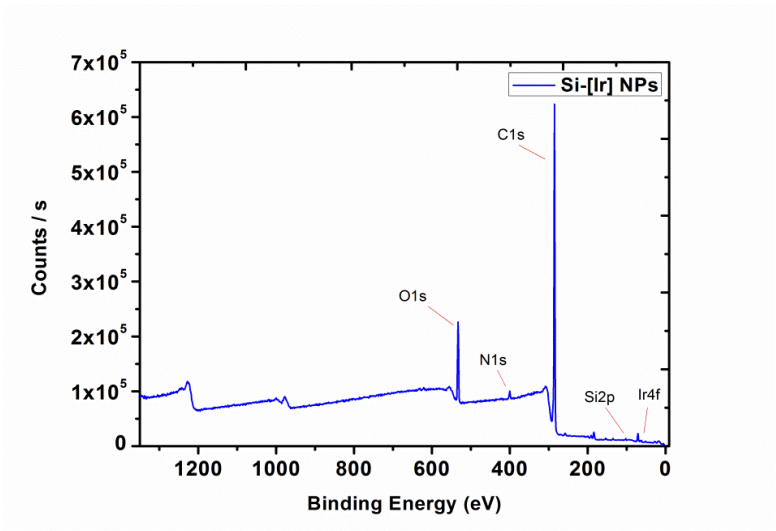

Figure 15. XPS spectrum of Si-[Ir] NPs in the survey scan.

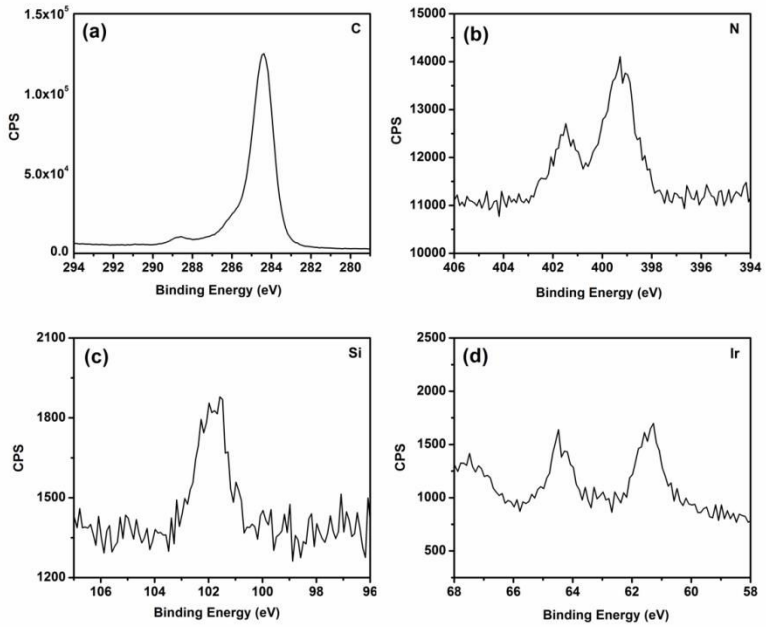

Figure 16. XPS spectra of Si-[Ir] NPs in the element scan. (a) C atom (b) N atom (c) Si atom (d) Ir atom.

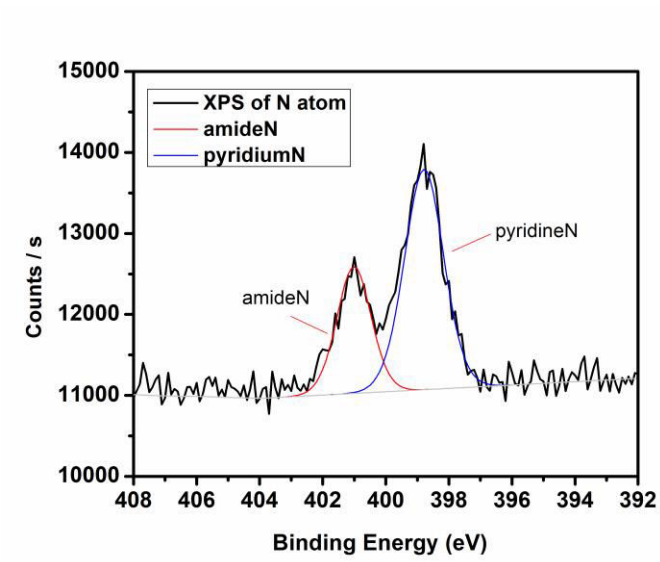

Figure 17. N atom scan of XPS spectrum of Si-[Ir] NPs

Table 6. XPS data for Si-[Ir] NPs

	Peak, eV	FWHM, eV	Atomic ratio, %
C1s	284.80	2.58	86.5
O1s	532.58	3.04	10.77
N1s	400.04	3.77	2.13
Si2p	101.93	2.74	0.59
Ir4f	61.66	0.61	0.02

Table 7. XPS survey of N atom in Si-[Ir] NPs

	Peak, eV	FWHM, eV	Atomic ratio %
amideN	400.59	1.51	37.96
pyridineN	398.40	1.36	62.04

6.3.3 Photophysical properties

The photophysical measurements were performed in both, aerated MeOH and ProCell solution. As shown in Figure 18, Si-COOH NPs exhibit a broad absorption band below 400 nm in MeOH. The Ir complex shows absorption bands at 259, 284, 347 and 360 nm, which are assigned to the $^1\pi\pi^*$ transitions. In this case, the ^{1}MLCT bands appear at 417 and 460 nm. As mentioned before, we could quantify the concentration of Ir complex in the Si-[Ir] sample by monitoring its absorbance. In this case, the concentration of Ir complex in Si-[Ir] NPs is adjusted to be of 10^{-5} M. Si-[Ir] NPs present dual emission (Figure 20) when exciting at λ_{ex} =370 and 388 nm, one band with center at 475 nm is originated from the Si NPs and another band with center at 636 nm is attributed to the Ir complex. The excited state lifetime (detection at 636 nm) is 230.1 ns for the Ir complex and 238.3 ns for the Si-[Ir] NPs (Table 8).

Then the photophysical properties were also studied in a ProCell solution and listed in Table 9. Figure 19 presents the UV-Vis absorption spectra of Si-[Ir] NPs and Ir complex in ProCell solution. The Si-[Ir] NPs and Ir complex show no significant shift in absorption compared to MeOH solution. Figure 21 presents the emission spectra in ProCell solution, Si-[Ir] NPs display the same emission profile as in MeOH solution, being the band at 636 nm attributed to the Ir complex. The excited state lifetime (detection at 636 nm) is longer in the ProCell solution, being 713.4 ns for the Ir complex and 708.8 ns for the Si-[Ir] NPs. The luminescent quantum yields of both are 12%.

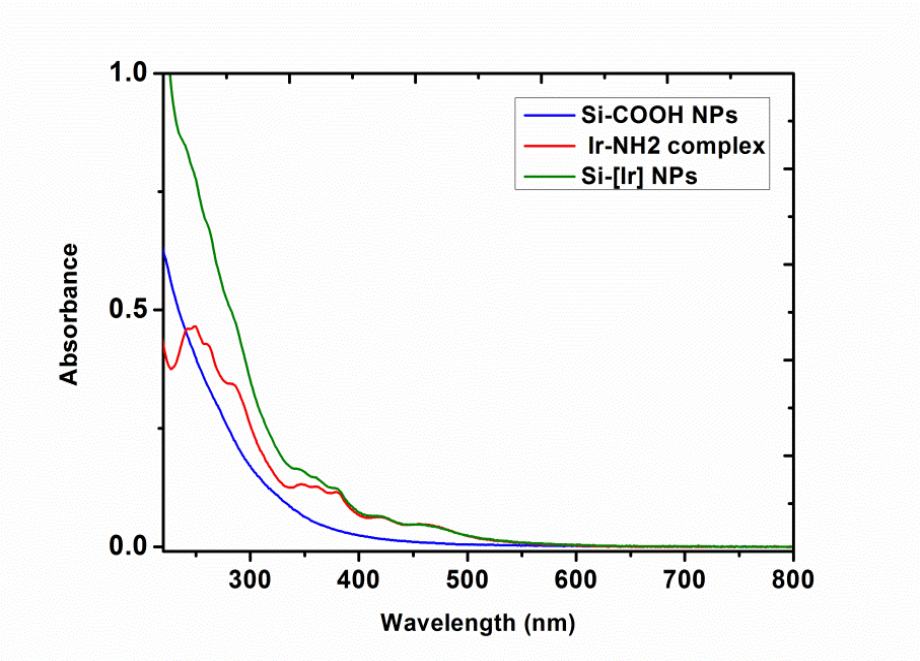

Figure 18. UV-Vis absorption spectra of Si-COOH NPs (blue), Ir complex (red) and Si-[Ir] NPs (green) in MeOH solution. [Ir complex] = 10^{-5} M.

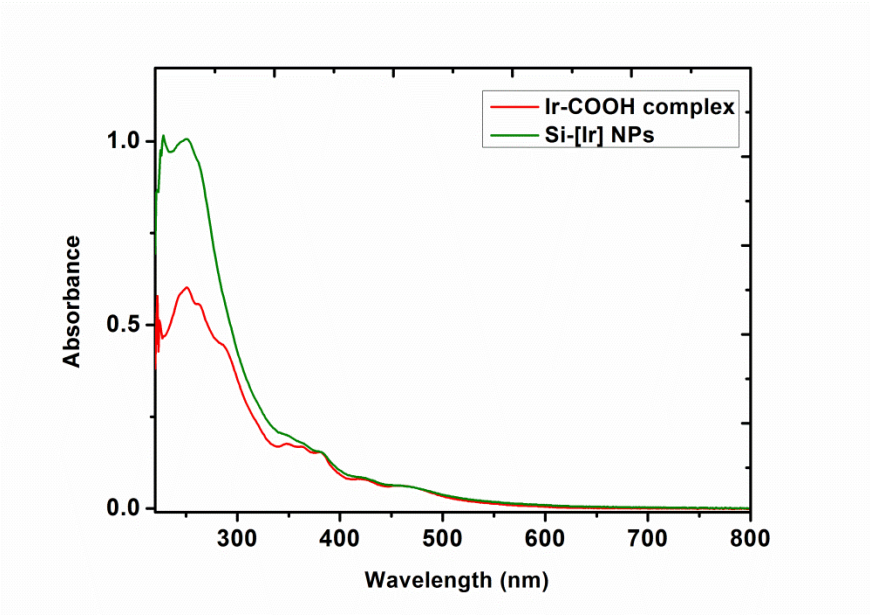

Figure 19. UV-Vis absorption spectra of Ir complex (red) and Si-[Ir] NPs (green) in ProCell solution. [Ir complex] = 10^{-5} M.

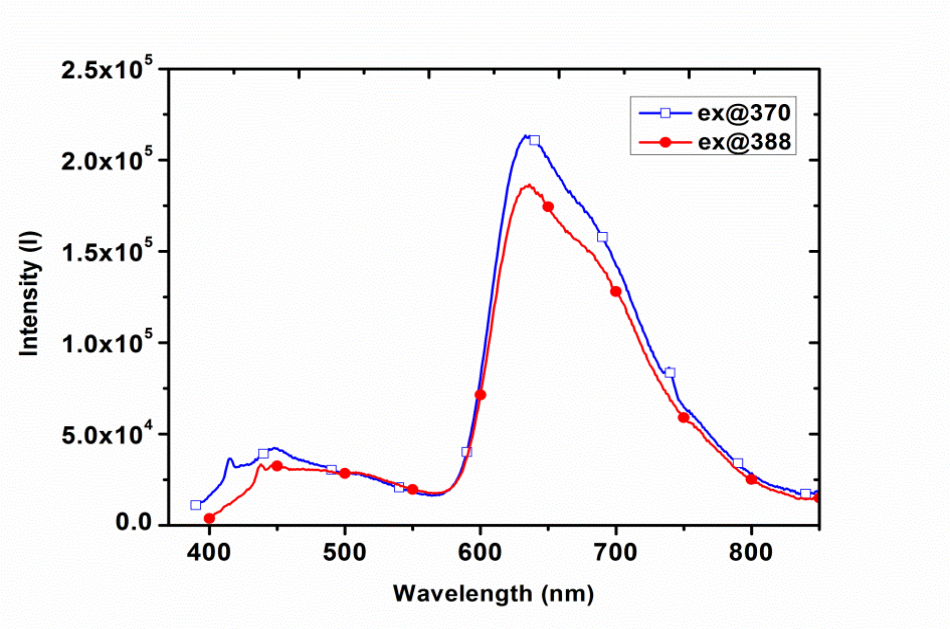

Figure 20. Emission spectra of Si-[Ir] NPs in MeOH solution.

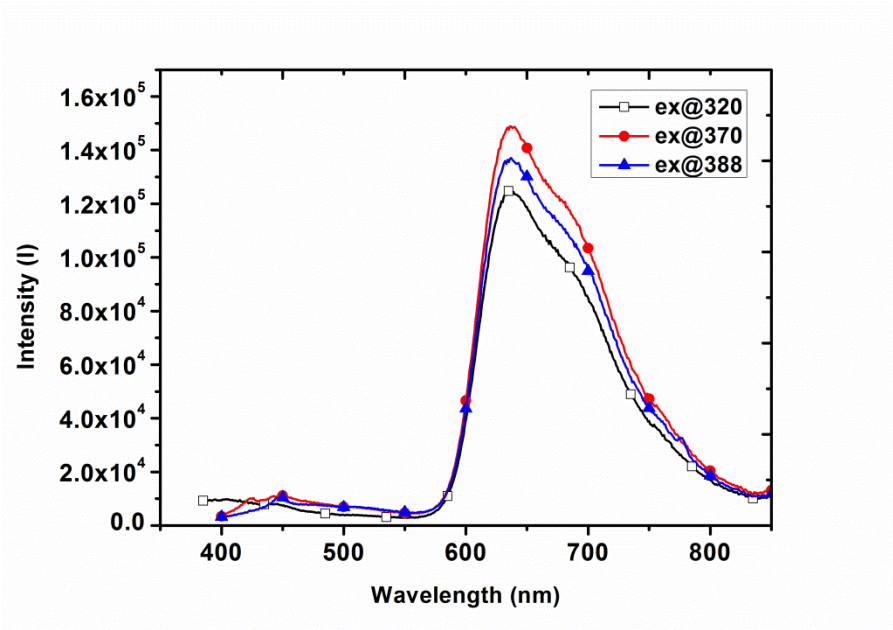

Figure 21. PL spectra of Si-[Ir] NPs with different excitation wavelength in ProCell

Table 8. Photophysical data for Si-COOH NPs, Si-[Ir] NPs and Ir-NH_2 complex in MeOH.

	$\lambda_{absorption}$, nm	$\lambda_{emission}$, nm	Lifetime τ, ns
Si-COOH NPs	268(shoulder)	475[b]	0.27 (68.0%), 2.11 (28.4%), 8.55 (3.6%)[d]
Si-[Ir] NPs	245, 288, 347, 379, 417, 460	475, 636, 690[b]	0.31 (85.7%), 2.83 (12.3%), 8.47 (2.0%)[d]
			238.3[e]
Ir-NH_2 complex	243, 249, 259, 284, 347, 360, 379, 417, 460	636, 690[c]	230.1[e]

a. All the samples were prepared in aerated MeOH. b. λ_{ex} = 370 nm. c. λ_{ex}= 440 nm. d. λ_{ex} = 375 nm and collected at 470 nm. e. λ_{ex} = 440 nm and collected at 636 nm

Table 9. Photophysical data for Si-[Ir] NPs, and Ir-COOH complex in ProCell

	$\lambda_{Absorption}$, nm	$\lambda_{Emission}$, nm	Lifetime τ, ns
Si-[Ir] NPs	250, 380, 420, 460	470, 636, 690[b]	0.32 (64.0%), 2.83 (24.7%), 12.02 (11.3%)[d]
			189.7 (22%), 708.8(78%)[e]
Ir-COOH complex	250, 263, 286, 348, 362, 380, 420, 460	636, 690[c]	713.4[e]

a. All the samples were prepared in aerated ProCell solution. b. λ_{ex} = 375 nm. c. λ_{ex} = 440 nm. d. λ_{ex} = 375 nm and collected at 470 nm. e. λ_{ex} = 440 nm and collected at 636 nm.

6.3.4 Electrochemiluminescence (ECL)

The ECL properties of four different samples, Ir complex, Si-[Ir] NPs, SiNP + Ir complex (mechanical mixture) and Rubpy standard were measured in ProCell solution. The mechanical mixture is in order to compare the influence between the covalent binding and non-covalent binding of Ir complex on the Si NPs. The concentration of the Si-[Ir] NPs solution in PBS and ProCell was evaluated through the absorbance of the sample toward the Ir complex at 10^{-5} M. The ECL curves are shown in Figure 22. Rubpy shows two peaks at +0.93 and +1.18 V vs Ag/AgCl (1M KCl) respectively.

These values are in agreement with those reported by Bard *et al*. for the system $[Ru(bpy)_3](PF_6)$ /TPA in aqueous solution containing Rubpy in low concentration and TPA in the micro molar range.[30-32] The detailed mechanism is described in Scheme 2 (6.2.4).

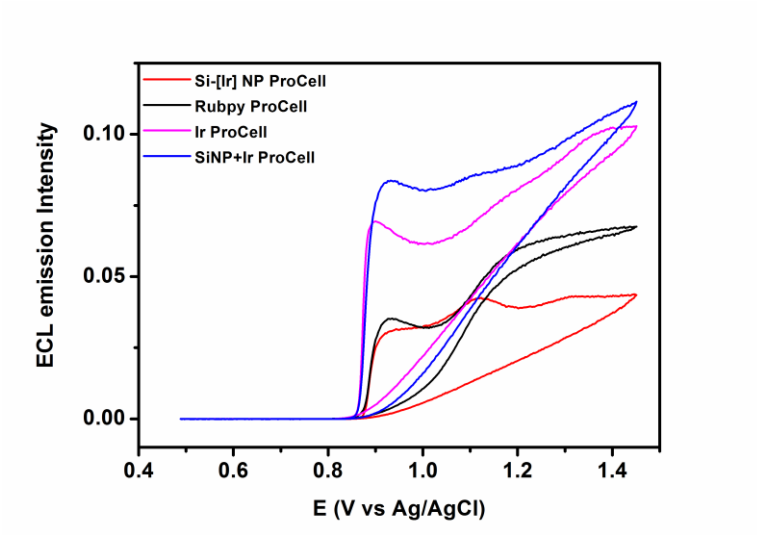

Figure 22. ECL Intensities of Rubpy (black), Si-[Ir] NPs (red), Ir complex (pink), SiNP+Ir (mechanical mixture) (blue) in Procell using GC as working electrode. Potential scan rate 100 mV/s.

For Si-[Ir] NPs, three broad waves at +0.93 V, +1.11 and +1.31 V vs Ag/AgCl (1M KCl) are observed. The first peak (+0.93 V) can be correlated to the one observed for the Rubpy (voltage at which TPA is oxidized), while the third peak (+1.31 V) should correspond to the potential of direct oxidation of the Ir complex. Indeed, the third peak is also present in the curve of the Ir complex. Interestingly, the second peak (+1.11 V) appears in both Si-[Ir] and SiNP + Ir mechanical mixture (with weaker intensity), but is not observed in the Ir complex alone. We think the carboxylate groups play a role in this redox process and we need more experiments to prove it.

To evaluate the efficiency of the new system compared to the Rubpy standard, chronoamperometry measurements were done. As shown in Figure 23, in this experiment, the ECL was generated by a chronoamperometry pulse at +1.4 V for 2 s (repeated for 3 times). The ECL intensity decreased in the following order: Ir complex > SiNP + Ir > Rubpy > Si-[Ir]. This result shows the ECL is active in this nanoparticle system. However, it is possible to note that the presence in solution of the Si-COOH NPs is decreasing the efficiency. We also performed the photocurrent experiments pulsing the sample for a longer time (2 sec.) at +1.4 V (Figure 24) to investigate the

influence of the diffusion rate of the nanoparticles on the ECL efficiency. We noticed that the free label (Ir complex) presents higher efficiency than Si-[Ir] NPs in opposite tendency to our hypothesis that Si NPs can enhance the ECL efficiency. We believe that ECL is generated only on the electrode surface and since the mass of the Si-[Ir] system is much higher than the one of the free label, it takes longer time to diffuse to the reaction zone, resulting in lower efficiency than the free Ir complex. The Si NPs (10.5 K Daltons) have 10 times mass heavier than CDs (1 K Dalton). The bigger size of Si-[Ir] NPs, is expected to result in slower diffusion to the electrode and reducing it ECL performance. The mass diffusion of Si-[Ir] NPs is still under investigating.

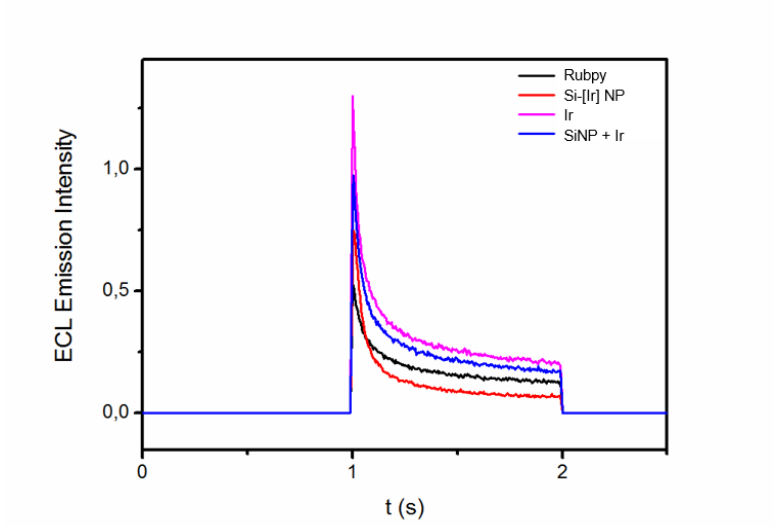

Figure 23. ECL Intensities in time of Rubpy (black), Si-[Ir] NPs (red), Ir complex (pink) and SiNP + Ir (mechanical mixture) in ProCell

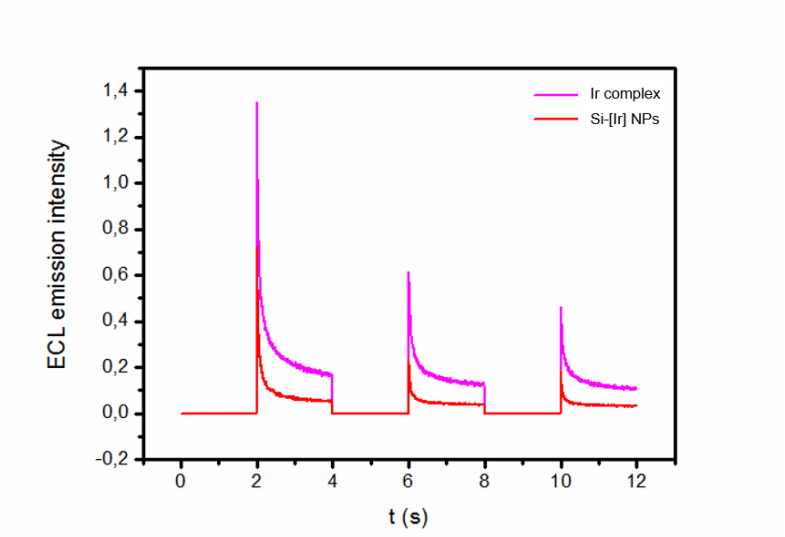

Figure 24. ECL Intensities in time of Si-[Ir] NPs (red) and Ir complex (pink) in ProCell

We also measured the ECL emission spectra (Figure 25) to evaluate the nature of the emissive excited state generated by this process. As it can be noticed the emission bands of the Ir complex and the Si-[Ir] NPs are both centered at 623 nm, this is also consistent with the emission spectra observed upon photoexcitation. The efficiency values are reported in Table 10. The ECL efficiency of Rubpy is 1.00 as standard, Ir complex shows higher efficiency, 1.77, mechanical mixture of SiNP +Ir shows 1.47, and Si-[Ir] NPs shows 0.75.

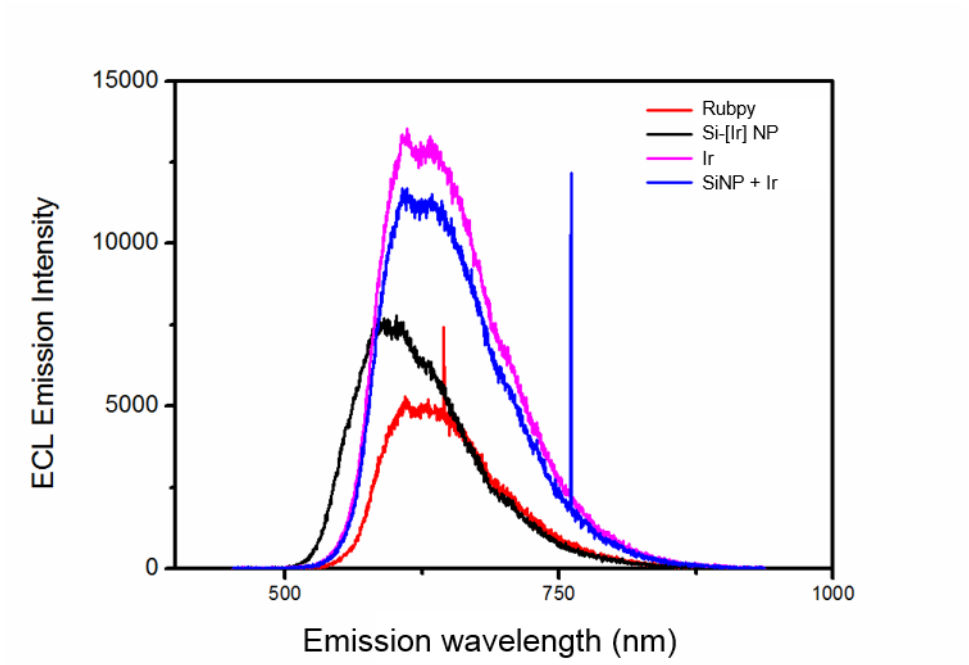

Figure 25. ECL emission spectra of Rubpy (black), Si-[Ir] (red), Ir complex (pink) and SiNP+ Ir (mechanical mixture) in ProCell

Table 10. ECL Efficiencies of Si-[Ir] NPs in ProCell solution on GC electrode.

	ECL efficiency ($I_{complex}/I_{Rubpy}$)
Rubpy	1.00
Ir	1.77
Si-[Ir] NP	0.75
SiNP + Ir	1.47

a. Rubpy was used as reference considering that its ECL efficiency is 100%

6.4 Conclusion

We have synthesized metal complexes coated carbon dots/silicon nanoparticles and studied their use in ECL applications. All the materials were fully characterized by FT-IR, XPS and photophysical measurements. The presence of several functionalities on the particle's surfaces keeps the systems remain soluble in aqueous solution and can be used as multilabel imaging tools. The ECL efficiency of C-[Ru] NPs shows identical value to the efficiency of the $[Ru(bpy)_3]^{2+}$ standard, stating that carbon dots do not disturb the ECL performance and the complexes linked to the CDs surface maintain the ECL activity. On the other hand, Si-[Ir] NPs show lower ECL efficiency than the Ir complex here studied, and it might be due to the slower mass diffusion of bigger nanoparticles. However, the diffusion of the particles should be deeply studied since as we have observed, ECL performance can decrease due to the slower mass diffusion to the electrode surface. Also the work is still in progress to optimize the systems and to evaluate the number of complexes per particle.

6.5 Experimental Section

General Information and Materials

All reagents and solvents were purchased from Sigma-Aldrich and Alfa and used without any further purification unless specifically noticed. The Ru(bpy)2-bpy-COOSu complex was provided by Roche. The Carbon dots were synthesized by following previously reported procedures.[21] The Ir-COOH complex was obtained from a former group member and was further functionalized with one more step to achieve the amide bond to from the Ir-NH_2 complex.

Optical Measurement

All the measurements were performed at a pressure of 1 atm and at room temperature unless specifically noted. UV-Vis absorption spectra were acquired with a Shimadzu UV-3600 UV-Vis-NIR spectrophotometer. Steady-state emission spectra were recorded on a Fluorolog 3 (HORIBA Jobin-Yvon IBH FL-322 spectrometer) equipped with a 450 W xenon arc lamp, double-grating excitation and emission monochromators (2.1 nm mm^{-1} of dispersion; 1200 grooves mm^{-1}), and a TBX-04 detector. Emission and excitation spectra were corrected for the xenon lamp, monochromators and detector efficiency by standard correction curves. Time-resolved measurements were performed using the PicoHarp 300 equipped with time correlated single photon counting (TCSPC) system on the FT-300 (PicoQuant), where a laser source 375 (or 440) nm was applied to excite the samples. The laser was mounted directly on the sample chamber at 90° to a Czerny-Turner type emission monochromator (2.7 nm mm^{-1} of dispersion; 1200 grooves mm^{-1}) and collected by a PMA-C 192M single-photon- counting detector. Signals were collected using EasyTau software, and data analysis was performed using FluoFit software (PicoQuant). The quality of the fit was assessed by minimizing the reduced $\chi 2$ function and by visual inspection of the weighted residuals. FT-IR experiments were measured in solid state using an attenuated total reflectance (ATR) method with Shimadzu IRAffinity-1.

XPS measurement

X–ray Photoelectron Spectroscopy (XPS) measurements were performed by a Thermo Scientific K-Alpha X-ray Photoelectron Spectrometer using a monochromatic AlKα radiation ($h\upsilon$ = 1486.6 eV). Survey measurements were performed with a 200 eV analyzer pass energy and a 1 eV energy step size to calculate the atomic concentrations. Element scans were performed with a 50 eV analyzer pass energy and a 0.1 eV energy step size to obtain the chemical state information. All the obtained binding energies were referenced to carbon 1s peak at 284.8 eV.

Electrochemistry

The electrochemical characterization of Ruthenium functionalized Carbon Dots (C-Ru) and $Ru(bpy)_3PF_6$ have been carried out in N,N-Dimethylformamide (DMF)/0.1 M tetra-butylammonium hexafluorophosphate ($TBAPF_6$). Oxygen was removed by purging the DMF solution with high-purity Argon. A typical three-electrode cell was employed, which was composed of a glassy carbon working electrode (3 mm diameter, 66-EE047 Cypress Systems), a platinum wire as counter electrode, and a silver wire as quasi-reference (QRE) electrode. A CHI750C Electrochemical Workstation (CH Instruments, Inc., Austin, TX, USA) was used. The potential of the reference electrode was calibrated after each measurement using Ferrocene/Ferrocenium (Fc/Fc^+) redox couple as the internal standard. The formal potential of Fc/Fc^+ is 0.464V for DMF against the KCl saturated calomel electrode (SCE).

The GC electrodes were stored in ethanol, and before experiments were polished with a 0.05 μm diamond suspension (Metadi Supreme Diamond Suspension, Buehler) and ultrasonically rinsed with deionized water for 5 minutes and ethanol for 5 minutes. The electrodes were electrochemically activated in the background solution by means of several voltammetric cycles at 0.5 Vs^{-1} between the anodic and cathodic solvent/electrolyte discharges. All the CVs were performed at 0.1 Vs^{-1}. For C-Ru CVs were carried out at scan rates ranging from 0.05 to 1 Vs^{-1}.

Electrochemiluminescence

To record the ECL data a home-made system was employed. Consisting in electrochemical cell based on a home-made glassy carbon (Tokai Inc.) disk electrode (3 mm diameter) and Pt (3 mm diameter) as the working electrode, which was closely facing (a few millimetres) the PMT. The reference electrodes employed was a Ag/AgCl (1M KCl) from CHI-Instruments and it was separated from the catholyte by glass frits. A platinum wire served as the counter electrode. The system was controlled using an Autolab electrochemical workstation PGSTAT101 (Metrohm, The Netherlands) coupled with a photosensor module with photomultiplier tube (PMT, Hamamatsu, H10723-01, Japan). The H10723 PMT is a photosensor module containing a metal package PMT, a low-power consumption high-voltage power supply circuit, and a low-noise amplifier. The amplifier converts the PMT current output to a voltage output so that signal can be easily processed. For the ECL vs time experiments, the pulsing potential was set at 1.4 V vs Ag/AgCl (1M KCl). The pulse width was 1s. The photocurrent produced by the PMT was directly converted to a voltage signal through the photosensor module and acquired by the external input channel of the analog-to-digital converter (ADC) of the Autolab. The transients and the faradic currents were

managed by using the software NOVA provided with the Autolab. The ECL spectra were acquired using a calibrated electron multiplying charge couple device (EM-CCD) camera (A-DU970N-UVB Andor technology, Newton EM-CCD) coupled with a spectrograph (Andor Technology, Shamrock 163). The ECL relative intensity of the complex and C-Ru NPs compared to $[Ru(bpy)_3]^{2+}$, (I/I_{Ru}), where I is the integrated signal of the sample for 1s and I_{Ru} is the integrated signal of Rubpy under the same conditions. The values are the average of three different measurements. The working electrode was mechanically cleaned before each run as above mentioned for the electrochemical measurements. As reference $[Ru(bpy)_2(bpy\text{-}COOH](PF_6)$ (bpy-COOH = 4-carboxypropyl, 4´-methyl- 2,2‘-bipyridine) 10^{-5} M in Procell was used.

Synthesis of C-[Ru] NPs

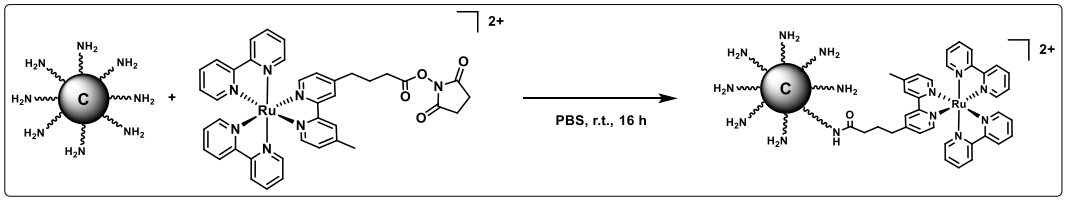

Carbon dots (18 mg) were dissolved into 10 mL of PBS (pH = 7.4). 5 mL H_2O solution of Ru(bpy)2-bpy-COOSu (89 mg) was added above the previous solution slowly. The reaction was stirred at room temperature for 12 hours. After the reaction, the solvent was removed with a rotary evaporator and washed with dichloromethane to remove the excess of Ru complexes. The CD_Ru nanoparticles were purified by size exclusion chromatography (LH-20) to yield a red powder. (20 mg)

Synthesis of Si-[Ir] NPs

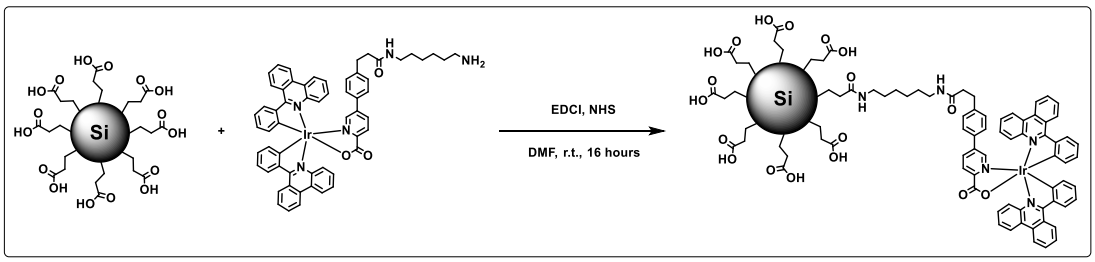

Si-COOH NPs (10 mg), Ir complex (6.62 mg, 5.9 μmol), EDCI (2.72 mg, 17.6 μmol), and NHS (2.02 mg, 17.6 μmol) were dissolved in 2 mL of dry DMF. Et_3N (10 μL, 71.7 μmol) was added and stirred at room temperature for 16 hours under Ar atmosphere. After the reaction time, DMF was removed under vacuum and the crude sample was purified by size exclusion chromatography (LH-20) to get a red solid (~5 mg).

6.6 References

1. L. Hu and G. Xu, *Chem. Soc. Rev.*, 2010, **39**, 3275-3304.
2. M. M. Richter, *Chem. Rev.*, 2004, **104**, 3003-3036.
3. M.-J. Li, P. Jiao, M. Lin, W. He, G.-N. Chen and X. Chen, *Analyst*, 2011, **136**, 205-210.
4. J. I. Kim, I.-S. Shin, H. Kim and J.-K. Lee, *J. Am. Chem. Soc.*, 2005, **127**, 1614-1615.
5. I.-S. Shin, J. I. Kim, T.-H. Kwon, J.-I. Hong, J.-K. Lee and H. Kim, *The Journal of Physical Chemistry C*, 2007, **111**, 2280-2286.
6. S. Zanarini, E. Rampazzo, L. D. Ciana, M. Marcaccio, E. Marzocchi, M. Montalti, F. Paolucci and L. Prodi, *J. Am. Chem. Soc.*, 2009, **131**, 2260-2267.
7. S. Zanarini, E. Rampazzo, S. Bonacchi, R. Juris, M. Marcaccio, M. Montalti, F. Paolucci and L. Prodi, *J. Am. Chem. Soc.*, 2009, **131**, 14208-14209.
8. M.-J. Li, Z. Chen, N. Zhu, V. W.-W. Yam and Y. Zu, *Inorg. Chem.*, 2008, **47**, 1218-1223.
9. Y. Wang and A. Hu, *Journal of Materials Chemistry C*, 2014, **2**, 6921-6939.
10. D. P. Puzzo, E. J. Henderson, M. G. Helander, Z. Wang, G. A. Ozin and Z. Lu, *Nano Lett.*, 2011, **11**, 1585-1590.
11. M. L. Mastronardi, E. J. Henderson, D. P. Puzzo, Y. Chang, Z. B. Wang, M. G. Helander, J. Jeong, N. P. Kherani, Z. Lu and G. A. Ozin, *Small*, 2012, **8**, 3647-3654.
12. A. Gupta, S. Hartner and H. Wiggers, Nanoelectronics Conference (INEC), 2010 3rd International, 2010.
13. X. Xu, R. Ray, Y. Gu, H. J. Ploehn, L. Gearheart, K. Raker and W. A. Scrivens, *J. Am. Chem. Soc.*, 2004, **126**, 12736-12737.
14. Y.-P. Sun, B. Zhou, Y. Lin, W. Wang, K. A. S. Fernando, P. Pathak, M. J. Meziani, B. A. Harruff, X. Wang, H. Wang, P. G. Luo, H. Yang, M. E. Kose, B. Chen, L. M. Veca and S.-Y. Xie, *J. Am. Chem. Soc.*, 2006, **128**, 7756-7757.
15. H. Liu, T. Ye and C. Mao, *Angew. Chem. Int. Ed.*, 2007, **46**, 6473-6475.
16. A. B. Bourlinos, A. Stassinopoulos, D. Anglos, R. Zboril, V. Georgakilas and E. P. Giannelis, *Chem. Mater.*, 2008, **20**, 4539-4541.
17. H. Zhu, X. Wang, Y. Li, Z. Wang, F. Yang and X. Yang, *Chem. Commun.*, 2009, 5118-5120.
18. S.-L. Hu, K.-Y. Niu, J. Sun, J. Yang, N.-Q. Zhao and X.-W. Du, *J. Mater. Chem.*, 2009, **19**, 484-488.
19. S. C. Ray, A. Saha, N. R. Jana and R. Sarkar, *The Journal of Physical Chemistry C*, 2009, **113**, 18546-18551.
20. L. Tian, D. Ghosh, W. Chen, S. Pradhan, X. Chang and S. Chen, *Chem. Mater.*,

2009, **21**, 2803-2809.
21. D. Mazzier, M. Favaro, S. Agnoli, S. Silvestrini, G. Granozzi, M. Maggini and A. Moretto, *Chem. Commun.*, 2014, **50**, 6592-6595.
22. S. Ruan, J. Qian, S. Shen, J. Zhu, X. Jiang, Q. He and H. Gao, *Nanoscale*, 2014, **6**, 10040-10047.
23. M. Algarra, M. Perez-Martin, M. Cifuentes-Rueda, J. Jimenez-Jimenez, J. C. G. Esteves da Silva, T. J. Bandosz, E. Rodriguez-Castellon, J. T. Lopez Navarrete and J. Casado, *Nanoscale*, 2014, **6**, 9071-9077.
24. S.-T. Yang, L. Cao, P. G. Luo, F. Lu, X. Wang, H. Wang, M. J. Meziani, Y. Liu, G. Qi and Y.-P. Sun, *J. Am. Chem. Soc.*, 2009, **131**, 11308-11309.
25. H. Y. Ko, Y. W. Chang, G. Paramasivam, M. S. Jeong, S. Cho and S. Kim, *Chem. Commun.*, 2013, **49**, 10290-10292.
26. X. Zhang, Y. Zhang, Y. Wang, S. Kalytchuk, S. V. Kershaw, Y. Wang, P. Wang, T. Zhang, Y. Zhao, H. Zhang, T. Cui, Y. Wang, J. Zhao, W. W. Yu and A. L. Rogach, *ACS Nano*, 2013, **7**, 11234-11241.
27. F. Wang, Y.-h. Chen, C.-y. Liu and D.-g. Ma, *Chem. Commun.*, 2011, **47**, 3502-3504.
28. Y. Dong, N. Zhou, X. Lin, J. Lin, Y. Chi and G. Chen, *Chem. Mater.*, 2010, **22**, 5895-5899.
29. Y.-M. Long, L. Bao, J.-Y. Zhao, Z.-L. Zhang and D.-W. Pang, *Anal. Chem.*, 2014, **86**, 7224-7228.
30. D. Ege, W. G. Becker and A. J. Bard, *Anal. Chem.*, 1984, **56**, 2413-2417.
31. Y. Zu and A. J. Bard, *Anal. Chem.*, 2000, **72**, 3223-3232.
32. W. Miao, J.-P. Choi and A. J. Bard, *J. Am. Chem. Soc.*, 2002, **124**, 14478-14485.

CHAPTER 7

Instrumental Methods

Abstract

In this thesis, many experimental techniques were used in order to characterize the properties of materials. Here we describes the most important instrumental methods and their principles.

7.1 UV-Vis absorption measurement

When the light passes through a medium, the light is absorbed and the absorbance (A_s) of a medium at the given wavelength (λ) is defined as $A_s(\lambda) = -\log(I_s/I_0)$, where I_s is the intensity of the light that has passed through the sample, I_0 is the intensity of incident light before passing through the sample. Without the scattering and the aggregation of samples problems, the absorbance follows the Lambert-Beer law as following equation:

$$A_s(\lambda) = -log\left({}^{I_s}/_{I_0}\right) = \varepsilon(\lambda) \cdot l \cdot c$$

where ε is the molar absorption coefficient (in L mol^{-1} cm^{-1}), l is the path length of the light through the medium (in cm), and c is the concentration (in mol L^{-1}). However, the Lambert-Beer law is limit to measure in low concentration samples. In high concentration samples, the linear relationship is not valid anymore. Normally the absorbance measured should below 1.00.

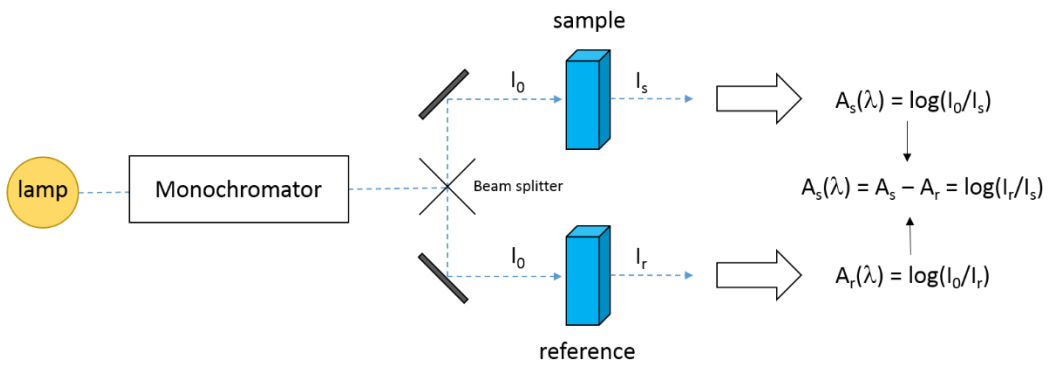

Figure 1. Schematic representation of UV-Vis absorption measurement.[1]

Figure 1 presents the most used double beam setup for absorption measurements. The incident light is split in two beams and directed through each of two cuvettes, one with the sample solution and the other containing solvent as a reference. Absorption spectra shown in this thesis were recorded on the UV 3600 UV-VIS-NIR spectrophotometer from Shimadzu.

7.2 Emission measurement

The general setup of spectrofluorometer to acquire an emission spectrum is shown in Figure 2. The excitation light passes through a monochromator and shoots on the sample (a few percent of the incident light goes to a reference channel). The luminescence generated from the sample, collected at the angle of 90°, is passed through a second monochromator and then reaches a detector. The reference channel uses for correcting the wavelength-intensity dependence of the excitation light.

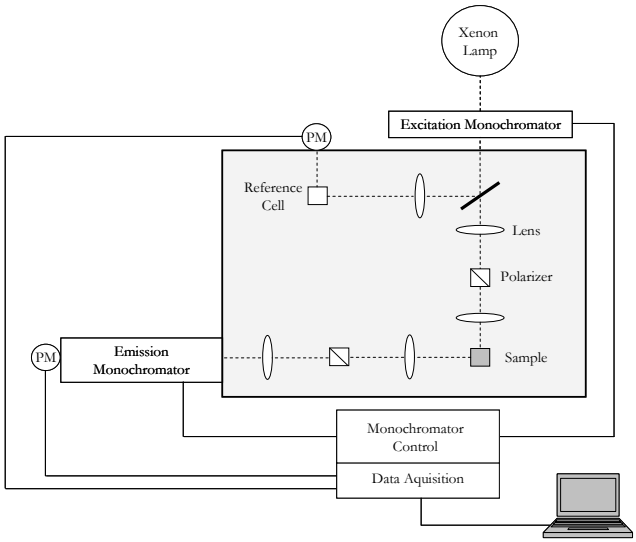

Figure 2. Schematic representation of emission steady state setup.

Steady-state emission spectra in this thesis were recorded on a HORIBA Jobin-Yvon IBH FL-322 Fluorolog 3 spectrometer equipped with a 450 W xenon arc lamp as the excitation source, double-grating excitation and emission monochromators (2.1 nm mm^{-1} of dispersion; 1200 grooves mm^{-1}), and a TBX-04 single-photon-counting device as the detector. Emission and excitation spectra were corrected for source intensity (lamp and grating) and emission spectral response (detector and grating) by standard correction curves.

Emission quantum yield were measured in optically dilute solutions which the absorbance should below 0.1 at excitation wavelength, and compared to reference by the following equation:[2]

$$\Phi_s = \Phi_r \left[\frac{A_r(\lambda_r)}{A_s(\lambda_s)}\right]\left[\frac{I_r(\lambda_r)}{I_s(\lambda_s)}\right]\left[\frac{n_s^2}{n_r^2}\right]\left[\frac{D_s}{D_r}\right]$$

where s and r represent the sample and reference, Φ is the quantum yield, *A* is the absorbance at the excitation wavelength (λ), *I* is the intensity of the excitation light at the excitation wavelength (λ), *n* is the refractive index of the solvent, and *D* is the integrated intensity of the luminescence. *fac*-$Ir(ppy)_3$ (Φ = 0.97), Quinine bisulfate in 1.0 N sulfuric acid (Φ = 0.546) and $Ru(bpy)_3Cl_2$ in air-equilibrated acetonitrile (Φ = 0.028) are commonly used for the references.

Figure 3 shows another way to measure the quantum yields which is by an absolute method[3] with an integrating sphere. It collects all the emitted photons with a calibrated photodiode and sets them into relation with the number of absorbed photons.

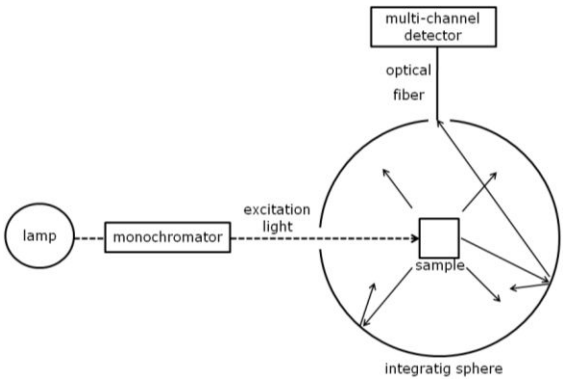

Figure 3. Schematic representation of an integrating sphere setup for quantum yield measurement.

In this thesis, all the quantum yields were performed at a fixed excitation wavelength by using a Hamamatsu Photonics absolute PLQY measurements system (C11347-11) equipped with L9700-01 CW Xenon light source (150 W), monochromator, integrating sphere, and photonics multi-channel analyzer.

7.3 Time resolved Spectroscopy measurement

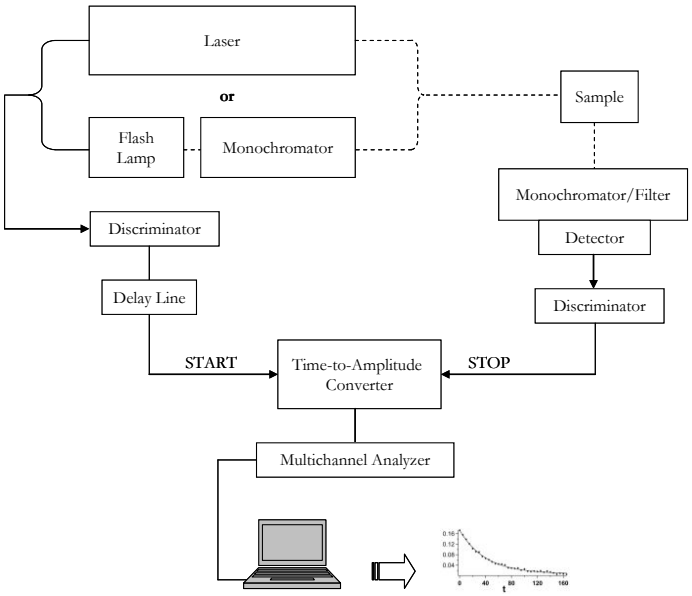

Figure 4. Schematic representation of time correlated single-photon counting (TCSPC) setup.

To understand the time dependent behavior of excited states, the time-resolved techniques is very important tool to apply and acquire the excited states lifetime. Single photon counting (SPC) is a technique based on the ability to detect and count

individual photons to measure the luminescence decay of a sample (Figure 4). The time profile of the decay is determined by measuring the time difference between the sample excitation and the concomitant photon emission detected by the photomultiplier. During the measurement, an electrical pulse is created and directed to the "start" input of the time-to-amplitude (TAC) converter. The electrical response to the sample luminescence is used as the "stop" signal for the TAC. The start pulse initiates the charging of a capacitor while the stop pulse terminates it. The time between the two pulses, which is proportional to the final voltage, is then calculated. Several repetitions of this measurements result in the creation of a histogram of events that corresponds to the luminescent decay curve.

In this thesis, the time-resolved measurements were performed using the PicoHarp 300 equipped with time correlated single photon counting (TCSPC) system on the Fluoro Time 300 (PicoQuant), where a laser source was applied to excite the samples. The laser was mounted directly on the sample chamber at 90° to a Czerny-Turner type emission monochromator (2.7 nm mm^{-1} of dispersion; 1200 grooves mm^{-1}) and collected by a PMA-C 192M single-photon- counting detector. Signals were collected using EasyTau software, and data analysis was performed using FluoFit software (PicoQuant). The quality of the fit was assessed by minimizing the reduced $\chi 2$ function and by visual inspection of the weighted residuals.

7.4 Transmission Electron Microscopy (TEM)

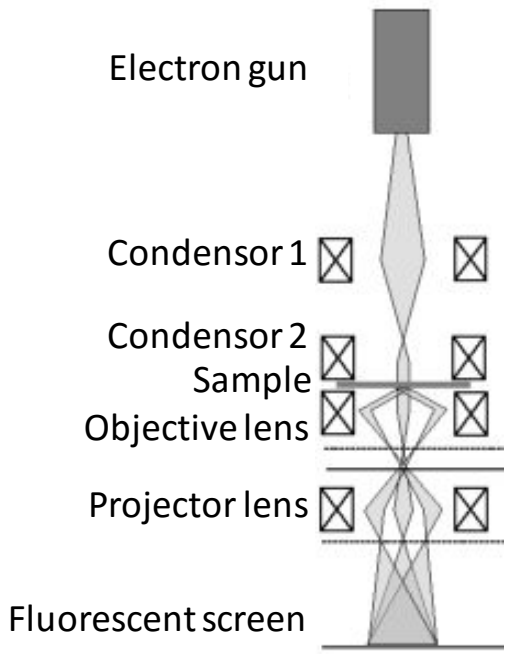

Figure 5. Diagram of a transmission electron microscope.

Transmission Electron Microscopy (TEM) is a powerful technique to produce images of a sample using a high-energy electron beam with energy between 100 to 300 keV in high vacuum. Figure 5 shows the diagram of a TEM instrument. The electron beam source (electron gun) is connected with a high voltage source (100–300 kV), and emit electrons into the vacuum. Then the electrons are the accelerated and focused by the condensers towards the sample, and the electrons that are transmitted through the sample are detected by the fluorescent screen and processed by the image recording system. The condenser lens plays an important role of forming the beam. The condenser lens is not only to focus the light onto the sample but also controlling the diameter of the electron beam. In lower magnification, the electron beam is spread onto the object to illuminate a larger area. When high magnification is applied, the electron beam is strongly condensed onto the object.

7.5 Scanning Transmission Electron Microscope[4]

Excepting TEM, scanning transmission electron microscope (STEM) also gains a lot of attention in examining the samples in atomic scale. As a result, the STEM technique has image resolution up to sub-Å range, provide information on the element composition and electronic structure. Figure 6 presents the diagram of a STEM.[5]

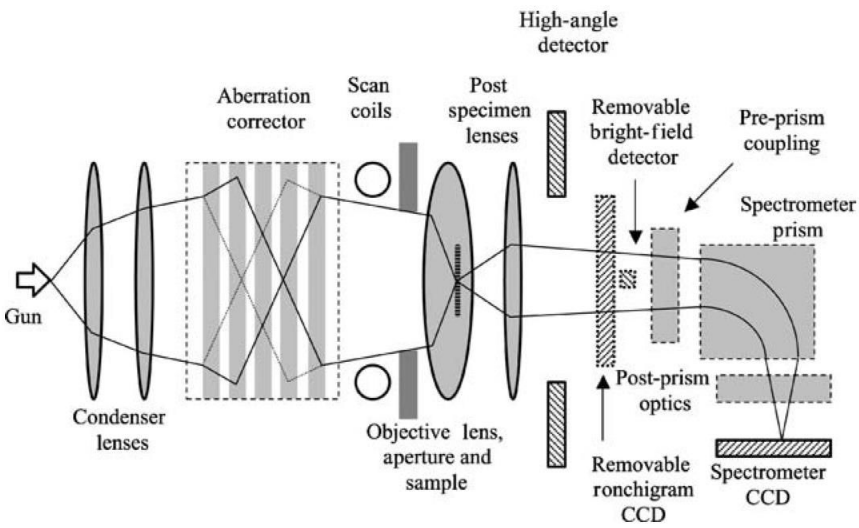

Figure 6. Diagram of a scanning transmission electron microscope. Reprinted with permission from *Annu. Rev. Mater. Res.*, **2005**, *35*, 539–569

The difference between STEM and TEM is that for TEM, a large area of sample is illuminated, the transmitted electron beam is magnified by the lens system after the sample and collected the whole image at once. While in STEM, the electron beam condenses to a tiny probe in an order of 1Å before reaching to the sample and scan the sample in the specific area. Then the electrons are collected to form the image as

function of position. Also STEM has multiple detectors can be used simultaneously, bright field (BF) detector collects the transmitted electron beam and performs the image as in TEM; annual dark field (ADF) detector, surrounds the transmitted beam, collects the scattered electrons in different angles. To have a high contrast image, the high-angle annual dark field (HAADF) detector can be used. The reason is that the high Z (atomic number) atoms scatter the electron to high angles stronger than lighter atoms, resulting the contrast in the image is proportional to Z^2.

7.6 Confocal Microscopy

Confocal microscopy has widely utilized in modern biology and chemistry imaging. The advantage of using confocal microscopy over conventional optical microscopy is to control the depth of field, eliminate out-of-focus light, and collect serial optical sections from thick sample. The basic structure of a confocal microscope is shown in Figure 7.

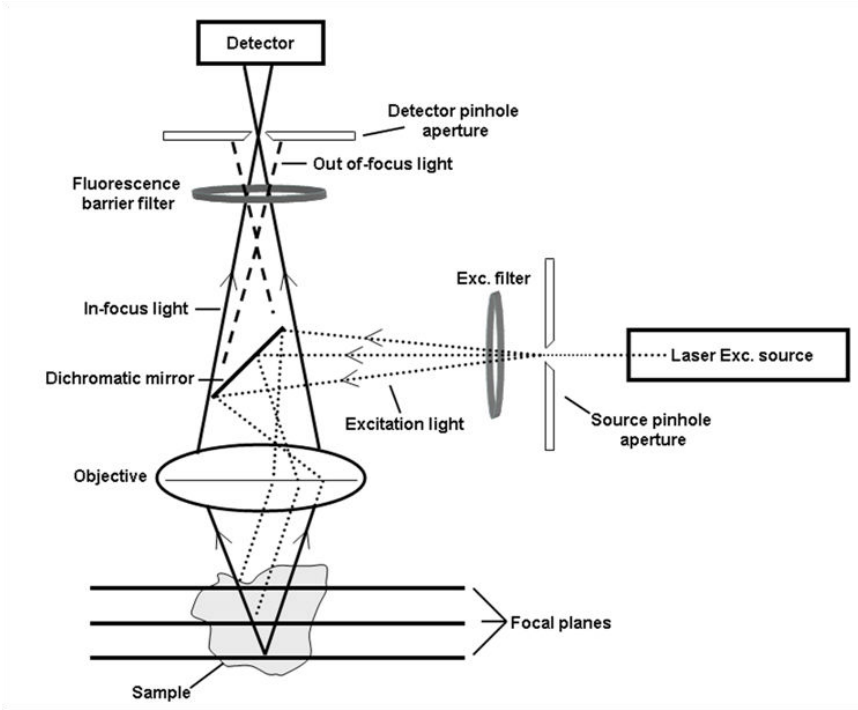

Figure 7. Schematic representation of a confocal microscope.

The coherent light source (e.g. laser) passes through a pinhole and is reflected by a dichromatic mirror and scans a defined focal plane of the specimen. The fluorescence from the specimen is directed back through the objective, passes through the mirror and is focused trough detector pinhole aperture, and finally is collected by a detector. Due to only a small fraction of the out-of-focus fluorescence emission is delivered through the pinhole aperture, most of extraneous light is blocked and does not contribute to the resulting image, this technique offers higher resolution. In contrast to

traditional microscopes, the whole sample is illuminated by an intense light source and the fluorescence from the sample is directly projected onto the detector. Modern confocal instruments are equipped with multiple laser sources, a scan head, electronic detectors (photomultipliers) and a computer for acquisition, processing, and analyzing the images.

In this thesis the confocal images were acquired by using Zeiss LSM 710 confocal microscope with 63× magnification and numerical aperture (NA) 1.3 of Zeiss LCI Plan-NEOFLUAR water immersion objective lens (Zeiss GmbH, Germany).

7.7 X-ray photoelectron spectroscopy (XPS)[6]

X-ray photoelectron spectroscopy is a powerful surface analytical tool due to the extremely sensitivity and ability to distinguish the signal from the vast majority of atoms present in the sample. Figure 8 shows an example of XPS process, when an incident X-ray (200~2000eV) is applied, an electron from the K shell is ejected from the atom (1s electron). The photoelectron is then collected by the electron multiplier detector and analyzed by the electron spectrometer to acquire the kinetic energy (E_k).

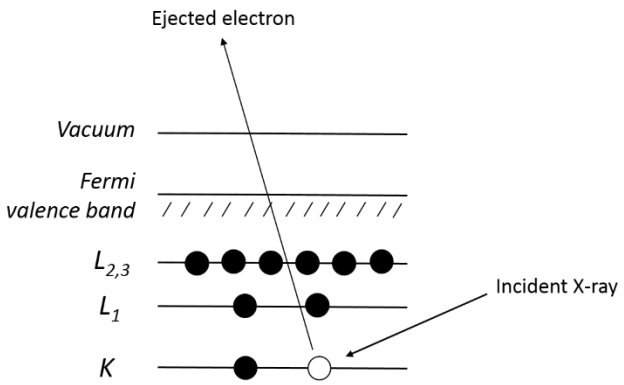

Figure 8. Schematic diagram of the XPS process.

The binding energy of the electron (E_B) can identify the electron both from its parent element and the atomic energy level. It can be described as below:

$$E_B = h\nu - E_k - W$$

where $h\nu$ is the photo energy, E_k is the kinetic energy of the electron and W is the spectrometer work function. The binding energy is easy to calculate from those three parameters which are known or measurable.

In this thesis, the XPS measurements were done by a Thermo Scientific K-Alpha X-ray Photoelectron Spectrometer using a monochromatic AlKα radiation (hν =

1486.6 eV). Survey measurements were performed with a 200 eV analyzer pass energy and a 1 eV energy step size to calculate the atomic concentrations. Element scans were performed with a 50 eV analyzer pass energy and a 0.1 eV energy step size obtain the chemical state information. All the obtained binding energies were referenced to carbon 1s peak at 284.80 eV.

7.8 Electrochemistry[7]

Cyclic Voltammetry (CV)

Cyclic voltammetry is the most used electroanalytical technique. It is performed by connecting an electrochemical potentiostat to an electrochemical cell. The cell contains a sample solution and three electrodes: working electrode (WE), reference electrode (RE) and counter electrode (CE). A cyclic voltammogram is obtained by applying the working electrode potential swept linearly between two voltages at a fixed rate. Figure 8 shows the cyclic voltammogram. As the potential is swept back and forth, it crosses the formal potential, E_0, of an analyte and a current flows through the electrode that either oxidizes or reduces the analyte.

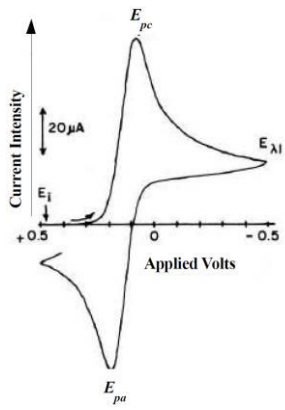

Figure 9. Cyclic voltammogram

From Figure 9, two peaks are obtained when the potential sweep back and forth, the peak potential for the anodic sweep, E_{pa}, and the peak potential for the cathodic peak, E_{pc}. The difference between E_{pc} and E_{pa}, ΔE, can be calculated, and if the redox couple is reversible, then the relationship $n\Delta E = 59n$ mV holds true, where *n* is the number of electrons involved in the redox couple. Also, the anodic peak current, i_{pa}, is equal to the cathodic peak current, i_{pc}, so that the relationship $(i_{pa}/i_{pc}) = 1$ also holds true for the reversible redox couple. Besides, if 59 mV< ΔE <100 mV, the redox couple is described as quasi-reversible, and if ΔE >100 mV, the redox couple is described as

irreversible. The formal potential E_0 for a reversible redox couple is termined as the average of the two peak potentials as follows:

$$E_0 = \frac{(E_{pa} + E_{pc})}{2}$$

Differential Pulse Voltammetry

Differential Pulsed Voltammetry (DPV) technique is used in this thesis. The advantage to use pulse voltammetric techniques because it can increase the detection limits to 10^{-8} M, by substantially increasing the ratio between the faradic and non-faradic currents. Figure 10 shows the potential-time curve. The signal comes from the application of fixed-amplitude pulses on a linear potential ramp. The current is sampled twice: before the pulse application (at point 1 in the Figure 10) and again late in the pulse life (point 2 in Figure 10). The first current is instrumentally substracted from the second and this current difference is plotted versus the applied potential, resulting in the differential pulse voltammogram. For the reversible redox couple, it shows the symmetrical peaks; while irreversible reaction shows unsymmetrical peaks.

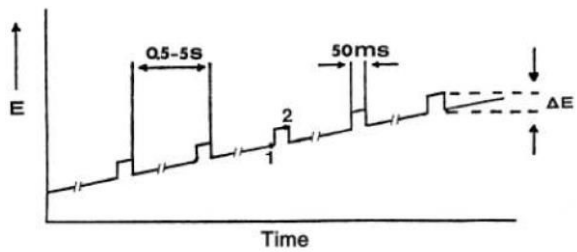

Figure 10. An example of applied potential versus time in DPV.[8]

The electrochemical characterization was performed using a CHI750C Electrochemical Workstation (CH Instruments, Inc., Austin, TX, USA). A conventional three electrode cell configuration was used consisting of a silver wire as quasi-reference electrode (QRE), a platinum wire as counter electrode and a 3 mm diameter glassy-carbon disk , GC (66-EE047 Cypress Systems) as working electrode. 0.1 M tetrabutyl ammonium hexafluorophosphate ($TBAPF_6$) was used as supporting electrolyte. Both Cyclic voltammetry (CV) and Differential Pulse Voltammetry (DPV) were applied for all Ir complexes. All the measurement was corrected by using ferrocene (Fc) as reference.

7.9 Reference

1. B. Valeur and M. N. Berberan-Santos, *Molecular fluorescence: principles and applications*, John Wiley & Sons, 2012.
2. G. A. Crosby and J. N. Demas, *The Journal of Physical Chemistry*, 1971, **75**, 991-1024.
3. J. C. de Mello, H. F. Wittmann and R. H. Friend, *Adv. Mater.*, 1997, **9**, 230-232.
4. S. Pennycook, A. Lupini, M. Varela, A. Borisevich, Y. Peng, M. Oxley, K. Van Benthem and M. Chisholm, in *Scanning Microscopy for Nanotechnology*, Springer, 2007, pp. 152-191.
5. M. Varela, A. R. Lupini, K. v. Benthem, A. Y. Borisevich, M. F. Chisholm, N. Shibata, E. Abe and S. J. Pennycook, *Annu. Rev. Mater. Res.*, 2005, **35**, 539-569.
6. J. F. Watts and J. Wolstenholme, *An Introduction to Surface Analysis by XPS and AES, by John F. Watts, John Wolstenholme, pp. 224. ISBN 0-470-84713-1. Wiley-VCH, May 2003.*, 2003, **1**.
7. A. J. Bard and L. R. Faulkner, *Electrochemical methods: fundamentals and applications*, Wiley New York, 1980.
8. J. Wang, *Analytical electrochemistry*, John Wiley & Sons, 2006.

Summary

The aim of this thesis in titled “Luminescent Nanomaterials for diagnostic applications” is the synthesis, characterization and bio-applications of ultrasmall (< 5 nm) nanomaterials. In particular silicon nanoparticles, Si NPs, is the focus of this work. As shown in Figure S1, the work of this thesis deals with the modification of the silicon nanoparticles surface with sugars and luminescent labels, and the nanomaterials are applied for cellular imaging. In addition, a series of iridium(III) complexes were synthesized and used for electrochemiluminescence (ECL) application. ECL is an imaging tool that generate, in luminescent molecules, emissive excited states without light excitation. It has gained a lot of attention in many bioassays because of its sensitivity. The Si NPs were decorated with metal complexes to improve the excited state properties and in particular the luminescent lifetimes. A comparison with carbon dots is presented, investigating both silicon and carbon nanoparticles in ECL experiments.

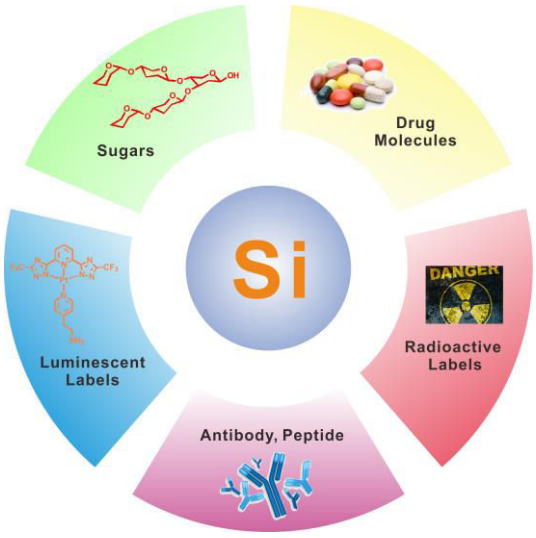

Figure S1. Silicon nanoparticles and their surface modification

This thesis is organized into 7 chapters, in chapter 1, a brief introduction on the materials as well as an introduction to luminescent labels, such as organic fluorophores, metal complexes and quantum dots, for optical imaging and on the diagnostic methods used in clinic nowadays. In addition, an introduction on silicon nanoparticles (Si NPs) and their preparation methods from the literature. Finally to help the reader on not so common techniques, the principle of electrochemiluminescence (ECL) is presented.

Chapter 2 presents the novel iridium(III) complexes for ECL applications. A π conjugated N^N (1H-pyrazole[5,4-h]quinoline) ligand is introduced, and together with two C^N (dfppy, ppy, pq or piq) ancillary ligands, coordinated to Ir(III) ions leading to four cyclometalated complexes. The complexes depicted in Figure S2 have been isolated in good yields and their photophysical an electrochemical properties fully investigated. Also, the single crystal structure of **3** was obtained and showed the octahedral geometry typical of the iridium compounds, with two phenylisoquinoline at trans position, and one N^N ligand coordinated to the metal ion. ECL measurements were performed using three methods: annihilation, TPA co-reactant and BPO co-reactant methods. Complexes **1**-**3** showed weak ECL efficiency in annihilation and TPA co-reactant methods due to the unstable redox species and unmatched energy level against to TPA. However, in BPO co-reactant method, all complexes exhibited medium to strong ECL efficiency compared to $[Ru(bpy)_3]^{2+}$ standard, especially the complex 4 displayed 2.18 times higher efficiency than $[Ru(bpy)_3]^{2+}$. (Figure S2)

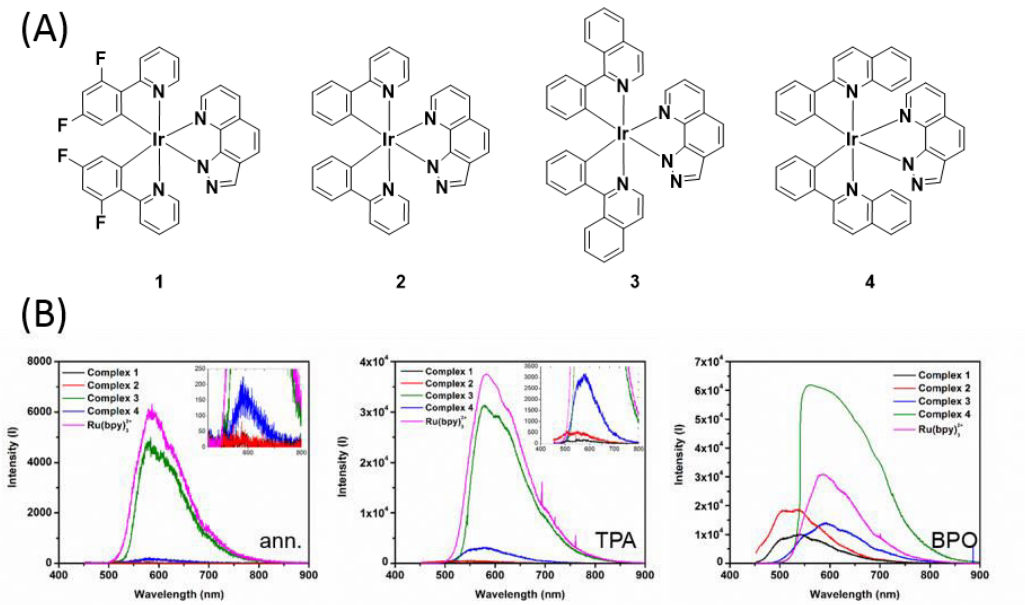

Figure S2. (A) The structure of Ir(III) complexes. (B) Electrochemiluminescence spectra of Ir complexes 1-4 in different method. (Left) annihilation method (middle) TPA co-reactant method (right) BPO co-reactant

In chapter 3, we describe the functionalization of Si NPs with two different functional groups, amino and carboxylate. TEM/STEM imaging showed that the particles have a size of 3.1 nm for Si-NH_2 NPs, and 3.9 nm for Si-COOH NPs. Both particles were fully characterized by FT-IR and XPS measurements. Also the luminescent properties are discussed.

In chapter 4 the Si-COOH NPs are further coupled with glucose (Si-Glc NPs) and use for bioimaging. The in vitro study (Figure S3) showed that Si-Glc NPs were rapidly uptaken by HeLa cells, and the particles are localized in the lysosome (overlap coefficient 0.84) and a small portion in the endoplasmic reticulum, ER (overlap coefficient 0.62). The Si-Glc NPs fast internalization is most likely due to the presence of glucose transporter (GLUT) which exist in many cancer cells. A comparison with Si-COOH NPs, that are also taken into the HeLa cells, and located in lysosome (overlap coefficient 0.87) and endoplasmic reticulum, ER (overlap coefficient 0.86). Cell viability tests revealed that both Si NPs were biocompatible and no toxic to HeLa cells. Even at high concentration (100 µg/mL), the cell viability was estimated to be, 80.7% for Si-COOH NPs and 84.5% for Si-Glc NPs.

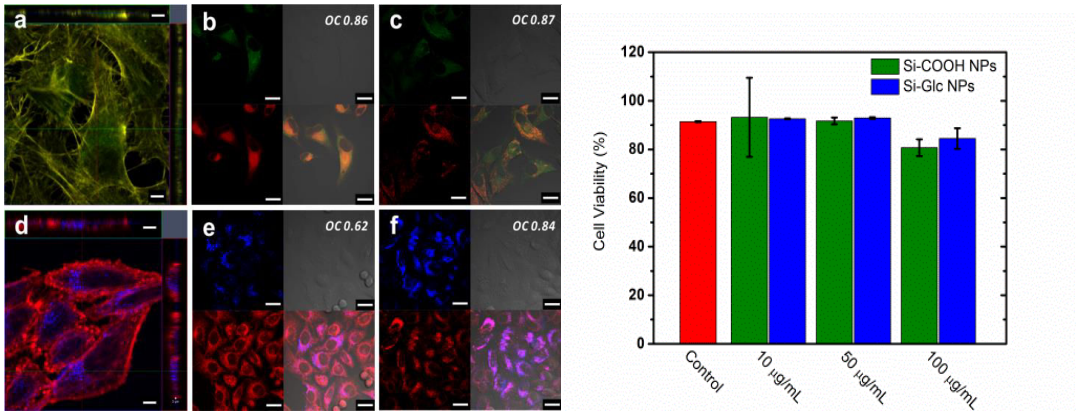

Figure S3. (left) Confocal imaging of Si-COOH NPs at 100 µg/mL (a) – (c) and Si-Glc NPs at 100 µg/mL (d) – (f) internalized in HeLa cells. (a) Z stack of Si-COOH after 24 hours incubation. (b) Cellular localization of Si-COOH in ER. (c) Cellular localization of Si-COOH in the lysosome. (d) Z stack of Si-Glc after 24 hours incubation. (e) Cellular localization of Si-Glc in ER. (f) Cellular localization of Si-Glc in lysosome. Scale bar: 5 µm for (a) and (d); 20 µm for (b), (c), (e) and (f). (right) Cell viability test of Si-COOH and Si-Glc NPs with different concentration, 10, 50 and 100 µg/mL in HeLa cells after 24 hours incubation.

Chapter 5 describes the coupling of Si NPs and platinum(II) complexes. Two Pt(II) complexes, Pt-CF_3 and Pt-tmp, were synthesized and conjugated to Si-COOH NPs. Both nanoparticles were characterized by FT-IR, XPS measurements. Si-[PtCF3] NPs showed an interesting aggregation induced emission (AIE) effect. The nanoparticles were dispersed in MeOH solution and water as unfavorable solvent was added. With increasing water fraction, the emission intensity increases and the emission maximum bathochromic shift. (Figure S4) The enhanced emission is due to the stacking of Pt(II) complexes, (see the chapter for details) and the aggregation protects the luminescence

by dioxygen quenching. Also due to the formation of a Pt-Pt interaction, a new transition band, metal-metal-to-ligand charge transfer (MMLCT), is generated and the emission is bathochromic shift and the emission quantum yield increases. However, in the Si-[Pttmp] NPs, the AIE effect is not observed. Furthermore, both Si-[PtCF3] and Si-[Pttmp] NPs were uptaken into HeLa cells, indicating that those particles are good luminescent labels for bioimaging.

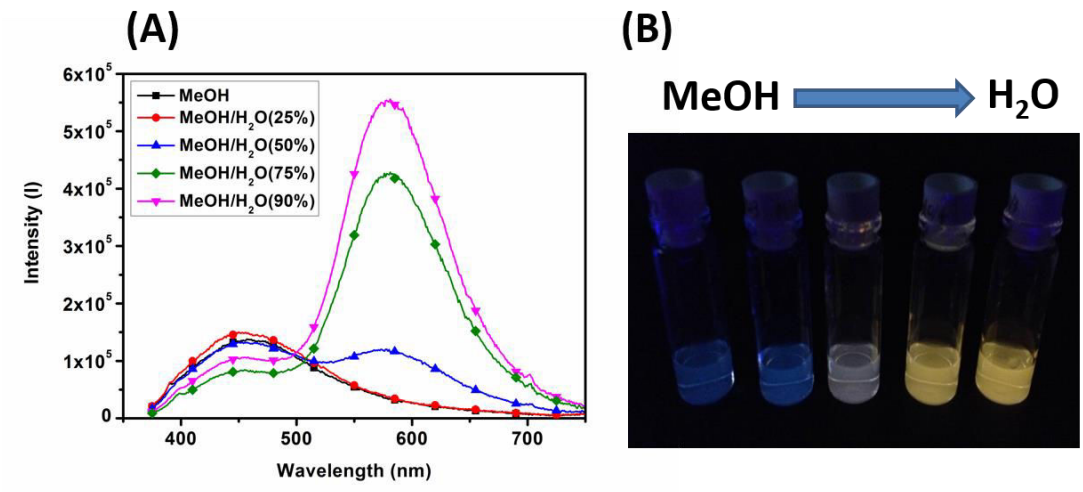

Figure S4. (A) Emission spectra of Si-[PtCF3]-2 NPs in MeOH/water mixed solvent with different fraction of water and excitation at 340 nm. (B) Samples with increasing amount of water fraction under UV lamp.

Chapter 6 reports two systems, ruthenium complex conjugated carbon dots, C-[Ru] NPs, and iridium complex conjugated silicon nanoparticles. In order to compare the ECL efficiency with the standard, $[Ru(bpy)_3]^{2+}$, the concentration of metal complexes on the NPs is monitored by UV-Vis absorption and fixed at 10^{-5} M. The ECL experiments were done in ProCell solution using TPA as co-reactant and applying a voltage at +1.4 V on glassy carbon electrode. Interestingly the metal complexes are not quenched and keep same performance when binding to the carbon dots. (Figure S5) From the ECL emission spectra, C-[Ru] NPs exhibited a slighter higher ECL efficiency (107%) than $[Ru(bpy)_3]^{2+}$ alone (100%). The other system, Si-[Ir] NPs, exhibited lower ECL efficiency (75%) which might due to the slow mass diffusion of Si NPs. However work is still in progress to optimize the systems and to evaluate the number of complexes per particle.

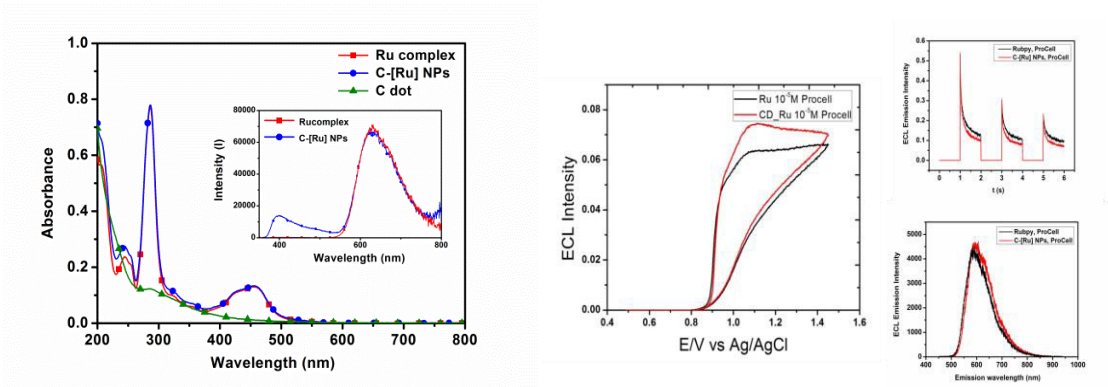

Figure S5. (left) UV-Vis absorption spectra of C dot, C-[Ru] NPs and $Ru(bpy)_3$ used as standard, in water. Inset: emission spectra of C-[Ru] NPs and the standard in water. (right) CV and ECL measurements of the investigated system.

Chapter 7, discusses the instruments and techniques used in this thesis, as well as the experimental details are summarized.

In conclusion, this thesis shows that ultrasmall nanoparticles can be an interesting tool in diagnostics and imaging *in vitro* and eventually *in vivo*. We demonstrate the synthesis and surface modification of Si NPs. Glucose modified Si NPs show high cellular uptake and biocompatibility, and it is highly potential for further applications and in particular work is progress to look at the crossing of the blood brain barrier for brain imaging. Also, Pt(II) modified Si NPs exhibit an interesting AIE effect and enable for bioimaging. Novel ECL labels based on Ir(III) complexes and on the nanoparticles where the surface has been modified with metal complexes is shown. These two systems, with high ECL performance, give us new directions for the design of new ECL probes.

This work was supported by the Helmhotz Virtual Institute “Functional nanomaterials for multimodality cancer imaging” (Nano-Tracking, Agreement Number VH-VI-421). The work described was done in cooperation with other units: Max Planck Institute of Colloids and Interfaces (Berlin, Germany), Helmholtz-Zentrum Dresden-Rossendorf (Dresden, Germany), University of Heidelberg (Heidelberg, Germany), University College Dublin (Dublin, Ireland) and Monash University (Melbourne, Australia).

Acknowledgements

Four year PhD life is an exciting and adventurous journey. Thanks all of you who company and support me during the period of my PhD study. I spent a wonderful time in Münster, and Strasbourg. First of all, I would like to thank my supervisor, Prof. Luisa De Cola. Thank you for offering me this opportunity to join this amazing group. We have a challenge project and you always come up new ideas and help me a lot. Also thanks the financial support from the nanotracking project.

It is pleasure to spend first year PhD in Münster, my starting point of the journey. Thank you Cheng-Han, Fan-Chi and Zhen, you explain and teach me a lot of German styles so that I can familiar with the life in Germany in a short time. Thank you Strassert, you are so kind to teach us the photophysics and the experimental techniques. Thanks Simone, not only for copper story but also the daily life, we have so much fun in exchange the language, you are a grateful Italian teacher! Thanks to Naveen, always bring us crazy ideas share funny stories. Thank you Noviyan, gave me some suggestion to deal with the problem. Thanks Henning, help me solve a lot of paper work in German. Thanks to Cristina, you are always so kind with me. Thanks all the members in Münster, Seda, Jesus, Lola, Claudia, Malte, I have a memorable German life.

Moving to Strasbourg and built up a new lab, it is a really difficult work and thanks all the people who clean, organize and set up the lab together. Especially Henning, Nadia, Mia and Alessandro, we spent all the week to organize three thousand chemicals! In addition, in the beginning, it is hard to start new life in France. I would like to thank Youssef and Ricardo, you are so kind to help me to deal with all the French problem, show me the French culture and improve my French. Also the Taiwanese friends I met in Strasbourg, thank you for giving me a lot of information to live in France.

During the stay in Strasbourg, firstly I would like to thank Claire for doing all the administrative works. Thank you Ines for taking care of all the order of chemicals and solvents so that we can focus in the research. Thanks to my partner, Nadia, we have been through all challenges from Münster to Strasbourg. Because of your help, I can manage and handle this project. Thank you Eko, you are so helpful not only in solving problem and giving ideas, but also in sharing your opinions and experiences. Thanks to Dedy for all the cell experiments. Besides, we spend great time together in conference and also ski for all the winter season. Thanks Pengkun, a wonderful chef with crazy mind, for the XPS measurements. Because of you, I acquire a lot of living skills,

cooking, haircut, etc. Thanks to Amparo, always gives me the suggestion and advice for the presentation and writing. Thank you Elena, without your help, I can't finish all the ECL part.

Thanks to Matteo and Alessandro for the Pt complex story, offer me the ligand and save me time. You guys always look so strict and cool but I know you are very kind to help. Thanks Serena for the ECL measurements. Thanks to Federica, show me the ski skill we have a great time in Lille. Thank you Stephan, you make a great DFT calculation and I think you can be a good father as well. Thanks to Valentin and Céline, help me to do all the administrative work in Karlsruhe. Thanks to Shaojun, the Chinese leader in ISIS, for organizing Chinese meeting and dinner. Thanks to Di for the TEM measurements. Also all the member in Strasbourg, Mia, Deane, Veronika, Laura, Leana, Loic, Etienne, Remi, Giacomo, Francesca, John, Angélique, Hiroki, Frank, thank you very much for all the help and discussion.

Thanks to nanotracking project, I have an opportunity to visit Prof. Peter Seeberger's group for one month. I would like to thank Chian-Hui, you are so kind to teach me the sugar chemistry and we have good times in Berlin. Thank you Priya and Silvia, it is really happy to meet you and work together, also show me the beauty of Berlin. Also thanks to the partner of nanotracking project, Dr. Stephan and Sebastian, for the collaboration in Si NPs.

In addition, Youssef, John, Amparo and Damiano, thank you for helping me to read the thesis and translate the summary to French.

Finally, I would like to thank my parents and grandparents. I am very thank you that give me the freedom to choose what I want and study abroad. Also thanks my sister and brother to take care of my family. Although it is far away from home, I still miss you a lot!

Curriculum Vitae

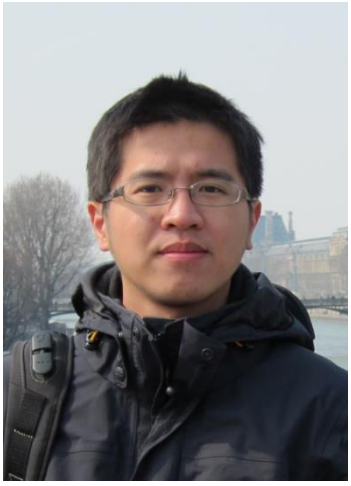

Personal Information

First name: **Chien-Wei**
Surname: **HSU**
Nationality: Taiwanese
Birthday: 17.03.1986
Birthplace: New Taipei city, Taiwan
Current Address: 21 rue de l'Argonne,
67000 Strasbourg, France
E-mail: cwhsu@unistra.fr
chien-wei.hsu@kit.edu

Education

11. 2011 – 09.2015

PhD student, Institut de Science et d'Ingénierie Supramoléculaires (I.S.I.S.)
Univesité de Strasbourg, France
Thesis title: Luminescent nanomaterials for diagnostics applications (Supervisor: Prof. Luisa De Cola)

07. 2008 – 06. 2010

Master in Chemistry, National Tsing Hua University, Taiwan.
Thesis title: Synthesis of neutral Cu(I), Ag(I) and Au(I) complexes and their photophysical properties (Supervisor : Prof. Yun Chi) GPA: 3.91/4.00

09. 2004 – 06. 2008

Bachelor in Chemistry, National Cheng Kung University, Taiwan
GPA: 3.75/4.00, Rank: 1/63

Professional Experience

09.2012 – present

Working experience in Institute of Nanotechnology, Karlsruhe Institute of Technology, Germany (Prof. Luisa De Cola Group)

02.2014 – 03.2014

Short term visit Prof. Peter Seeberger group, Max Planck Institute of Colloids and Interface, Germany

11.2011 – 09.2012

Working experience in Westfälische Wilhelms - Universtät Münster, Germany

(Prof. Luisa De Cola Group)

07. 2010 – 09. 2011

Research assistant, Department of Chemistry, National Tsing Hua University, Taiwan

Research: Synthesis of Ru(II) complex for DSSCs application

09. 2008 – 01. 2010

Teaching assistant, Department of Chemistry, National Tsing Hua University, Taiwan

Publication

Paper

1. Sugar-functionalized silicon nanoparticles for imaging and analysis of low-affinity carbohydrate/carbohydrate interactions (manuscript in preparation)
   Chian-Hui Lai, Julia Hütter, Chien-Wei Hsu, Hidenori Tanaka, Luisa De Cola, Bernd Lepenies,* and Peter H. Seeberger*
2. Photoluminescent 3D lanthanide MOFs with a rare (10, 3)-d net based on a tripodal organic linker. *CrystEngComm*, **2014**, *16*, 6469-6475
   Qing-Yuan Yang, Mei Pan*, Shi-Chao Wei, Chien-Wei Hsu, Jean-Marie Lehn and Cheng-Yong Su*
3. Pure White-Light and Yellow-to-Blue Emission Tuning in a Single Crystal of Dy3+ Metal-Organic Framework. *Chem. Commun.*, **2014**, *50*, 7702-7704
   Qing-Yuan Yang, Kai Wu, Ji-Jun Jiang, Chien-Wei Hsu, Mei Pan*, Jean-Marie Lehn and Cheng-Yong Su*
4. Harvesting Highly Electronically Excited Energy to Triplet Manifolds: State-Dependent Intersystem Crossing Rate in Os(II) and Ag(I) Complexes. *J. Am. Chem. Soc.* **2012**, *134*, 7715-7724
   Cheng-Chih Hsu, Chao-Chen Lin, Pi-Tai Chou*, Chin-Hung Lai, Chien-Wei Hsu, Chen-Huey Lin and Yun Chi*
5. Ru(II) sensitizers with a tridentate heterocyclic cyclometalate for dye-sensitized solar cells. *Energy & Environmental Science*, **2012**, *5*, 7549-7554
   Chien-Wei Hsu, Shu-Te Ho, Kuan-Lin Wu, Yun Chi*, Shih-Hung Liu and Pi-Tai Chou*
6. Systematic Investigation of the Metal-Structure–Photophysics Relationship of emissive d^{10}-Complexes of Group 11 Elements: The Prospect of Application in Organic Light Emitting Devices. *J. Am. Chem. Soc.* **2011**, *133*, 12085
   Chien-Wei Hsu, Chao-Chen Lin, Min-Wen Chung, Yun Chi*, Gene-Hsiang Lee, Pi-Ti Chou*, Chin-Hao Chang* and Pin-Yang Chen

Patent

1. 2-phenyl-6-azolylpyridine-based ligand and group VIII transition metal complex Chi, Yun; Hsu, Chien-Wei; Ho, Shu-Te *US patent* **2013**, US20130018189 A1
2. 4, 4'-dicarboxy-2, 2'-bipyridine derived tridentate ligand, metal complex containing the same, and application thereof. Chi, Yun; Li, Cheng-Xuan; Yang, Shen-Han; Wu, Hsin-Pei; Wu, Kuan-Lin; Hsu, Chien-Wei; Chang, Shih-Han *US patent* **2012**, US 20120247561 A1
3. Emissive transition-metal complexes with both carbon-phosphorus ancillary and chromophoric chelates, synthetic method of preparing the same and phosphorescent organic light emitting diode thereof. Chi, Yun; Hung, Jui-Yi; Lin, Cheng-Huei; Chou, Pi-Tai; Pai, I-Hsuan; Hsu, Chien-Wei *US patent* **2009**, US2009/0209756 A1

Poster (oral) and conference

1. Synthesis and characterization of silicon nanoparticles for bioimaging (E-MRS 2015 Spring, oral presentation) C.-W. Hsu and L. De Cola*
2. Silicon Nanoparticles for bioapplications. (5th EuCheMS) C.-W. Hsu, N. Licciardello, D. Septiadi, S. Hunoldt, K. Viehweger, H. Stephan, L. De Cola*
3. SILICON NANOPARTICLES: From Synthesis, Characterization to Application in Biomedicine. (ICP2013) C.-W. Hsu, N. Licciardello, D. Septiadi, S. Hunoldt, K. Viehweger, H. Stephan, L. De Cola*
4. Photophysical properties of Cu(I), Ag(I), Au(I) metal complexes with d^{10} electronic configuration. (24th ICOMC) C.-W. Hsu, Y. Chi*, C.-C. Lin, and P.-T. Chou*

Awards

- Award of outstanding student for academic achievement in 2005&2006
- Tasco Chemical Corporation Scholarship in 2007

UNIVERSITÉ DE STRASBOURG

EDSC
École Doctorale des Sciences Chimiques

Chien-Wei Hsu

Luminescent Nanomaterials for diagnostic applications

Résumé

Le travail de cette thèse intitulée "Nanomatériaux luminescents pour des applications en diagnostic" consiste en la synthèse, la caractérisation et les applications en bioimagerie des nanomatériaux. Des nanoparticules de silicium ont été synthétisées et modifiées avec des groupements fonctionnels (amino, carboxylate, sucre et complexes de platine(II)) sur la surface et appliquées dans l'imagerie cellulaire avec des cellules HeLa. En outre, l'ensemble des nanoparticules de silicium modifiées avec des complexes de platine(II) présentent un effet d'émission d'agrégation induite (AIE) intéressant. Par ailleurs, une série de complexes d'iridium(III) ont été synthétisés permettant d'obtenir une émission allant du jaune au rouge. Ces complexes d'iridium(III) ont en outre été utilisés pour une application en électrochimiluminescence (ECL). L'ECL est un outil d'imagerie qui génère des émissions sans excitation lumineuse et qui attire de plus en plus l'attention dans les analyses biologiques. Des nanosytèmes de « carbon dots » et des nanoparticules de silicium modifiés avec des complexes métalliques ont également été étudiés pour des propriétés en ECL.

Résumé en anglais

The work of this thesis titled "Luminescent Nanomaterials for diagnostic applications" is synthesis, characterization and bioimaging applications of nanomaterials. Silicon nanoparticles were synthesized and modified with different functional groups such as amino, carboxylate, sugar and platinum(II) complex on the surface, and applies for cellular imaging at HeLa. Moreover, the assembly platinum(II) complexes modified silicon nanoparticles exhibit an interesting aggregation induced emission (AIE) effect. In addition, a series of iridium(III) complexes were synthesized with tunable emission color from yellow to red. Those iridium(III) complexes were further used for electrochemiluminescence (ECL) application. ECL is an imaging tool that generate emission without light excitation and has gained more attention in many bioassays. Besides, nanosystem of metal complex modified carbon dots and silicon nanoparticles were also investigated the ECL properties.